Measurement of the Size Distribution of Rocks on a Conveyor Belt Using Machine Vision

Tony Brian Lange

A thesis submitted to the Faculty of Engineering, University of the Witwatersrand, Johannesburg, in fulfillment of the requirements for the degree of Doctor of Philosophy in Electrical Engineering.

Johannesburg, 1990.

DECLARATION

I declare that this thesis is my own, unaided work. It is being submitted for the Degree of Doctor of Philosophy at the University of the Witwatersrand, Johannesburg. It has not been submitted before for any degree or examination at any other University.

fifth day of July 1990

ABSTRACT

This research is concerned with the online measurement of the size distribution of rocks on a conveyor belt. The measurement process developed in this thesis is based upon experimental work as a consequence of intractable mathematics developed when extrapolating models of ideal particle systems to rocks on the conveyor belt.

Initial experimentation and background theory motivate the use of machine vision incorporating two-dimensional image processing and analysis techniques for the rocksize measurement. The measurement process thus consists of images of rockscenes which are processed to produce traces, from which populations of chord-length intercepts are measured and finally converted to size distributions.

The traces or rock boundaries are produced by combining edge detection, thresholding and morphological techniques. Because of occlusion and the random nature of the rock patterns, the edge detection and segmentation process is error prone. Thus the boundary patterns must be subjected to edge correction to produce corrected segmented-edge patterns from which chord-lengths can be measured.

The rockstream on the conveyor belt is a stochastic process where each image and associated chord-length distribution is a sample of the random variable rocksize distribution. Thus because of the stochastic nature of the rockstream and rock-segmentation errors, existing analytical and inversion techniques produce meaningless size distributions when transforming from chord-length. Thus a new approach is developed where the chord-length distributions are processed statistically with moment or morphological methods to transform the populations of chord-length distributions into meaningful size data.

The first moment of the measured chord-length distribution allows for the determination of average-sieve size with a variance of between 5-25% over a size range of 6:1. Weighted moment methods produce distributions which are visually and qualitatively indicative of the sieve size distribution of rocks on the conveyor belt. Weighted moment method also present data from which the proportion by mass of larger rocks to smaller rocks may be estimated.

To my wife

Karen

ACKNOWLEDGEMENTS

I would like to thank the following persons and institutions for their generous support and invaluable advice during the course of this research work.

My supervisor, Professor H. Hanrahan of the University of the Witwatersrand for his guidance and solid support. His suggestions and insight to the problems encountered had a profound effect on the outcome of this research.

Mr G. Sommer, Director of the Measurement and Control Division of Mintek, who's confidence, enthusiasm and encouragement during this work is greatly appreciated.

Dr I. Barker and Dr D. Hulbert both of Mintek, for their invaluable advice on certain aspects of mathematics and statistics confronted during this research. In particular, the long and tortuous discussions with Dr Barker were invaluable in sorting out the many ambiguities associated with this work.

Professor B. Stewart for providing the initial momentum to this research work, and Professor R. King for his comments on my work.

Dr E. Oosthuyzen of Mintek who introduced me to the extraordinary world of mathematical morphology.

Dr D. Salter for his inspiration and unbounded support of this work.

My colleagues P. Mailer, and Dr O. Pauw who discussed and advised on many diverse aspects encountered during this investigation.

Mintek for allowing and for providing the facilities with which to carry out this research. There are also numerous members of the Measurement and Control Division who helped with hardware development as well the laborious experimental work on the conveyor belt-test rig. The Mintek Librarians are also to be thanked for assisting me with the literature surveys.

Dr. L. Lange, my brother, who provided much advice and discussions on the philosophical aspects of this work.

My Parents, Marion and David Lange, and youngest brother Steven, for their support, encouragement and patience.

My wife Karen for her help, advice, encouragement, and especially her tolerance during demanding times.

CONTENTS

i DECLARATION ii
ii ABSTRACT iii
iii DEDICATION iv
iv ACKNOWLEDGEMENTS v
v CONTENTS vi
vi LIST OF FIGURES xi
vii LIST OF TABLES xxiii
viii SYMBOLS AND NOTATION xxiv

1 INTRODUCTION 1
1.1 PROBLEM STATEMENT AND RESEARCH OBJECTIVE 1
1.2 BACKGROUND 2
1.2.1 The Rock Material 5
1.2.2 Particle Size, Shape and Distribution 7
1.3 LITERATURE SURVEY 12
1.3.1 Review of rock size instruments 13
1.3.2 Review of size theory 16
1.3.3 Review of machine vision and image processing 18
1.3.4 Summary and Conclusions 19
1.4 RESEARCH PHILOSOPHY 19
1.5 THESIS FORMAT 20

2 THE INSTRUMENT SYSTEM STRUCTURE 23
2.1 INTRODUCTION 23
2.2 NOTATION AND SYMBOLS 24
2.3 JUSTIFICATION OF VISIBLE LIGHT FOR REMOTE SENSING 25
2.4 THE AMBIGUITY IN IMAGES 28
2.5 IMAGE GENERATION FROM SURFACES 29
2.5.1 Introduction 29
2.5.2 Shape from shading 30
2.5.3 Partial surface or selective feature recovery 33
2.5.4 Conclusion 34
2.6 2-D VERSUS 1-D IMAGE PROCESSING 35
2.6.1 Introduction 35
2.6.2 Thresholding of Profiles 35
2.6.3 Separate and Piled Rock Piles 37
2.6.4 Advantages of 2-D Images 40
2.6.5 Acute angled lighting to improve rock identification 48
2.6.6 Conclusion 51

2.7 SAMPLING THE ROCKS - A STOCHASTIC PROCESS 52

2.7.1 Introduction 52

2.7.2 Developing a statistical model of Ω 52

2.7.3 Observation restrictions 54

2.7.4 Digitization restrictions 55

2.7.5 Sampling restrictions 57

2.8 DATA PROCESSING AND FLOW 59

2.9 CLOSURE 62

3 THE MEASUREMENT OF SIZE FROM CHORD LENGTH AND AREA 63

3.1 INTRODUCTION 63

3.2 BACKGROUND TO STEREOLOGICAL METHODS 63

3.3 SECTIONING THE ROCKSTREAM Ω 64

3.3.1 Sections and Traces 64

3.3.2 The Ambiguity of *Unfolding Size Distributions* 68

3.3.3 Modelling and Sectioning the Rockstream 69

3.4 DERIVING THE SIZE DISTRIBUTION OF SPHERES 74

3.4.1 Introduction 74

3.4.2 Areal profile distributions from spheres 75

3.4.3 Chord length distributions from spheres 78

3.4.4 Lineal analysis of spheres and IUR probes 82

3.5 DERIVING THE SIZE DISTRIBUTIONS OF RANDOMLY SHAPED PARTICLES 83

3.5.1 Introduction 83

3.5.2 King's Method 84

3.6 PARTICLE INTERCEPT DISTRIBUTIONS 86

3.6.1 Linear intercept distributions of particles of known shape 87

3.6.2 Linear intercept distributions of arbitrary shaped particles. 90

3.7 DERIVING AN ANALYTICAL MODEL FOR THE ROCKSTREAM 95

3.7.1 Introduction 95

3.7.2 Modelling the measurement process 96

3.7.3 Deriving a final expression 106

3.8 CONCLUSION 107

4 IMAGE PROCESSING I : ROCK BOUNDARY DETECTION 108

4.1 INTRODUCTION 108

4.1.1 Image Processing Terminology 108

4.1.2 Notation and Convention for Image Processing 109

4.2 SEGMENTATION OF ROCKSCENES 110
4.2.1 A conflicting requirement for "generic" and "custom" algorithms. 110
4.2.2 Review and Introduction to Segmentation techniques 112
4.2.3 Combining Image Processing Processes 114
4.3 ROCK BOUNDARY DETECTION OR ROCK EDGE DETECTION - ASSOCIATED ERRORS 115
4.4 THRESHOLDING FOR ROCK REGION EXTRACTION 123
4.4.1 Global and local thresholding 123
4.4.2 Histogram-tail thresholding 129
4.5 ROCK EDGE DETECTION USING CLASSICAL EDGE DETECTION METHODS 133
4.5.1 Using Edge detection to Complement Thresholding 133
4.5.2 Edge Detection and Image Filtering 133
4.5.3 Two stage Rock Edge Detection Algorithms 135
4.5.4 The Uncertainty Principle 137
4.5.5 Rock Edge detection using Shadows 138
4.5.6 Rock Edge detection using Differential Techniques 142
4.6 PRE-FILTERS 149
4.6.1 Nearest Neighbourhood Averaging Filters 150
4.6.2 Median filters 156
4.6.3 Summary 158
4.7 CLOSURE 159

5 IMAGE PROCESSING II : EDGE CORRECTION AND THE FINAL ALGORITHM 160

5.1 INTRODUCTION 160
5.2 THE "JOINING" ALGORITHM FOR EDGE CORRECTION 161
5.2.1 Labelling 163
5.2.2 The Noise Filter or Spot Remover Ψ_f. 164
5.2.3 Closing the Gaps and Joining Ψ_V 171
5.2.4 Results of Experimentation with Rock Piles 174
5.2.5 Summary 175
5.3 MATHEMATICAL MORPHOLOGY FOR EDGE CORRECTION 176
5.3.1 Why use Mathematical Morphology ? 176
5.3.2 Introduction to Mathematical Morphology 176
5.3.3 Definitions of Morphological Operations 177
5.3.4 Spot removal 181
5.3.5 Fusing gaps 183
5.3.6 Removing holes 183

5.3.7 Varying the size of structural elements 185
5.3.8 Morphological Edge detection 186
5.4 THE FINAL ALGORITHM 190
5.4.1 Introduction 190
5.4.2 The Total System 190
5.4.3 Primary operations Ψ_1 193
5.4.4 Correction and Combining operations Ψ_2 193
5.4.5 Discussion 194
5.4.6 Examples of the resultant Edge patterns 195
5.5 CONCLUSION 197

6 EXPERIMENTS AND TESTS TO DERIVE CHORD-LENGTH DISTRIBUTIONS 198
6.1 INTRODUCTION 198
6.2 THE OBJECTIVE OF THE ROCKSIZE TESTS 198
6.3 THE ROCK MATERIAL 199
6.4 EXPERIMENTAL RIGS 201
6.5 CHORD-LENGTH DISTRIBUTIONS FROM STATIONARY ROCK PILES 206
6.5.1 Separate rocks - Quartzite 206
6.5.2 Touching rocks - Quartzite 209
6.5.3 Piled rocks - Granite 211
6.5.4 Piled rocks - Granite - Rosin Rammler distributions 213
6.5.5 Observations and Comments 215
6.6 CHORD-LENGTH DISTRIBUTIONS FROM CONVEYOR BELT ROCK-STREAMS 216
6.6.1 Practical problems with the conveyor belts 220
6.7 SUMMARY 221

7 CONVERTING CHORD-LENGTH TO SIZE 222
7.1 INTRODUCTION 222
7.2 EXPLICIT INVERSION METHODS 223
7.2.1 Deriving explicit analytical solutions 223
7.2.2 Linear Inversion Methods 227
7.2.3 Constrained linear Inversion 234
7.2.4 King's solution 236
7.3 MOMENT METHODS 242
7.3.1 Cumulative Chord-length Distributions 242
7.3.2 Weighting the Chord-length distributions 246
7.3.3 Comparison of King's method with Cumulative and Weighted Methods 252

7.3.4 Moments of Chord-length Distributions 252
7.3.5 A New Moment Relationship 254
7.4 A NEW ROCKSIZE MEASUREMENT PHILOSOPHY 259
7.5 MORPHOLOGICAL SIZE MEASUREMENTS 261
7.5.1 Defining a sizing Criterion 261
7.5.2 Sizing using Morphological OPENING 263
7.5.3 Sizing using Morphological EROSIONS 270
7.6 INTERPRETATION OF THESE NEW MEASUREMENTS 273
7.7 SUMMARY 274

8 CONCLUSION AND RECOMMENDATION 276
8.1 SUMMARY OF WORK UNDERTAKEN 276
8.2 CONCLUSIONS 278
8.3 FUTURE WORK 279

9 REFERENCES 281

10 APPENDICES

Appendix A Selected Definitions of Particle Size A1
Appendix B Sample calculations of weighted chord-length distributions and moments. B1
Appendix C Sample calculation using a simplified version of King's solution. C1
Appendix D Sample calculation of Direct and Constrained Linear Inversion D1

LIST OF FIGURES

page

1.1 Schematic diagram of an autogenous gold plant, indicating the milling section where the rocksize measuring system would be installed. (a) Feedforward and (b) feedback control schemes. 4

1.2 Graph showing the optimal output size distribution of slurry from a mill in gold plants for maximum gold recovery. 5

1.3 Photograph of run-of-mine material on a conveyor belt. (Photograph was taken with a 35mm still camera.) 6

1.4 Photograph of a conveyor-belt with partially sized material. 6

1.5 (a) Histogram of a relative number-distribution. (b) Corresponding (continuous) relative-frequency distribution. (c) Cumulative distribution of histogram. (d) Cumulative (continuous) frequency distribution. 9

1.6 (a) Example of converting a number distribution to a mass distribution. (b) Example of the error caused by the conversion of number to mass distributions. 11

1.7 Ideal output from the rocksize instrument. 11

1.8 Principle of operation of the MSD-95. 13

2.1 Definition of (a) an image and (b) a profile. 24

2.2 Set representative model of the conveyor belt. 25

2.3 Block diagram of the link between images and the rockstream. 26

2.4 Schematic diagram of the rocksize instrument based on machine vision. 28

2.5 The model relating the irradiance **I** as captured in an image to the surface z of Ω and the illuminating light. 31

2.6 A conceptual relationship between processing time and errors versus the complexity of the methodology required for extracting a surface from an image. 33

2.7 Calculating chord length distributions from 1-D profiles. 36

2.8 Image of (a) separated and (b) touching rocks. The touching rocks in figure 2.8(b) are the same rocks as in figure 2.8(a) except they were pushed together. 38

2.9 Profiles taken from row 100 in figures 2.8(a) 2.8(b). 38

2.10 Examples of how ridges and other features on the surface of a rock may cause a rock to be split (segmented) into fragments when thresholding. Original image is shown in figure (a). Figure (b) shows a vertical profile *column 121*, and figure (c) shows the horizontal profile row 40. Both profiles have been threshold at $t = 120$, and possible points for erroneous splitting are shown as thin dotted lines, while the true points for splitting are shown as heavy dashed lines. 39

2.11 Multiple probe lines improving the sampling of all material on the conveyor belt. 40

2.12 Example of a profile extracted from an image for the purpose of 1-D rock identification. (a) Sample image and (b) gray level profile $g_{98}(x)$ taken from image and perceived rock edges. 41

2.13 (a) The ideal threshold $X_t(g)$ (b) $X_{t=60}(g_{98})$ (c) $X_{t=140}(g_{98})$. 42

2.14 Results of thresholding figure (a) at different values of t. Figure (b) is the histogram of (a). The gray level thresholds selected are, (c) t=50, (d) t=90, (e) t= 110, (f) t= 130, (g) t=170 (h) t=190. 43

2.15 Errors that occur with thresholding; bridges and holes. 44

2.16 Profiles $g_{93}(x)$, $g_{98}(x)$, $g_{101}(x)$ showing how they extend the knowledge about an area in the image. In area A there is conformation that a rock is present. In area B profiles $g_{93}(x)$, [illegible] $g_{98}(x)$, confirm that there could be a rock but profile $g_{101}(x)$ indicates that this pa[illegible] the image could be the edge of rock or that there is noise in this part of the image. 46

2.17 Original images (a) and (b) and corresponding profiles. Profile (a) is column 121 from image (a), and profile (b) is row 20 from image (b). 47

2.18 Setup for low angled lighting for rock edge enhancement. 48

2.19 Images and corresponding profiles $g^{\theta^\circ}(x)$ taken from row 100 for various angles of lighting θ°. For the above images $\theta = 78^\circ, 66^\circ, 55^\circ, 47^\circ, 36^\circ, 30^\circ$ going from top to bottom repsectively. 49

2.20 Plot of average chord length measured from all possible probe lines in the horizontal direction versus different angles of incidence θ°. 50

2.21 Gray level histograms of an image illuminated with light at three angles of incidence. Each histogram curve has been smoothed with a 3-point moving average filter. 50

2.22 Graph showing the "deterioration" of the correlation coefficient R_{xy} between the profile at 76° and the same profile taken at lower angles of incidence. 51

2.23 (a) Measuring chord-length distributions $f_\Omega(D, t_i)$ at intervals from the rockstream which is a stochastic process. (b) Showing a hypothetical joint probability distribution p_D for a size histogram of two classes, D_1 and D_2. 53

2.24 Limitations of machine vision. 54

2.25 Sampling the rockstream. 56

2.26 The problem of pixel resolution versus the proportion of the belt sampled. In (a) the full width of the belt is scanned. In (b) only a small portion of the belt is covered providing finer resolution. 56

2.27 (a) Diagram showing ideal time sampling of the rock stream passing under the camera, and (b) the two actual methods that can be implemented given the restrictions of hardware. 58

2.28 Block diagram of the three stages of processing to transform images to size knowledge. 60

3.1 (a) Example of a structure consisting of a polyhedral in a cube. A plane section exposes the polygon profile of the particle. (b) the sets X_3 , X_2 , $X_1$and X_0 . (c) The boundary and interiors of 1 3-D and 2-D object. 65

3.2 Using two plane probes T_2 at different orientations to section a rock particle of (a) spherical, (b) rectangular and (d) random shape. 67

3.3 Sectioning a convex (a) and non-convex (b) particles showing the potential for ambiguity in estimating the number of rocks from sections. 68

3.4 Measuring *areal* distributions of a number of rocks using a hypothetical thin section T_2. 72

3.5 Measuring *chord-length* distributions of a number of particles using a hypothetical section T_1. 72

3.6 Measuring chord-length distributions with a two stage sampling scheme of applying T_2 and then T_1. 73

3.7 Measuring chord-length distribution using the two stage sampling scheme as given in figure 3.6 except in this case the chord lengths are measured on projected areas of the rocks. 73

3.8 Sectioning a sphere of radius R to gives a profile $r(z)$. 75

3.9 Probability density function $\phi(r \mid R)$ for a sphere (radius R) sectioned by a plane. 76

3.10 (a) The intersection of a sphere of radius R by a linear probe line resulting in a chord of length l_i. (b) Cylinder of radius d_i within which all intercepts l_i will have a length $d_i \leq l_i \leq 2R$. 79

3.11 Probability density function for intercepts lengths through a sphere of diameter D. 80

3.12 (a) Intersection of a polydispersed system of spheres with a random probe line. (b) Hypothetical chord-length distribution resulting from the linear intersections occuring in (a). 81

3.13 Areal intercept distributions of various particles after Paul (1981). These particles are (1) β-tetrakaidecadron, (2) cube, (3) truncated octahedron, (4) dodecahedron, and (5) sphere. 87

3.14 Linear intercept distributions $F(l/l_{max})$ of a deformed cube with different face turn angles α after Naumovich and Kriskovets (1982). (a) Deformed cube with $\alpha = 15°$. (b) $F(l/l_{max})$ for $\alpha = 15°$. (c) (b) $F(l/l_{max})$ for $\alpha = 30°$. 88

3.15 Linear intercept distributions of ellipsoids, cube and prism after Nuamovich and Warren (1978). The axes ratios for the ellipsoids are given for each distribution. 88

3.16 A hypothetical resultant chord length distribution of two classes of deformed cubes, where the one class is twice the size of the other and that there are equal quantities of particles in each class. 90

3.17 Linear intercept distributions of irregular shaped particles that have been separated. Each distribution is an average of between 20-40 distributions measured. (Note 1 pixel = 1mm in the x direction, ie across the belt.) 92

3.18 Linear intercept distributions of the same irregular shaped particles except they have been left touching. Each distribution is an average of between 20-40 distributions measured. (Note 1 pixel = 1mm in the x direction, ie across the belt.) 93

3.19 Linear intercept distributions resulting from the mixing of equal portions of rock of size 6-9m and 9-13mm, for non-touching and touching situations. 94

3.20 A conceptual thick section for a single rock. 99

3.21 A thick section for piled rock showing how the image tends to sample only surface rocks and pull them into a thick section. 100

3.22 Influence of the physical arrangement of a loading chutes relative to the conveyor belt of the spatial distribution of rocks on the conveyor belt. (a) Vertical loading, (b) Side loading. 101

3.23 Assuming a spatial distribution of rocks over the conveyor belt. 102

3.24 The umbra and domain of support of an object or function in one-dimension. 103

3.25 The result of projections of (a) sparsely distributed particles, (b) overlapping particle, and (c) piled rocks. 103

3.26 (a) The correct spacing of probe lines for a rockscene. (b) Closely spaced probe lines used to obtain more intercepts. 105

3.27 The number of chord measured per rock is a function of its maximum caliper diameter $H(X)_{max,1}$ in a direction perpendicular to the direction of the probes T_1. 106

4.1 (a) Discretized representation of the image with address conventions of the pixels. (b) Rockstream q providing a stream of images $I_{p,q}$. 109

4.2 Q filter analogy for segmentation performance versus the variety of scenes to be segmented. 111

4.3 Block diagram of a simple parallel image processing architecture. 115

4.4 Example of the synthetic entities from which size is to be measured. (a) Segmented regions of the rocks where each rock-region is given a label. (b) Edges or the boundaries of the rocks. 117

4.5 Schematic diagram of portion of (a) an edge pattern, and (b) a segmented areal pattern of rocks (synthetic), showing how chord-length measurements may be made on both types of patterns. 118

4.6 (a) Close up view of an edge pattern showing how edges take up finite space and can distort a chord measurement to give a chord length ranging from L_{inner} to L_{outer}. (b) Close up of segmented regions showing that there is no ambiguity with regard to the edges and a chord-length measurement. 120

4.7 (a) 4- or 8- connectivity on a rectangular grid. (b) Example of a string of pixels forming and edge in 4- or 8- connectivity. (c) Example of pixels forming a closed region with 4- or 8- connectivity. 121

4.8 Errors in size measurements on labelled area patterns due to (a) merging, (b) islands, (c) splitting, and (d) gaps and islands in an edge image. 122

4.9 (a) Example of an image of a *mono-layer* of *separated* rocks. (b) Gray level histogram of (a). (c) The rockscenes after global thresholding at $T = 90$. 125

4.10 (a) Two examples of images of overlapping and occluding rocks from Ω . (b) Histogram of the images. (c) Resultant segmented images, with threshold at $T = 120$ for both images. 126

4.11 Example of using local thresholding to segment rock images, equations 4.8 and 4.9. (a) Original image. (b) Global thresholding at $T = 100$. Segmented images using local thresholding with T_s=100 and (c) k=0.1, (d) k=0.5. 128

4.12 Classifying pixels at the tails of the gray level histogram. 131

4.13 Example of selecting of T_{low} and T_{high} from the gray level histogram. 131

4.14 Example of thresholding a rockscene to obtain a first estimate of the location of areas rock and non-rock. (a) Original image, (b) histogram, (c) threshold at $T = 130$, (d) threshold at $T = 40$ and the image inverted to give non-rock as white areas. 132

4.15 (a) Original image of rocks. (b) Threshold image of the image $T = 100$. (c) Result of a Laplacian edge detector (section 4.5.5) on image (a). 133

4.16 The edge detection process consisting of low level edge detection with a subsequent edge analysis and correction stage. 136

4.17 (a) Schematic diagram of experimental setup to enhance shadows for quick edge-detection. (b) Combining shadow images to detect a continuous rock-boundary. 140

4.18 (a) Rock scene illuminated from above I_v, (b) north I_n, (c) east I_e, (d) south I_s, and (e) west I_w. (f) Result of summing all images together I_{sh} as given by equation [4.18] with the exception that $\varepsilon = 0$. (g) Global thresholding of the resultant combined shadow image I_{sh}. (h) Global thresholding of the above image I_v. 141

4.19 Masks (a) and (b) are for the Prewitt (c=1) and Sobel (c=2) operator, (c) is the Roberts operator. 143

4.20 Template matching operator masks (a) Kirsch (b) 3- level. 143

4.21 Laplacian operator mask. 143

4.22 The ideal edge detector. 144

4.23 (a) Original. Results of the application of (b) *Prewitt* (c) *Roberts* (d) *Sobel* and (e) *Laplacian* edge detectors on a scene of large and small rocks. 145

4.24 (a) Original image. Results of the application of the (b) *vertical* and (c) horizontal gradient operators to a scene of large rocks. (d) Result of combining the output from the vertical and horizontal gradient operators using the rms operator as given in equation [4.22]. 146

4.25 (a) A scene of separate rocks. (b) Edge patterns of separate rock scene after application of the Laplacian. (c) Scene of the same rocks in figure 4.25(a) except they have been pushed together. (d) Edge pattern of the touching rocks shown in (c) after application of the Laplacian operator. 148

4.26 Block diagram showing a prefilter being applied to an image before edge detection in order to reduce the amount of noise resulting from differential operators. 149

4.27 Example of the smearing caused by a filter on a (a) clean and (b) noisy 1-D step edge. (c) shows the result of applying a laplacian edge detector to a clean edge and (d) shows the result of applying the laplacian edge detector to a filtered edge. 150

4.28 The mask for a 3x3 nearest neigbour averaging (NNA) mask. 152

4.29 Example of applying the nearest neighbourhood averaging (NNA) filter to images of large (a) and small (b) rocks. 152

4.30 (a) Three-dimensional view of the gray level function from part of the image of a rock scene. (b) Three dimensional view of the same image function after application of the nearest-neighbourhood averaging filter, showing how the edges have been smoothened and "smeared out", and the images cleared of sharp impulses. 153

4.31 (a) Raw image. (b) Image (a) after lowpass filtering with a 3x3 NNA filter. Results of the application of (c) Prewitt, (d) Roberts, (e) Sobel, and (f) Laplacian edge detectors to *large* rocks. 154

4.32 (a) Raw image. (b) Image (a) after lowpass filtering with a 3x3 NNA filter. Results of the application of (c) Prewitt, (d) Roberts, (e) Sobel. and (f) Laplacian edge detectors to *small* rocks. 155

4.33 Result of median filtering to an image of large rocks. (a) Original. (b) Original after image median filtered with a cross 3x3 window. (c) Original image median filtered with a square 7x7 window. (d) Laplacian (e) Prewitt and (f) Sobel edge pattern of filtered image in (b). 157

5.1 (a) A rectangular grid showing which pixels can be connected to the central pixel according to the 4 and 8 neighbourhood rule. (b) Definition of the entities or islands E_i in the edge image E_d according to the 8-neighbourhood rule. 160

5.2 Schematic diagram showing the sequential operations to be performed by the joining algorithm. 162

5.3 Block diagram of the joining algorithm. 163

5.4 Example of labelled entities from which their size can be calculated. 163

5.5 Examples of applying the spot remover to edge patterns E_{∇^2} , resulting from the application of the Laplacian operator ∇^2 to quartzite rockscenes of size range (a) -50+38mm (b) -25+19mm. (i) original, (ii) result of the Laplacian, (iii) result of spot remover. 165

5.5 cont. Examples of applying the spot remover to edge patterns E_{∇^2} , resulting from the application of the Laplacian operator ∇^2 to quartzite rockscenes. (c) -13.5+9.7mm, (d) -50+13.5mm. (i) original, (ii) result of the Laplacian, (iii) result of spot remover. 166

5.6 Results of varying A_n to achieve different amounts of filtering, (a) original, (b) $A_n = 10$, (c) $A_n = 20$, (d) $A_n = 40$, (e) $A_n = 80$. 167

5.7 Images showing how the size of the entities in E_{∇^2} change with average rock size. (a) -75+50mm, (b) -50+38mm, (c) -38+25mm, (d) -25+19mm, (e) -19+12.7mm, (f) -12.7+9.35mm, (g) -9.35+6.15mm, and (h) -6.15mm. 168

5.8 Graph of $A(F_t)$ versus $\ddot{f}_D$. Data is derived from static images of scenes of piled sieved granite. 169

5.9 Schematic diagram showing a scheme to for classifying the entities E_i as either $E_{\partial x}$ and E_n . 170

5.10 Example of a filtered edge patterns E_f showing *gaps* that need closing as well as a number of *unnecessary edge elements*. The image was captured from dynamic quartzite rock scenes on the conveyor belt test-rig (See chapter 6). 171

5.11 Example of the search pattern from a Northern extremity. 173

5.12 A typical result of over-joining. 173

5.13 Results of applying the joining algorithm to (a) small (b) medium (c) large (mixed) rocks. 174

5.14 Results of applying the joining algorithm to piles of rock of wide (mixed) size distribution. 174

5.15 Examples of chord-length distributions measured from rock boundary patterns constructed by the joining algorithm. The images processed were of static images of granite, (see chapter 6). 175

5.16 Detailed example of erosion and dilation of a structure A by horizontal probe B. 178

5.17 Examples of structuring elements used for morphological operations on rectangular grids. 178

5.18 Example of erosion and dilation using a circular probe, after Maragos (1985). 179

5.19 Examples of (b) dilation and (c) erosion of (a) a rock boundary pattern E_{v2} using a 3x3 cross-probe as shown in figure 5.17. 179

5.20 Examples of morphological opening and closing operations with a horizontal 3x1 structure. 180

5.21 Definition of the top and umbra for a 1-D signal. 181

5.22 (a) Edge pattern E_d . Opening E_d with a (b) 3x3 *cross* and (c) *circle* structure of size 1. Figure 5.27 gives the definition of the circle structure. 182

5.23 (a) Edge pattern E_d . (b) After opening E_d with a 3x3 *cross* structure of size 2. (c) After opening E_d with a *circle* structure of size 2. 182

5.24 Example of closing gaps between entities in an edge image E_{v2} with a 3x3 *cross* structuring element (size 1) to produce fused edge images E_V . Rock is -38+25mm quartzite. (a) Edge image, (b) $E_V = E_{v2} \oplus B$. 183

5.25 Example of closing gaps between entities in an edge image E_{v2} with a 3x3 *cross* and *circle* structuring element (size 1 and 2) to produce fused edge images E_V . (a) Edge image, (b) $E_V = E_{v1} \oplus B$, (c) $E_V = E_{v2} \oplus 2B$. Rockscene is dolomite (-38+25mm) captured from the conveyor belt. 184

5.26 Example of closing holes in segmented areas resulting from thresholding using a cross probe of size 2. 185

5.27 (a) A *Box* shaped probe can be decomposed into a *vertical* and *horizontal* probes of smaller size. (b) A *cross* and *box* probe can be used to compose a *circle* probe. 186

5.28 Example of the morphological edge detector as applied to a binary entity. (a) Original image X. (b) $X \ominus B$. (c) The difference $X - (X \ominus B)$. 187

5.29 Morphological edge detection applied to a scene of large rocks (-38+25mm). (a) Original image. (b) Morphological edge detection with no pre-filtering. (c) Morphological edge detection with *NAA* pre-filtering. Probe structure used is a 3x3 cross. 188

5.30 Examples of morphological edge detection applied to rock edges. The raw images shown have been prefiltered using the *NAA* filter. The probe used is a circle. The above figures show pairs consisting of the original image and the result of the morphological edge detection for (a) -50+38mm, (b) -38+25mm, (c) -25+19mm, (d) -19+13.7mm, (e) -13+9.35mm, and (f) -9.35+6.15mm size distributions. 189

5.31 Simplified block diagram of the final algorithm Ψ showing the two main blocks of (i) primary parameter detection, and (ii) edge correction and the combining stage. 191

5.32 Detailed block diagram of the processes in Ψ as implemented in pilot plant conveyor-belt tests. 192

5.33 Edge E^*_{ax} patterns for scenes of large rocks. 195

5.34 Edge patterns E^*_{ax} for scenes of small rocks. 196

5.35 Edge patterns E^*_{ax} for scenes of mixed rocks. 196

6.1 Schematic diagram of the image processing system in the "rock lab". 203

6.2 Schematic diagram of the image processing system used for dynamic image capture on the closed-loop conveyor belt system. 203

6.3 Photograph of the image capture system as used in the rock lab. 204

6.4 Photograph of the closed loop conveyor belt system used for dynamic image capture. 204

6.5 Schematic diagram of the experimental rig used for dynamic rock size measurement tests. 205

6.6 Examples of rock images of separated quartzite rock. 207

6.7 Typical example of resultant chord-length distribution measured with chord probes spaced 25, 5 and 1 pixel(s) apart. Image is 200x200 pixels. 207

6.8 Example of chord-length distributions measured on the same image of separated quartzite rocks taken in the *x* (row) and *y* (column) direction. 208

6.9 Comparison of chord-length distributions measured from scenes of separate and touching quartzite rocks. 209

6.10 Comparison of chord-length distributions measured from scenes of separate and touching quartzite rocks. 210

6.11 Examples of images of touching quartzite rocks. (a) -38+25mm, (b) -12.7+9.35mm. 211

6.12 Resultant chord length distribution as measured using the joining algorithm on piled granite rock scenes. 212

6.13 Examples of rock piles mixed according to the Rosin Rammler distribution function. (a) n=2.0, (b) n=0.5. 213

6.14 Chord-length distributions resulting from the application of the joining algorithm to rock size distributions of granite mixed according to the Rosin Rammler distribution. 214

6.15 Examples of dynamic images of piled rock scenes as captured from the pilot-plant conveyor belt using the line-scan camera. (The photgraphs presented are 35mm stills of the video monitor.) Belt speed was 0.5ms^{-1} and material is gold bearing quartzite. (a) -50+38mm, (b) -19+12.7mm, (c) -50+12.7mm, (d) -38+12.7mm. 217

6.16 Chord-length distributions resulting from the application of the morphological algorithms to size groups of rocks. In each of the above four graphs, three chord-length distributions are presented. Each chord-length distribution is measured from a different image captured at random from the rockstream of given size. 218

6.17 Comparison of chord-length distributions resulting from the application of morphological algorithms to various size groups of rocks. 219

7.1 (a) Example of a *raw* chord-length distribution $g_k(L_i)$ which has been filtered. Two moving average filters of length 3 and 5 were applied to the distribution sequentially. (b) Result of numerical differentiation of two filtered distributions. 227

7.2 Mapping of the 200 element $p(L_k)$ to a 5 element linear or log array $p(L_k')$. 230

7.3 Results of using direct linear inversion to solve for the size distribution given a measured chord-length distribution of size -38+25mm. The dark histogram is the ideal response from the inversion process, while the other histograms are the responses of linear inversion to five individual chord-length distributions measured from conveyor-belt scenes. 233

7.4 Results of adding different combinations of small errors (<1%) or perturbations to *the* chord-length distribution which gives the ideal response, showing the undesirable sensitivity of direct linear inversion methods. 233

7.5 Results of using constrained linear inversion. The solid histogram is the ideal distribution. The other histograms are the results of applying measured chord-lengths distributions from rockstreams of size range (a) -19+13mm and (b) -25+19mm. 235

7.6 Results of using constrained linear inversion. The solid histogram is the ideal distribution. The other histograms are the results of applying measured chord-lengths distributions from rockstreams of size range (a) an equal mixture by mass of -25+38mm and -50+75mm, and (b) only -50+38mm. 236

7.7 Chord-length distributions of rocks $p(L)$ as measured from different sized conveyor-belt rockstreams before the application of King's method. 239

7.8 Sieve-size distributions as derived by kings formula [7.12]. Note the correction term $C(M,\beta)$ is assumed to be zero, and $\beta = 1.25$ so that most of the solutions are positive, ie $F_i(D) \geq 0$. 240

7.9 The effect on sieve-size distributions as derived by King's formula [7.12] after replacing the spike at the shorter chord-lengths of $p(L)$ with a ramp going from 0.0 to 0.04 for the first 10 values. This effectively removes the spike lying against the vertical axis as shown in figure 7.7. $\beta = 2.40$ and $C(M,\beta) = 0$. 241

7.10 Two typical chord-length distributions measurements $g(L)$obtained from conveyor-belt rockstreams. (Adjacent probes used.) 243

7.11 Cumulative chord-length distributions $P(L)$ as measured from moving rockstreams. 244

7.12 Cumulative chord-length distributions $P(L)$ measured from static images of granite rockscenes with the rock-size distributions synthesized according to the Rosin-Rammler function. 245

7.13 Amplified chord-length distributions $p_i^*(L_k)$. 248

7.14 Amplified distributions $p_k^*(\alpha, L)$ with $\alpha = 1,2,3$ for the same rocksize distribution. 249

7.15 Amplified distributions $p_{\alpha=2,i}^*(L_k)$ for different rocksize distributions. 250

7.16 Amplified chord-length distributions $p_{\alpha=2,i}^*(L)$ measured from conveyor belt tests with varying quantities of large rock (-75+50mm) being added to the rockstream. 251

7.17 Plot of the calculated width of the size distributions $\sigma(D)$ versus the true width of a few size classes according to table 6.1, calculated by the relationship [7.43]. Note that the distributions of each size class was assumed to uniform, and was normalized by the average size of each class. 254

7.18 The average chord-length μ_{L_j} measured for each rock stream with size distribution $f_j(D)$, versus the geometric average $\overline{D_{g_j}}$ of each rockstream. 256

7.19 Plot of the first moments of chord-length distribution $\mu_{L_{i,j}}$ measured for each rock stream versus time t_i. Each time interval ΔT is approximately 25s. (a) Actual data, (b) data filtered with a 3 element moving average window. 257

7.20 Plot of standard deviation $\sigma(\mu_{L_j})$ and average $\overline{\mu_{L_j}^*}$ of the first moments of the chord-length measured for each rock stream Ω_j of different average sieve size $\overline{D}$. 258

7.21 Plots of the average first moment of chord-length distribution $\mu_{L_i,j}$ measured for each rockstream versus the mass of large rock (-38+25mm) added to the belt already covered with small rocks (-12.7+9.5mm). 258

7.22 Extracting parameters such as slopes at the origin m_1, m_2 or cumulative percentage passing p_1, p_2 from the normalized cumulative frequency distribution of chord-lengths. 260

7.23 Sample set of circles of size $r = 1 \ldots p \ldots 5$. 264

7.24 Set of circles after successive transformations $\psi_\lambda(X^{\lambda-1})$ 265

7.25 Block diagram of the algorithm implemented to calculate the morphological size distribution using the *opening* operation 266

7.26 Resultant opened-images and difference images W_λ after morphological openings with cross probes λB of varying size. 267

7.27 The first-moment functions $v_{\circ,\mu_j}(\lambda)$ measured from the difference sets of successively opened images of different rocksize distributions Ω_j. 268

7.28 The *integrals* or *cumulative* of the first-moment functions $V_{\circ,\mu_j}(\lambda)$ measured from the difference sets of successively opened images of different rocksize distributions Ω_j, and normalized to 1. 269

7.29 *Differences* of the first moment functions of the chord-length distributions $v_{diff_j}(\lambda)$ measured from the difference sets of successively opened images of different rocksize distributions Ω_j 269

7.30 Schematic diagram of the algorithm used to obtain the *erosion* size functions. 270

7.31 Example of successive erosions of an image. 271

7.32 (a) The first moment function $v_{\ominus,\mu_j}(\lambda)$ of the chord-length distributions measured from different rockstreams Ω_j which have been eroded. (b) The same data as in (a) except the distributions have been transformed into density functions. 272

LIST OF TABLES

page

3.1 Table of traces and corresponding parameters caused by the intersection of structure X with section T. 66

3.2 Table showing the relationship between the dimensions of traces Z, objects X, and corresponding sections T. 66

6.1 Table of size classes used for testing quartzite rock material. 200

6.2 Table of size classes used for testing granite rock material. 200

6.3 Table of mixed size classes used for testing quartzite rock material on the conveyor belt. 216

SYMBOLS AND NOTATION

Sets and Morphology

$\Re$	set of real numbers
$\mathbf{Z}$	set of integer numbers
$\mathbf{D}$	domain of a function
$\mathbf{V}$	range of a function
X, Y, Z	(captial letters) Euclidean or digital set under study
X	set of rocks in an image
X^c	complement of set X, or non-rocks
x, y, z	elements of sets X, Y, Z respectively
X_m	set X of dimension m
X_i	i'th rock or set
X_w, X_o	wood, water
∂X	boundary of set X
$\overset{o}{X}$	interior of set X
$H(X)$	caliper diamter of set X
Y	set of non-rocks
α	rock phase of a set
β	non-rock phase of a set
λ	label given to the elements of a set X
λ_i	label given to the elements of a rock set X_i
$Z(X)$	trace of set X
$d(Z)$	dimension of trace Z
T	probe set
T_1	linear probe set
T_2	planar probe set
$\uparrow$	hits, when one set intersects another
$\cup$	union of sets
$\cap$	intersection of sets
$\subset$	proper subset
$\subseteq$	subset
$\in$	element of
$\forall x$	for all x
Ω	set representing the rockstream
Ω_q	q'th rockstream
Ω_R	subset of portion of the rockstream visible to the eye/camera.
$\mathbf{U}$	the universal set, representing all parts of the rocks stream and conveyor-belt
$\varnothing$	empty set

$A \oplus B$	dilation of set A by set B
$A \ominus B$	erosion of set A by set B
$AOB, \quad A_B$	opening of set A by set B
$AOB, \quad A^B$	closing of set A by set B
A_b	the translate of set A by b
$U(f)$	the umbra of function f
$T(f)$	the top of function f
S	the domain of the $U(f)$ of function f
$g_{m,n}$	gray level morphological filter of parameter m,n
$N[]$	the number of
$L[X]$	the length of set X m, or pixels
$A[X]$	the area of set X m^2, or pixels^2
$V[X]$	the volume of set X m^3, or pixels^3
$A, \quad L$	area, length
$l, \quad l_i$	length, and the i'th length
$A^*, \quad L^*$	actual measured area and length of an entity
ψ_λ	sizing function with respect to λ

Images

(x, y)	domain of a two dimensional image
i, j	indices for pixels in a discrete 2-D image
$I = I(x, y)$	continuous image
$I = I(i, j)$	discrete image
$I_1, \quad I_2$	one and two dimensional images respectively
$I_{p,q}$	p'th image from the q'th rockstream
I_{sh}	image resulting from shadow algorithm
$I_N, \quad I_S, \quad I_E, \quad I_W, \quad I_V$	shadow images illuminated from the north, south, east, west and above
$g(x)$	profile from an image or a 1-d image
$\Gamma(x, y)$	input image to a image transform
$F_p(x, y)$	output image from an image transform
$G(x, y)$	output image from image transform
$\hat{G}(x, y)$	output image from median filter
$H(x, y)$	kernel image for convolution operations
$T, \quad T_g, \quad T_{low}, \quad T_{high}$	threshold, global threshold, low and high thresholds
$T(i, j)$	local threshold
$W(x, y)$	local window of an image

$\overline{F}$	mean gray level of an image
g	gray level
z_{Ω}	surface function of the rockstream Ω
∇^2	Laplacian operator
$\mathbf{L}$	direction of light source
$\mathbf{V}$	direction of viewer
$\mathbf{N}$	surface normal
η	intensity of illuminant
ρ	surface albedo
Θ	function which combines images

Transformations

Ψ'	image processing and transformations
Ψ'_c	process to transform chord-length distributions to size distributions
Ψ'_1	primary image processing stage - edge detection
Ψ'_2	secondary image processing stage - edge correction
Ψ_{∇^2}	Laplacian edge detection
Ψ_{NNA}	nearest neighbourhood averaging filter stage
Ψ_f	noise filter / spot remover filter
$\Psi_{\vee}$	joining algorithm
Ψ_{morph}	morphological process or image transformation
I_e	transformed image
μ	measurement process
E_d	binary image of edges
E_X, E_X^*	binary (transformed) image of rocks resulting from thresholding
$[E]'$	inverse of binary image E
E_f	filtered binary image E
E_n	noise elements ina binary image
E_Y	binary image of non-rock resulting from thresholding
E_i	*i'th* entity in a binary image
$E_{\partial X}$	entities in a binary image which represent the true rock edges
$E_{\partial X}^*$	estimated or partial set of the true rock edges in a binary image
$E_{\partial X}^*$	corrected set of edge entities in a binary image
E_{Δ}	set of missing true edges in a binary image
E_{Δ}^*	estimated set of missing edges

E_{∇^2}	binary edge pattern resulting from thresholding the results of a Laplacian edge detection process
E_{mask}	resultant binary image after masking
$E_{\partial X,Y}$	binary image with rock edges and non-rock being one phase
K	maximum gray level
g	gray level of a given image
$h(g)$	gray level histogram of an image
$H(g)$	cumulative gray level histogram of a given image
$g_{max,h(g)}$	the gray value corresponding to the peak in $h(g)$
$g_{H_p(g)}$	the gray value corresponding to the p'th percentile of $H(g)$
A_i	area of an entity E_i
$E_{<A_n}$	set of entities in a binary image with area less than A_n
A_{E_i}	average area of all the entities in a given binary image
$A_{\min}$	minimum area of entities
$d_{\max}$	maximum distance between entities
C_X	centre of a rock X
C_{E_i}	centre of given entity
$X_t(g)$	set of rocks after thresholding a 1-D image or profile g
θ	angle of incidence of illumination
$g_i(x)$	i'th row or column profile extracted from an image
$g^{\theta}(x)$	i'th row or column profile extracted from an image with the image scene illuminated at angle θ
R_{xy}	correlation coefficient between row/column x and y
Φ	function relating chord-length distributions to size distributions
$K(x,y)$	kernel function
M	characteristic size parameter measured, eg length Larea A
$p(M)$	number density distribution of size parameters measured
$p(M \mid D)$, $\phi(M \mid D)$	conditional density distribution of size parameter M for a given characteristic rocksize D
$\overline{M}$	average of parameter measured
$\overline{M}_D$	conditional moment of parameter M
$g(M)$	relative number distribution of size parameters measured
$\mathbf{p}(L)$	chord-length density vector
$\mathbf{f}(D)$	rocksize (sieve/volume) distribution vector
$\mathbf{f}^*$	estimated size density vector
$\mathbf{A}$	kernel matrix

$\mathbf{A}^{-1}$	inverted kernel matrix
$\mathbf{A}^T$	transpose of matrix A
$\mathbf{I}$	identity matrix
$\mathbf{P}(L)$	matrix of chord-length density vectors
$\mathbf{f}(D)$	matrix of rocksize density vectors
Λ	eigenvalue vector
β	scaler parameter to King's solution
$C(M,\beta)$	correction term to King's solution
$p^*(L)$	amplified or weighted chord-length density distribution
$a(L)$	weighting function
α	weighting parameter for weighting function
m_o	slope at origin
$Mes = \mu$	measurement on
λ	scalar sizing parameter for morphological transformations
W_λ	morphological size fraction
$\nu_{\circ,\mu}(\lambda)$	first moment function of the chord-length distributions resulting from opening.
ν_{diff}	differences between the first moment functions
$\nu_{\ominus,\mu}(\lambda)$	first moment function of the chord-length distributions resulting from erosion

Rocksize distributions

D	characteristic size of a particle (m)
$\overline{D}$	average size of a particle in terms of dimension D
s_d	standard deviation of the rocksize distribution
g_d	skewness of the rocksize distribution
$\overline{D}_g$	geometric average of a uniform rocksize distribution
D_i	average characteristic size of the i'th discrete size interval
ΔD	size class width
D_{min}, (D_{max})	minimum (maximum) size of a class interval
C_k	shape factor of dimension k
D^k	characteristic dimension raised to the k'th dimension
N	number of particles
n_i	number of particles in class i
I	number of classes in a size distribution
N	total number of particles for a given particulate system
f_i	relative number frequency of particles in class I, or discrete size distribution
$f(D)$	continuous relative frequency distribution of particles

$f(D,t)$	continuous relative frequency distribution of particles as a function of time
f_λ	morphological size distribution as a function of λ
$f_X(\lambda, B)$	morphological size distribution of rocks X in terms of probe B as a function of size paramter λ
f^*	estimated size distribution
$F(D)$	cumulative size distribution
$\bar{f}$	average size distribution of a system of particles
$\bar{f}'(t)$	first derivative of the average size distribution of a rocks as a function of time
w_i	mass of material in size class i
W	total mass of a given particulate system
$W(D)$	cumulative size distribution by weight (mass)
$\dot{m}_\Omega$	mass flowrate of the rockstream
v_{belt}	conveyor-belt velocity
Ξ	physical arrangement of the conveyor belt and loading shutes
ρ	density of material
N_V	number of particles per unit volume
$N_{V,i}$	number of particles in size class i per unit volume
N_A	number of areal intersections per unit area
H, $(\overline{H})$	(mean) tangent or caliper diameter
R	radius of a sphere
$\overline{R}$	mean radius of a group of spheres
r	radius of the circular intercept through a spheres
$F(r)$	size distribution of spheres of radius r
$f(r)$	size distribution circles of radius r
A	area
V	volume
L	length or chord length
μ_D^n	the n'th moment of the size distribution $f(D)$
μ_n	the n'th moment of a distribution
t	time
ΔT	time interval
T_s	image sampling time interval
τ	small time interval (delay)
ε	time over which the statistics of the rockstream are stationary
Θ	a function which determines how the rocks are distributed upon the conveyor belt

Probability

$A, B, \ldots G$	events A, B ...
ζ	a measure on some event
Ξ	the set of measures on all events
$Pr\{\}$	probability
$p()$	probability density function
$p(.\mid.)$	conditional probability density function
$P()$	cumulative probability density function
$E\{\}$	expected value

1 INTRODUCTION

1.1 PROBLEM STATEMENT AND RESEARCH OBJECTIVE

There is a need in the mineral processing industry to measure the size distribution of rocks on a moving conveyor belt. This thesis is concerned with the measurement of this rock-size distribution which will be used primarily for the control and optimization of *comminution* processes. Comminution is the reduction in size of mined rock material from large particles to smaller ones, so that the minerals contained in the ore, may be liberated. In particular it is believed that this rocksize measurement will allow for the improvement of optimal control strategies in milling circuits especially multivariable and adaptive control of run-of-mine milling (Hulbert, 1990). In addition to the optimization of comminution processes, metallurgists have also hypothesized that a continuous rocksize measurement will at the very least provide additional insight into the mechanisms of comminution processes of which very little is known.

The problem is that a viable on-line instrument to measure the size distributions of rocks on a conveyor belt has not been readily available to the mineral processing industry, (Grannes, 1986). Consequently the benefits of an on-line realtime-measurement of rocksize are generally unknown, and much doubt surrounds the usefulness of such a measurement to the mineral processing industry. Thus the uncertainty associated with this measurement has created a dilemma in that the development of such an instrument has been difficult to justify.

The South African mining and mineral processing industry nevertheless initiated this research program and motivated for this measurement. This measurement is of particular relevance to the gold mines where a declining gold price and increased production costs have led to intensive efforts to optimize the efficiency of the gold plants. A commercial rocksize measuring system is available; however unsatisfactory performance of this instrument on various mine plants, in particular with run-of-mine rock material, instigated the research effort into this elusive measurement.

Taking belt cuts, and performing off-line sieving and weighing is the method normally used for measuring the size distribution of rocks on a conveyor belt. Although this method does give accurate sieve size data for the particular samples taken, errors do occur when extrapolating to the full rock stream because of the limited number of samples and large sample intervals. In addition, these methods of sizing are time-consuming, labour-intensive, and require large and costly capital equipment. The cost aspect of these factors become worse if these methods are automated, (Herbst et al, .. 87).

Herbst et al (1987) suggest that a more suitable approach to sieving, is to use a *non-contact* measuring system employing optical imaging together with image processing and analysis techniques, ie *machine vision*. This approach overcomes the material handling and sampling problem, and is appropriate for continuous on-line measurement. However there is a belief in the industry that such an instrument cannot be built, especially one based on *machine vision*. One of the strongest and logical argument for this stance is that "one can only see the top layer of material on the belt, and is hence ignoring what is below. Therefore how can one measure what you cannot see or probe ?"

In response to the above difficulties the following research objective was created: "*To investigate and develop a technique based on machine vision for measuring the size distribution of rocks on a conveyor belt, on-line and in realtime, and at a reasonable cost to the mining industry* ". This thesis is thus concerned with the underlying fundamental research required to meet this objective up to and including pilot plant experiments. Included within this objective is the justification of machine vision for this measurement as well the validation of associated hypotheses put forward for this measurement. One major hypothesis is that rocksize measurements can be obtained from *lineal analysis* of the images taken from the rockstream on the conveyor belt.

From test results on a pilot-plant conveyor-belt system, it will be shown empirically that the above hypothesis is valid, and that useful rocksize information is produced within the framework of certain limitations. It will also be shown that sound stereological principles underpin the measurement process developed, although a full model and an analytical proof thereof is difficult to complete (chapter 3).

1.2 BACKGROUND

This research forms the foundation for an industrial instrument based on the above hypothesis which is being constructed at present. The instrument will be installed in the harsh environment on the mineral processing plants, where minimum maintenance is of a high priority. The ideal rocksize instrument must thus conform to the following specifications: The instrument must be non-intrusive which has obvious advantages as far wearing down of parts is concerned. The instrument must also be reliable so that plant downtime is minimized, and mineral production is not hindered by any part of the control system or associated instrumentation failing. In particular, some of the environmental factors which have to be taken into consideration are: a large operating temperature range, (-10 to 40 °C) and a corrosive and dusty atmosphere where the equipment could be exposed to rain or high-pressure hoses. (Dust is one major disadvantage as far as a vision system is concerned). The instrument must also be immune to electromagnetic interference (EMI) from large machinery found on mineral processing plants.

The objects of interest in this research are the piles of rocks to be found on the conveyor belts on these mineral processing plants. This rock material contains minerals such as gold and platinum which are to be extracted by metallurgical processes. The first stage in this metallurgical process is milling which grinds *rocks* or large particles down to a *paste*[1.1]. Rock material and water are fed into one end of a mill, and a slurry or mud is output from the other end, see figure 1.1. It is desirable to optimize this milling process in order to minimize energy consumption, maximize mass-throughput, and ensure that the particle size-distribution of the final product namely the slurry falls within a certain specification. Maintaining this slurry particle-size specification is important because slurry particle size influences the cost and efficiency of the mineral recovery processes further downstream in the plant. Figure 1.2 shows how the efficiency of mineral benification is affected by slurry-particle size. Slurry particle size is in turn affected by the milling process and hence rocksize. There is thus an indirect but nevertheless tangible link between rock size and the cost and amount of the final product being produced.

Optimization of the milling process implies that *control systems* must be installed on the plants. Herbst and Rajamani, (1982) have suggested that rocksize should be treated as the principal measured and controlled variable in milling and crushing control systems. Yacher et al (1985) pointed out that *coarse-ore feed* size in mill operations is one of the main uncontrolled disturbances. De Kok and Lloyd (1982) comment that segregation of coarse and fine rock during storage causes surges downstream which is particularly deleterious in run-of-mine mills. Thus the need for a rocksize measurement for mill control, and in particular for *run-of-mine (autogenous)* mill control. There is also a need for rocksize measurements to and from crushers and other process units, where the input and output rocksize distributions need to be monitored.

Figure 1.1 shows two proposed control configurations (feedforward and feedback) for a gold milling plant using a rocksize measurement as part of the input to the system. The *feedforward* system will allow for the necessary control actions to be taken on the mill to compensate for the size of the material being fed into the mill. According to prevailing control requirements, the *feedback* configuration could allow for a coarser or finer rock feed to be fed in to the mill by modifying rock-blasting techniques back in the mine.

[1.1] Paste, slurry or mud are terms for mixtures of finely ground rock particles mixed with water.

The rock material from the mine is transported via conveyor belts to the mineral processing plants see figure 1.3. The width of the conveyor belts feeding autogenous and other mills range from approximately 0.5m to 2m. The belts move at velocities of between 0.1 to 5 ms^{-1} (typically 0.3-0.5 ms^{-1}), providing a feed rate as high as 1000 tons/hr. Most of these conveyor belts are protected by some form of galvanized-sheet steel shelters providing adequate protection from the elements.

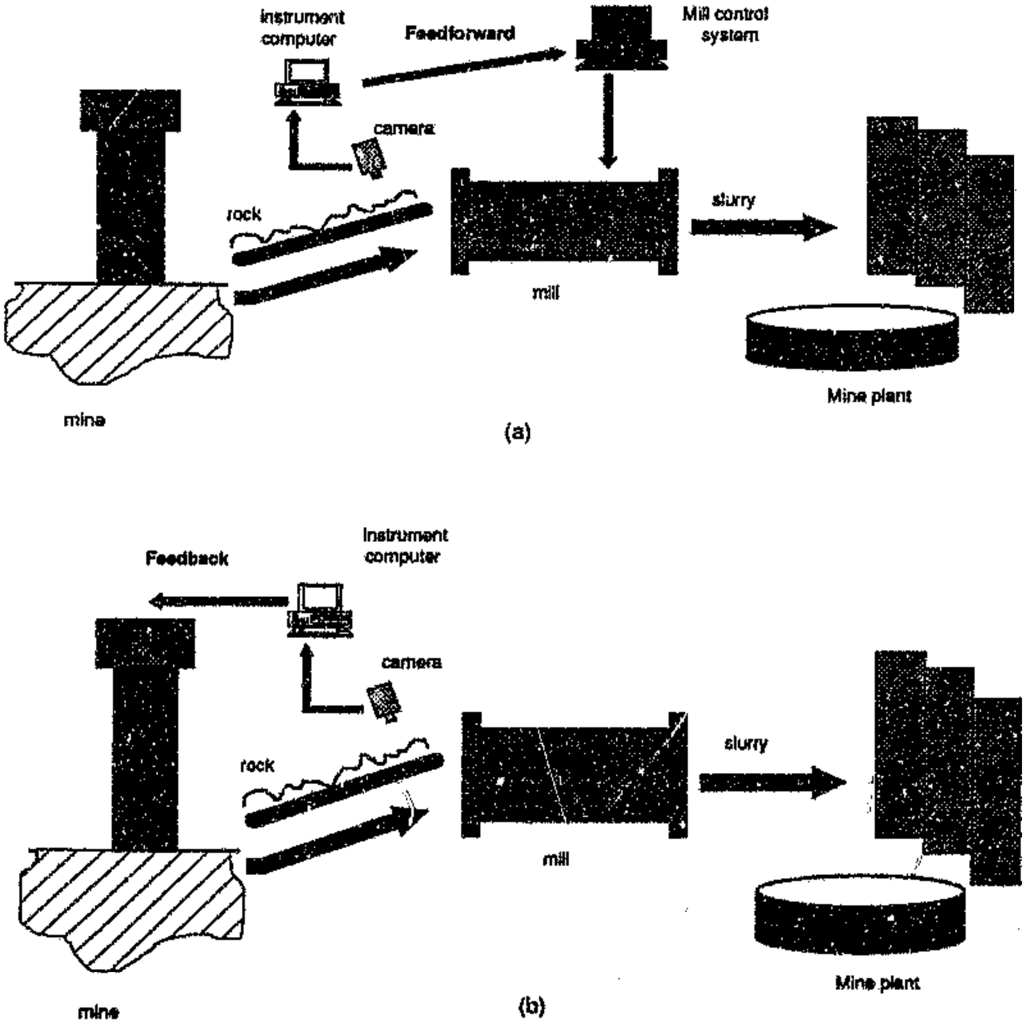

Figure 1.1. Schematic diagram of an autogenous gold plant, indicating the milling section where the rocksize measuring system would be installed. (a) Feedforward and (b) feedback control schemes.

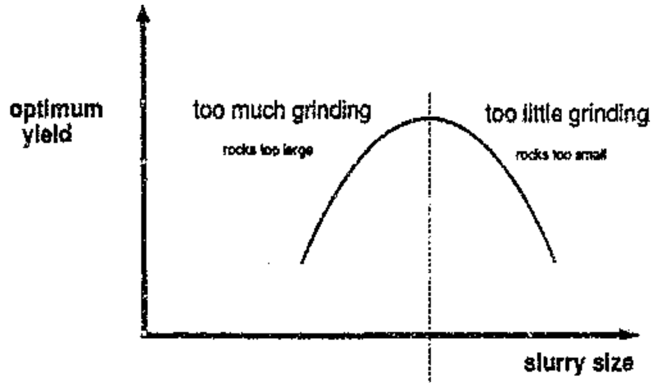

Figure 1.2. Graph showing the optimal output size distribution of slurry from a mill in gold plants for maximum gold recovery.

1.2.1 The Rock Material

The rock material transported on the conveyor belts may be considered to be classified into two broad groups, (1) *run-of-mine*, and (2) *sieved* rock material.

Run-of-mine material is brought up from underground and is fed directly into *autogenous mills*. In many cases this material is stored in bunkers or on storage heaps, which is then fed to the mills. This helps to buffer and smooth the erratic supply of rock material the from underground, and also provides some form of rock classification and size selection to be implemented.

This rock material is random in shape, colour and size, and the instantaneous mass-flow rate of the rockstream on the conveyor belt is usually inconsistent and sometimes "random". The size range is very large and may range from rocks as large as a half a metre across to mud, consisting of very fine particles of tens of microns. If very damp, which is usually the case, the fine rock material tends to form agglomerates (mud) which looks like large individual rocks. In addition, the larger rocks are often covered with clumps of fine particles due to the sticky nature and high viscosity of the mud (slurry).

Sieved or pre-sized rock material is pre-screened or sized with a "grizzly" or system of sieves. This material usually falls into a relatively narrow size range and the flow stream is usually steady and consistent as opposed to the run-of-mine material. A typical size range is for example 25 to 38mm.

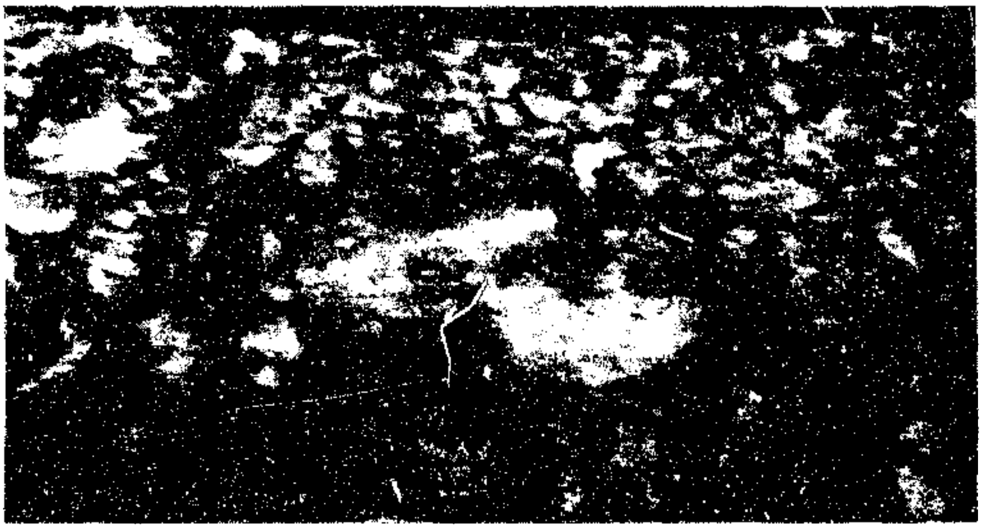

Figure 1.3. Photograph of run-of-mine material on a conveyor belt. (Photograph was taken with a 35mm still camera.)

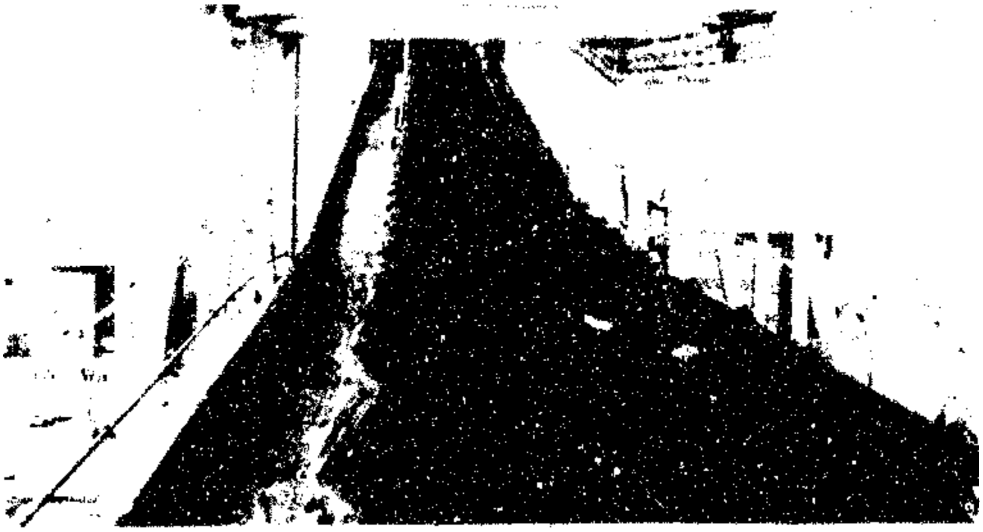

Figure 1.4. Photograph of a conveyor-belt system with partially sized material.

The characteristics of the rock material within the two groups above tend to differ from mine to mine, and from belt to belt feeding different mills on the same plant. For example, two adjacent streams on the same plant may look totally different because they are being fed from different points of a stock pile, or from different mine shafts. The rock material characteristics which differ are: Chemical and mineral content, size and shape distributions, colour, texture, and moisture content.

In addition, the physical arrangement and amount of material loaded onto a particular conveyor belt varies spatially and with time, causing an unsteady flow as mentioned before. This is because of the irregular manner in which the rock material is dumped on the conveyor belt from other conveyor belts, chutes and hoppers. This results in the rock material covering the belt in many different patterns and structures. Slow moving belts (<0.1ms-1) are loaded very heavily, with material lying up to a half a meter high, while high-speed belts may be loaded with a thin layer of fine material (<10mm), with few large rocks (100 mm's in size) sparsely distributed on top. Because of the irregular loading patterns there are times when much of the belt is exposed. The flow of rock material on the conveyor belt can thus be summarized as being a function of a number of complex parameters, these being the *architecture* of the conveyor belt and equipment used to load the conveyor belt, as well as the *rock material* itself as discussed above.

1.2.2 Particle Size, Shape and Distribution

This thesis focuses on the measurement of rocksize. This subsection thus provides background on the concepts of size and its relation to shape. Standard methods for presenting size data are also discussed.

The following two questions are crucial to the solution of this rocksize measurement problem. What is the *size* of a rock, and how is the size of a particle (rock) measured ? Unfortunately there are no fixed answers to these questions, and this measurement problem is thus fraught with ambiguities. The size of rocks or naturally occurring objects is an almost subjective observation and *each class of objects appears to have its own standard for size measurement.* Luerkens and colleagues (1987) comment, "there is a major uncertainty in particle characterization which is due to the lack of precision in the definition of the terms which are claimed to be measured". They continue to state that the nature of the uncertainty in the measurement of particle properties (eg size), as related to their definition is fuzzy (in the colloquial sense). Despite this uncertainty with the definition of size, the following is a fairly succinct definition of particle size. "*Particle size can be defined as the characteristic dimension of the material that can best represent the state of subdivision of its* *constituting particles*", (Sresty and Venkateswar, 1980), (Stockham, 1978). Matheron (1975) also provides an unambiguous criterion for size based on morphological transformations which is described by Serra (1982), see chapter 7.

An important objective in measuring the size of rocks, is thus to identify and calculate a *characteristic dimension* of the rocks which is *useful* to the milling process. This not trivial because the measurement of the size of irregular shaped particles on the basis of some characteristic dimension is very much dependant on the particles' ***shape***, the ***method*** of measurement, and the area of ***application*** of the size information (Allen, 1981).

The importance of shape and the method of measurement is demonstrated by the following example. What is "larger", a thin rod of radius r_1 or a sphere of radius r_2, where both objects have the same volume and $r_2 = 10r_1$? If *volume* is the sizing criterion then both objects have the same size, however if they are resting on a table in a stable position and the *height* above the table's surface is the size criterion, then the sphere would be larger. However if the rod is standing upright, then it is larger. Hence size is an ambiguous issue if the exact circumstances and method of measurement are not properly stated. What is apparent is that the comparison of the size of objects with vastly different shapes is very ambiguous. If shape can be taken into consideration when sizing particles, then the ambiguity of comparing different shaped objects can be disregarded, eg a *sphere* of radius r and a *cube* of size a are totally and unambiguously defined.

Unfortunately the shapes of irregular objects are very difficult to define precisely. When one examines the myriad of shapes in nature (in our case rock particles), Underwood (1970) comments "*that it is not surprising that most discussions of shape wax philosophical or artistic rather than quantitative*". He continues that only the most regularly shaped objects can be expressed quantitatively and for the complex and irregular shaped particles encountered in nature, one must be content with descriptions which are largely indirect or approximate. For example, qualitative terms such as "angular" and "spherical" may be used to give some indication of the nature of the particle's shape. Although these qualitative terms are inadequate for quantitative analysis, there are other quantitative methods for describing particle shape. These are shape factors and shape coefficients (Allen, 1981) which may be used to reduce results from different sizing methods eg sieving and microscopic techniques, to a common level.

Usually the size of particles is expressed in terms of the diameter of a circle or sphere, which is equivalent to the particle with regard to some stated property (Heywood, 1972), (Stockham, 1978). For example, a unit cube has the same volume as a sphere of diameter 1.24 units, and hence its equivalent diameter is the volume diameter $d_v = 1.24$ units. See Appendix A for examples of a number of selected definitions of particle size.

In the mineral industry the *sieve* or *mesh* diameter is the accepted standard and is used extensively on mineral processing plants for the classification of rocks into various size ranges. Sieving is the only independent measurement against which the methods developed during this research can be compared. Another class of diameters are statistical diameters such as Martin or Ferret diameters (Allen, 1981) which are dependant on the randomness associated with the measurements.

The *number* size distribution of particles is defined as follows. Let a group of N particles be sized according to a characteristic dimension D into I size classes, where D_i is the average size of that class, ΔD_i is the class width, and D_{max} is the dimension of the largest particle or class. Within each class D_i, a quantity n_i particles is counted. The relative *number frequency* f_i of the particles in each size class D_i is given by equation 1.1, also shown in figure 1.5(a).

$$f_i = \frac{n_i}{N} \qquad \text{where} \qquad \sum_{i=1}^{I} n_i = N \qquad \text{and} \qquad \sum_{i=1}^{I} f_i = 1 \tag{1.1}$$

The number distribution f_i of the particles sizes is usually displayed graphically in the form of a histogram, as shown in figure 1.5(a) where depending on the definition, D_i can be taken as the midpoint, start, or end of each class, (Underwood, 1970). For convenience it is assumed that all class widths ΔD_i in a distribution are equal. If ΔD_i is made very small then $f_i \rightarrow f(D)$ a continuous function of D , where $\int_0^\infty f(D)dD = 1$, figure 1.5(b).

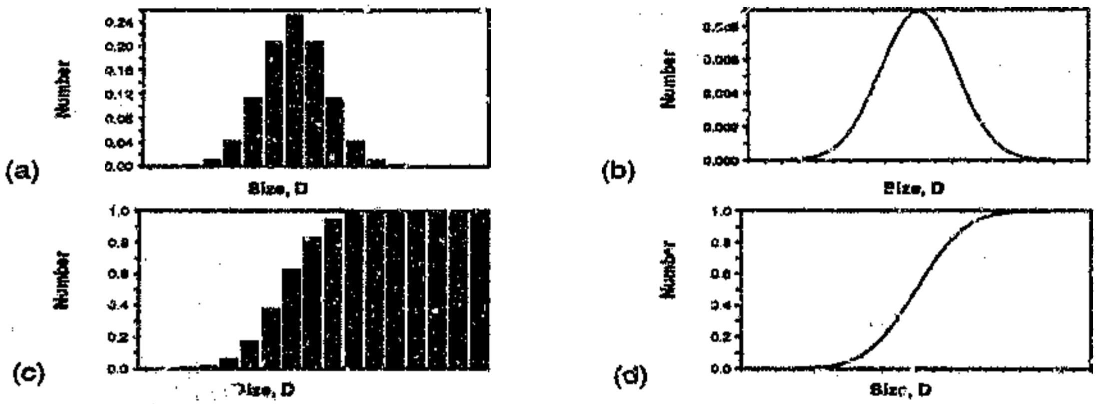

Figure 1.5. (a) Histogram of a relative number-distribution. (b) Corresponding (continuous) relative-frequency distribution. (c) Cumulative distribution of histogram. (d) Cumulative (continuous) frequency distribution.

Size data collected on particle (rock) distributions with imaging methods are usually *number* distributions f_i. However size data collected with sieving methods are the fractions by *mass* of material w_i which have been passed by the sieve of size D_i and caught by a sieve of size D_{i+1} where $D_i < D_{i+1}$. A mass or volume distribution as produced by sieving is usually the type of distribution requested in the mineral processing industry.

All size distribution data (number or mass) can be approximated by the following general histogram where we plot $C_k n_i D_i^k$ versus $C_k d^k$ where C_k is a shape factor and k indicates the dimension of the parameter measured. A number frequency distribution of $\frac{n_i}{N}$ can be converted to a weight or mass distribution $\frac{w_i}{W}$ as follows:

$$\frac{w_i}{W} = \frac{\rho C_3 n_i D_i^3}{\sum_i^I \rho C_3 n_i D_i^3} \qquad 1.2$$

where w_i is the mass of material in size interval D_i to D_{i+1}. W is the total mass of material sieved, I the number of class intervals, and ρ is the density of the material. In practice the conversion from number distributions to weight distributions is generally inaccurate and error prone (Stockham, 1978). This is because the transformation requires weighting the number fractions with an exponentially increasing D^3, figure 1.6(a). These weighted proportions are thus sensitive to sampling and experimental errors, especially in the larger size range where the method requires raising these errors to higher powers. For example, in a 1 to 10mm distribution a single particle error of 10mm has the same weight as a thousand particles of 1mm counted in error! See figure 1.6(b). In addition, the grouping of the observed diameters into frequency intervals which are in practice broad and non-uniform, makes accurate estimation of the average sizes in each class impossible. Small class intervals and large number counts N help to minimize errors in converting number distributions to volume distributions. However even N=25 000 samples may not be adequate, (Kawakami, 1988).

For historical reasons metallurgists have preferred to use the *cumulative* size distribution curve, figure 1.5(c) and 1.5(d), to the relative frequency curves as shown in figure 1.5. Although the integral of the relative frequency distribution tends to hide details of the distribution, the fraction of material within a certain size range may be read directly off the curve, and the slope of the curve gives a good indication of the spread or deviation of the rock sizes.

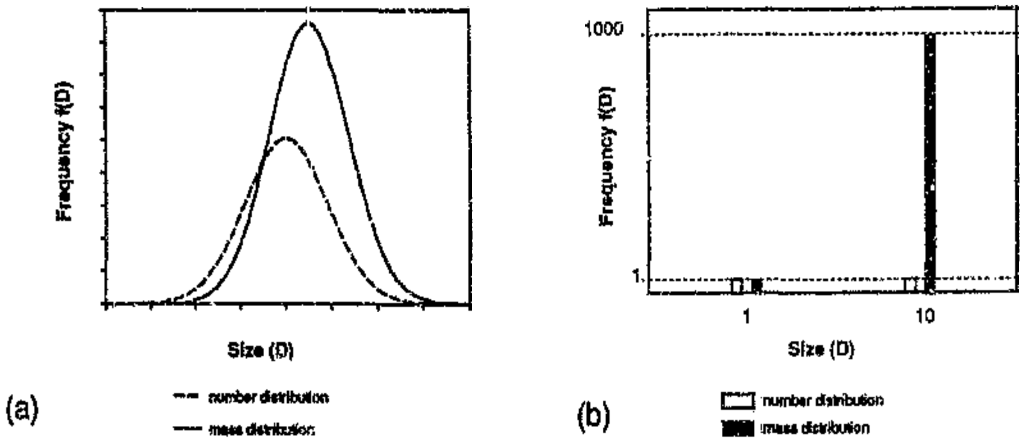

Figure 1.6. (a) Example of converting a number distribution to a mass distribution. (b) Example of the error caused by the conversion of number to mass distributions.

The fraction of particles by *number* less than size D_r is given by $F(D_r)$

$$F(D_r) = \sum_{i=0}^{D_r} f(D_i) \quad < 1 \qquad D_r < D_{max} \tag{1.3}$$

and the fraction of particles by *weight* less than size D_r is given by $W(D_i)$ where

$$W(D_r) = \sum_{0}^{D_r} \rho C_3 f_i D_i^3 \qquad D_r < D_{max} \quad \text{and} \quad f_i = f(D_i) \tag{1.4}$$

The functions $F(D_r)$ and $W(D_r)$ which are normalized to 1 are referred to as the "S" curve or the "cumulative percent passing frequency curves". It has been suggested that a realtime graphic display of $F(D_r, t)$ or $W(D_r, t)$ would be the ideal output of the rocksize instrument, also known as a waterfall display, with time t and size axes as shown in figure 1.7.

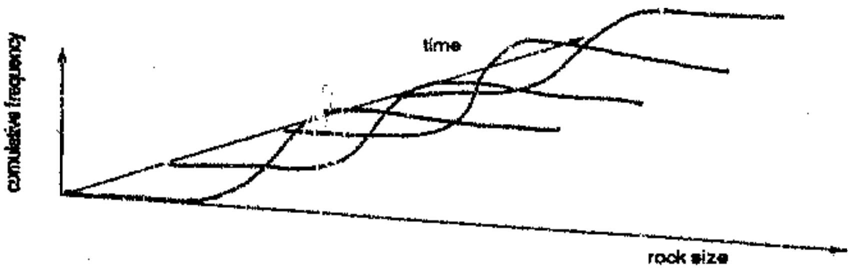

Figure 1.7. Ideal output from the rocksize instrument.

Although the full size distribution for a group of particles (whether in relative frequency or cumulative frequency form) is the ideal data to have, it is often not possible in practice to obtain such data. For mineral processing purposes metallurgists have often indicated that a simple and concise indication of the *average* size and the *dispersion* of the material size is generally adequate. These sample statistics are legitimate for both rocksize characterization and comparison, bearing in mind the different types of distributions available. In many cases statistics computed directly from measured data give a better basis for sample comparison than for example some derived diameter converted to mass data. The statistics usually required are the mean rocksize $\overline{D}$, variance s_D^2 or standard deviation $\sigma(D)=\sqrt{(s_D^2)}$, and skewness g_D. These statistics are defined below for a *number* distribution f_i as opposed to a volume or weight distribution.

$$\overline{D}=\sum_i^I \frac{n_i}{N} D_i \qquad s_D^2=\sum_i^I \frac{n_i(D_i-\overline{D})^2}{N-1} \qquad g_D=\sum_i^I \frac{n_i}{N}(D_i-\overline{D})^3 \qquad 1.5$$

In particular the "cumulative percentage passing of some size" is very common size measurement. This is point D_p read off the "S" curve where $\sum_{i=0}^{D_p} f_i = p\%$. Obviously two or three more points from the "S" curve would desirable as well. (The median is measured when $p=50$).

1.3 LITERATURE SURVEY

The size measurement of rocks and particles has been around since the time of the ancient Egyptians who developed and used *sieving* techniques, (Heywood, 1970), (Allen, 1981). Even today sieving and the use of "grizzlies" have been the main methods for large particle sizing. It was only from about the mid-seventies that alternative methods for on-line particle size measurements on conveyor belts became available. Presently there is no *generic* rocksize instrument acceptable to the mining industry for any on-line installation on mineral processing plants. There are however a number of sizing instruments installed on some plants (not necessarily mineral processing), where the unique nature of the material to be inspected for size, has allowed for the relatively successful operation of a vision-based instrument. The sizing of pellets and fruit which have simple shapes and are usually arranged in a mono-layer[1.2] on the conveyor belt, are examples of the successful installation of a vision-based sizing instrument.

[1.2] Objects arranged in a *mono-layer* are all visible from a top view with none of the particles obscuring one another.

This subsection is divided up into three parts. Section 1.3.1 reviews work directly related to the development of a rock-size instrument, section 1.3.2 reviews the theory of size measurement and the multi-disciplinary science of *stereology*. Because image processing is the methodology with which this rocksize problem is to be solved section 1.3.3 reviews briefly image processing literature with special reference to industrial applications.

1.3.1 Review of rock size instruments

A variety of rock-size analyzers using methods other than sieving (ie imaging) have been developed and are available. The first system to be developed was the ARMCO AUTOMETRICS MSD-95 material size distribution transmitter (Vignos, Elber and Gallagher, 1976), which uses one dimensional image processing techniques. This instrument was developed at the Julius Kruttschnitt Institute in Australia and is now manufactured by ARMCO. Through the use of an optical sensor, this instrument scans the surface of the rocks along a *line* parallel and near to the centre line of the belt. This effectively allows for the detection of the *shadows* or dark gaps between the rocks and ultimately rock chord length as the shadows delineate the rocks boundaries. As the shadows are thus important to the measurement process they are accentuated by illuminating the rocks with *low incident* light. The light intensity pattern as output from the optical sensor is compared to a threshold, and values higher than the threshold are deemed to correspond to the presence of rocks. The chord lengths of the rocks are then estimated by knowing the belt speed and measuring the time the signal remains above the threshold. See figure 1.8 below.

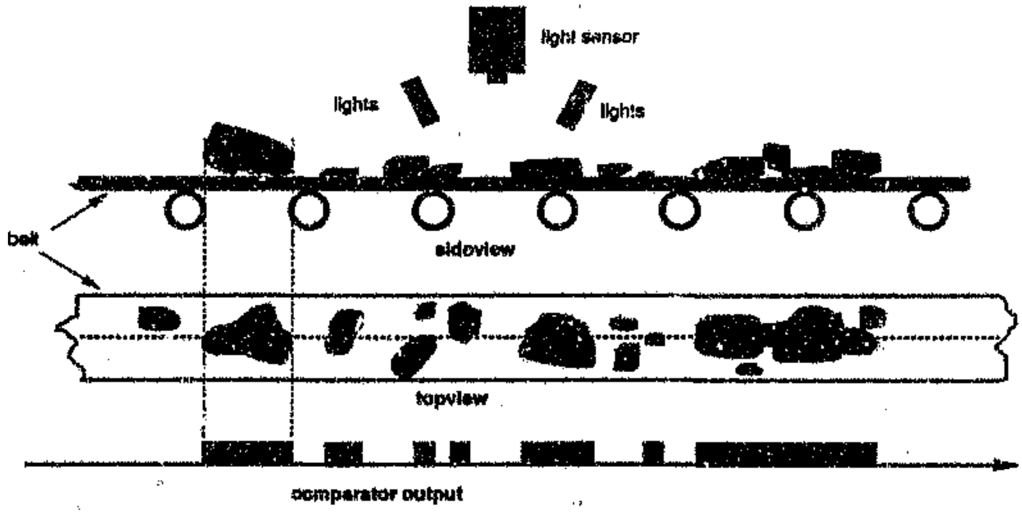

Figure 1.8. Principle of operation of the MSD-95.

Although the MSD-95 provides an online estimation of chord-length distributions which are related to size, the system has severe limitations. The instrument only measures rocks in the centre of the belt resulting in a bias in the measurement because the material on either side of the probe line is ignored. This bias can be disregarded if the rocks are *uniformly* distributed over the full width of the belt which is highly unlikely. Observations of the rocks on conveyor belts show that there are in general significant variations in size across the *width* of the belt. Thus the estimation of the size distribution from these chord-length distribution taken from the centre of the belt is highly biased because this sampling scheme basically ignores the rest of the material on the belt. In addition the system is highly dependant on the absolute value of the ambient light intensity and the rock colour which can vary with time as well as the angle of incidence. During this research it has also been found that the light intensity profile as measured by the sensors is generally not representative of the physical topology of the rocks, ie the detected shadows are not necessarily edges. There are high probabilities that many shadows are not rock edges, and many rock edges do not give rise to shadows dark enough for detection. This problem is particularly acute with angular shaped rocks piled together on conveyor belts.

Eriksen (1978) discusses an instrument to measure particle size distribution of ferromanganese and silicomanganese using a laser beam. In this application particles falling off the end of a conveyor belt (in free flight), interrupt a laser beam. The duration of interruption is measured and knowing the velocity of the rocks in free fall allows for the calculation of chord lengths. These random chord lengths are related to Ferret diameters and size distribution is then estimated from these Ferret diameters. This instrument does depend on a number of assumptions; that orientation and lateral distribution of the falling particles is uniform and random; that all particles fall with the same velocity, and that no rotation occurs during the time of intercept. Another very important assumption is that there is no overlap of particle projections. Most of these assumption are unrealistic, however Eriksen comments that to his surprise a simple but empirical statistical relationship between the volume V and chord length L was found $V = (k.L)^{3/2}$, which is very encouraging.

A system using two dimensional image processing was developed by CONTAC engineering in Chile (Yacher et al, 1985). This instrument compensates for the main criticism of the MSD 95 and the laser system in that it captures a full image of the rocks on the conveyor belt which is scanned over its full area thus eliminating the bias of the MSD-95 where only one centre line of the belt or rocks is scanned. Yacher and co-workers do not describe the type of rock scenes processed, and it is mentioned that "because of computer time and resources ", the analysis is restricted. They also comment that "the measurement of lengths along exploratory lines does correspond to standard ore size distribution analysis such as weight distribution or sieve size". Berger (1985) comments that there could be problems with the simple processing used to binarise the images, and the possible joining together of adjacent objects. According to results presented in this paper (Yacher et al, 1985), the average size measurement output by the system is consistent with the output of the MSD-95 optical instrument.

Berger (1985) comments further that the MSD-95 and the CONTAC system are weak because of their dependence on chord lengths selected arbitrarily to measure size. Wigeson (1987) also comments that linear intercepts cannot be used for size measurements as they are too ambiguous. In this thesis it will be shown to the contrary that these linear-intercept probes if properly understood, are inherently very powerful tools for determining size distribution. In response to his conclusion, Berger developed more complex algorithms where the size measurement is based on area instead of chord lengths. Berger used segmentation and region analysis algorithms in order to identify and thus segment the rocks in each image. However a major problem to arise was that the software processing time was of the order of a half an hour or more on a minicomputer for an image of size 350x350 pixels square. Although the objective of Berger's research was not to develop a real-time system, a "reasonable" processing time is critical to the development of an instrument applicable to the mining industry where system time constants play an important part in control systems design.

Berger's results indicate that the measurement of rocksize is not impossible, as his system was able to classify rocks as either "small", "medium" or "large". In his dissertation he presents some fairly good as well as bad results for several individual images. These varied results together with the fact that each image captured is only a tiny sample of all the material on the belt, implies that the measurement will be *statistical* and that *averages* must be considered.

Grannes (1986) describes an instrument to measure the size distribution of Taconite pellets on rotating beds. The pellets are basically spherical in shape with uniform surface characteristics thus forming scenes of simple objects. Grannes describes imaging techniques such as thresholding and symmetry based edge detection, and obtained size measurements which compare satisfactorily with sieve size. However the shapes of the objects in the scenes analyzed are simple, (close to spherical) which is a decisive factor for accurate object recognition. Grannes is also the first to discuss the problem of *blurring* caused by *moving* images and the fact that system accuracy decreased at speeds above 0.5m/sec, a serious limitation.

The capture of *high speed* images from conveyor belts and associated blurring of these images has generally been avoided by most investigators of rock-size measurements on conveyor belts. Yacher et al (1985) mention that their belts were moving at $2ms^{-1}$ but no mention is made of blurring which should be ≈ 70mm for every meter of image. Rudolph (1987) tackled this blurring problem by designing and building a custom video camera for the specific purpose of capturing high images of rocks off conveyor belts. The camera is based on a two dimensional CCD image sensor with an adjustable shutter speed, which could operate at up to 1ms.

Wigeson (1987) developed some fast segmentation algorithms that work on scenes of rock fragments resulting from open-pit blasting. His methods are based on template matching for edge-detection and a rule-base which led to an area measurement for the estimation of particle size. Wigeson does not comment on the stereological aspects of his measurement problem, but concludes that relating areas of the segmented images to sieve size, is a major problem to be tackled. Wigeson in his work also comments on the ambiguities that arose in trying to perform accurate rock recognition which influenced his results greatly.

1.3.2 Review of size theory

Conceptually the objective of this rocksize-measurement problem, is to determine the *internal structure* of a pile of rocks (body) lying on a conveyor belt. This to be done from *observations* made of the *top-surface* of this pile of rocks. The internal structure of a body refers to the spatial and geometrical arrangement of the constituents or sub-structures of the specimen, which includes size and shape information.

The rocksize problem is similar to the problem of estimating the amount of a mineral present in an ore body by examining a microscopic sections taken from samples of the ore body. The measurement of the parameters of the three dimensional (3-D) structures of opaque specimens, such as the ore bodies and in this case a pile of rocks, has been investigated for many years, and much success has been achieved with similar types of problems in fields diverse as metallurgy, botany and medicine. The problem reduces to determining the internal structure of the 3-D specimen from observations made on *plane sections* cut from specimens. These sections being only two dimensional samples of the specimen, give biased information about its three-dimensional structure. Here the deep problem of relating solid geometry to plane sections is compounded with questions of sampling variability, bias, choice of sampling design and inference. Consequently *stereological* methods have evolved through the years to try and provide unbiased estimates of the three dimensional structure from the two dimensional information, (Underwood, 1970), (Weibel, 1980a 1980b), (Moore, 1985), (Gunderson, 1986).

Stereology is a multi-disciplinary science based on *stochastic geometry* of which Baddeley (1982) provides an informal review. We refer the reader to Santalo (1976) and Matheron (1975) for an extremely detailed background to the topics of "integral geometry and geometric probability" and "random sets and integral geometry" respectively. Although these areas of mathematics are beyond the scope of this thesis, it is evident that there are some very powerful and fundamental concepts on which stereology is based. *Stereology provides statistical* estimates of the parameters of the structure (Nicholson, 1978), through the use of zero (points), one (lines), or two (planes) dimensional random probes on random sections. A generalization to higher planes is also possible (Davy and Miles, 1977). The selection and application of these random probes to estimate structure parameters is not trivial as is demonstrated by 'Bertrands Paradox' (Papolous, 1965), where the importance of specifying and understanding the frame of reference for geometric probabilities and models being applied is emphasized (Miles, 1977).

Stereological methods may be split into two broad categories (Nicholson, 1970). The *first* category concerns the estimation of average aggregate properties such as the volume fraction V_V or surface area fraction S_V of a particulate system. The earliest estimation of aggregate properties is the areal analysis of Delesse (1848) to determine the mineral composition of rock. DeHoff and Rhines (1961), and R.E. Miles (1977) give a good introduction to stereology showing how stereological models can be built up to estimate parameters like the volume fraction of some particulate system under investigation. Underwood (1970), and Weibel (1979, 1980) provide a very good background to these estimators as well. Rigorous and comprehensive theory of stereological estimators have been made by Miles and Davy (1976), and Davy and Miles (1977) present a wide class of unbiased ratio estimators. See also Miles and Davy (1977) for sampling subregions or quadrats. Most of the these papers deal with convex shaped particles and Miles (1984) gives stereological formulae for not-necessarily-convex particles.

The *second* group of estimation techniques is the determination of the *size distribution* of particles within a particulate system, which depends very much on shape and in general has been based on the analysis of dilute systems of spheres. These techniques date from Wicksell (1925) who made a biometric examination of corpuscles. Through an integral equation he related the size frequency of spherical particles to that of circular intersections on a random plane of intersection. This result was later extended to ellipsoidal particles by Wicksell (1926). The methods used to analyze these particles are based on section diameters, the Scheil and Schartz-Saltykov methods, section area methods (Johnson-Saltykov), and section-chord methods (Cahn and Fullman), see Underwood (1970) for details. Goldsmith (1967) later developed the integral equation relationship for spherical particles embedded in a thin slice and Kendall and Moran (1963) summarize these frequency function relationships. Underwood (1970) chapter 5.3 provides a detailed description of the various methods developed over the years by various researchers for determining particle size measurements.

Unfolding size distribution of the rocks from *linear intercepts* (chords) taken off projections of the rocks is part of the objective of this research. The use of linear probes was investigated as far back as 1733 with "Buffon's needle problem" (Kendall and Moran, 1963:70), where the probability p of a line of length L intercepting a fixed grid of parallel lines spaced distance d apart, $L < d$ is estimated. Buffon obtained $p = \frac{2L}{\pi d}$, which when given L and p allows for the estimation of d. This could be also interpreted as a random line probing the unknown contents of a fixed circle C of radius d, where the frequency of the encounters between the probe and the fixed needle yields an estimate of the needle's length. In fact given any curve S within C having finite length $L(S)$, the mean number of intersection points between S and a random probe line l is

$$E\{\text{number of intersections}\} = E\{S \cap l\} = \frac{2L(S)}{\pi d} \qquad 1.6$$

Baddeley (1982) comments that it is remarkable that equation [1.6] does not depend on the geometric configuration of S within C , but does depend on the probability distribution of l . Equation [1.6] can be interpreted as an estimator of the length of an unknown curve based merely on its intersection with random linear probes. This result can be extended to encompass other geometrical shapes and probes of higher dimensions in which suitable choices of the probability density of the parameters of the probes can lead to some remarkable expressions for some of the mean values associated with random lines (Baddley, 1982). Note that the uncritical application of stereological estimators can result in biased or erroneous results.

However what is important is that the use of random intercepts on geometric structures can provide information on that structure which is the basis behind the reasoning for using linear intercepts in this work for inferring rocksize measurements. We refer the reader to Santalo (1976), Matheron (1975) and Kendall and Moran (1963) for in-depth discussions on geometric probability and other subjects related to stereology which are beyond the scope of this thesis. Other references are Smith and Guttman (1953) who use linear intercepts to estimate for example grain boundary area, Fullman (1953) who developed size measurement methods based on lineal and area analysis of spheres, plates and rods.

1.3.3 Review of machine vision and image processing

Machine vision which encompasses image processing and analysis are the methods chosen to perform this rocksize measurement. Fortunately the basic technology for capturing and processing images has been investigated for many, years and many machine-vision applications and image-processing techniques have been developed, (Pratt, 1981), (Gudmundsson, 1986), (Spomer, 1988), (Yang and Sengupta, 1988), (Warnecke et al, 1985). For online applications and automated inspection refer to West et al (1988). We also refer the reader to Nishihara and Crossley (1988), Darwish and Jain (1988), Boerner and Strecker (1988) and Siew et al (1988) all from the same IEEE PAMI issue, for examples of up to date reviews of a number image processing applications in industry. Not only has the methodology and the technology to handle and process images efficiently for industrial applications been established, but the advancements in digital electronics, computer and software engineering are accelerating continuously, making the application of machine-vision in industry a viable technique.

As the field of machine vision and its related areas and applications is so vast, only those references where applicable, will be referred to in this thesis.

1.3.4 Summary and Conclusions

A number of investigations have been carried out with regard to rock or particle size measurement and numerous instruments and mathematical techniques have been developed for this purpose. What is apparent is that these systems have been developed on the basis of a number of assumptions, for example assuming *spherical* and *convex* particles, *low density* particle distributions, *monolayers* arrangements, and low scene speeds. These assumptions make the rocksize problem easier to solve, and must thus be taken into account when evaluating these systems as far as rocksize measurements are concerned. In addition most instruments developed do not work satisfactorily on rockstreams on mineral processing plants thus providing incentive for this research.

No *direct* references or work in available literature could be found with regard to the estimation of rocksize from rock piles and rockstreams using stereology. In addition, the assumptions made with regard to stereological measurements in other applications as found in the literature are generally not applicable to moving rockstreams as found in the mining industry.

1.4 RESEARCH PHILOSOPHY

The philosophy adopted towards this research has been influenced by the practical aspects of ultimately engineering a real instrument for installation on a plant. From the beginning, an *empirical* and *experimental* approach was developed in order to verify certain concepts, crucial to the measurement, which were very much in doubt. For example, the use of chord lengths to measure size had to be verified. In addition programs to develop certain infrastructure such as DC lighting systems, and camera hardware for the capture of ***high quality moving*** images, which proved to be a major stumbling block, were initiated as the problems manifested themselves.

The development image processing software and hardware systems which would lead to a *"fast"* and economical implementation of a rocksize instrument for moving images was of high priority because of limited time and finance. This resulted in an initial selection of techniques on an adhoc basis from the literature. As experience and evidence built up, a more refined experimental program was developed in order to compensate for the peculiarities of the rockstream and other possible oversights.

The above approach was effectively to "take a dive into the deep end", because without performing a scientific and logical investigation from first principles, it was postulated that the measurement could be made. This approach was selected, because from the literature surveys and initial experimentation, researchers appeared to be confronted with insurmountable obstacles through the development of rocksize-measurement techniques based on a strictly analytical bottom-up approach. This bottom-up approach over the years has involved without any dramatic success, much effort to extrapolate size measurement models based on spheres to complex shaped particles. Luerkens and co-workers (1987) state that, although an instrument may measure the size of spheres perfectly from a characteristic dimension, perfect spheres rarely occur in nature, and any size instrument still leaves one in *doubt* as to the worth of its reading for irregularly shaped particles.

In this research attempts were made to use existing techniques which had limited success. As a result a new philosophy was created where it was assumed that the output of the instrument does not have to be forced to provide sieve size directly, although the output should be meaningful and correspond to sieve size. This philosophy opened the door to the application and development of some new techniques for measuring conveyor-belt rock size because the limiting objective of sieve size was not a prerequisite.

Finally it must be noted that a full mathematical treatment and development of a model of the techniques developed in this thesis have been tackled piecewise where appropriate. However a rigorous mathematical treatment tying up all the possible factors affecting the measurement is an immense task which falls beyond the scope of the thesis as shown in chapter 3. It is the opinion of the author that the experimental and heuristic evidence developed in support of this measurement is sufficient in itself.

1.5 THESIS FORMAT

Globally this thesis is divided into two parts, the first being the introduction, background and discussion of the rocksize problem, (chapters 1,2 and 3). The second part of the thesis (chapters 4,5,6, and 7) describes the solutions developed for the rocksize problem, and is structured in a manner comparable to the progression of sequential transforms required by a rocksize instrument to transform images of rock scenes to size data.

Chapter 1 of this thesis *introduces* the problem of measuring the size distribution of rocks on a conveyor belt. The *rock material* on the belt, the specifications for an ideal instrument, as well as the proposed area of application of such an instrument is described. *Background* is given on the definition of size and how shape is inextricably linked to the determination of particle size distribution. This introduces the ambiguity of this measurement which is strongly coupled to the irregular shapes of the rocks. Various research programs to develop a rock size instrument are also discussed, together with a summary of *literature* pertaining to *image processing* and the estimation of size from using *stereological methods*, in particular linear probes. The chapter is concluded with the philosophy [illegible] during this research and the thesis format.

In *chapter 2* various methods of non-intrusive measurement of rocksize is discussed, and the motivation for *machine-vision* techniques is given. The theory behind the generation of images from rockstreams together with the proposed processing to obtain size, is then proposed. This includes an overview of the sequence of processing states which transforms an image to size information. The system structure for this task as well as assumptions made with regard to this instrument system are also presented.

In *chapter 3* the transformation of measurements on section traces to the final sieve size distribution using *stereological* methods is described. Traces (usually two dimensional) are of a lower dimension to the three-dimensional objects (rocks) to be sized. There is therefore an inherent loss of information, and consequently the estimation of 3-D structure parameters from traces becomes a difficult application of the deconvolution problem. However it is shown that if assumptions are made with regard to the shape of particles, for example spheres, then valid formulae for size estimations can be developed. This is extended to more arbitrarily shaped particles with associated errors and limitations, where formulae for extracting size distributions from areal and linear traces are described. The use of *linear probes* to probe the traces and which give chord-length distributions is then motivated.

All the models described in this chapter have been derived under many assumptions. Thus at the end of chapter 3, an attempt is made to derive an explicit stereological model of rockstream that does not require any assumptions except that the rockstream can be a stochastic process. Derivation of this model proves to be very difficult, and it is concluded that for practical purposes such a model is perhaps superfluous in the light of such difficulties such as the accurate modelling of the rockstream dynamics. The problems encountered in deriving the model motivates the empirical approach and alternative methods developed in this research to solve this rocksize problem.

In *chapter 4* the initial image-processing for extracting traces from images of rockscenes is developed. The objective of the image processing is to extract *edge boundaries* of the projected rock images which are valid traces for making linear-intercept measurements. The extraction process involves image-processing techniques such as thresholding and edge detection, which are used to transform and filter the rock image content into *edge patterns*. However chord-length measurements on these traces tend to be meaningless because of the effects of occlusion and touching which introduce rock identification errors and noise into the edge patterns.

Thus in *chapter 5* further image processing and analysis techniques are derived in order to correct the errors in the edge patterns. The techniques include those of *mathematical morphology* which generally avoid or reduce the problems arising from the use of traditional or classical imaging methods. The algorithms developed for repairing the errors in the edge patterns include the *"joining"* and *"morphological"* algorithms.

In *chapter 6* the experimental set-up and some examples of *results* ie raw chord-length distributions, measured in the laboratory and from a conveyor-belt pilot-plant are presented. The software used to derive these results are the transformations described in chapters 4 and 5. Note that the images used in developing the algorithms used in chapters 4 and 5 are derived from experimental rigs described in chapter 6.

In *chapter 7* methods for the transformation of raw linear or chord distributions to size distributions are developed. Existing methods of particle size inversion (some in a modified form) which include linear inversion, constrained linear inversion and King's method are implemented. These methods are shown to provide useful size information, but problems still remain due to the unique and ambiguous nature of the rocksize inversion problem. As a result some relatively simple but powerful techniques are developed which transform the chord length data to a form which is useful, but which does not relate directly to sieve size distributions. These techniques are termed *cumulative*, *weighting* and *moment* transforms, and it is suggested that new measurement standards are adopted from these techniques and similar techniques. A number of new morphological sizing techniques are also presented which also produce "size" information as a result of a new philosophy which states that any measurement which is useful, repeatable and conforms to Matheron's size criteria can be used. Thus a new standard for rock-size measurement is proposed, which can be used in the mining industry especially for control purposes.

In *chapter 8* we summarize on the work achieved and conclude the thesis. Recommendations for further research and areas for improvement are also discussed.

2 THE INSTRUMENT SYSTEM STRUCTURE

2.1 INTRODUCTION

The automatic and non-intrusive inspection of rocks to measure rocksize implies the use of *remote-sensing* techniques where radiation is used to examine the specimen under investigation. In general the derivation of knowledge using remote sensing consists of the following sequential stages (West, 1988) :

i) *Interrogation.* The specimen to be analysed is interrogated by an energy input.
ii) *Modulation.* The specimen interacts with this interrogating energy varying its characteristics and modulating this energy with useful information.
iii) *Sensing.* The modulation is sensed and recorded for subsequent analysis.
iv) *Perception.* The modulation is analyzed so as to deduce the relevant characteristic of the specimen.
v) *Understanding.* The perceived characteristics are then related to the fundamental properties of the specimen.

Thus in order to realize a rocksize instrument using remote sensing, the instrument system must encompass the above five stages. In this chapter the philosophies, architecture and structure for a rocksize instrument based on machine vision and incorporating the above five stages is selected and motivated. The energy selected for interrogation is the visible part of the spectrum (light), and thus the method to be used for *modulation* and *sensing* is **machine vision.** In order to *perceive* and *understand* images so that a rocksize distribution can be derived, the instrument must be endowed with **artificial intelligence** (AI) capabilities similar to man (Maragos, 1985).

Two subareas of AI are *computer-vision* and *pattern-recognition* which attempt to emulate the human visual system in order to understand and interpret unconstrained scenes containing many different objects in different orientations and positions. A branch of computer vision is *image processing* in which image to image transformations such as enhancement, feature extraction, and segmentation are performed. *Pattern recognition* discriminates between populations of patterns via a search for features or invariant attributes.

Techniques of remote-sensing using light result in the creation of two-dimensional intensity patterns from which size distribution is to be inferred. The theory behind the creation of these images, and the motivation for a data-processing structure to infer rocksize from these images are the main subjects of this chapter. In particular, the elementary low and high level tasks of image processing and pattern analysis for rock-recognition and size-measurement are broadly outlined.

2.2 NOTATION AND SYMBOLS

Throughout this thesis certain symbols and abbreviations will be used to describe the objects to be transformed and the systems which perform the transforms. ***Signal processing*** is the central concept of where the ***objects*** (signals) are input to and output from systems. All signals are defined to be a subset of the Euclidean space unless specified otherwise. The objects to be manipulated can be either *signals* or *sets*. An m-dimensional (m-D m=1,2,3 ..) ***function*** represents and refers to a multilevel signal, whereas an m-D ***set*** refers to m-D binary (two-level) signal. Function processing systems can accept and output m-D signals, whilst set processing systems can only input and output binary signals. A subset of function processing systems can input functions and output sets.

$\mathbf{R}$ and $\mathbf{Z}$ represent the set of real and integer numbers respectively. $\mathbf{D}=\mathbf{R}_m$ or $\mathbf{D}=\mathbf{Z}_m$ is the *domain* set on which signals are defined. $\mathbf{V}=\mathbf{R}$ or $\mathbf{Z}$ is the range set on which signals take values. Capital letters X, Y, denote sets, whilst points of a set are denoted by small $a, b, \ldots x, y, z$. $\{x{:}P\}$ denotes the set of points satisfying some property P. $f{:}A \rightarrow B$ denotes a mapping f whose domain is A and range is a subset of B. A certain phase X can be represented in m dimensions by X_m. For example X_2 represents the phase X in a two dimensions image.

An ***image*** is defined a collection of points on a closed domain $\mathbf{D}_2=\mathbf{R}_2$ where $I{:}\mathbf{D}_2 \rightarrow \mathbf{V}$. When digitized the image becomes $I{:}\mathbf{Z}_2 \rightarrow \mathbf{Z}$. The two dimensional ***image*** $I=I_2$ can be also be considered a multilevel signal (function) represented by a two parameter function in the 3-D Euclidean space as $I=I(x,y)$, $x,y \in \mathbf{D}$. A profile I_1 , is a subset of I_2, where $I_1=I{:}\mathbf{D}_1 \rightarrow \mathbf{V}$, $\mathbf{D}_1 \subset \mathbf{D}_2$. A profile can also be represented by a function $g=g(x)$ where $x \in \mathbf{D}$. See figure 2.1.

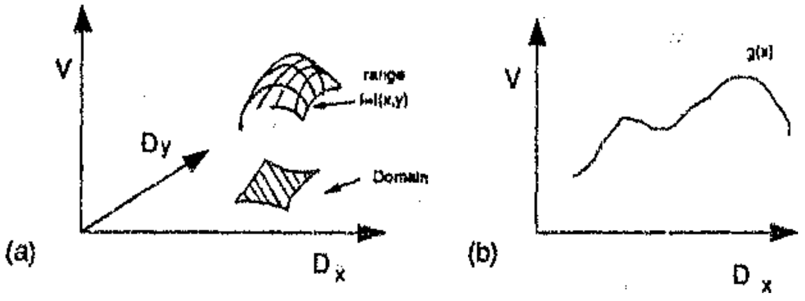

Figure 2.1. Definition of (a) an image and (b) a profile.

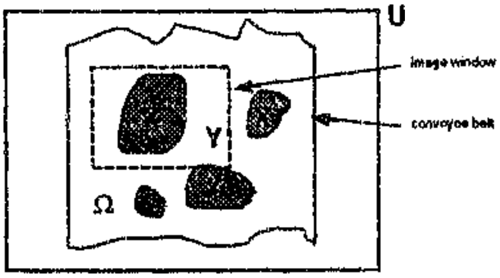

Figure 2.2. Set representative model of the conveyor belt.

The *rocks* and *conveyor belt* will now be defined in terms of set theory (figure 2.2). The universe which includes the conveyor belt structure and the rockstream is denoted by the universal set $\mathbf{U} = \{u : u \in \mathbb{R}_3\}$. The rockstream on the conveyor belt is itself defined to be a three dimensional matrix Ω , $\Omega \subset \mathbf{U}$. It is assumed that the rockstream Ω is made up primarily of two disjoint phases, the rocks (grains) X , and the air gaps between the rocks (pores) Y , where $Y = X^c$, and $X \cup X^c = \Omega \quad X \subset \Omega, \quad Y \subset \Omega$. It is assumed that the rocks and air do not mix, ie X and Y are disjoint and that $X \cap Y = \varnothing$. The i'th rock is denoted by X_i where $X = \cup\{X_i\}$. If water (X_o) and wood (X_w) exist in the rockstream then $X \cup Y \subset \Omega$ because $(X_w \cup X_o \cup X \cup X^c) = \Omega$. It is assumed that the quantity of wood and water on the conveyor belts is small thus both X_w and X_o are ignored. It is also assumed that each rock is discernible from its neighbour ie that $X_i \cap X_j = \varnothing \quad \forall \quad i \neq j$.

2.3 JUSTIFICATION OF VISIBLE LIGHT FOR REMOTE SENSING

In this subsection the utilization of light for remote sensing as opposed to other types of radiation is justified. Note that the *ideal* objective of the remote sensing system is to extract a *full* geometric description of *all* the particles making up the rock stream Ω from which size distribution can be measured.

The measurement principle behind the proposed remote sensing system is that the interrogating radiation incident on the rocks (I_i) is modulated by the properties of Ω_3 , and produces a reflected or backscattered radiation (I_r) which is sensed as a 2-D intensity pattern I_2 (figure 2.3). If it is assumed that the modulation process is a function of the size distribution of Ω namely $f_\Omega(D)$, then it should be possible to estimate $f_\Omega(D)$ from the analysis of the sensed patterns in the image I_2 .

There are however many different types of radiation and associated interrogation and modulation mechanisms which could be used to implement the measurement system shown schematically in figure 2.3. The different types of radiation include the electromagnetic spectrum, acoustics, and particle radiation such as electrons and nuclear particles.

The choice of radiation is coupled very strongly to the response of the various modulation mechanisms to *size* properties of the rockstream Ω as opposed to other properties such as shape, surface texture, dielectric, refractive, reflective, and polarization properties. The properties of the radiation which interact with the rockstream Ω and influence the sensed image patterns, include the bandwidth, ie monochromatic radiation, intensity, source radiation pattern, and whether the radiation is incoherent, and coherent (lasers), or structured.

Figure 2.3. Block diagram of the link between images and the rockstream.

Thus there are a number of radiation mechanisms with which the on-line interrogation and sensing can be done, (Regtien, 1986), (Jarvis, 1983). These include,

(i) attenuation mechanisms (eg ultrasonics) which is dependant on the transmission characteristics of the rocks, ie path-length and hence their size,

(ii) time of flight techniques using pulsed ultrasonics or microwaves, which can allow for the height of the rocks above a reference plane to be measured

(iii) scattering and refractive methods where radiation such as light, microwaves, sound, and lasers illuminate the rockstream which reflect the radiation to a sensor and creates an image (Ylitalo, 1986).

The selection of the most appropriate technique is also dependent on

a) The spatial density N_V of the rocks X ,

b) the actual number of rocks that may be sampled,

c) The wavelength λ of the probing radiation relative to the rocks' sizes especially the smaller rocks, as well as,

d) The influence of the surrounding environment which should be minimized.

The rocks in Ω can be closely packed and the spatial density n_V high, although the opposite is also true. In addition the number of rocks n_L per unit length of belt can range from one or two rocks to a few thousand depending on the sizes of the rocks and the mining application. High n_V or low n_L imply that acoustic or laser methods utilizing diffraction and scattering as used with particle sizing methods for slurries cannot be applied because of group and environmental effects. With high n_V time of flight methods using ultrasound to build up contours maps are also not feasible because of scanning and resolution problems related to the beam widths. In addition the reference height of each rock on the top of Ω changes randomly with time and position as well. Acoustic-pulse-echo methods are also not feasible for sizing rocks arriving randomly and with very sudden changes in height (size) for on line measurements. Ultrasonic imaging is also not feasible because for example the attenuation in air is quite high for the frequencies needed to resolve a millimetre. Refer to Herment et al (1987) for more comments on the limitations of ultrasonic imaging, and Aldridge and Clement (1982) who comment that "there is no ultrasonic equivalent of the photographic plate". However Lalouche et al (1989) have performed 3-D image reconstruction. The use of ultrasonic holography may hold some potential except that these methods rely on liquid baths and visible light to obtain the image, Szilard (1982 chap. 3 and 4) and Krautkramer (1983 chap. 9.4). Finally how does one process these resulting holograms ?

Microwaves techniques have intrinsic problems such as absorption by moisture, and scattering and absorption by the conveyor belt steel structure (Carr-Brion, 1987) which do not make them feasible for rocksize measurement. Laser ranging methods are a possibility, except for expense (Lee 1988). For most of these methods *image reconstruction* and the subsequent *object recognition* are common major problems.

It is thus concluded that remote sensing using a vision (imaging) system is the best method with which a working system may be developed within a reasonable time and for a reasonable cost. The advantage of light is that the image I is easy to obtain without the scanning, resolution and other problems present with for example microwaves and ultrasonics, one of the most important being multipath scattering which can be ignored with light.

An *image I* is now defined as the 2-D intensity pattern produced by visible radiation reflected from the 3-D surface of Ω . The physical measurement system thus consists of an appropriate light source(s), camera for sensing and capturing images of rocks lying on the belt, a frame-grabber with which to digitize these images, and a computer where image processing and analysis techniques will calculate rocksize from the digitized images. These rocksize results are then to be displayed on monitors to plant operators or fed into process-control computers.

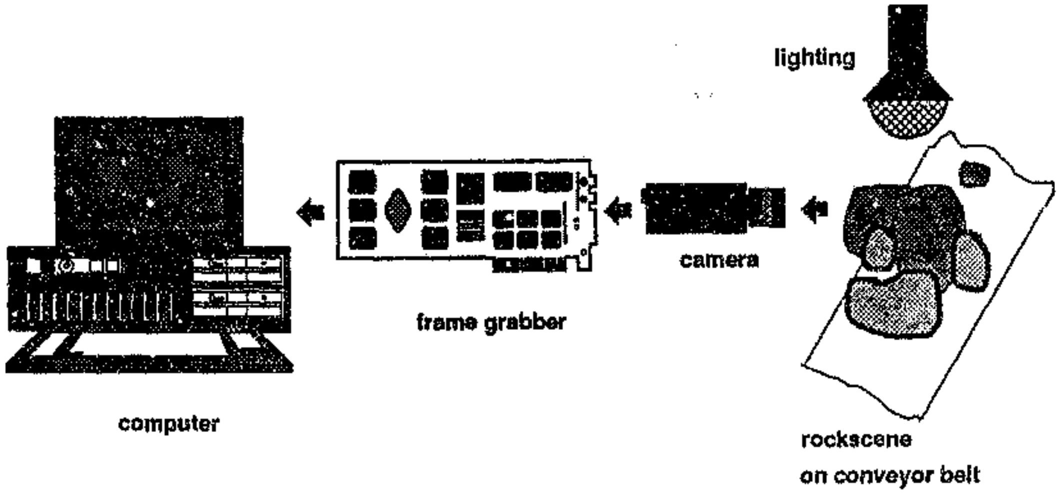

Figure 2.4. Schematic diagram of the rocksize instrument based on machine vision.

2.4 THE AMBIGUITY IN IMAGES

Rocksize measurement using machine-vision techniques is appealing from an intuitive point of view because *observations* of the rockstreams allow one to gauge *qualitatively* the size of the rocks and how the size distribution changes with time. Part of the objective of this thesis is however to extract meaningful *quantitative* size measurements of moving rocks from conveyor-belts. The problem here is that the quantification of qualitative patterns presented in the images, is inherently a subjective process dependant on the observer and his powers of *perception*. In addition each individual perceives things differently and as Serra (1982) states, "we see only what we want to look at".

The interpretation and understanding of images which are only *representations* of the real 3-D world, introduce some unique problems especially the ambiguity of object recognition. Serra (1982) states that "among the very vague notions with which we live, that of an image opens up a world which is particularly rich with meanings, suggestions ... and with *ambiguities* !" Ambiguities in images imply that there is *more than one* possible interpretation or mapping of the image contents. For example Pentland (1984) presents an image which could be interpreted correctly as being either a crater or hill depending on what *a-priori* knowledge the observer has been given. It is therefore important to keep in mind the fact that imaging and image understanding is an inherently ambiguous discipline unless sufficient a-priori information is supplied.

Serra comments further we have "feelings" about images, and to ask one to be precise and to describe an image is very difficult if not impossible. An engineer or a scientist requires an objective and quantitative description from an image, a task which can only be partially accomplished by *limiting* the scope of the interpretation associated with an image, which is undesirable. In the same way, the machine-vision system must limit or filter out all objects from images which are *not* related to size, in order to make the quantification of image content manageable. However an image filtering operation is an exceedingly difficult task because there is a large amount of information to be considered in images, and object recognition problems in such images does not preclude indiscriminate filtering.

2.5 IMAGE GENERATION FROM SURFACES

2.5.1 Introduction

The result of the remote sensing process is a **2-D image** from which characteristic or statistical diameters and hence size, will be measured. However in order to make any size measurements, geometric details of the rocks related to their size in the 3-D world must be available from the 2-D image. There is thus a need to establish unambiguous links between 3-D rocks and 2-D images, showing that *features* in the image are linked to the *geometry and hence size* of the rocks. In particular, can 3-D information of some object be derived from a 2-D representation of that object, especially when the 2-D information is corrupted or modified by *known* and *unknown functionals*, ie *noise* ?

In this section the generation of images from surfaces is modelled with the ideal objective of reversing this 3-D to 2-D process (figure 2.3) so that the 3-D *surfaces* may be *reconstructed* and size measured.

These transformation and modelling processes are essentially *object* and *information extraction* processes, which historically began in the 1940s in other application areas, and which has led to present *pattern-recognition* theory. Charniak and McDermott (1985) comment that "fortunately we know pattern recognition can be done, as we do it ourselves". There is thus much support and successful work being done in deriving models for 3-D reconstruction from 2-D data. For example Pentland (1984) points out that his model for reconstructing surfaces from images do correlate well with the human-image perception as well as biological vision systems.

Methodologies for pattern recognition and extracting size information from images fall into two main categories, I) *full* 3-D surface reconstruction methods, and II) *partial* or estimation methods which use stereology and other image-processing methods to extract only those features of interest. Included with the partial methods are the recently developed *morphological* methods, (Serra, 1982, 1988). None of the above two groups of techniques is independent of the other, and the methods used to measure size in this thesis is based on principles extracted from both groups of techniques.

Full 3-D surface reconstruction is the ideal methodology to use because it is reasonable to assume that size can be derived from the full geometrical and spatial description of the surfaces and interfaces of all particles in the scene under inspection. However because of occlusion, full 3-D methods will in general only be able to provide partial information of the top surface of Ω . On the other hand stereological methods do not require full 3-D geometrical descriptions of the objects in order to derive estimates of size. These methods, however do assume that the 2-D images are *accurate representations* of the objects under investigations.

Although full 3-D surface reconstruction is not used in this application the principles behind these methods discussed in section 2.5.2 establish the links between the image I and the rockstream Ω and assumptions made with regard to image processing adopted during this research. These links also help to clarify certain problems experienced for example with the MSD-95.

Within the group of 3-D surface-reconstruction methods are a number of sub-groups of techniques (Terzopoulos, 1988). These are : i) *shape-from shading* - Pentland (1984), Ferrie and Levine (1989), Penna (1989), Frankot and Chellappa (1988), ii) *stereoscopic methods* - Marr and Poggio (1979), Hu and Ahuja (1989), Herman et al (1984) iii) *structured-light techniques* - Shrikhande and Stockman (1989), Wang and Aggarwal (1988), Hu and Stockman (1989), Stockman et al (1988), iv) *shape-from-texture* and v) *shape-from-motion*.

2.5.2 Shape from shading

Shape-from-shading methods establish the relationship between the image irradiance and the shape of the scene-surface from which the image was generated. It is the information resulting from this interaction that any sizing technique must handle.

Shape-from-shading methods are posed mathematically as variational principles or partial differential equations and establish the foundations on which most image processing work is based. In discussing the relationship between Ω and I it is assumed that the intensities as measured in image I are equal to the irradiance of the scene under observation, ie that the sensing does not distort the image.

Let $I(x,y)$ be the observed image intensity pattern and $z_\Omega = z(x,y)$ the unknown surface function describing the top of Ω in terms of (x,y) in the euclidean space. The relationship between image intensity and objects' surfaces is shown is equation [2.1] (Frankot, 1988) where $\Re$ is some function, $z_x = \frac{\partial z}{\partial x}$, $z_y = \frac{\partial z}{\partial y}$, ρ is the surface albedo, $\mathbf{V}$ the direction of the viewer (camera), and $\mathbf{L}$ the direction of the light source.

$$I(x,y) = \Re(z_x, z_y, \rho, \mathbf{L}, \mathbf{V}) \qquad 2.1$$

It is assumed that $\Re$ is spatially invariant and that any point (x, y) on the reflectance map I is a function of a single point on the (x, y) plane, ie multiple reflections are ignored. An exact solution (z) to equation 2.1 does not always exist, and the problem is ill-posed (Terzopoulos, 1986b) or may consist of an infinite number of solutions (Frankot and Chellappa, 1988). Ferre and Levine (1989) point out that although practical experience indicates that surface z can be inferred from local analysis of shading, mathematical analysis supports the opposite. Both Pentland (1984), and Ferre and Levine (1989) continue to state that shape-from-shading techniques require considerable *a-priori* knowledge of the scene, and thus cannot be applied to an unfamiliar scene. Even the relaxation of the requirement of exact image recovery, to a *qualitative* description, still requires the setting of *constraints* and *assumptions*. For example because Pentland's technique assumes no *a-priori* information, the image recovery is necessarily imprecise. However most researchers conclude that analysis of shading can provide useful descriptions of scene properties, for example Terzopoulos (1988) has developed some useful algorithms for shape determination.

Pentland (1984) derives a similar model to equation 2.1 to describe image formation. Consider figure 2.5 in which a single light source (no secondary illumination) at **L** irradiates an elemental surface with unit normal **N**. Assume further that the surface has a Lambertian reflectance function (Pentland, 1984). The intensity recorded at each point in the image is given by

$$\mathbf{I} = \rho\eta(\mathbf{N} \cdot \mathbf{L}) \qquad 2.2$$

where η the intensity of the illuminant. This simplified irradiance equation is a function of six unknowns, because each unit vector (**I**,**N**,**L**) is defined by two parameters, for example I should be written $I(x, y)$. Both Pentland (1984) and Ferrie et al (1989) have used different methods to reduce the number of unknowns. For example, one can assume that **L** is known or one can use constraints from differential geometry (Ferrie et al, 1989).

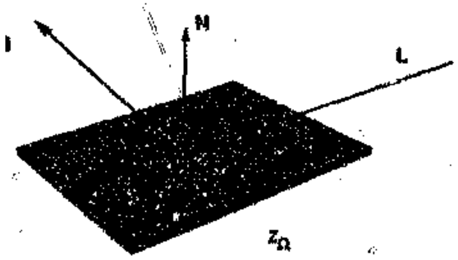

Figure 2.5. The model relating the irradiance **I** as captured in an image to the surface z of Ω and the illuminating light.

If a small homogeneous region is being examined then it is reasonable to assume that L, ρ, and λ are constant. This allows us to calculate the first and second derivatives of I with respect to (x, y) which is denoted $d = \frac{d}{d(x,y)}$ and where

$$
\begin{aligned}
d\mathbf{I} &= d(\rho \mathit{leta}\mathbf{N} \cdot \mathbf{L}) \\
\Rightarrow d\mathbf{I} &= \rho\eta(d\mathbf{N} \cdot \mathbf{L})
\end{aligned}
\qquad 2.3
$$

and

$$
\begin{aligned}
d^2\mathbf{I} &= d^2[\rho\eta(d\mathbf{N} \cdot \mathbf{L})] \\
\Rightarrow d^2\mathbf{I} &= \rho\eta(d^2\mathbf{N} \cdot \mathbf{L})
\end{aligned}
\qquad 2.4
$$

Equations [2.2], [2.3] and [2.4] demonstrate that there is a close relationship between the measured *image intensity* pattern (I) and the *surface* (z) of the scene being investigated. Not only does the image intensities depend on the surface normals [2.2], but the first [2.3] and second [2.4] derivatives of the image intensities depend on the first and second derivatives of the surface normals too. These relationships are significant because they establish some means with which the location of certain geometric features of the rocks may be determined. If the edges of the rocks are assumed to be surfaces with relatively high curvature or large changes in direction, ie gradients, then the location of relatively similar gradients in the image function should correspond to the physical location of the rocks' edges.

However many assumptions are made with regard to these models [2.2, 2.3, 2.4] of which cognizancemust be taken, for example *local sphericity*, Pentland (1984). Factors such as imperfect knowledge of the light sources, observation errors, occlusion, multiple sources, and reflections etc, as found in piled rock have also been ignored. Thus the application of the above models to real images will result in *ambiguities* and problems which are very difficult to solve in practice (Frankot and Chellappa, 1988).

Aside from shape from shading as discussed above there are the *stereo-imaging* and *structured light* techniques for 3-D surface reconstruction. Stereo-imaging techniques, Hoff and Ahuja (1989), Herman et al (1984) also have great potential for building up 3-D surfaces. However large processing times, as well as the ambiguities peculiar to these techniques does not make them suitable and affordable for this online application. According to Shrikhande and Stockman (1989), structured-light techniques provide as good or better accuracy than *shape-from-shading* and are inexpensive. However these methods generally provide only a sparse density of surface normals and have long processing times.

2.5.3 Partial surface or selective feature recovery

The objective of this research is to reconstruct Ω given I_l and I_r . Thereafter the subsequent size of the rocks will be derived from the model of the surface z_Ω of the rockstream Ω . However this reconstruction methodology is not really viable because of the large computational burden, and the fact that this type of transformation is based on models which are *approximations* and to certain extent ambiguous, as was shown in section 2.5.2.

In addition to the massive computing and other problems associated with surface reconstruction techniques, we need to ask, "is the *accurate* recovery of the 3-D surface z_Ω a *necessary* requirement to measure rock size ?" It is hypothesized that a *partial* recovery of z_Ω from which some size parameter could be extracted and which requires less computation, could be sufficient for the estimation of rocksize.

The above hypothesis is argued as follows. Shading analysis and reconstruction still only allows for the reconstruction of the *top surface* of the rockstream, which is only a sample of Ω . Thus the estimation of the rest of the size distribution of the constituents is reliant upon statistics. The *inevitability* of statistics together with recognition that true reconstruction is practically impossible and that it has its own problems, makes alternative methods such as stereology, which only requires partial information as provided by sections, a good candidate for rocksize measurement. It is hypothesized further that *selective feature extraction* is a more viable image processing objective, assuming that the features relating to size can be extracted and that the cost thereof is less than that of full image surface reconstruction.

It is thus suggested that a balanced methodology falling between the very complex (full image reconstruction) and simple (selective feature extraction) techniques, should satisfy the requirements of this measurement system, which at least is a measurement every few minutes on a powerful PC. Figure 2.6 shows the trade-off between a complex solution requiring a large amount of processing to achieve low errors versus the simple solution requiring less processing.

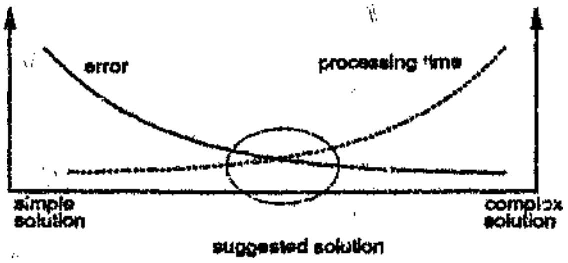

Figure 2.6. A conceptual relationship between processing time and errors versus the complexity of the methodology required for extracting a surface from an image.

2.5.4 Conclusion

A number of techniques for modelling the process of illuminating a scene with light to sensing reflected intensities in an image were discussed above. As found in the literature most of these techniques have generally been applied to scenes of simple objects, or single objects of relatively complex shape, eg a rock or face against a simple background, (Pentland, 1984). Thus the response of these techniques to scenes of complex objects is unknown. In addition it appears from the literature that most shape-from-shading techniques have been used in academic applications, where the large amount of computation required precludes these techniques from use in cost-effective realtime applications, although Terzopoulos (1986a) has developed faster algorithms.

The probability of accurate estimation of the surface geometry of all the rocks using 3-D modelling techniques is very small because of ***fundamental*** loss of information when transforming from 3-D to 2-D, and phenomena such as occlusion. As a consequence, a compromise between an accurate solution with low error requiring large processing times and expensive hardware, and a real-time system requiring less expensive hardware and producing less accurate results, must be found in order to a realize a workable instrument.

Noting that the accuracy of a system is only as good as its worst part, it must be asked whether the effort required for the accurate 3-D reconstruction of images is justified ? The principle of operation of the MSD 95, which is the simple 1-D image-processing supports the theory that no accurate reconstruction is required. However the problems with this instrument argues for the employment of more complex processing such as 2-D image processing as opposed to one dimensional processing.

It is finally concluded that a solution of *partial* surface recovery or *selective* feature extraction from rockscenes which falls between 3-D and 1-D processing is the most practical and viable method with which to recover size information from images for size estimation.

2.6 2-D VERSUS 1-D IMAGE PROCESSING

2.6.1 Introduction

Although the use of machine-vision is justified, the preference for two-dimensional image processing as opposed to one-dimensional image processing still has to be justified. In this subsection the use of the *full* 2-D image to obtain more information and knowledge for better rock identification is motivated.

As mentioned in chapter 1, a commercially-available rocksize instrument, the MSD-95, uses one-dimensional image processing to gauge rocksize. The measurement technique used by the MSD-95 relies on the assumption that the reflected light intensity represents the presence or height of the rocks above the belt as given by equation [2.5]. *Bright* areas are rocks X, and *dark* areas the voids Y in between the rocks, .

$$z_\Omega \propto I \qquad 2.5$$

However as is given in equation [2.1] and [2.2], the relationship linking the image and rockstream surface is more complex than that shown in [2.5].

2.6.2 Thresholding of Profiles

As part of the motivation for the utilization of 2-D images, this subsection examines 1-D profiles in order to reveal the limitations and ambiguities arising from operations such as thresholding. The profiles $g(x)$ are extracted from images taken off the top of Ω where by *observation* the rocks can be identified with almost a hundred percent certainty. Subjecting the profiles to a *thresholding* operation effectively emulates the operation of the MSD-95.

Thresholding *classifies* $g(x)$ into two classes by means of threshold value $t = a$ which gives rocks $X_1 = X_t(g)$ and the non-rocks $X^c = X_t^c(g)$ where

$$X_t(g) = \{x \in \mathrm{D} : g(x) \geq t\} \qquad -\infty < t < +\infty \qquad 2.6$$

$$X_t^c(g) = \{x \in \mathrm{D} : g(x) < t\} \qquad -\infty < t < +\infty \qquad 2.7$$

as shown in figure 2.7. A linear-intercept (chord-length) distribution $p(L)$ is then calculated by estimating the length L of the i'th rock $[X_t(g)]_i$ where $L_i = L[X_t(g)]_i$ and $[X_t(g)]_i \subset X_t(g)$. See figure 2.7.

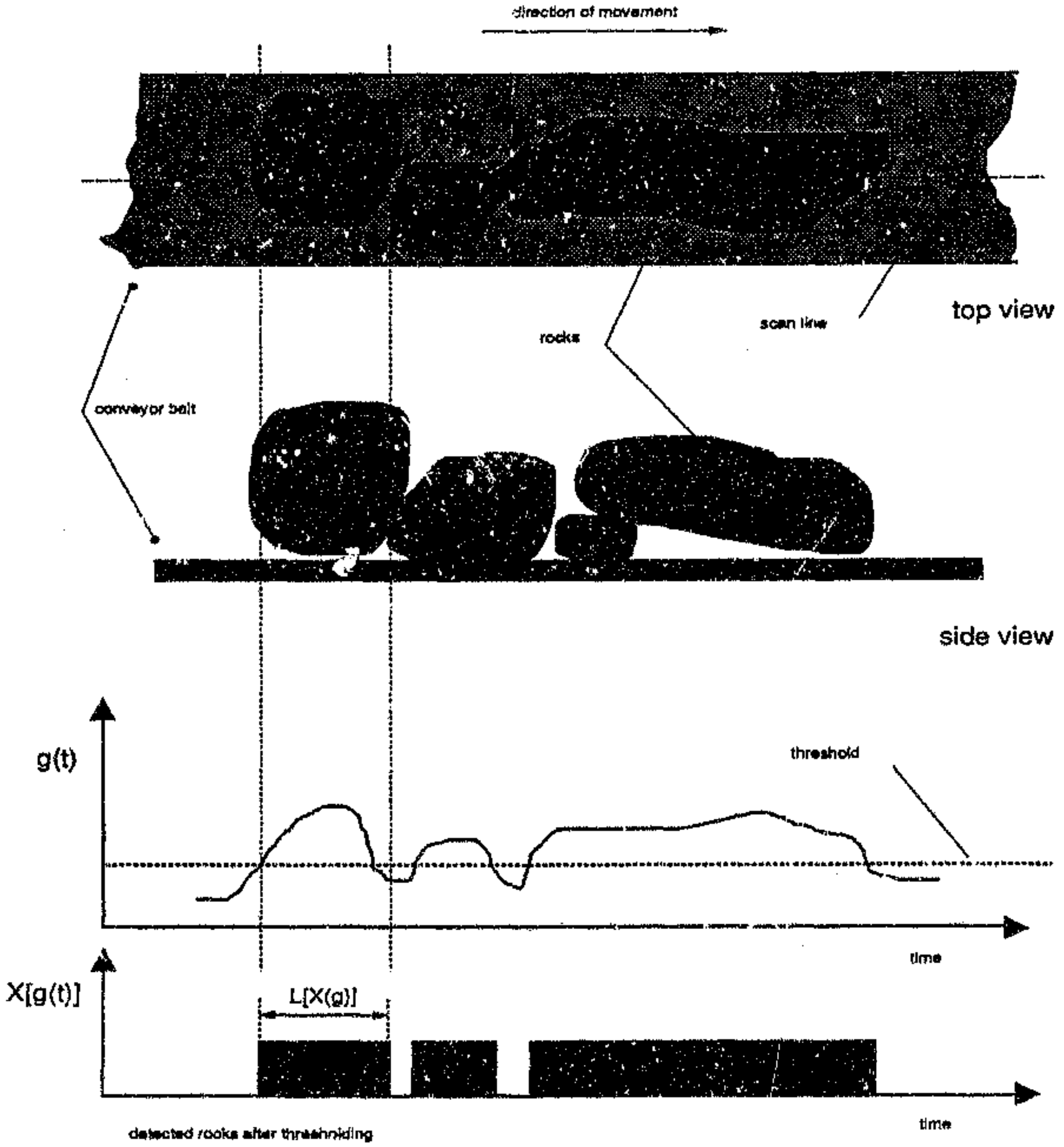

Figure 2.7. Calculating chord-length distributions from 1-D profiles.

2.6.3 Separate and Piled Rock Piles

Although the objective in this subsection is to justify the use of 2-D images because of certain inadequacies with 1-D images, thresholding of 1-D profiles should not be rejected totally out of hand. There are instances when profiles provide sufficient information for valid and accurate rock-identification. This only occurs when the rocks X are *not piled* together and the spatial density N_V is low, ensuring that the rocks don't touch each other. A homogeneous background of sufficiently different contrast to the rocks also improves the validity of this operation making the rock identification process trivial as shown in figure 2.8(a) and 2.9(a). Both the 2-D image and 1-D profiles can be used for unambiguous rock identification.

However when rocks are piled up or at least touching as found on the rockstream, probability of false-rock identification is increased as shown in figure 2.8(b) and 2.9(b). It can be seen in figure 2.9(b) that the unambiguous inference of the presence of an individual rock is more difficult with profiles than with 2-D images.

The main causes of errors resulting from the use of 1-D profiles from piled rockscenes are that

(1) The sensed irradiance from the rock scene ie image $I(x, y)$ is not always directly proportional to the height of the rocks above the belt $z_0(x, y)$. In many cases with non-touching objects the assumption that $I(x, y) = z_0(x, y)$ is valid and transformation and $X_t(g) = X$ is fairly accurate. However this assumption is rendered false when rocks are (a) piled together causing their height above the belt to vary randomly, and (b) their surface texture is rough, not always concave with geometric protrusions and indentations. For example, a shadow occurring on a rock's surface that is physically high above the reference surface, is usually sensed as being below a selected threshold and is hence classified as non-rock Y splitting a single rock into two as shown in figure 2.10(b) and (c).

(2) The chord-length measurement $L[X_t(g)]$ is very dependant on the selected threshold t (see figure 2.13), but because the level of irradiance varies across and along the length of the belt, ie is a function of x and y, biases are introduced when thresholding.

(3) A single 1-D profile taken from the centre of the belt only samples a small portion of the rockstream Ω and the rocks on either size of the rockstream centre are ignored. Because the distribution of rock across the belt is generally not homogeneous, the measurement will have an inherent bias. In order to reduce this bias more chord lines should be sampled. See figure 2.11.

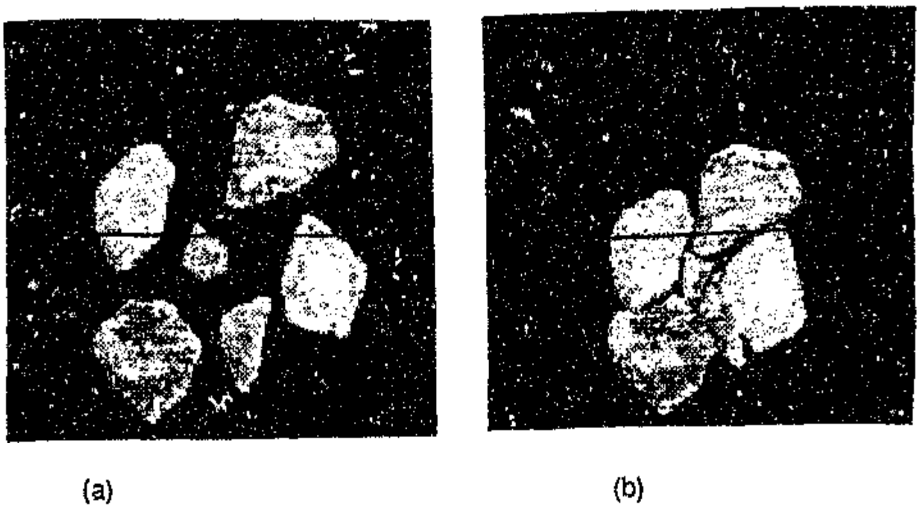

Figure 2.8. Image of (a) separated and (b) touching rocks. The touching rocks in figure 2.8(b) are the same rocks as in figure 2.8(a) except they were pushed together.

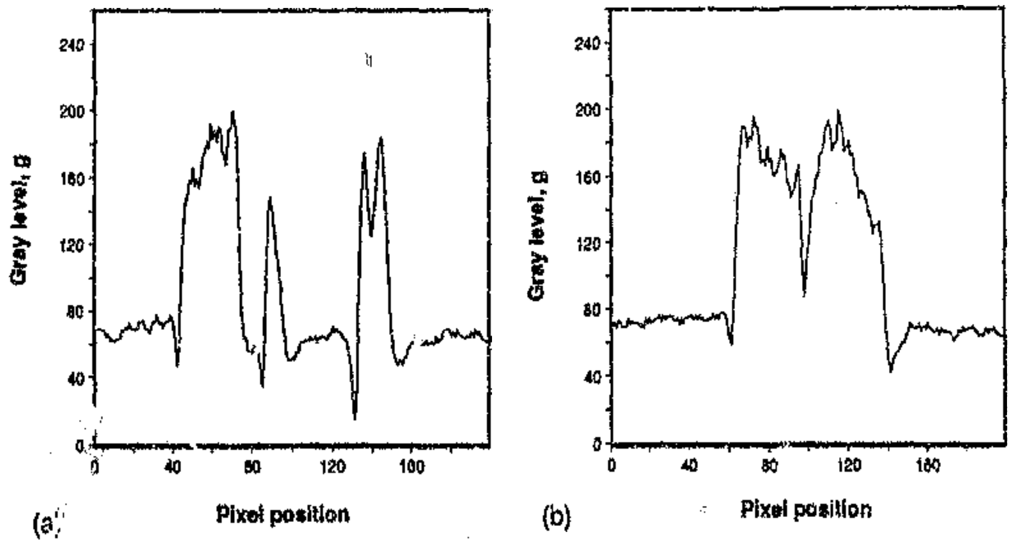

Figure 2.9. Profiles taken from row 100 in figures 2.8(a) 2.8(b).

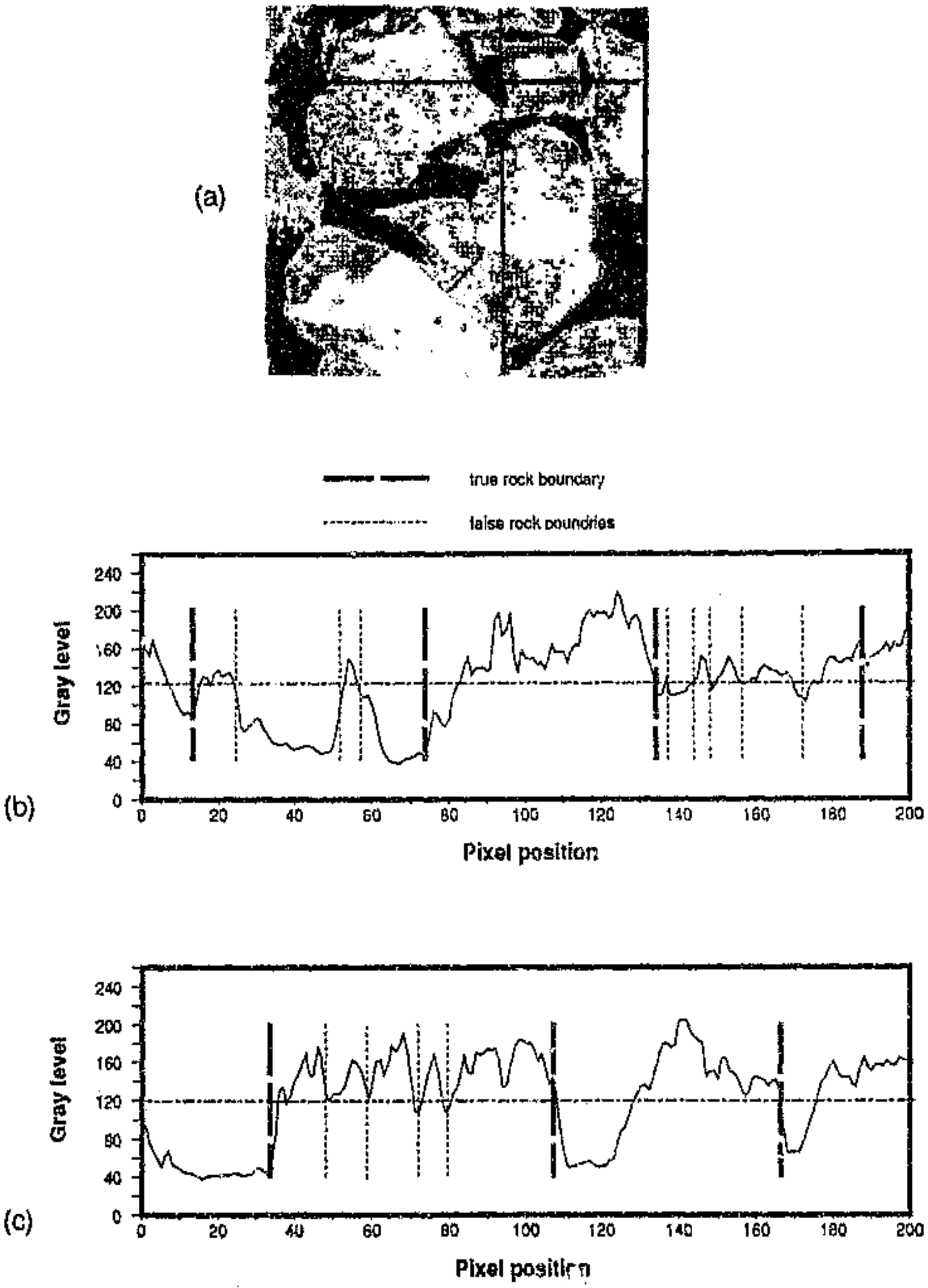

Figure 2.10. Examples of how ridges and other features on the surface of a rock may cause a rock to be split (segmented) into fragments when thresholding. Original image is shown in figure (a). Figure (b) shows a vertical profile *column 121*, and figure (c) shows the horizontal profile row 40. Both profiles have been threshold at $t = 120$, and possible points for erroneous splitting are shown as thin dotted lines, while the true points for splitting are shown as heavy dashed lines.

2.6.4 Advantages of 2-D Images

Two dimensional images provide two distinct advantages over the use of 1-D profiles.

I Two dimensional images provide greater *access* to the material on the conveyor belt, thus removing some of the bias caused by sampling a small portion of the surface area of the belt as the MSD-95 does. (Point 3 in subsection 2.6.3).

II. Two dimensional images provide for less ambiguous identification of rocks. This stems simply from the fact that higher order dimensional data provides more *information* and *insight.*

I *MORE SAMPLING - LESS BIAS*

A 2-D image allows for the conveyor belt to be sampled over its full width through the use of a number of parallel or orthogonal probe lines. See figure 2.11. This multiple sampling includes more rocks into the estimation process, as well as increasing the number of chords processed, both factors which will reduce the bias and variances in the measurements (chord lengths) to be made.

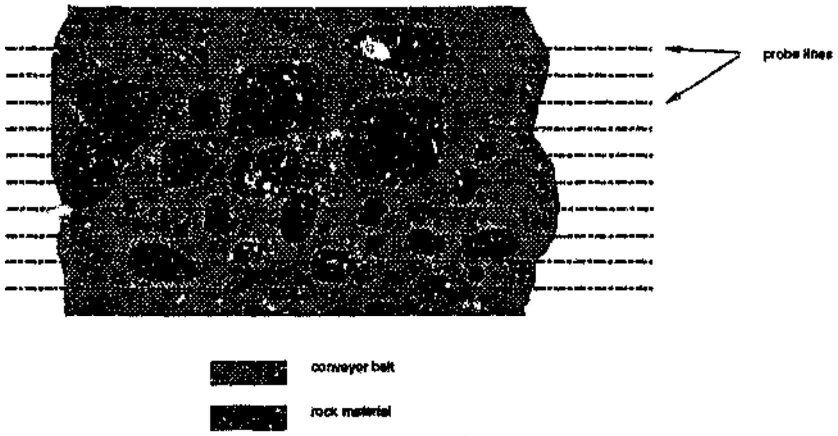

Figure 2.11. Multiple probe lines sampling of all material on the conveyor belt.

II *MORE INFORMATION - LESS AMBIGUITY*

Two-dimensional images provide more information to resolve the ambiguities associated with rock identification. As a first step towards demonstrating the usefulness of 2-D images, it will be shown that probe lines adjacent to the main probe line, extends the knowledge available by forming a pseudo 2-D image, where *a-priori* the observer can corroborate the existence and edges of a rock. The need to use *a-priori* knowledge is unavoidable, for example it is known that rocks cannot have isthmuses, holes or be perfectly square, thus features implying such structures can be filtered out.

Consider a single probe which returns a profile $g_{98}(x)$ taken from the 98'th horizontal row in the image 2.12(a)[2.1] as shown in figure 2.12(b). The locations of the perceived "true[2.2]" rock edges in $X_t(g_{98})$ are shown at the bottom of figure 2.12(b). Note that it not the absolute position of the these edges to the x-axis that is important for size measurement, but rather the *relative* distances between the edges of $X_t(g_{98})$ because it is assumed that the length measurement function $L()$ is linear, ie $L(\gamma X) = \gamma L(X)$ so that for a size distribution $p(\gamma L) = \gamma p(L)$ where γ is a scalar.

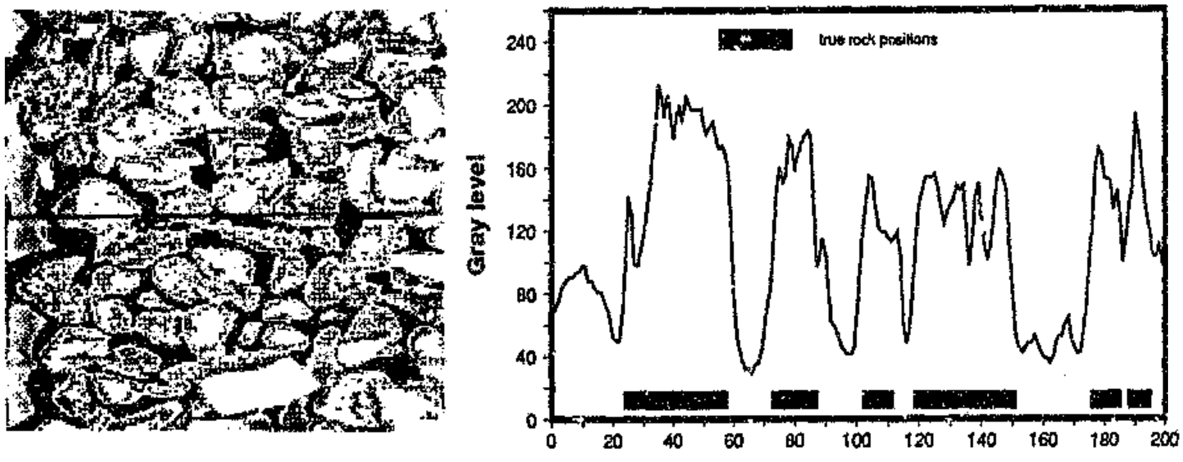

(a) (b)

Figure 2.12. Example of a profile extracted from an image for the purpose of 1-D rock identification. (a) Sample image and (b) gray level profile $g_{98}(x)$ taken from image and perceived rock edges.

The threshold rock profile $X_t(g)$ is strongly dependant on the threshold t and this is demonstrated by comparing the two profiles $X_{t=60}(g_{98})$ and $X_{t=140}(g_{98})$ shown in figure 2.13(b) and (c), which do not correlate very well with profile $X_t(g_{98})$ shown in fig. 2.13(a).

[2.1] This image was taken off a pilot plant conveyor belt system moving at $0.5 ms^{-1}$. Ω consists of quartzite in the size range 13-19mm. The image presented is a sub-image [200x200] pixels of an original [512x512] image.

[2.2] The "true" rock position is identified by human visual inspection and analysis to which there is no equal as far as AI is concerned. These rock boundaries are located because of a priori knowledge of the expected shape of the rocks and prior examination and learning of the rocks in the full 2-D image.

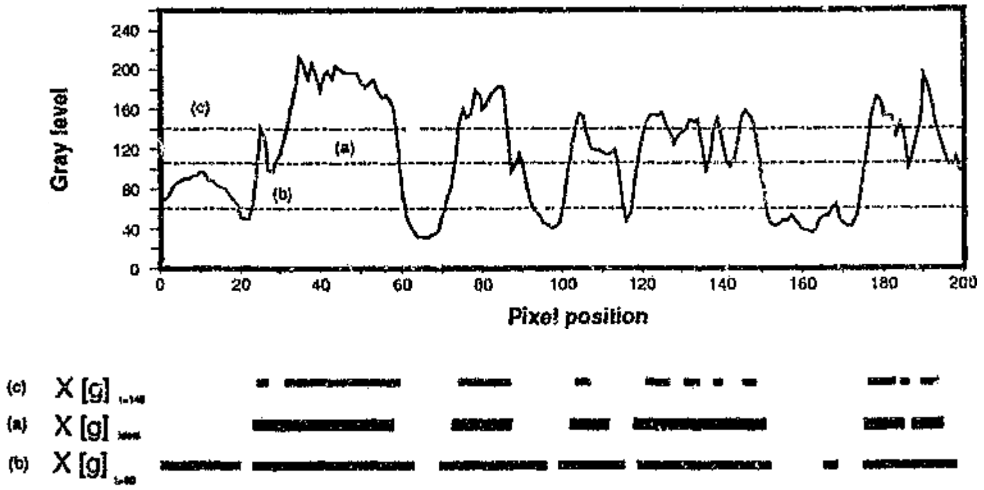

Figure 2.13. (a) The ideal threshold $X_t(g)$ (b) $X_{t=60}(g_{98})$ (c) $X_{t=140}(g_{98})$.

This dependence on t is illustrated further in figures 2.14(a)-(f) which show binary images extracted from image 2.12(a) by the 2-D threshold operator which is simple extension of equation [2.6 and 2.7] and is given in equation [2.8] where it is assumed that white=X, black=X^c.

$$[X_2]_t(I) = \{(x,y) \in \mathbf{D}\times\mathbf{D} : I(x,y) \ge t\} \quad \left\{ \begin{matrix} \infty < t < \infty \\ I(x,y) \in \mathbf{V} \end{matrix} \right\} \qquad 2.8$$

An important difference arises when analyzing the 2-D and 1-D images and profiles respectively. This is that erroneous features can be identified and described with *less ambiguity* in 2-D images than from 1-D profiles. This can be seen in figure 2.14 where the rocks are almost unambiguously identified even with the segmentation errors. This reinforces the conclusion that given piles of rocks, the topology is almost impossible to estimate accurately or with confidence from a *single 1-D profile* and that the 2-D image will be more useful as shown in figure 2.14(a). The importance of *a-priori* knowledge is demonstrated clearly in figure 2.14 where the threshold images (c)-(h) could be identified as being rocks or for example a close up view of sponge pores, in which cases the joining between the features in the image is justified.

There are two main type of rock identification errors that arise from thresholding. These are (1) the connecting *bridges* between rocks, which *merge* perceived areas of one rock with another, and (2) the *cavities* or holes in the interior of the rocks. See the threshold images in figure 2.14 and the errors in figure 2.15.

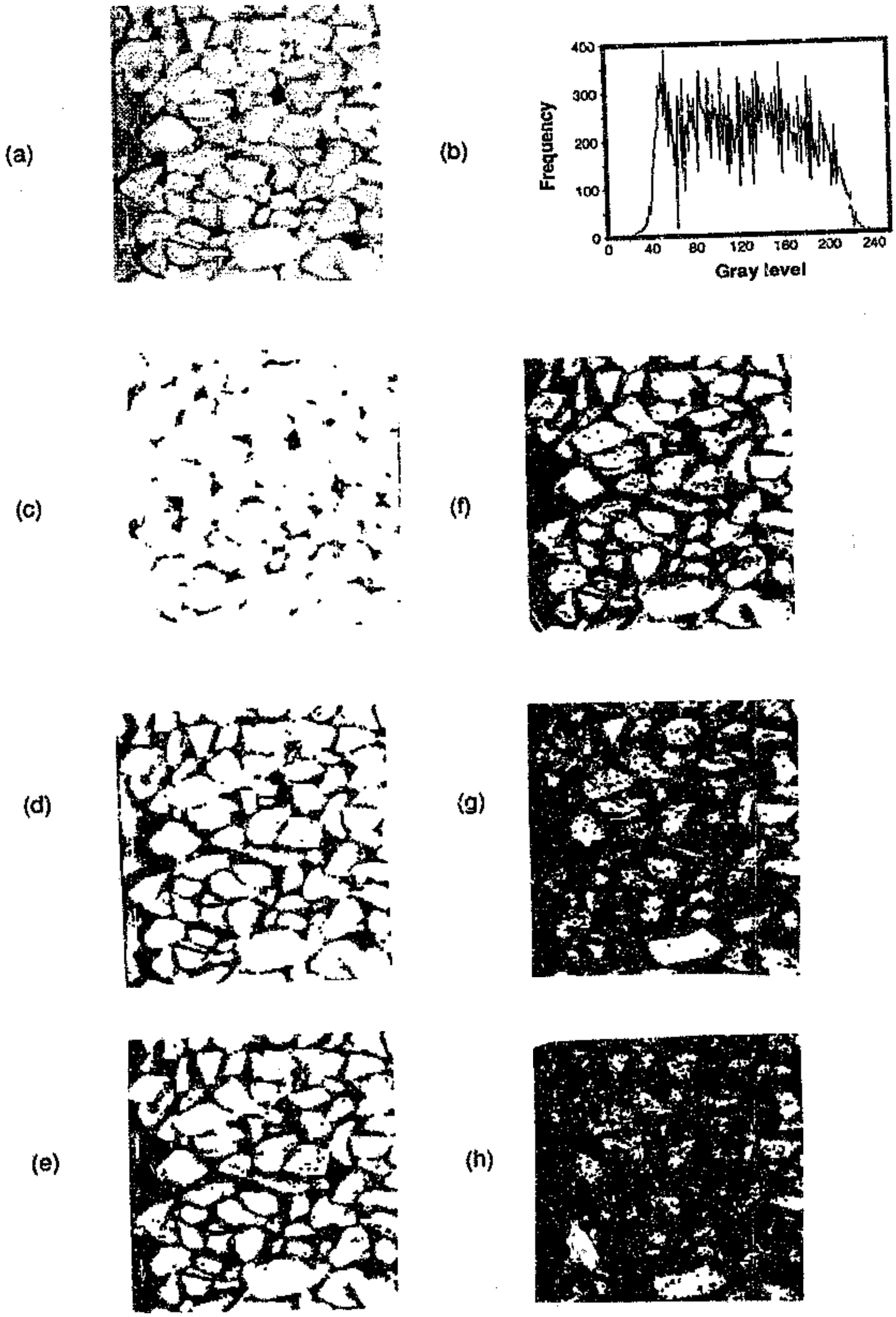

Figure 2.14. Results of thresholding figure (a) at different values of *t*. Figure (b) is the histogram of (a). The gray level thresholds selected are, (c) *t*=50, (d) *t*=90, (e) *t*= 110, (f) *t*= 130, (g) *t*=170 (h) *t*=190.

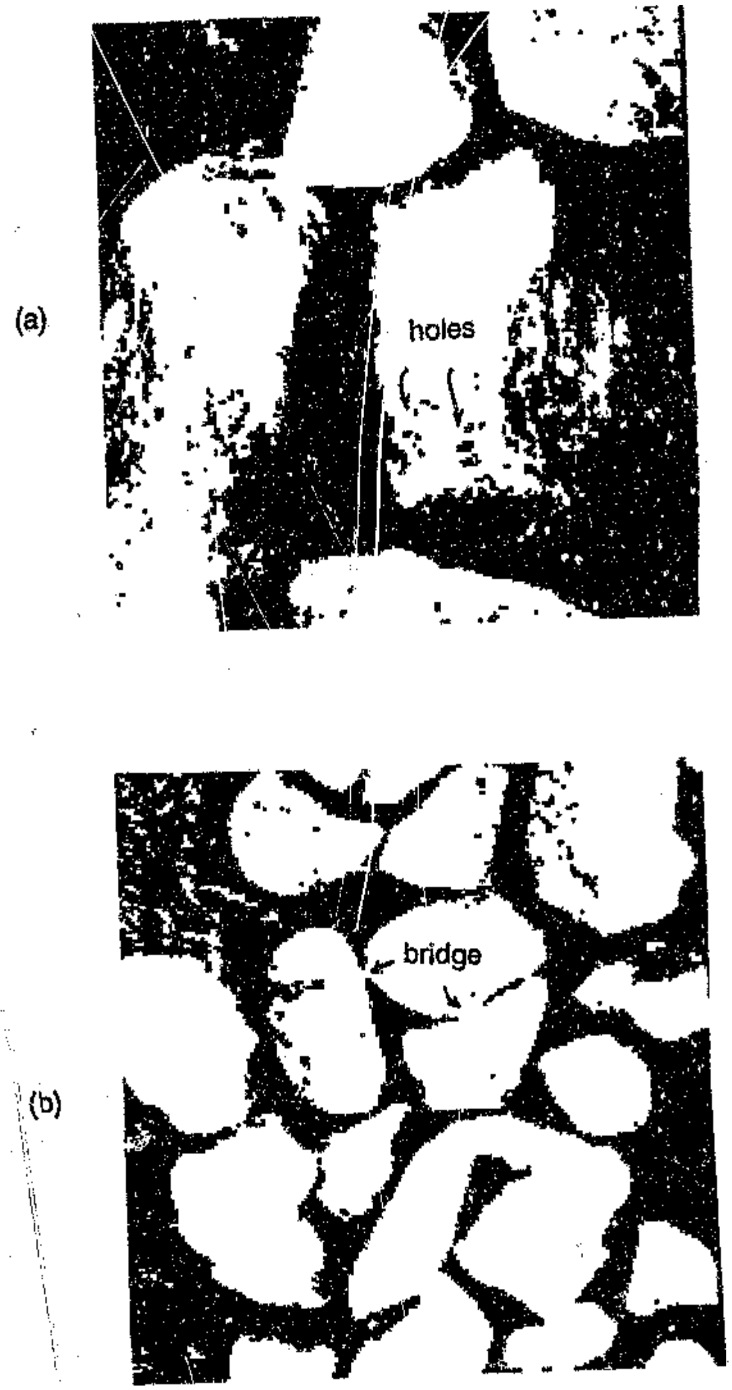

Figure 2.15. Errors that occur with thresholding; bridges and holes.

It is known a-priori and heuristically that the narrow connecting bridges between rocks as well as holes cannot physically occur. Yet these bridging and hole errors are difficult to resolve given only a one dimensional profile. With 1-D profiles, it is difficult to differentiate between *erroneous bridges* and the *true continuum* of a real rock, and *holes* and *genuine gaps* are often identical.

It is suggested that these identification ambiguities are the major cause of errors in the measurement of chord-lengths, especially when simple thresholding is used. If however the size range and shape of the rocks are *known* a-priori, then the appropriate 1-D filtering may be applied in order to derive the particles of known size. (But if the rocks size is known, then why make the measurement ?)

However inspection of *adjacent* profiles can reduce errors and ambiguities when identifying and predicting the shape of a rock. For example, inspection of adjacent profiles $g_{95}(x)$ and $g_{101}(x)$ in fig 2.16 reduces the uncertainty associated with the classification of $g_{98}(x)$ into rock X and non-rock Y especially with regard to the oscillations of g_{98} in the vicinity of points A in figure 2.16. A possible measure of how well adjacent profiles fit together could be done by cross-correlating the profiles locally or piecewise to confirm or reject a local classification. This is essentially a pattern recognition and matching process where it is assumed *(a-priori)* that *the shapes of the near adjacent profiles cannot change too much from the profile under inspection*. Ideally we would thus like to inspect all profiles, and in the limit the set of all adjacent profiles becomes the continuous 2-D image, equation [2.8], which provides much more *knowledge* for a better *understanding* of the contents of the signals.

$$I(x,y) = \{g_y(x) \in V : (x.y) \in \mathbb{D}_2\} \qquad 2.8$$

With 2-D signals the correlation between neighbouring parts of profiles around a point in the image is extended to the consideration of sub-areas of the images extending radially outwards from the point of interest. Thus a noise impulse which in the 1-D cross section looks like a valid boundary between two rocks is easy to identify if the surrounding area is identified as part of the continuous surface of a rock, see figure 2.17. This 2-D knowledge can be utilized in more complex manner by allowing for AI rules based on heuristic or a-priori knowledge to be formulated for improved rock identification and hence rocksize measurement (Berger, 1985).

Despite the advantages of 2-D processing, there will always be uncertainties with object or rock identification because the third dimension is still lacking.

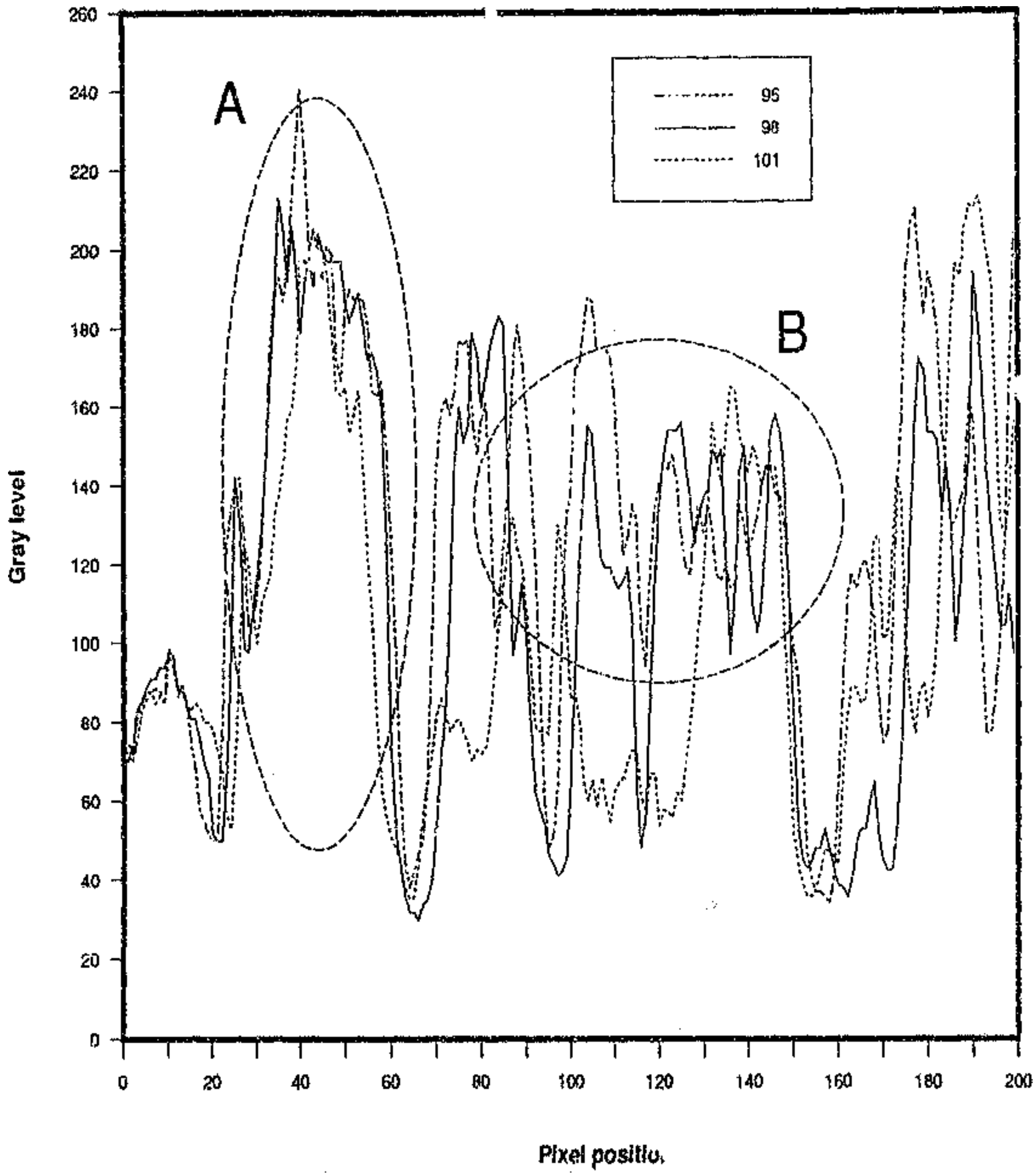

Figure 2.16. Profiles $g_{95}(x)$, $g_{98}(x)$, $g_{101}(x)$ showing how they extend the knowledge about an area in the image. In area *A* there is conformation that a rock is present. In area *B* profiles $g_{95}(x)$, and $g_{98}(x)$, confirm that there could be a rock but profile $g_{101}(x)$ indicates that this part of the image could be the edge of rock or that there is noise in this part of the image.

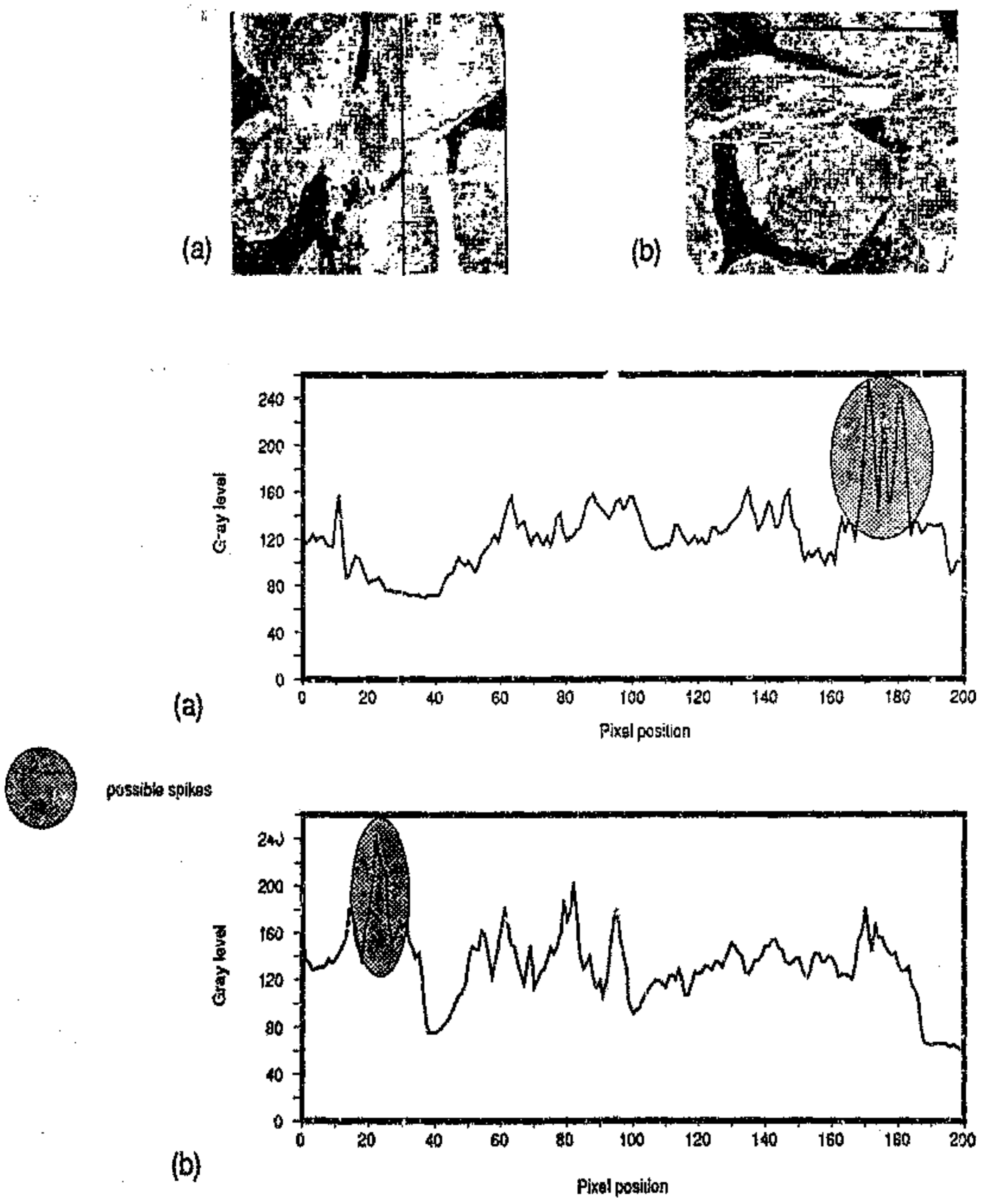

Figure 2.17. Original images (a) and (b) and corresponding profiles. Profile (a) is column 121 from image (a), and profile (b) is row 20 from image (b).

2.6.5 Acute angled lighting to improve rock identification

In order to reduce the ambiguity of rock identification designers of the MSD-95 use *acute-angled* lighting to enhance the *shadows* between the rocks. This shadow enhancement technique effectively forces the gray level of the areas of image-function associated with the spaces between rocks to be lower, thus increasing the probability that such voids will be classified as non-rock when thresholding. Figure 2.18 shows the setup for implementing this shadow strategy.

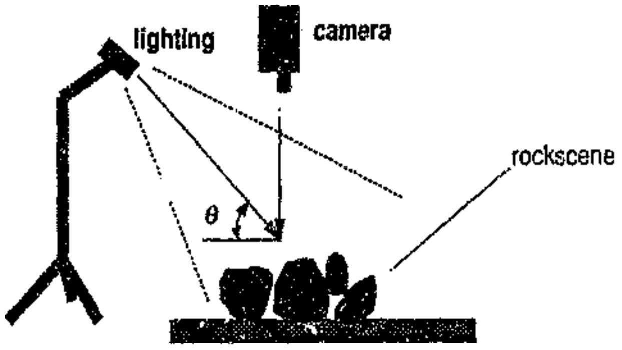

Figure 2.18. Setup for low angled lighting for rock edge enhancement.

However as mentioned previously, the surface of the rocks as found on conveyor belts are in general not convex and are highly angular with ridges and hillocks. Thus low-angled light will amplify the shadows caused by these surface features in addition to the gaps between rocks, subsequently increasing the incidence of *false edges* which counteracts the advantages of using acute angled lighting for emphasizing the rocks' boundaries.

Thus there are optimum or critical angles of illumination to be chosen. Figure 2.19 shows scene and corresponding profile changes as a function the angle of the light intensity $\theta°$. (The angle is measured from the horizontal.) Note that the apparent shape and size of the rocks change with $\theta°$ where the rocks become smaller and the valleys become larger. This causes biasing in the measurements which is evident in figure 2.20 which shows the average chord length measured as a function of $\theta°$. Figure 2.21 shows how the gray-level histogram changes with θ as well. In the gray-level histogram the pixels are shifted away from the bright to dark which corresponds to shifting parts of an object to background hence decreasing the size of the rocks. This dependence of rock shape and size is demonstrated further in figure 2.22 which shows the cross correlation coefficient R_{xy} between a sample profile $g^{76°}(x)$ illuminated with light at 76° and the *same* profile illuminated with lower angled light, ie $\theta < 76°$.

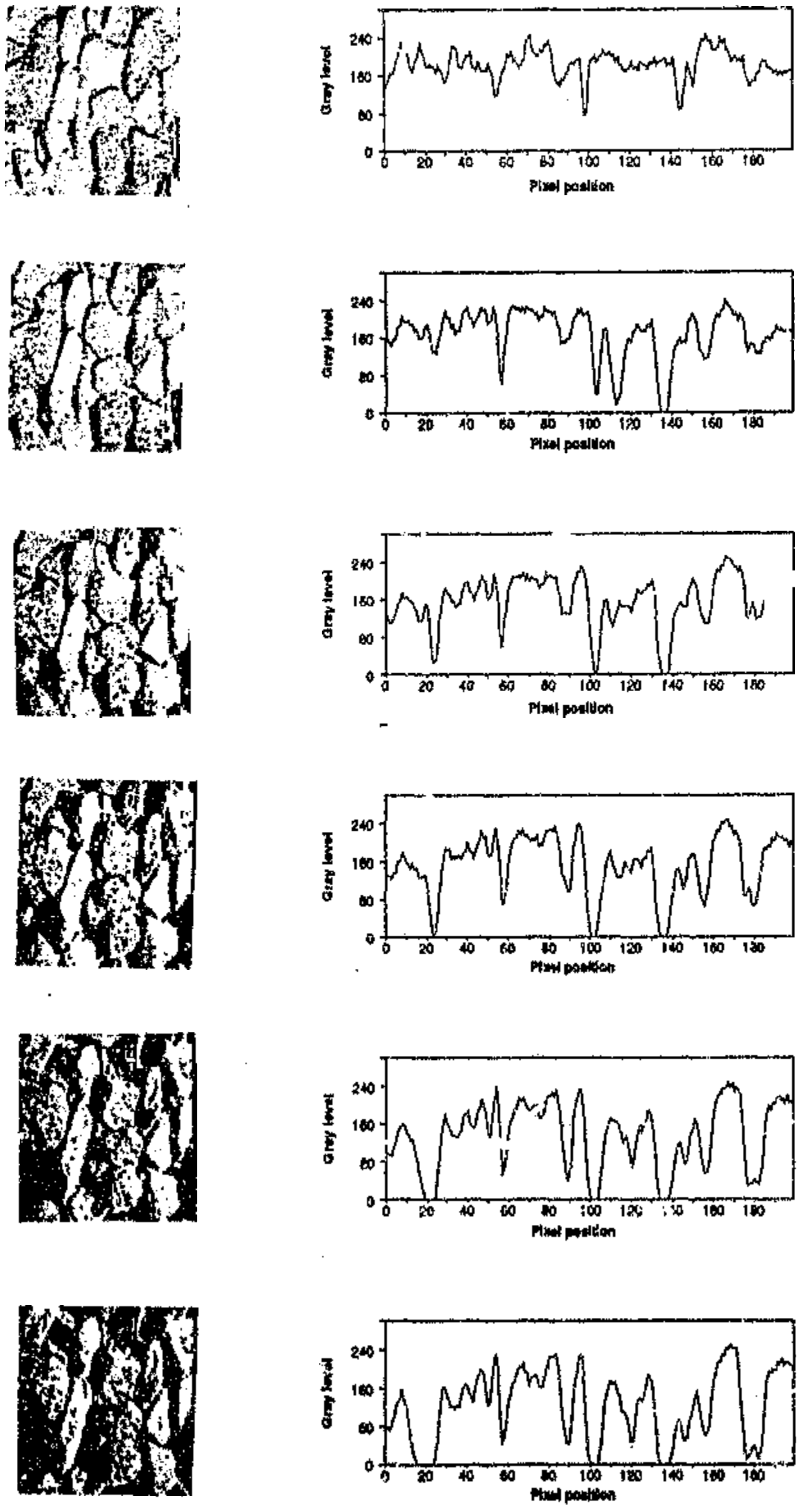

Figure 2.19. Images and corresponding profiles $g^{\theta^\circ}(x)$ taken from row 100 for various angles of lighting θ°. For the above images $\theta = 78^\circ, 66^\circ, 55^\circ, 47^\circ, 36^\circ, 30^\circ$ going from top to bottom repsectively.

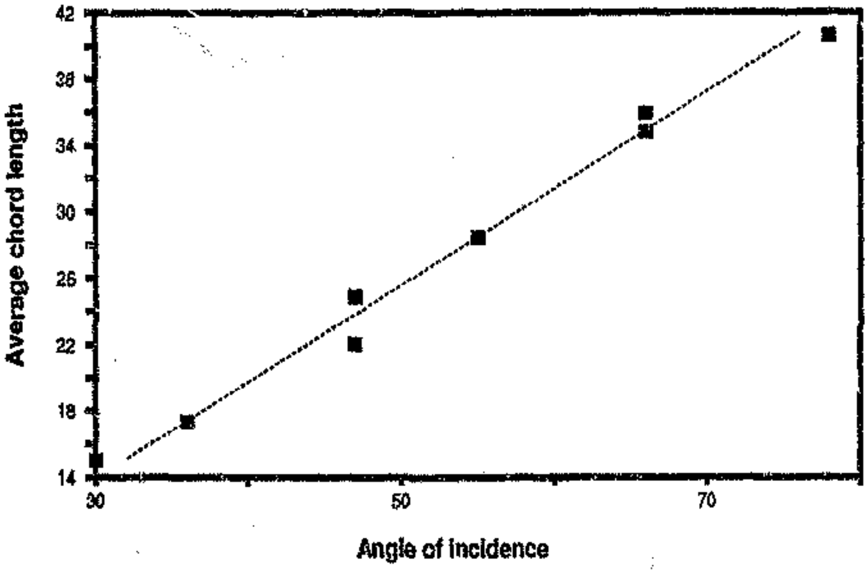

Figure 2.20. Plot of average chord length measured from all possible probe lines in the horizontal direction versus different angles of incidence θ°.

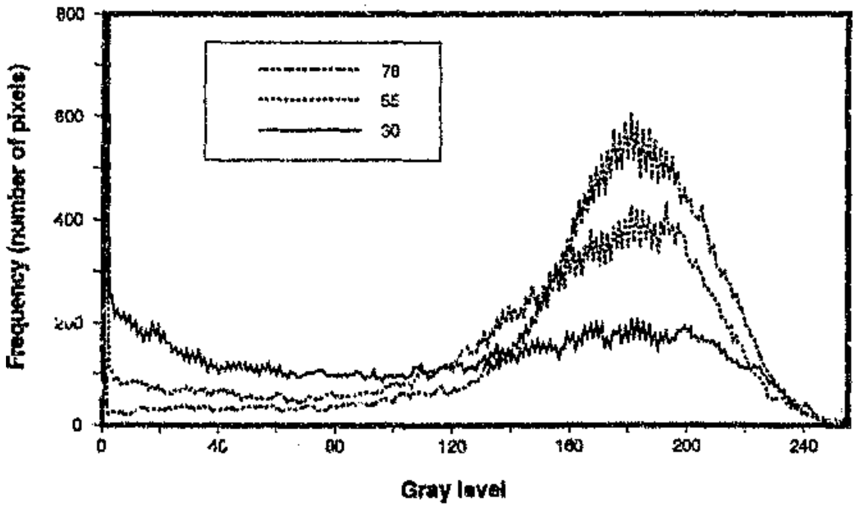

Figure 2.21. Gray level histograms of an image illuminated with light at three angles of incidence. Each histogram curve has been smoothed with a 3-point moving average filter.

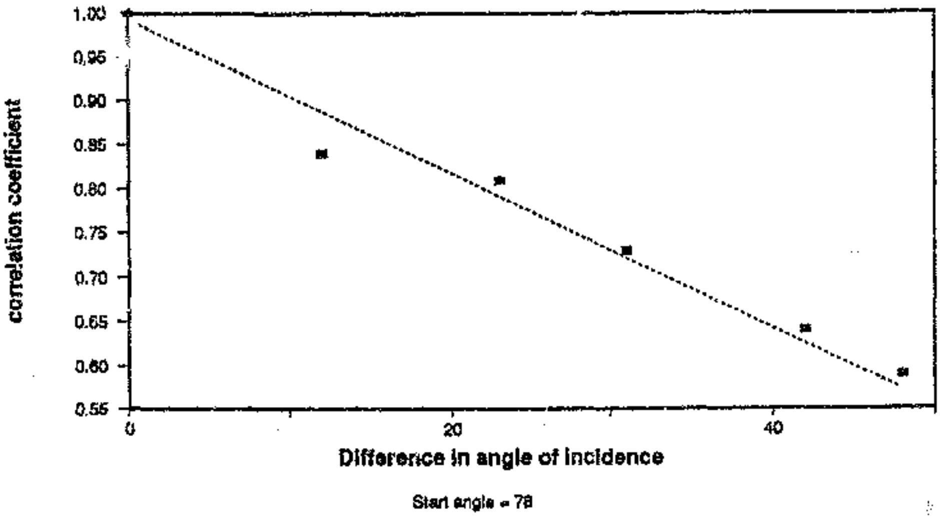

Figure 2.22. Graph showing the "deterioration" of the correlation coefficient R_{xy} between the profile at 76° and the same profile taken at lower angles of incidence.

2.6.6 Conclusion

Although the image and its profiles are in general not contour maps of the rocks in the image, they are closely related. The above observations don't *prove* but reinforce the intuition that 2-D images do provide more knowledge with which to reduce the ambiguities associated with rock identification. Obviously if 2-D image processing is to be introduced for rock identification, it must be *efficient* and obtain the appropriate results with reasonable accuracy in order to justify its application over the simpler and less costly 1-D processing.

It is also concluded that angled light is useful in *separating* touching rocks in rock-piles because the true rock edges are accentuated. As a result slightly angled light was used during this research to enhance edges. However the increase in errors caused by the amplification of "false edges" on the rocks surfaces offsets the advantages of clearer edge detection. Obviously rocks or objects with *smooth* surfaces will benefit from this scheme.

2.7 SAMPLING THE ROCKS - A STOCHASTIC PROCESS

2.7.1 Introduction

In section 2.5 it was established that accurate recovery of the surface geometry of the rockscene is difficult and will not be pursued. In addition it was shown in section 2.6 that there are many ambiguities associated with the identification of the rocks even with 2-D processing. Because of the erratic nature of the flow of the rockstream Ω any quantitative measurement made on the images features will vary not only from image to image, but within an image as well. Therefore any measurement on Ω must be statistical, and will be a function of random spatial as well as temporal parameters. This implies that the rocksize measurement will consist of *estimates* or expected values with related biases and variances because as is shown in section 2.7.2 the rockstream is effectively a *stochastic* process.

Physically the measurement process will consist of taking a snapshot of portion of the rockstream at a particular time, analyzing the image and measuring size data which will be statistical and have errors associated with it. This measurement process is to be repeated continuously to produce an online measurement every time interval ΔT where $t = \Delta Ti$ and i is the i'th time interval to give $f_{\Omega}^{*}(D, \Delta Ti)$ where f^{*} is an estimate of f. Consequently the rockstream must be sampled appropriately to reduce common problems associated with sampling these being, bias, large variability, or low confidence in the output data, (Larson, 1982).

There are three main groups of sampling restrictions or limitations that affect the measurement of parameters from rockstream images. These are, (i) observation restrictions, (ii) hardware or digitization restrictions, and (iii) frequency response limitations, discussed in subsections 2.73, 2.7.4, and 2.7.5.

2.7.2 Developing a statistical model of Ω

A rock of size D passing a point on the belt at time t is a ***random*** event with some measure ξ which has a *probability Pr* associated with it. The set of all rocks over all time of all sizes D $0 < D \leq D_{max}$ is the set Ξ of all possible events which is *certain* and has a probability of occurring of 1. All subsets of Ξ are events too, and have probabilities of $Pr < 1$ associated with them. In reality, only a number of rocks pass a point on the belt at time t to give a set of events $\{..\xi_i..\} \subset \Xi$ which has an associated rock ***size distribution*** $f_{\Omega}(D)$ for that particular moment. Thus as the rocks pass by a point the rocksize distribution $f_{\Omega}(D)$ will vary randomly with time because the elementary events of rocks of certain sizes being sampled, varies randomly. Thus the rockstream can be modelled as a stochastic process (Papoulis, 1965) $f_\Omega(D,t)$ with the random variable of interest being the rocksize distribution which varies "randomly" with time and where D is some equivalent-size or characteristic-diameter.

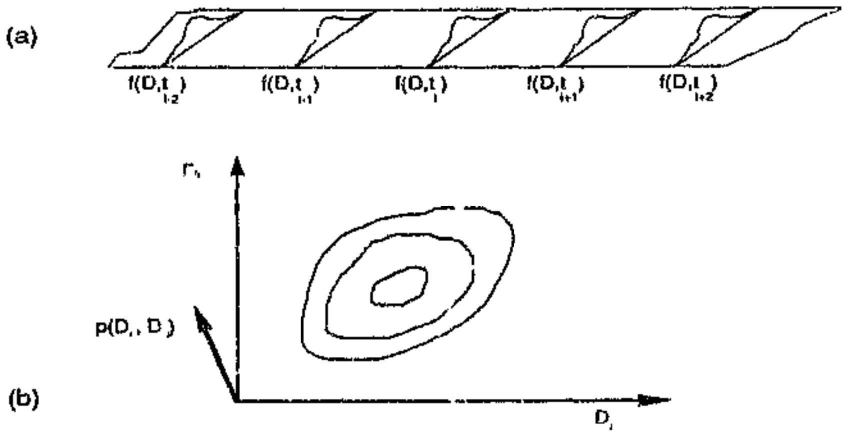

Figure 2.23. (a) Measuring chord-length distributions $f_\Omega(D,t_i)$ at intervals from the rockstream which is a stochastic process. (b) Showing a hypothetical joint probability distribution p_D for a size histogram of two classes, D_1 and D_2.

The stochastic process is shown schematically in figure 2.23(a) where a sample of the size-density distribution $f_\Omega(D,t_i)$ is measured every ΔT intervals. Note that the size-density distribution $f_\Omega(D,t_i)$ is a continuous function and is itself not a probability density distribution. However each and every single point $f(D_i)$ on the distribution $f_\Omega(D,t)$ is related every other point and a ***joint probability-density distribution function*** $p_D(\ldots D_{i-1},D_i,D_{i+1}\ldots)$ exists where $1 \le i \le n$ and n is the number of points in a rocksize histogram $f_\Omega(D_i,t)$.

For a continuous rocksize distribution $f_\Omega(D,t)$ the number of points is infinite and the joint probability distribution p_D is of infinite dimensions. Figure 2.23(b) shows the joint probability distribution for a two point histogram where the axis of $p_D\{(p(D_1),p(D_2)\}$ comes out of the page. The function $p_D\{(p(D_1),p(D_2)\}$ is a 2-D surface. If either D_1 and D_2 are kept constant then either probability density distributions $p(D_1)$ or $p(D_2)$ associated with a two class size histogram may be derived.

It can thus be seen that in order to characterize the size distribution of the rocks on the conveyor belt fully, it is necessary to determine the statistics and/or probability distributions for an ***infinite or large*** number of points associated with $f_\Omega(D,t)$, which is impossible because the tools of mathematics are incapable of handling such a problem, (Barker, 1990). The point to be made here is that the rocksize *measurement* process of a rockstream is inherently limited, and at best the statistics or probability density distributions of only a finite number of points associated with $f_{\Omega}(D, t)$ can be determined. It must also be noted that statistics associated with the size distribution such as *average-rock size* $\bar{f}(D)$, or the *variance* $\sigma(D)$ in rock size, are also dependent on the joint probability density distribution p_D.

Note that all these probability density functions eg $p_D(D)$ and associated statistics, are *not* necessarily *stationary* which complicates the measurement process even further.

2.7.3 Observation restrictions

This restriction occurs because only portion of the rockstream Ω can be observed. In particular only the *surface* of the *top layer* of rocks facing the observer is sensed due to the opacity of the rocks, and portions of an observed rock are likely to be hidden from view due to occlusion, figure 2.24. This restrictions limits the extent with which the instrument is able to probe the interfaces between the rocks X. This limitation is undesirable because the ideal solution to the measurement problem is based upon the assertion that *total knowledge of the relative spatial relationships of the surfaces of each and every rock, will allow for the unambiguous identification and estimation the size of each particle, and hence the full size distribution.*

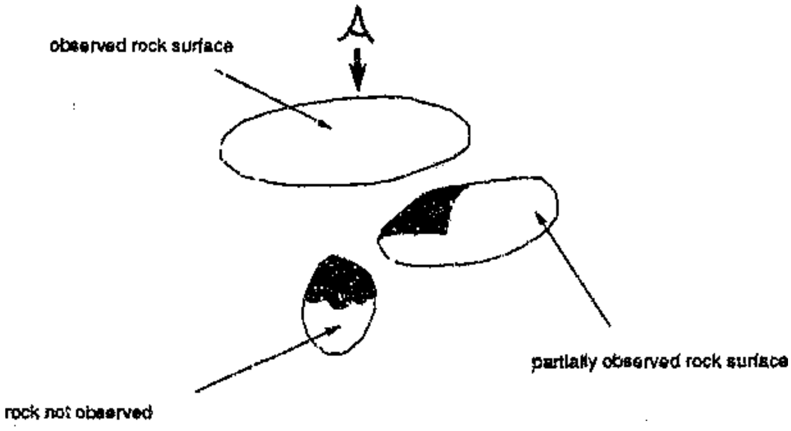

Figure 2.24. Limitations of machine vision

This observational-sampling problem poses a fundamental question, of whether the restricted view or subset of the rockstream $\Omega_R \subset \Omega$, can provide valid information for *estimating* the size distribution of the rockstream Ω. It is hypothesized that Ω_R will allow for the estimation of certain properties of the size distribution of Ω, $f_{\Omega}(D)$ through the use of stereological methods, but within limits (chapter 3). This assertion is unique only in the context of these rocks on a conveyor belt. This is because stereological methods have already been applied to a multitude of geological, metallurgical and biological problems where the size distributions of the particulates of a larger body have been estimated from their sections or their projections, see Weibel (1979),(1980). In stereology numerous mathematical models have been developed to cope with each particular application. However the rocksize problem is unique and different in a number of ways, which makes modelling the rockstream for the application of stereological techniques difficult. In particular

i) No sectioning can be performed on the rockstream.

ii) Only the top layer of the sample can be seen which is inherently a nonhomogeneous and non-isotropic particulate system. (The assumption of the homogeneous dispersion the particles in a structure has been justified in many other sizing problems.)

iii) The number of samples to be dealt with in an image is very low compared to microscopic and other sizing applications using stereological methods.

iv) The spatial density N_V of the rocks is very high which results in occlusion.

A possible solution to avoiding this restricted view problem is to ensure that $\Omega_R \rightarrow \Omega$. This could be done by mechanically rearranging the rock feed on the belt into a sparsely distributed mono-layer, with low N_V. This would allow each individual rock to be unambiguously represented in the final image with no overlap and occlusion. Hence accurate statistical or equivalent diameters may be measured, for example projected area, perimeter or ferret diameter, See appendix A. However this solution is not feasible because the redesign and retrofitting of the required mechanical hardware is not financially justifiable. Speeding up the conveyor belt can spread the rocks out into a sparser distribution, however the possibility of mechanical breakdown is increased dramatically, and the loading from hoppers etc must be smooth and continuous which is almost impossible to achieve. Reduced mass-throughput as well as mechanical wear and reliability are other reasons for concern here. It is the fact that the rocks are piled together on the belt that creates the unique measurement problems addressed in this thesis.

2.7.4 Digitization restrictions

The next set of *sampling restrictions* is due to the limitations of the hardware. The rockstream Ω must be sampled in three orthogonal directions where the distance along the belt x is a function of time $x = x(t)$ See figure 2.25.

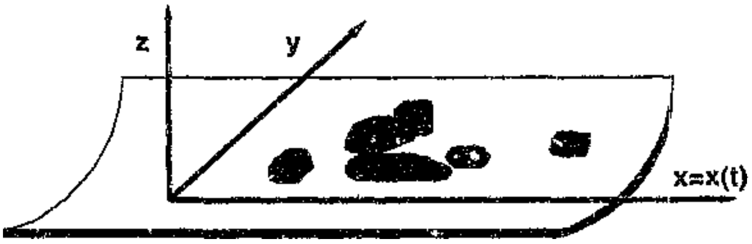

Figure 2.25. *Sampling the rockstream*

An ideal system will capture an infinite number of sequential images with no part of the rockstream left unsampled. Each image would span the full width of the belt, and each pixel will be infinitesimally small with infinite resolution. Obviously this is not possible because of finite memory and processing speed of computer hardware.

Thus two sampling decisions must be made. These are (i) The number and spacing of images to be captured, and (ii) pixel resolution, ie the ratio of millimetres to pixels which is the proportion of the belt scanned for a fixed amount of computer memory. Pixel resolution is a major point of contention as shown in figure 2.26. In 2.26(a) there are more larger rocks of coarse resolution available with little or no possibility of resolving the smaller rocks. In 2.26(b) the smaller rocks are resolved but there is little possibility of sampling the large rocks fully. A possible solution to this problem is to sample portions of the belt at high resolution using a number of image systems operating in parallel, an undesirable and expensive solution.

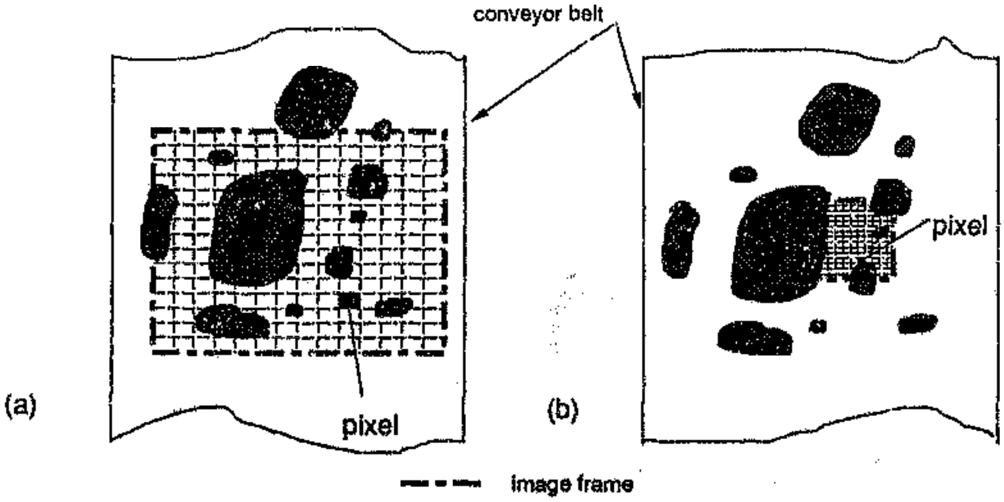

Figure 2.26. The problem of pixel resolution versus the proportion of the belt sampled. In (a) the full width of the belt is scanned. In (b) only a small portion of the belt is covered providing finer resolution.

2.7.5 Sampling restrictions

Associated with the hardware restrictions are sampling restrictions which affect the *frequency response* of the instrument and the bandwidth of the output signal $f_\Omega(D,t)$. Scenes of Ω are captured at finite intervals and processed at finite processing speed resulting in a sparse sampling of Ω. In addition the number of rocks per image on average can be very low which leads to a large variance in the statistics of the rocks per image. A important sampling objective is thus (a) to try and gather as many samples of rocks together in order to decrease the variances of the measurements by taking advantage of the *law of large numbers* and averaging, and (b) to decrease biasing caused by insufficient sampling. This is done by scanning the full width of the belt and capturing as many images as quickly as possible to be processed. The outputs from each processed image are then combined together to give an estimate of the average rocksize distribution.

In order to facilitate this averaging scheme to reduce the variances it is assumed that the stochastic process $f_\Omega(D,t)$ is *stationary* over a short period of time, ie that $f_\Omega(D,t)$ and $f_\Omega(D,t+\varepsilon)$ have the same statistics for a period of time $\varepsilon < T_s$. If the sampling time is T_s and the time delay between images being captured is ΔT then the number of images n processed and averages is given by

$$n = \frac{\varepsilon}{\Delta T} \qquad \Delta T < \varepsilon \tag{2.9}$$

If μ_{D_i} and $\sigma_{D_i}^2$ are the average size and variance of the size distribution associated with image I_i, then the mean and the variance for n images in a sampling period of ε is given by

$$\overline{\mu_\varepsilon} = \frac{1}{n}\sum_{i=1}^{N} \mu_{D_i} \tag{2.10}$$

$$\overline{\sigma_\varepsilon^2} = \frac{1}{N^2}\sum_{i=1}^{n} \sigma_{D_i}^{\;2} \tag{2.11}$$

because $\mu_i = \mu_{i+1}$ and $\sigma_i = \sigma_{i+1}$ for $i = 1 \ldots n-1$. It is also assumed that the covariances are zero, ie the image samples are independent of each other.

Two sampling methods for collecting images and averaging their results can be implemented, (i) a *continuous* periodic sampling method, and (ii) a periodic *batch* sampling method, where groups of images are captured on a relatively continuous basis for a short period of time, periodically. See figure 2.27.

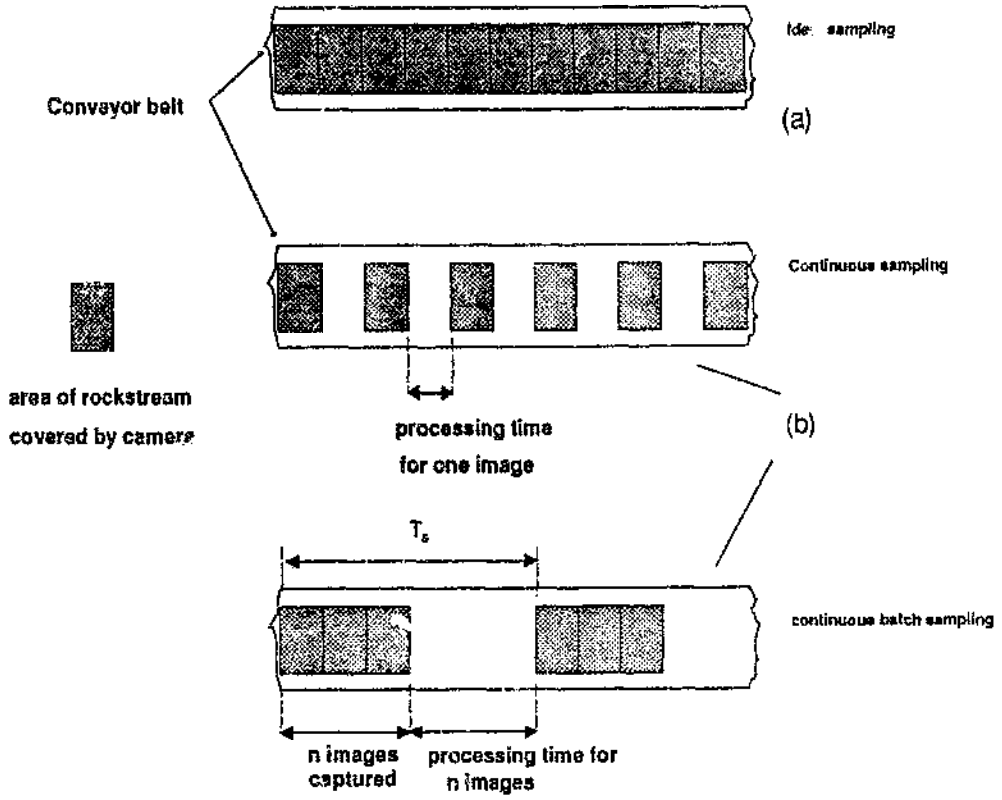

Figure 2.27. (a) Diagram showing ideal time sampling of the rock stream passing under the camera, and (b) the two actual methods that can be implemented given the restrictions of hardware.

In addition to sampling enough rocks by capturing enough images, it is important that the image sampling rate of the instrument be *fast* enough to ensure that the *changes* in the rocksize distribution $f_\Omega(D,t)$ may be observed with significant resolution (re Shannon sampling theorem, Stanley, 1975) . $f_\Omega(D,t)$ is a function of time and it is the *dynamic behaviour* of $f_\Omega(D,t)$ that is of interest as well as the absolute measurement of $f_\Omega(D,t)$. Averaging the average rocksize output from a number of successive images $I(t_i)$ to reduce variances has the undesirable effect of low-pass filtering the output signal, and reducing $\bar{f}'$ where

$$\bar{f}' = \frac{\partial \bar{f}_\Omega(D,t)}{\partial t} \qquad 2.12$$

Note that the highest resolution of the dynamic behaviour of the rocksize distribution is also dependent upon the maximum size of rocks in Ω, which determines the minimum size of the image required and thus the distance between successive images and hence the sampling sampling of measured rock parameters.

2.8 DATA PROCESSING AND FLOW

From the previous sections it is concluded that the task of the rocksize measurement system will be to relate the raw input data (image) to parameters of the physical events (size properties) that caused the image. Given that this measurement will be based on machine vision, the flow of data through the system conceptually can be broken down into an acquisition stage (which includes interrogation, modulation and sensing), followed by three sequential stages of image and knowledge processing in order to understand and derive knowledge as shown in figure 2.28. These stages are:

I) *Acquisition* where the reflected and modulated light is recorded as an image.

II) *Image transformation* which includes the identification and extraction of characteristics from the images of Ω which are uniquely related to size.

III) *Measurement* of these characteristics

IV) *Interpretation* of these measurements to a form readily understood eg a transformation to sieve size.

We can represent stages II, III, and IV by the following

$$I_e = \Psi(I) \qquad 2.13$$

$$p(M) = \mu(I_e) \qquad 2.14$$

$$f(D) = \Psi_c[p(M)] \qquad 2.15$$

where	I	is the image as captured by a camera
	I_e	is the transformed image
	Ψ	is the image transformation
	μ	is the measurement process
	$p(M)$	is the population of characteristic diameters or parameters M related to rock size
	$f(D)$	is the required size distribution
	Ψ_c	if the process to calculate the full size distribution from the parameters

The input to Ψ is the raw image I and the output is a binary image I_e. The objective of process Ψ is to obtain a *compact* description of the size related properties in image I which should be complete and meaningful as far as rock size measurements are concerned. This is essentially a *filtering* task which removes or suppresses image features not related to size (Williams, 1988) and amplifies or isolates those features related to size. This filtering is required because in general AI and machine-vision techniques are in a primitive stage of evolution, and the more complex the contents of the image to be analyzed, the larger and more difficult the computing task, which is not always deterministic.

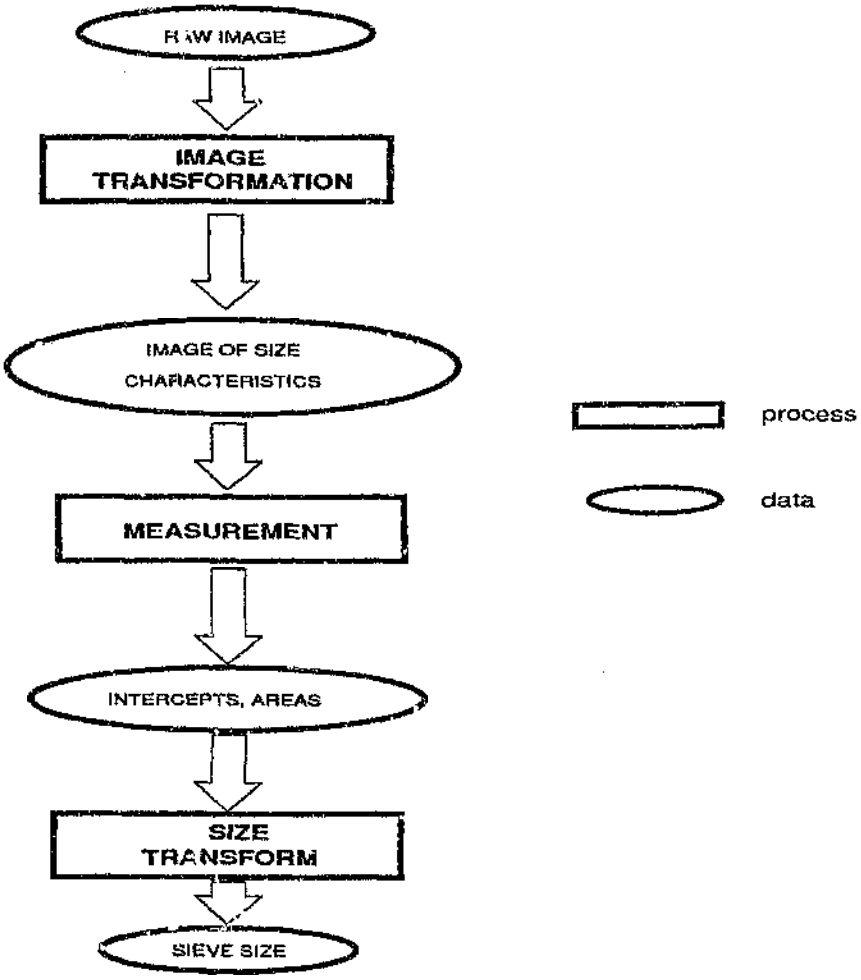

Figure 2.28. Block diagram of the three stages of processing to transform images to size knowledge.

From the analysis of the rock images (section 2.5) it is hypothesized that the size-related features to be extracted are the rock edges. This is based on the assumption that the physical edges of objects are fundamental descriptions of the objects and that the rock edges do relate or project to transitions in surface orientation or texture, (Chen and Medioni, 1989), (Marr and Hildreth, 1980).

The edge detection stage Ψ can conceptually be broken down into two interlinking tasks of low- and high-level machine-vision. The low-level task is the detection, localization and characterization of edges in the image function. These resultant primitive edge sets are imperfect and contaminated with noise. There is thus uncertainty with regard to the validity of these edges for size measurement because most local edge detection algorithms cannot discriminate classes of edges classified syntactically, in particular between rock edges which are due to surface aberrations and those which are due to the rock's perimeter. There is thus a requirement for the higher level tasks to classify edges into perimeter edges and other edges construed as noise. Refer to chapters 4 and 5.

Quantitative measurements μ are then made on the size dependant patterns in I_e to form a distribution of parameters $p(M)$ where $M = M_i$ is a characteristic of the geometric properties of the rocks of dimension i eg, length, surface area or volume. For this research lineal intercepts were chosen as the required parameters, where $M = L_1$. (The motivation for chord-length distributions is discussed in chapters 3 and 4). Although the measurement μ which renders $p(M)$ is presented as separate entity from Ψ, the combined process $\mu[\Psi]$ may be conceptually or algorithmically inseparable.

The last stage is the transformation Ψ_e of $p(M)$ to a required size distribution $f(D)$, where for traditional reasons $f(D)$ is required to be sieve size, (Allen, 1981). The transformation Ψ_e is not a trivial problem and a myriad of other transformations similar to Ψ_e can be found in numerous other areas of science and engineering. The transformation Ψ_e is by nature ambiguous, and epitomizes the essence of stereology. The parameter distribution $p(M)$ as measured from I_e is of a dimension lower than the distribution required, which is volume or sieve size. The problem with this transformation will be discussed in chapter 7 where it is hypothesized that a *modified* $p(M)$ may be adequate for mill or crusher control, and that a final conversion to sieve size may not be required.

When developing a system as depicted in figure 2.28 it is obvious that some means must be available for *monitoring* the progress of information flow and extraction. It is also important to gauge the impact of one system parameter on the final output. This is a very difficult task. The ability of Ψ to amplify size features while suppressing other features not related to size cannot be measured directly, and at present only qualitative observations can be used to gauge its efficiency. This is similar to other but not all image-processing tasks discussed in the literature which are generally developed on an ad-hoc basis with their performance evaluated from observations.

Because of the stochastic and non-stationary nature of the rockstream, the images are constantly changing. Thus no universal method exists which allows for the prediction of an image or edge pattern based on past images for the validation of a presently processed edge pattern. At best only data such as the parameter distribution $p(M)$ or estimates of the size distribution $f(D)$ (which is unreliable) can be predicted. This monitoring problem can be likened to the monitoring of a signal of large-dynamic range and wide bandwidth through a range of filters where the behaviour of the filters with regard to the signal has not been properly characterized or tested. This is because the large range of test signals (images) to the system cannot be determined or adequately synthesized for proper testing. Rockstreams with a narrower range of sizes and shapes will help to alleviate this monitoring problem, because the "signal" bandwidths are narrower.

Again it must be emphasized that the above knowledge processing structure ignores the realities of a real instrument and assumes the following. (i) Unambiguous images of the rocks are captured. This implies that the captured images are of good enough quality for image processing algorithms without having to resort to complex image *restoration* algorithms. (ii) The analysis of the rocks of Ω_R will allow for the estimation the size distribution of *all* the material lying on the belt.

2.9 CLOSURE

A simple model of the mechanism linking the rock scene on the conveyor belt to a *visual* image has been proposed, because the disadvantages of other methods of remote-sensing justifies the use of *machine-vision* for the rock-size measurement, and in particular 2-D image processing. The data processing consists of, extracting edges from captured images, measuring chord lengths, and then converting the chord lengths to some equivalent size distribution, eg sieve size. The rockscene images to be processed are naturally ambiguous, and this raises the following questions. "How accurately can size data be recovered from the images, and what level of processing complexity is sufficient considering the real-time specification ?" In addition, "How does one keep track of the flow of data through such a system when so many intermediate stages can only be evaluated subjectively by inspection. This problem is compounded with sampling limitations especially *occlusion* which limits the amount of rock to be seen and processed.

In this chapter it is hypothesized that rock-edges are the best features to extract from the images in order to derive rocksize. In chapter 3 the relationship between object size and lower dimensional sections will be derived in order to justify the objective of *rock edge* extraction, the methods and techniques which are then described in chapters 4 and 5.

3 THE MEASUREMENT OF SIZE FROM CHORD LENGTH AND AREA

3.1 INTRODUCTION

In chapter 2 it was hypothesized that *subsets* of size-related features in the images I of the rockstream surface Ω_g are sufficient for inferring the size distribution of the *total* rockstream Ω . These subsets are rock edges or boundaries from which chord lengths or areas can be measured.

In this chapter relationships for estimating size distributions from areal or chord-length distributions measured from 2-D images which have lost their "depth" information, are discussed. These relationships are not unique to this thesis and have been developed over many years by other researchers in other applications. However the derivation of these relationships are given or derived so that the problems and difficulties unique to the transformation (Ψ_c) of chord-length to rocksize for this application can be understood and contrasted against the instances in the literature where such sizing transformations have been successfully applied.

In particular the well known and classic case of estimating *sphere* size distributions from sections is discussed as a demonstration of the principle of *stereology*, which is the foundation upon which most measurement techniques and relationships that link section data to size have been developed.

What becomes apparent with stereological sizing techniques is that the analytical models as developed in this chapter are really only applicable to particles of *known* shape. For example, as the particles' shapes deviate from spherical or cubic, the estimation of the size distributions of *arbitrary shaped* particles from lower dimensional information can only be accomplished through models of *uncertain validity* (DeHoff, 1983). Although the models described here are for ideal particle systems, they highlight the stereological problems peculiar to the rocksize problem, that modelling the rockstream is extremely difficult and that existing techniques only apply to ideal or limiting particle systems.

3.2 BACKGROUND TO STEREOLOGICAL METHODS

Stereology (introduced in chapter 1) is a body of methods which allows for the *inference* of spatial geometrical structure upon the basis of *partial information* such as plane sections or projections onto planes (Miles, 1977). Stereology means literally "the knowledge of space" and although these methods are based on usually simple formulas, they are often derived by rather complex mathematical reasoning (Weibel, 1980). Although stereology has traditionally been dedicated to the extrapolation of two- to three-dimensional space from sections; methods for examining any n-dimensional structure with an s-dimensional probe ($s<n$), have, and are being continually developed (Miles, 1972). Stereological relationships exist only for populations of *many* particles, and any measurement made on a single irregular particle can only be considered a sample of a random variable. Stereological methods are thus *statistical* in nature and measurements from profiles obtained on *samples* by a section or probe, yield *estimates* which are *averages* and are affected by *sampling errors*. Thus much effort is reported in the literature for deriving *unbiased* stereological estimates, (Miles and Davy, 1976), (Cruze-Orive, 1980).

In stereology sections are taken from samples of a body structure, eg an aggregate of particles or a biological specimen, which are then analyzed by measuring *probes*. The probes return distributions of parameters, which are converted to estimations of the 3-D structural properties of the body by means of the theory of geometric-probability and integral-geometry. Data measured from the section traces could be for example, (i) the cross-section area, (ii) the perimeters, or (iii) the maximum-chord length of the profiles. There are numerous approaches to solving stereological problems which are reviewed by Underwood (1970). These are based on factors such as (a) the number of particles to be examined, (b) their arrangement in space relative to one another, (c) their shape, (d) the method of sectioning or sampling, and (e) the desired parameters to be measured.

There are limitations to stereological methods. A plane section through a large number of randomly shaped particles without any assumptions regarding their shape and dispersion can only give estimates of for example, volume fraction, whilst serial-sectioning on the other hand can allow for the estimation of *size distributions*, or the *number of particles* (DeHoff, 1983).

3.3 SECTIONING THE ROCKSTREAM Ω

In this subsection we introduce the fundamental stereological operation of *sectioning* so that ***populations of parameters measured on one or two dimensional sections can be related to 3-D parameters***. This lays the foundation for the application of stereological principles to the rocksize problem which is presumed to be the only method of tackling this rocksize problem.

3.3.1 Sections and Traces

In this subsection we introduce the concept of particle sectioning and the resulting traces. Consider a polyhedral particle in cubic space which is characterized by its volume V, the surface area of its faces A, the length of its edges L and its corner points P, as shown in figure 3.1. A test plane intersecting the particle results in a *trace* which will be a polygon surface with area A', circumference L' and corner points P'. (After Weibel, 1980).

In terms of integral geometry (Santalo, 1976), a particle can be considered a convex solid or a closed point set because it has an outer surface. We can thus define four sets of points which make up the particle or the polyhedron above. X_3 Are the points internal to the object X, where $X_3 \subset X$ and $X_3 \propto V$. Similarly X_2 are the points on the surface of X where $X_2 \propto A$ and $X_2 \subset X$. X_1 are the points forming edges where $X_1 \propto L$ and $X_1 \subset X$. X_0 are points on the corners where $X_0 \subset X$ and $X = X_3 \cup X_2 \cup X_1 \cup X_0$. We also define the measurement of ***volume, area*** and ***length*** measures of a particle X as being $V = V[X]$, $A = A[X]$ and $L = L[X]$ respectively, where V, A and L are positive and increasing functions. We also define the boundary of particle X to be ∂X and its interior $\overset{o}{X}$. On a 2-D projection plane as shown in figure 3.1(c) ∂X is the edge and $\overset{o}{X}$ the projected area.

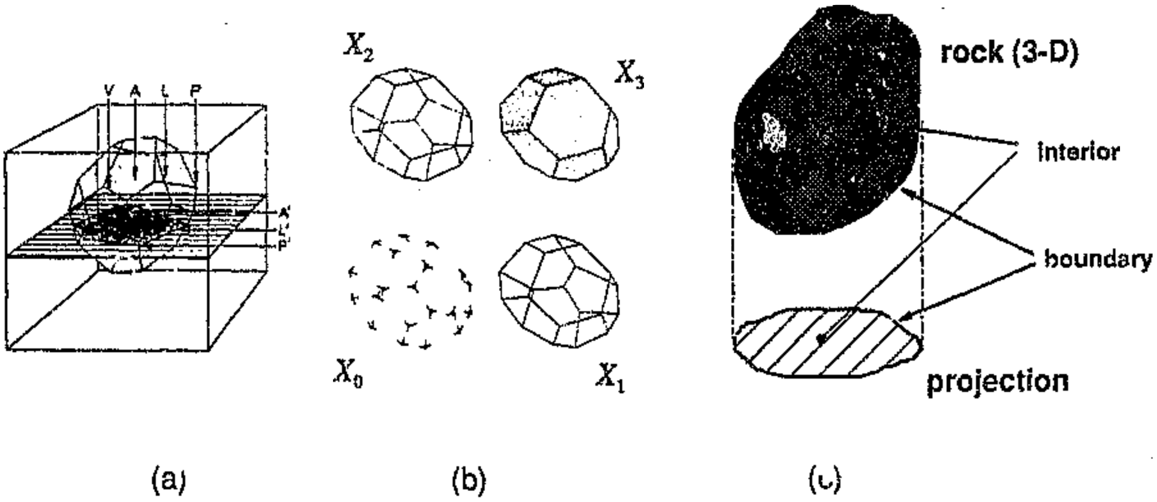

Figure 3.1. (a) Example of a structure consisting of a polyhedral in a cube. A plane section exposes the polygon profile of the particle. (b) the sets X_3, X_2, $X_1$and X_0. (c) The boundary and interiors of 1 3-D and 2-D object.

The trace $Z(X)$ of structure X after intersection with probe T is given by $Z(X) = X \cap T$. For a plane probe T_2, A' is a trace of V and L' is a trace of A. When sectioning a solid, the dimension of the trace Z is always smaller or equal to the solid's dimension. Table 3.1 and 3.2 (Weibel, 1980) summarizes all the possible intersections $Z = X \cap T$ of a 3-D solid X sectioned by probe T rigourously proved by Miles (, 1972), together with their dimensional relationships $d(Z) = d(X \cap T)$ respectively.

Table 3.1 shows the relationships that exist between the metric properties of an object, and its trace. For example sectioning an object of volume V will result in a trace of area A' which is a 3-D to 2-D mapping. Table 3.2 shows that sectioning a body of dimension $d(X)$ with a probe of dimension $d(T)$ produces a trace of lower dimension $d(Z)$ which generally obeys the relationship $d(Z) = d(X) + d(T) - n$ with the limiting condition $d(X) + d(T) \geq n$ where n is the dimension of the Euclidean space.

Table 3.1 **Table of traces and corresponding parameters caused by the intersection of structure X with section T**

	Section T			
Object	$V(T_3)$	$A(T_2)$	$L(T_1)$	$P(T_0)$
$V(X_3)$	$V'(X_3 \cap T_3)$	$A'(X_3 \cap T_2)$	$L'(X_3 \cap T_1)$	$P'(X_3 \cap T_0)$
$A(X_2)$	$A'(X_2 \cap T_3)$	$L'(X_2 \cap T_2)$	$P'(X_2 \cap T_1)$	$\varnothing$
$L(X_1)$	$L'(X_1 \cap T_3)$	$P'(X_1 \cap T_2)$	$\varnothing$	$\varnothing$
$P(X_0)$	$P'(X_0 \cap T_3)$	$\varnothing$	$\varnothing$	$\varnothing$

Table 3.2 **Table showing the relationship between the dimensions of traces Z, objects X, and corresponding sections T.**

		$d(T)$			
		3	2	1	0
	3	3	2	1	0
$d(X)$	2	2	1	0	
	1	1	0		
	0	0			

In the same way that the particle shown in figure 3.1 was sectioned to produce traces, the idea behind this research is that rocks on the conveyor belt will be sectioned to produce traces as shown in figure 3.2. It is intended to use the population of measurements on these traces to estimate the 3-D size parameters as required in this research. However it is obvious that a whole variety of traces or population of traces can be generated which depends on the geometry of the probe and particles and their relative *positions*. Thus if it is assumed that random distributions of particles are intercepted by sections the need arises to study *geometric probability* so that populations of measurements on traces can be related back to 3-D parameters as was given in the example in chapter 1.3.2.

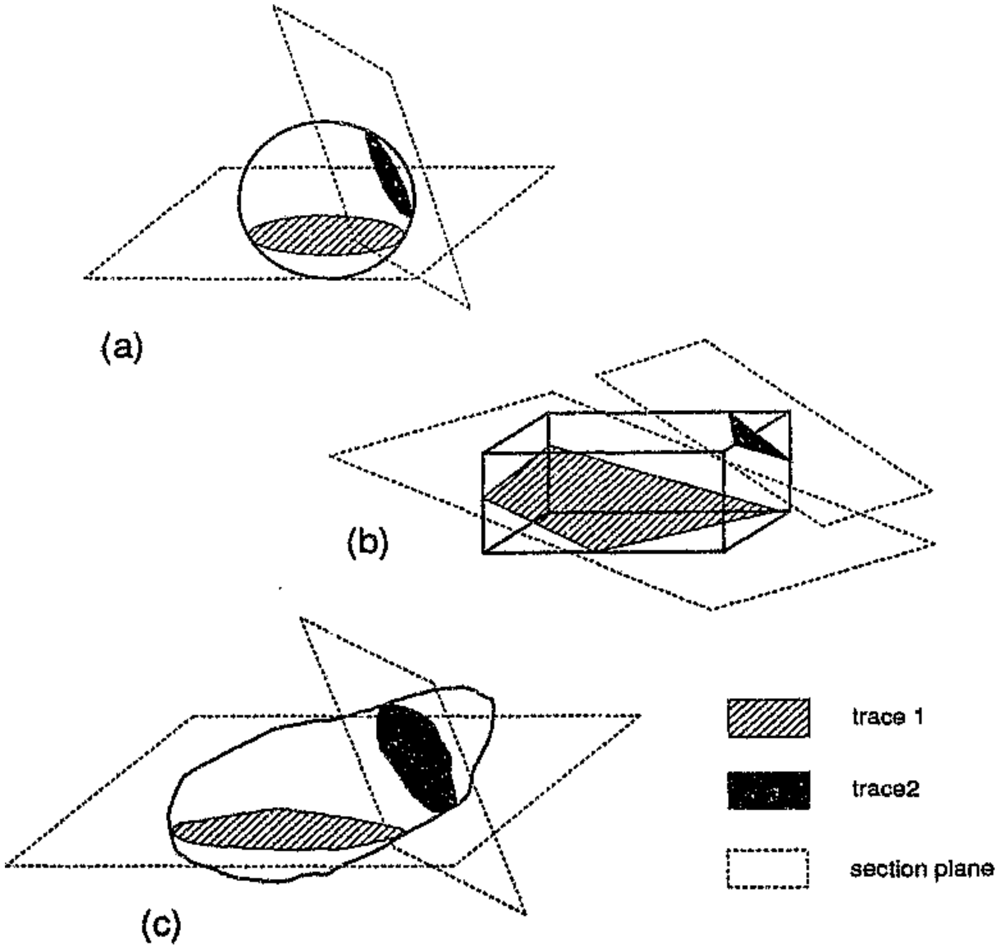

Figure 3.2. Using two plane probes T_2 at different orientations to section a rock particle of (a) spherical, (b) rectangular and (d) random shape.

Because the rocks in the rockstream cannot be physically sectioned as shown in figure 3.2, the traces for size measurements will be obtained by using methods described in section 3.3.3.

3.3.2 The Ambiguity of Unfolding Size Distributions

The ideal goal of this rocksize measurement problem is to derive a model which maps populations of 3-D objects with certain properties ie sieve size distributions, to populations of traces (profiles) resulting from sectioning as presented in figure 3.2 above. It is then required to invert this mapping so that the properties of the 3-D particles may be estimated. This inverse mapping is often referred to in the literature as the reconstruction of particle size distributions by *unfolding* the measured profile distribution. Unfolding is conceptually difficult to understand and in most cases is mathematically intricate and statistically unstable (Gundersen, 1986). In particular Cruze-Orive (1982) comments that departure from particles of relatively simple geometric shapes, leads to intractable models or even indeterminate ones for the unfolding process. This leaves one with the unpleasant choice of having to choose between unrealistic models, mathematically complex ones, or no solution at all. Gundersen also questions whether classical unfolding techniques are really worth pursuing because of the many assumptions which are made to make the problem more manageable, but which produces less credible results. For example sectioning a non-convex[3.1] object is inherently ambiguous because more than one trace may be produced as shown in figure 3.3, and unless high density serial sections are taken, nothing can be inferred about the topology of the objects sectioned, (DeHoff, 1982), (Weibel, 1980).

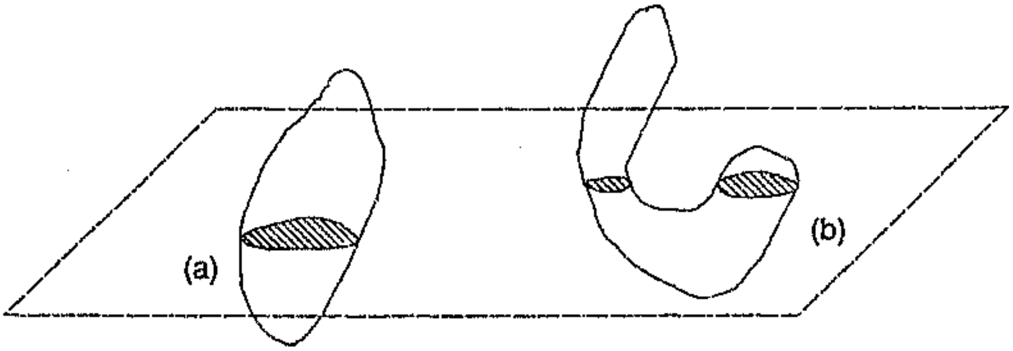

Figure 3.3. Sectioning a convex (a) and non-convex (b) particles showing the potential for ambiguity in estimating the number of rocks from sections.

[3.1] An object is convex if and only if a line connecting any two points in the object remains entirely within the object.

3.3.3 Modelling and Sectioning the Rockstream

The rockstream needs to be sectioned in order to create populations of section profiles from which parameters can be measured and then linked to the size distribution of the rockstream. Physically it is not possible to section (or slice) the rockstream Ω as is performed on biological and metallurgical samples for obvious reasons. It is thus hypothesized that

> *In order to estimate rocksize distribution, the principles of stereology can be applied to the images of top surface Ω_R of the moving rockstream Ω, where the image of the top surface Ω_R can be assumed to be the result of a **projection** of the top surface Ω_R* onto plane.

A general set-theoretical model will now be developed, which relates density distributions $p(M)$ of properties or parameters M measured on a section of the rockstream Ω to the size distributions of rocks X_3. For this exercise we will consider the property area A of the projections. The objective of this modelling exercise is thus to relate $p(A)$ measured from a sample of the rockstream Ω to the rocksize density distribution $p(D)$[3.2]. It is important to note that $p(D)$ is fixed sampled property of the rocks which gave rise to the image being analyzed, whereas $p(A)$ is assumed to be the probability density distribution of the area of projections or intercepts arising from projection or intercept of randomly distributed rocks in space. Instead of $p(A)$, other distributions such as $p(L)$ can be measured too. The size of a rock D can be any equivalent size parameter defined by the user which is appropriate to the application, for example sieve diameter or equivalent-volume diameter. We thus define a *sizing process* s which when applied to a rock X gives $s(X) = D$.

In developing the model the rockstream Ω is assumed to be infinite in extent and the plane probe $T = T_2$ is assumed to be infinitesimally thin. Assume that a rock X of size D or volume V is intersected by T to give a profile of area A. If an infinitesimally small part of the rock dX of volume dV is assumed to be sliced by the thin 2-D plane and results in a trace $dZ = dZ_2$, then

$$dZ(dX) = dX \cap T \qquad 3.1$$

However this intersection is conditional on the event that the plane hits the rock element ie $T \uparrow dX$ where "$\uparrow$" denotes hits, therefore $dZ = dX \cap T \mid T \uparrow dX$.

The area of the intersection is $dA = A[dZ]$ and thus the total profile area of the rock X is given by

---

[3.2] $p(D)$ can be either a volume or number distribution.

$$A = \{A[X \cap T] \mid T \uparrow X\} = \int_X \{A[dX \cap T] \mid T \uparrow dX\} dX \qquad 3.2$$

In order to derive the areal density distribution $p(A) = \frac{Pr\{A\}}{\int Pr\{A\}dA}$, the probability of measuring an area of A over the whole range of possible areas must be evaluated. According to probability theory (Papoulis, 1965) measuring the frequency of occurrence n_A of a certain event A over the total number of experiments N can provide an *indication* of the probability of that event occurring ie that $Pr(A) \approx \frac{n_A}{N}$. We will now refer to probabilities in the assumption that frequency of occurrences are valid indications of probability.

$Pr\{A\}$ is dependent on (i) the rock being present in the rockstream, (ii) the rock being intersected, and (iii) the profile being of area A, noting that all these events are ***dependent*** on one another as is shown in equation [3.2]. Thus the probabilities of the three events above must be evaluated over the whole rockstream Ω ie for all the rocks in order to derive $p(A)$. To measure $p(A)$ is the same as measuring $p(A[X \cap T] \mid T \uparrow X)$ because A cannot be measured if $T \cap X = \emptyset$. For convenience $A = A[T \cap X]$.

Let the probability of a rock X of size D being cut by the probe be $Pr\{T \uparrow X_D\} = Pr\{T \uparrow X \mid s(X) = D\}$. ***Also let $p_D(D)$ be the probability distribution associated with the occurrence of a rock of size D which can be assumed to be equal to the size distribution of all the rocks in the rock stream, ie*** $p(D) = f(D)$. Now from probability theory (Papoulis, 1965), $Pr\{A\} = \sum_i Pr\{A \mid B_i\}Pr\{B_i\} = \int_0^\infty Pr\{A \mid B\}p(B)dB$. Thus the probability of an intersection of the test probe with any rock in Ω is given by

$$p(T \uparrow X) = \int_\Omega Pr\{T \uparrow X \mid D\}d\Omega = \int_0^\infty Pr\{T \uparrow X \mid D\}p(D)dD \qquad 3.3$$

Similarly let the conditional probability of a profile area A being measured be given by $p(A \mid T \uparrow X_D \mid D)$, and the probability of a rock of size D being present *and* being hit by the section probe *and* the profile being of size A be denoted by $p(A, T \uparrow X, D)$. Now from probability theory (Papoulis, 1965)

$$Pr(A \mid B) = \frac{Pr(AB)}{Pr(B)} \quad \Rightarrow \quad Pr(AB) = Pr(A \mid B)Pr(B) \qquad 3.4$$

and by using the fact that $Pr\{A\} = \int_0^\infty Pr\{A \mid B\}p(B)dB$ we have

$$p(A,T \uparrow X_D\} = \int_{\Omega} Pr\{A,T \uparrow X_D, D\} d\Omega = \int_0^{\infty} Pr\{A \mid T \uparrow X_D \mid D\} \, Pr\{T \uparrow X_D \mid D\} \, p(D) dD \qquad 3.5$$

Now from equation [3.4] we have

$$p(A \mid T \uparrow X_D) = \frac{p(A,T \uparrow X_D)}{p(T \uparrow X_D)}$$

and now substituting equations [3.3 $\wedge$ 3.5*gives*

$$\Rightarrow \qquad p(A \mid T \uparrow X) = \frac{\int_0^{\infty} p(A,T \uparrow X_D, D) dD}{\int_0^{\infty} p(T \uparrow X_D, D) dD}$$

$$\Rightarrow \qquad p(A \mid T \uparrow X) = \frac{\int_0^{\infty} p(A \mid T \uparrow X_D, D) \, Pr\{T \uparrow X_D \mid D\} p(D) dD}{\int_0^{\infty} p(T \uparrow X_D \mid D) p(D) dD} \qquad 3.6$$

Equation [3.6] links the frequency distribution of profile areas $p(A \mid T \uparrow X_D)$ resulting from plane intersections of rocks, to the frequency distributions of rocks $p(D)$. Equation [3.6] does not necessarily have to be derived from *areal* profiles resulting from plane probes as was done above. This basic equation also holds for a probe of any dimension and associated profiles as listed in table 3.1. In this research it has been found be advantageous to measure *intercept lengths L* resulting from a linear probe intersecting a particle (figure 3.4) instead of areas A (figure 3.5).

However measuring chord-length distributions directly in space as shown in fig 3.5 is difficult to achieve practically. A useful result shown in section 3.4.3, is that provided certain rules are met with regard to IUR sampling, linear-intercept measurements made on two dimensional profiles (images) which are in turn sections of a 3-D structure, provide the same data as linear measurements made *directly* on the 3-D structure, see figure 3.6. This two stage probe scheme provides some flexibility for measuring intercepts on rocks that cannot be sectioned. It is thus from *chord-distributions* profiles measured from *projected plane sections*, that the size distribution of rocks was estimated in this thesis. See see figure 3.7.

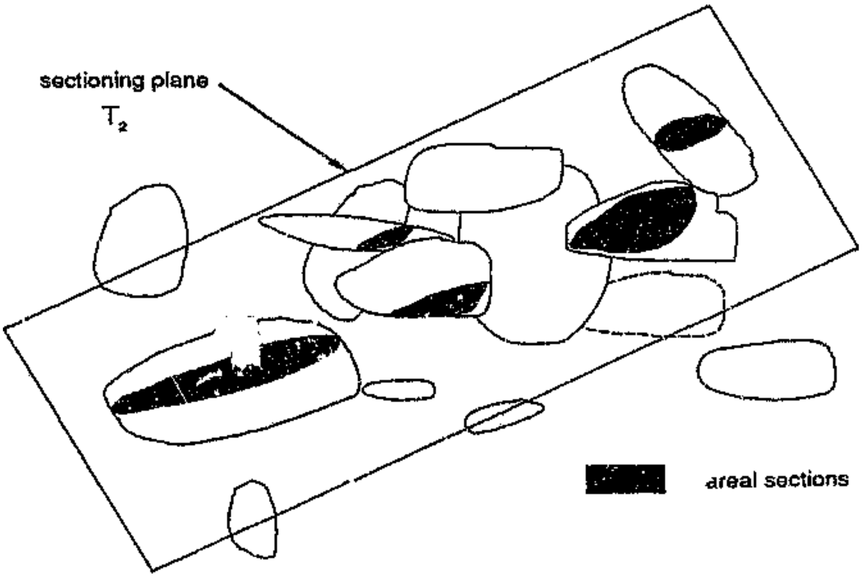

Figure 3.4. Measuring *areal* distributions of a number of rocks using a hypothetical thin section T_2.

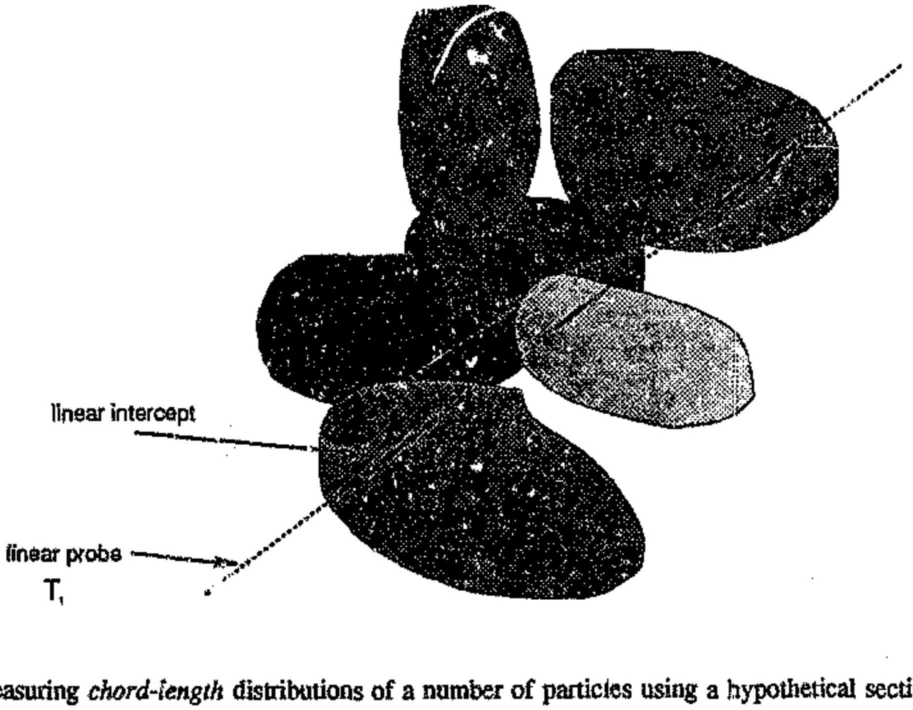

Figure 3.5. Measuring *chord-length* distributions of a number of particles using a hypothetical section T_1.

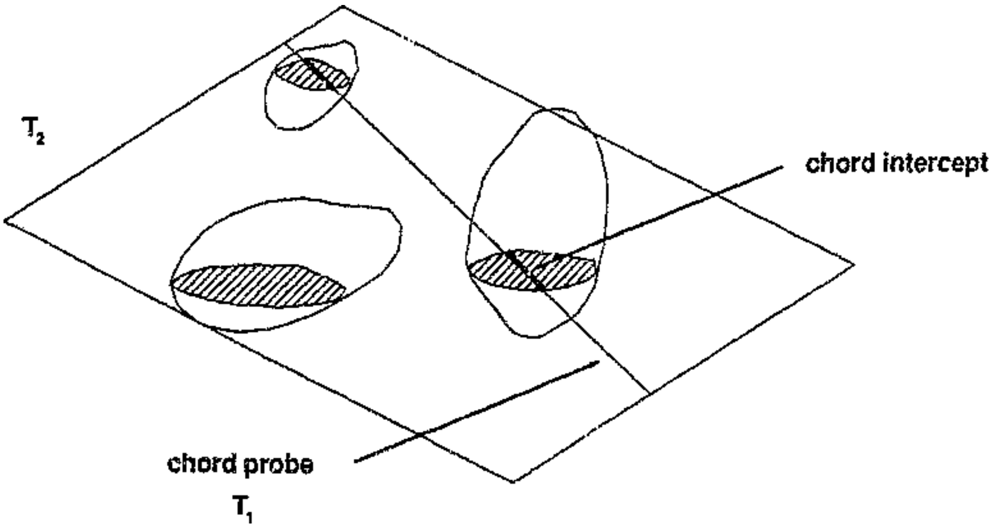

Figure 3.6 : Measuring chord-length distributions with a two stage sampling scheme of applying T_2 and then T_1.

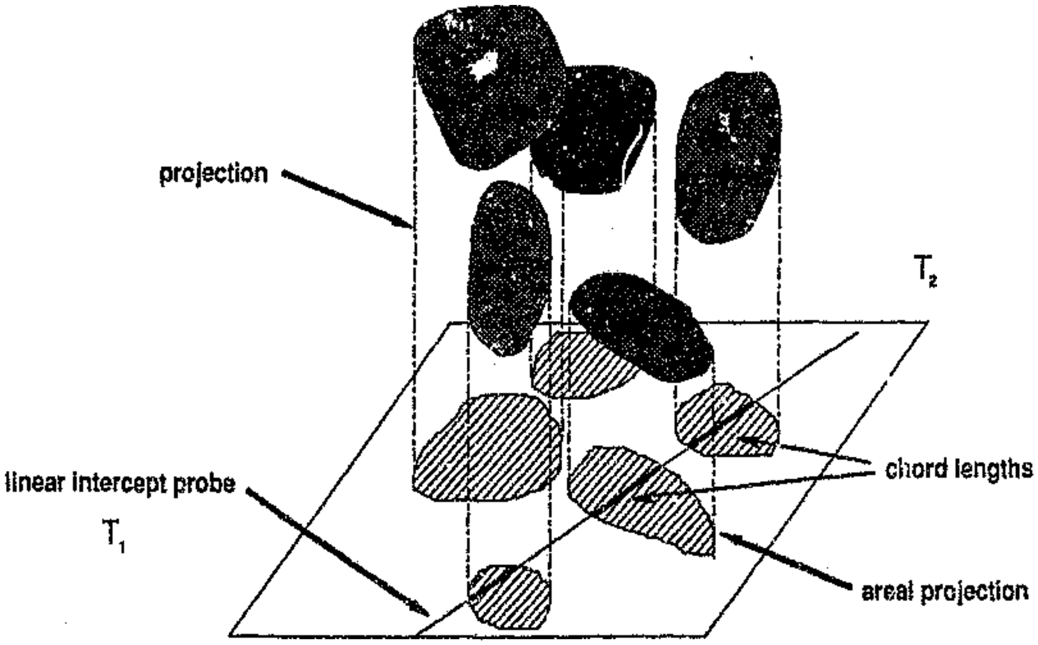

Figure 3.7. Measuring chord-length distribution using the two stage sampling scheme as given in figure 3.6 except in this case the chord lengths are measured on projected areas of the rocks.

3.4 DERIVING THE SIZE DISTRIBUTION OF SPHERES

3.4.1 Introduction

The synthesis of formulae from equation 3.[illegible] for "unfolding" relationships between populations trace parameters and 3-D properties of *irregular* particles under ***realistic*** conditions is a *difficult* if not impossible task especially as far as making *unbiased estimates* from single sections is concerned (DeHoff, 1982). This is because the probabilities of test probes intersecting the particles $p(T \uparrow X)$, and the probability of measuring a parameter of a certain value resulting from the test probe intersecting the particle, has to be evaluated using *geometric probability* which requires a ***describable*** object.

However with *ideal particles* under *ideal conditions* it is possible to derive analytical solutions relating the data from 2-D sections to the 3-D structures because the required geometrical probabilities for example $Pr\{T \uparrow X\}$ can be calculated. An ideal particle environment which allows for analytical solutions to be formulated can be assumed to be one of *sparsely* distributed (dilute) and *non-overlapping spheres* (Cruz-Orive, 1982), (Nicholson and Merckx, 1969). Although the derivation of these solutions are well researched in the literature, it will be explicitly demonstrated how such formulae are derived and why such analytical solutions cannot be applied to real arbitrarily-sized and shaped particles without making any major assumptions which are quite inappropriate as far as rocksize measurements are concerned.

A critical assumption made in the derivation of analytical size formulae or models concerns particle *shape*. The derivation of size distribution techniques from single sections (as opposed to multiple sections) is very dependent on the shape of the particles, and most of size estimation work generally assumes specific particle shapes, eg spheres, ellipsoids of fixed axis ratios, and certain polyhedrons. Although work has recently been extended to randomly shaped particles (Miles, 1985), (Gundersen, 1986), other assumptions such as convex particles, or shape which is invariant with size (King, 1982) are still required. Recently much work has also been done in making unbiased estimates of average stereological parameters such as $\bar{V}_V$ and σ_V^2 of volume distributions irrespective of shape, (Miles, 1985), (Missiaen and Thomas, 1989), (Gundersen and Jensen, 1985).

Thus the mapping of populations of parameters measured from profiles of random particles to higher dimensional data such as volume size for spheres is well established. The next subsection demonstrates in detail the mechanisms of this mapping which will be used to reveal the problems to be encountered when one deviates from this ideal, sparsely distributed population of spheres, to the randomly shaped and overlapping rocks as found on conveyor belts. Although linear intercepts is the method chosen for this rocksize problem (justified in chapter 4 and 5), both areal and linear intercepts of spheres are discussed, because both measurements are feasible with machine-vision systems.

3.4.2 Areal profile distributions from spheres

Consider a sphere of radius R centred at the origin and intercepted by a thin horizontal section T_2 parallel to the x-y axis (fig 3.8). Each section will produce a circular profile whose radius r depends on the position of the section from the centre of the sphere along the z axis where

$$r(z)=\sqrt{r^2-z^2} \qquad 3.7$$

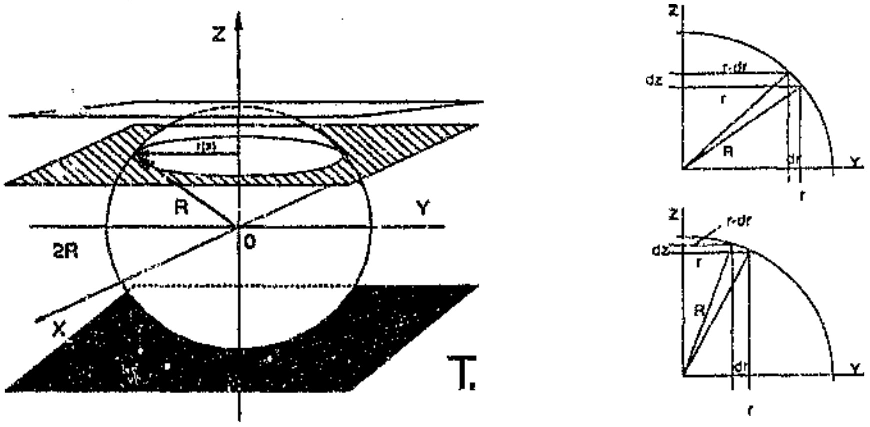

Figure 3.8. Sectioning a sphere of radius R to gives a profile $r(z)$.

The size distribution of profiles is determined by the probability density with which a profile of radius r_i falls into range $r>r_i>r-dr$. Because the sectioning plane is free to move up and down the z axis with no restriction, the probability measure must be related to dz, thus the probability of having r_i in the class $r, r-dr$ is

$$Pr\{r>r_i>r-dr\}=\begin{Bmatrix} dz/R & for & r\leq R \\ 0 & for & r>R \end{Bmatrix} \qquad 3.8$$

Now if $dz=z(r-dr)-z(r)$ then by [3.7] and [3.8] we get

$$dz=\sqrt{R^2-(r-dr)^2}-\sqrt{R^2-r^2}$$

$$\Rightarrow \quad Pr\{r>r_i>(r-dr)\,|\,R\}=\frac{1}{R}[\sqrt{R^2-(r-dr)^2}-\sqrt{R^2-r^2}] \qquad 3.9$$

If equation [3.9] is differentiated to give dz/dr then the probability density ϕ becomes

$$\phi(r \mid R)\,dr = \frac{r}{R\sqrt{R^2 - r^2}}\,dr \qquad 3.10$$

which depends on both r and R. Integrating equation. 3.10 between limits $r, r - dr$ gives

$$Pr\{r, r - dr\} = \int_{r-dr}^{r} \phi(r \mid R)\,dr = Pr\{r \mid R\} \qquad 3.11$$

The probability density function for $\phi(r \mid R)$ is given in fig 3.9 below. The above analysis shows that although all profiles are equally likely to occur, the probability density of profile radii varies with profile size, with 86% of all profiles likely to be greater then $\frac{R}{2}$. It can be shown that sectioning a large number of randomly distributed spheres that are not overlapping and of *identical* size will yield the same result as equation. [3.10].

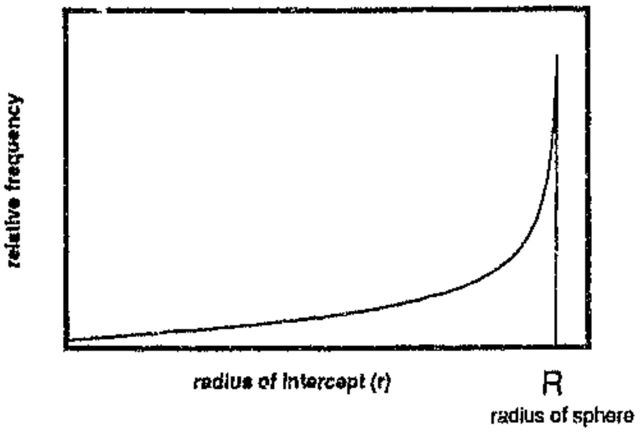

Figure 3.9. Probability density function $\phi(r \mid R)$ for a sphere (radius R) sectioned by a plane.

Although in this analysis the particle shapes have been restricted to spheres of a single size, the real world requires at least the analysis of groups of spheres of *different* sizes. We can assume *a priori* that the profile of sections obtained from a mixture of spheres of different sizes will be influenced by (i) the volume density of the number of spheres in each size class i N_{Vi}, (ii) the probability of hitting a sphere of a certain size, and (iii) the frequency distribution of profiles $\phi(r \mid R)$ that can be derived from each class of spheres. With spheres of different size both R and r vary and we have $F(R)$ and $f(r)$ are defined here to be the number size-density distribution for *spheres* and *sections* respectively.

The relationship between populations of spheres and random areas will be developed by calculating the contribution of a discrete size class of spheres to the population of profiles detected. Assume a volume V contains spheres of equal discrete size class $R_j = j\cdot\Delta R, j = 1..m$, where R_m is largest sphere. The number volume density of spheres in each class j is given by N_{Vj}. A section T_2 intersects volume V to give a number of profiles with radius $r_i = i\cdot\Delta r, r = 1..n$ with numerical profile density N_{Aj}. We will now use a result from stereology (DeHoff and Rhines, 1961), (Weibel, 1980). Assume a given volume contains a large number of convex particles with closed surface, randomly distributed so that all orientations are equally likely, we can expect that the number of profiles found per unit area of section is directly proportional to the product of numerical particle density and the mean tangent diameter, ie

$$N_A = N_V\cdot\overline{H} \tag{3.12}$$

Thus for each size class j we get

$$N_{Aj} = N_{Vj}\cdot\overline{H}_j = N_{Vj}\cdot 2R_j \tag{3.13}$$

and for a whole population of spheres where $\overline{R}$ is the average sphere size we have

$$N_A = N_V\cdot 2\overline{R} \tag{3.14}$$

The profile radii on the section falling the size range $r, r-dr$ contributed by spheres in the size class j is given by

$$N_{Aj}(r) = N_{Vj}\cdot 2R_j\cdot Pr\{r\mid R_j\} \tag{3.15}$$

Thus the total contribution of all the spheres to the profile of radii $r, r-dr$ is given by

$$N_A(r) = \sum_{j=1}^{m} N_{Aj}(r) \tag{3.16}$$

The number frequency for spheres of size R_j is

$$F(R_j) = \frac{N_{Vj}}{N_V} \tag{3.17}$$

where $N_V = \sum_j N_{Vj}$. Similarly the number frequency of profile radii is given by

$$f(r_i) = \frac{\int_{r-dr}^{r} N_A(r)dr}{\int_0^{\infty} N_A(r)dr} \tag{3.18}$$

Substituting [3.15] into [3.16] gives

$$N_A(r) = \sum_{j=1}^{m} N_{Vj} \cdot 2R_j \cdot Pr\{r \mid R_j\} \qquad 3.19$$

Dividing [3., 19] by [3.14] gives

$$\frac{N_A(r)}{N_A} = \sum_{j=1}^{m} \frac{N_{Vj} \cdot 2R_j}{N_V \cdot 2\bar{R}} \cdot Pr\{r \mid R_j\}$$

$$\Rightarrow \qquad f(r) = \frac{1}{\bar{R}} \sum_{j=1}^{m} F(R_j) \cdot R_j \cdot Pr\{r \mid R_j\} \qquad 3.20$$

Now let $\Delta R \to dR$ becoming infinitesimally small, and noting that only spheres of size $R > r$ contribute to the profiles in size range $r, r - dr$ transforms equation [3.20] to give

$$f(r) = \frac{1}{\bar{R}} \int_r^{R_m} F(R) \cdot R \cdot Pr\{r \mid R\} dR \qquad 3.21$$

Substituting $\phi(r \mid R)$ from [3.10] into [3.21] gives

$$f(r) = \frac{1}{\bar{R}} \int_r^{R_m} F(R) \cdot \frac{dR}{\sqrt{R^2 - r^2}} \qquad 3.22$$

which was first derived by Wicksell in, 1925. Tallis (1970), Underwood (1970), Weibel (1980) are amongst the many authors that derive and discuss of this formula. This formula relates the distribution of profiles $f(r)$ to the size distributions $F(R)$ of spheres.

The whole problem of estimating the size distribution of particles from areal cross-sections or traces revolves around solving for $F(R)$ in equation [3.21] given $f(r)$ for some $\phi(r \mid R)$. This deconvolution problem is made more complex because in many cases $\phi(r \mid R)$ is usually not known, or is of a nature which makes the inversion very difficult. For spherical particles the analytical relationship is as given in [3.22] and is the *Volterra* integral equation of the first kind. The solution of this equation will be discussed further in chapter 7.

3.4.3 Chord length distributions from spheres

Consider a single sphere of radius $R = D/2$ which is intersected by a random line a number of times figure 3.10. The intersection of the probe line T_1 with the sphere results in a chord of length l_i contained within the sphere, where

$$l_i = 2\sqrt{R^2 - d_i^2} \qquad 3.23$$

and d_i is the distance between the chord and the centre of the sphere. All chords lying on a cylindrical radius of d_i around the spheres centre will have the same length l_i, and further more all chords lying within this cylinder will have a length $d_i \le l_i \le 2R$.

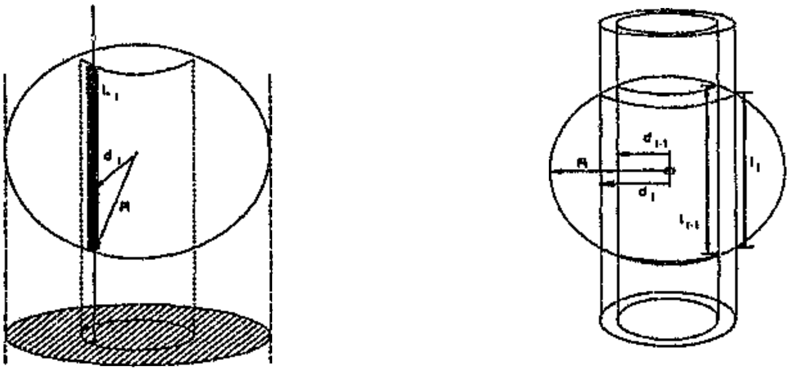

(a)

(b)

Figure 3.10. (a) The intersection of a sphere of radius R by a linear probe line resulting in a chord of length l_i. (b) Cylinder of radius d_i within which all intercepts l_i will have a length $d_i \le l_i \le 2R$.

The probability of a random line hitting the sphere is proportional to its projection area πR^2, and the probability that this line falls within the cylinder of radius d_i is πd_i^2. Thus the probability of an intercept of $l \ge l_i$ is

$$Pr\{l \ge l_i\} = \frac{\pi d_i^2}{\pi R^2} = \frac{D^2 - l_i^2}{D^2} \qquad 3.24$$

Similarly for $l \ge l_{i-1}$

$$Pr\{l \ge l_{i-1}\} = \frac{D^2 - l_{i-1}^2}{D^2} \qquad 3.25$$

Now subtracting [3.25] from [3.24] gives

$$Pr\{l\} = Pr\{l_{i-1} < l < l_i\} = Pr\{l \ge l_i\} - Pr\{l \ge l_{i-1}\}$$

$$= \frac{l_i^2 - l_{i-1}^2}{D^2} \qquad 3.26$$

If we let $\Delta l_i \to dl$ then

$$Pr(l)dl = 2dl \frac{l}{D^2} - \frac{(dl)^2}{D^2} \qquad 3.27$$

and if we let $dl \to 0$ then we get the probability density function of the intercept length through a sphere

$$f(l \mid D) = \begin{Bmatrix} \frac{2}{D^2} l & for \quad l \leq D \\ 0 & for \quad l > D \end{Bmatrix} \tag{3.28}$$

which shows that for a sphere $f(l \mid D)$ is linearly proportional to l. Thus each class size of sphere of size D yields a triangular distribution with a maximum at D. See figure 3.11. The same result can be obtained by considering a probe line intersecting a population of spheres of the same size dispersed randomly and uniformly.

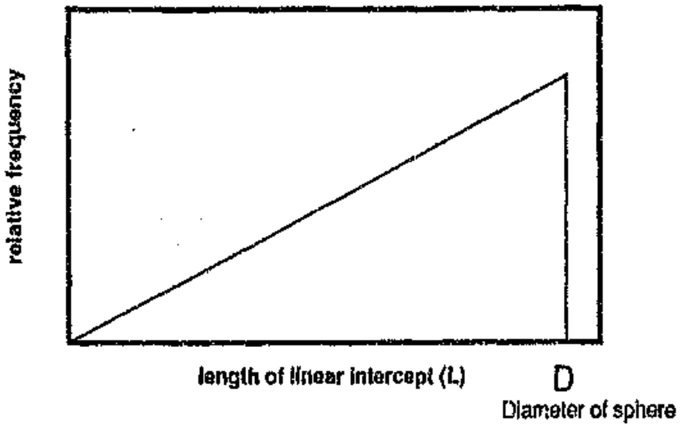

Figure 3.11 : Probability density function for intercepts lengths through a sphere of diameter D.

Consider now a population of spheres with varying diameter D and where a linear-intercept probe traverses the space containing these spheres as shown in fig 3.12. The resulting chord-length distribution depends on (a) the probability of intersecting the sphere which is proportional to its projected area, and (b) the position of the intercept relative to the sphere centre.

As a particular example consider four classes of spheres, uniformly distributed in space with numerical class densities $N_{V1}, N_{V2} N_{V3}, N_{V4}$. The resulting chord distributions will be the sum of the contributions of each class [3.29], shown graphically in fig. 3.12(b) where $N_{Li}(l) \approx \frac{2}{D^2} l_i$ to give

$$N_L(l) = \sum_{i=1}^{4} N_{Li}(l) \tag{3.29}$$

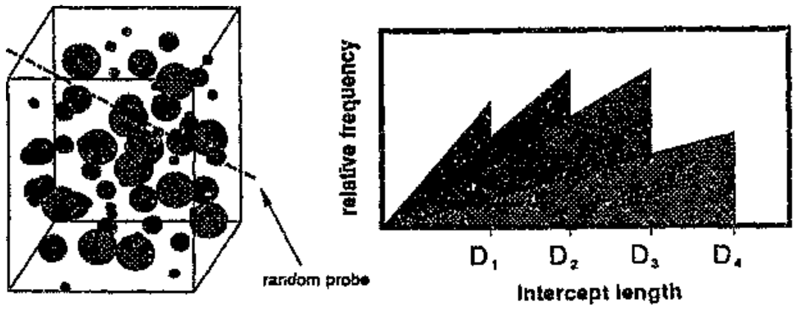

(a) (b)

Figure 3.12 : (a) Intersection of a polydispersed system of spheres with a random probe line. (b) Hypothetical chord-length distribution resulting from the linear intersections occuring in (a).

The deconvolution of the intercept distributions to the size distributions can be done either graphically or analytically, (Underwood, 1970). We will now derive the Cahn-Fullman (1956) integral equation which relates the distribution of chord lengths to the size distribution of a polydispersed system of spherical particles. The following derivation of this relationship is based on a methodology developed by (King, 1978).

In order to obtain a linear intercept of in the range l, dl the following events A,B and C must occur.

(i) A the sphere in the diameter range $D, D + dD$ must be present,

(ii) B the test line must intersect the sphere, and

(iii) C the length of the intersection must be in the range l, dl.

The following conditional probabilities are known :

$Pr\{C \mid B, A\} = \frac{2l \cdot dl}{D^2}$ if event B occurs or

$Pr\{C \mid B, A\} = 0$ if B does not occur and $l > D$

$Pr\{B \mid A\} = \frac{\pi D^2}{4D_{max}^2}$,

And $Pr\{A\} = f(D)dD$, where $f(D)$ is the particle size-density function. The number of chords in the size range l, dl is $p(l)dl = Pr\{C\}$. Now

$$Prob\{C\, B\, A\} = Prob\{C \mid B\, A\} Prob\{B \mid A\} Prob\{A\} \qquad 3.30$$

and

$$p(l)dl = Pr\{C\} = \int_A \int_B Pr\{C\, B\, A\} dB dA \qquad 3.31$$

Combining equation. [3.30] and equation. [3.31] and taking into account all possible outcomes as listed above, ie only intercepts which hit a sphere are of consequence (event ***B***) gives

$$p(l)dl = Prob\{C\} = \int_{l}^{D_{max}} \frac{2ldl}{D^2} \cdot \frac{\pi D^2}{4D_{max}^2} \cdot f(D)dD$$

$$\Rightarrow \qquad p(l) = \frac{\pi}{2}\frac{l}{D_m^2}\int_{l}^{D_m} f(D)dD \qquad 3.32$$

Again the objective of the last stage of particle size problem Ψ_c is to solve for $f(D)$ given $p(l)$, ie inverting equation [3.32].

3.4.4 Lineal analysis of spheres and IUR probes

In the above two sections 3.4.2 and 3.4.3 relationships were developed between areal (lineal) distributions, and the volume distribution of spheres. The rockstream will be sampled by capturing a 2-D image which is projected onto the plane, essentially providing a areal section $T_2 \cap X_\Omega$. It will be shown in chapter 4 that accurate areal calculations are costly and difficult to achieve with low error and minimal computing. There is thus reason to use *linear* intercepts despite the fact that unfolding methods based on random secants are according to Cruze-Orive (1982) inferior to ones based on diameters or areas. Although it is also difficult in practice to arrange for a linear intercept through a 3-D body, a two stage sampling process is a viable and practical method of making measurement on the rockstream Ω.

An important question is thus whether an intercept length distribution measured on random section profiles has the same probability density function as that of intercepts generated by random test line in space. King (1978) provides a proof showing that random sectioning followed by random chord testing does provide the same data as random chord testing through a sphere. Weibel (1982) also states that the above is true provided, (1) the spheres are sampled with the section plane in proportion to their diameters, and (2) the population of samples is sampled with a test line in proportion to the profile diameter as is shown on the LHS of equation. [3.29]. These two conditions are naturally satisfied if *isotropic uniform random* (IUR) sampling of both the structure and the section is performed.

$$L((X_3 \cap T_2) \cap T_1) = L(X_3 \cap T_1) \qquad 3.29$$

An *IUR test probe* is a probe in space where all *orientations and positions are equally* likely which is difficult to achieve in practice (Weibel, 1979, 1980).

3.5 DERIVING THE SIZE DISTRIBUTIONS OF RANDOMLY SHAPED PARTICLES

3.5.1 Introduction

In section 3.4 mathematically exact formulae were derived linking areal or linear intercept distributions to the size distribution of spheres. The derivation of these analytical relationships depends upon certain assumptions, the most important being (a) the ability to sample all the particles unambiguously and without bias which implies no overlapping and a sparse distribution of uniformly distributed particles in space, and (b) that the particles are spherical in shape. Unfortunately the determination of similar mathematically-exact formulae linking the size distribution of *non-spherical* particles which are not assumed to be arranged in space in a certain manner, to populations of measurements on random sections or traces, is a complicated problem if not almost impossible, (Weibel, 1980: chapter 8). However methods have been investigated for the estimation of particle sizes of regular shaped particles other than spheres such as plates or rods (Fullman, 1953), elliptical bodies (Tallis, 1970).

To overcome the difficulties in deriving relationships for arbitrary shaped particles, the formulae derived in section 3.4 for spheres are sometimes applied to arbitrarily shaped particles, especially if one can use "volume equivalent" measures for non-spherical particles. The errors resulting from the application of spherical formulae to no-spherical particles may become predictable depending on the deviation of the particles' shape from a sphere. Weibel (1980) states that for high order polyhedrons, errors resulting from applying formulae derived for simply shaped particles to irregular shaped particles are small, but for cubes and cylinders these errors become much larger. Thus when applying spherical solutions to irregular shaped objects it may be necessary to use parameters such as shape factors (Allen, 1981) in order to compensate for particles irregularity (Naumovich et al, 1982). However in general it has been found that for very irregular shaped particles such methodologies do not work very well. For example, in a related problem of estimating number densities N_V, DeHoff and Rhines (1961) comment that very large errors occur if elongated or flattened particles are treated as spheres. More complex shape modelling can reduce these errors, for example modelling particle shape with shapes such as tetrkaidecahedrons and dodecahedrons give better results for grain modelling and size distribution estimation because they approximate real particles better than spheres (Bodyako and Naumovich, 1980).

It can thus be surmised that ideally we would prefer to have a relationship between rocksize distribution and parameter distributions measured from images that are free from any of the gross assumptions required to minimise the complex and usually intractable mathematics arising from handling complex particle shapes. The next sub-section presents a well known analytical solution for handling irregularly shaped particles, that tends to handle some of the complex mathematics in a rather clever manner which precludes the use of unreasonable assumptions concerning particle shape.

3.5.2 King's Method

King (1982) has developed a very useful theory relating the distributions of measured parameters from traces to the mesh (sieve) size distribution of particles free of the limiting assumptions regarding particle size. The only assumption with his model is that *particle shape is invariant with particle size*. No other shape limitations are necessary. In this subsection an abridged derivation of his result taken from his paper is presented because it provides a useful analytical solution to the estimation of rocksize distribution while at the same time avoiding most of the other assumptions. More importantly it reflects the trade-off between the need to make assumptions to simplify the mathematics, against realistic and useful stereological relationships.

Let the measurement on a profile returned by a probe be M where M is for example cross-sectional area, or chord lengths which are random variables. The probability of obtaining a measurement M depends on the following events, (i) A a particle in the size range $D, D+dD$ is present. (ii) B the sampling plane or line hits the particle, and (iii) C the resultant measurement falls in the range $M, M+dM$. It is assumed that conditional probability densities $p(M \mid$ [illegible]$)$ as well as conditional means exist. This allows one to use equation [3.26].

Given the above events and the probability equation as derived in [3.6] we obtain the fundamental equation relating the probability density of the observed parameter M to sieve size D, which is given by

$$p(M \mid T \uparrow X) = \frac{\int_0^\infty p(M \mid T \uparrow X, D) Pr\{T \uparrow X \mid D\} p(D) dD}{\int_0^\infty Pr\{T \uparrow X \mid D\} p(D) dD} \tag{3.34}$$

see King (1982). The objective is to calculate $p(D)$ which is size-density function for mesh size D. Using geometric probability (Santalo, 1976, Kendall and Moran, 1963) $Pr\{T \uparrow X \mid D\}$ can be calculated to give $\overline{S}_D$, $\overline{K}_D$ and 1, for an IUR line probe, IUR plane probe, and projected area probe respectively. Defining the ν'th moment of the measured variable M as

$$\mu_\nu = \int_0^\infty M^\nu p(M) dM \tag{3.35}$$

and combining the above results of equations [3.34] and [3.35] together with the results that $Pr\{T \uparrow X \mid D\} = 1$ for a projected area probe gives

$$p(M) = \frac{\mu_v \int_0^{\infty} p(M \mid D) p(D) dD}{\int_0^{\infty} \overline{M_D^v} p(D) dD} \qquad 3.36$$

where $\overline{M_D^v}$ is defined as $\overline{M_D^v} = \int_0^{\infty} M^v p(M \mid D) dD$. $p(D)$ which is a number distribution is converted to a volume distribution with the following

$$f(D) = \frac{\overline{V}_D p(D)}{\int_0^{\infty} \overline{V}_D p(D) dD} \qquad 3.37$$

Combining equation. [3.36] and [3.37] and assuming that $\overline{M_D^v}/\overline{V}_D$ is invariant with D then gives

$$p(M) = \mu_v \int_0^{\infty} p(M \mid D) \frac{f(D)}{\overline{M_D^v}} dD \qquad 3.38$$

which is the basic convolution equation relating projected area profiles with the size distribution of not necessarily spherical particles. Note the similarity between the functional form of equations [3.38], [3.32] and [3.21].

In particular equation [3.38] can be derived to reflect the relationship between sectional areas and particle size (King, 1984) which is

$$p(A) = \overline{A} \int_{A}^{\infty\,1/2} p(A \mid D) \frac{f(D)}{\overline{A}_D} dD \qquad 3.39$$

and for measurements of random chord length (King, 1984) is

$$p(L) = \overline{L} \int_{kL}^{\infty} p(L \mid D) \frac{f(D)}{\overline{L}_D} dD \qquad 3.40$$

The solving of the above equations [3.38-40] for $f(D)$ requires the evaluation of $p(M \mid D)$, μ_v and $\overline{M_D^v}$ which must be measured experimentally or calculated. Because $\overline{M_D^v}$ and $p(M \mid D)$ both require shape dependent information even King's method is not totally free from the effects of shape. Note that no alternative analytical relationships could be found in the literature which relates profiles measured from sections to size distribution, where the shape of the particles can be totally disregarded.

In the next section discusses the significance and evaluation of $p(M \mid D)$ so that the above formulae can be applied.

3.6 PARTICLE INTERCEPT DISTRIBUTIONS

As mentioned in section 3.5, equations [3.38], [3.21], [3.32] all have a common conditional-probability distribution $\phi(r \mid R)$ or $p(M \mid D)$ which relates the probability density function of measurements to a particle of size D. These conditional probability density functions are totally dependent on the shape of the particle, and it is errors associated with these functions together with experimental errors in the determination of $p(M)$ (chapter 7), which cause the ambiguities and problems associated with the estimation of $f(D)$, (King, 1982, 1984), and (Naumovich and Warren, 1978).

Different populations of *homothetic* particles have different functional forms for $p(M \mid D)$. Homothetic particles have the same single regular shape and which only differ by a scale factor as the size changes (Serra, 1982). For example, the areal intercept distribution for spheres is exponentially shaped, and the linear intercept distribution for spheres is linear irrespective of size, section 3.4.1 and 3.4.2. These are however ideal cases, because the shape and size distributions of the irregular particles as found on the conveyor belt are complex and can change with time thus changing $p(M \mid D)$.

King (1984) comments that the key to the successful application of the deconvolution equations for the estimation of size distribution is a satisfactory knowledge of $p(M \mid D)$ which can be determined by a number of methods. The first is to screen (sieve) the particles with meshes that are closely spaced and then to measure random intercept distributions from these monosized samples, essentially a calibration procedure. King states that "the preparation of a monosized calibration sample is inconvenient and may be impossible". In addition he states that the particles being examined must be separated from one another which is laborious. The difficulty of this calibration is accentuated when one considers the practicalities of handling and accurately sieving the *large* rocks as found on conveyor belts. An alternative method is to perform Monte Carlo simulations on a computer where particles of known shape are generated and intersected by random test probes or sections, (Warren, 1985), (Naumovich and Kriskovets, 1982), (Paul, 1980), (Naumovich and Warren, 1978), (Warren and Naumovich, 1977). The simulation of irregularly shaped particles is not really feasible because modelling randomly shaped rocks which nevertheless fall into certain shape groups is very difficult.

In the next two subsections several areal and linear intercept distributions for particles of known shape as well as particles of irregular shape as found on the conveyor belts feeding material to the mines, will be presented. The purpose is to show the functional complexity of the intercept distributions $p(M \mid D)$ of conveyor-belt rocks.

3.6.1 Linear intercept distributions of Particles of known shape

Consider figure 3.13 in which areal-intercept distributions $p(A \mid D)$ of various particles of different shape are shown, (after Paul, 1980). In figure 3.14 are shown the chord-length distributions $p(L \mid D)$ for polydispersed systems of deformed cubes (Naumovich and Kriskovets, 1982), and in figure 3.15, ellipsoids, cubes, and a prism (Naumovich and Warren, 1978).

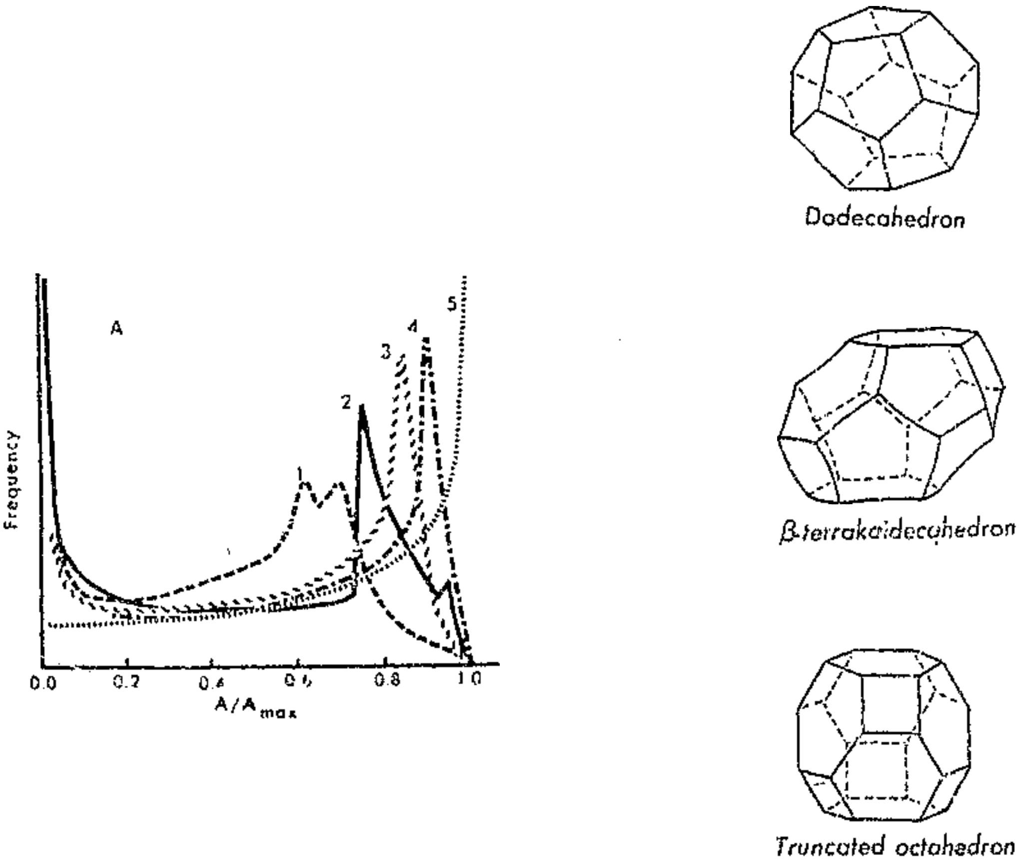

Figure 3.13. Areal intercept distributions of various particles after Paul (1981). These particles are (1) β-tetrakaidecadron, (2) cube, (3) truncated octahedron, (4) dodecahedron, and (5) sphere.

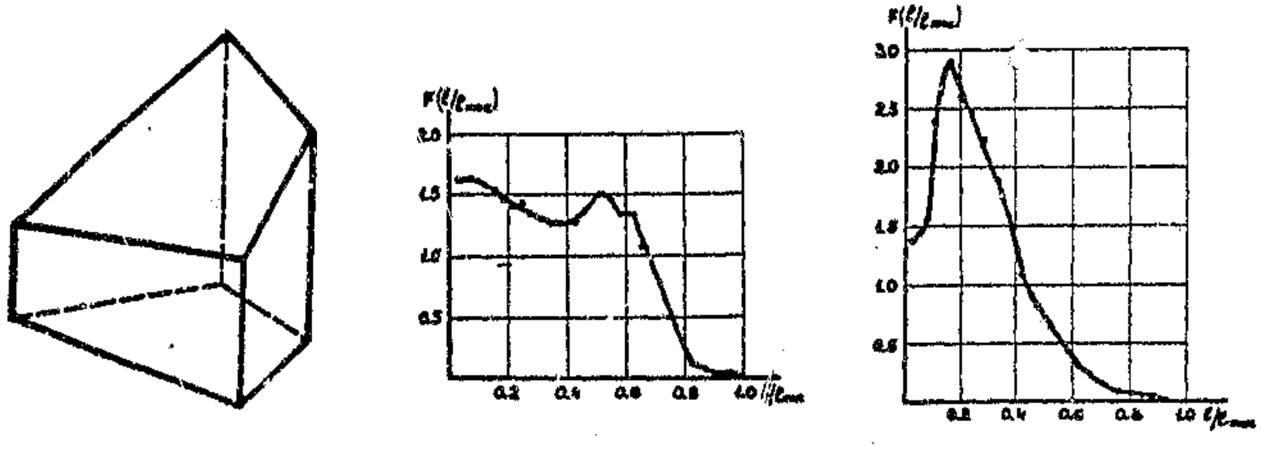

(a) (b) (c)

Figure 3.14. Linear intercept distributions $F(l/l_{max})$ of a deformed cube with different face turn angles α after Naumovich and Kriskovets (1982) (a) Deformed cube with $\alpha = 15°$. (b) $F(l/l_{max})$ for $\alpha = 15°$. (c) $F(l/l_{max})$ for $\alpha = 30°$.

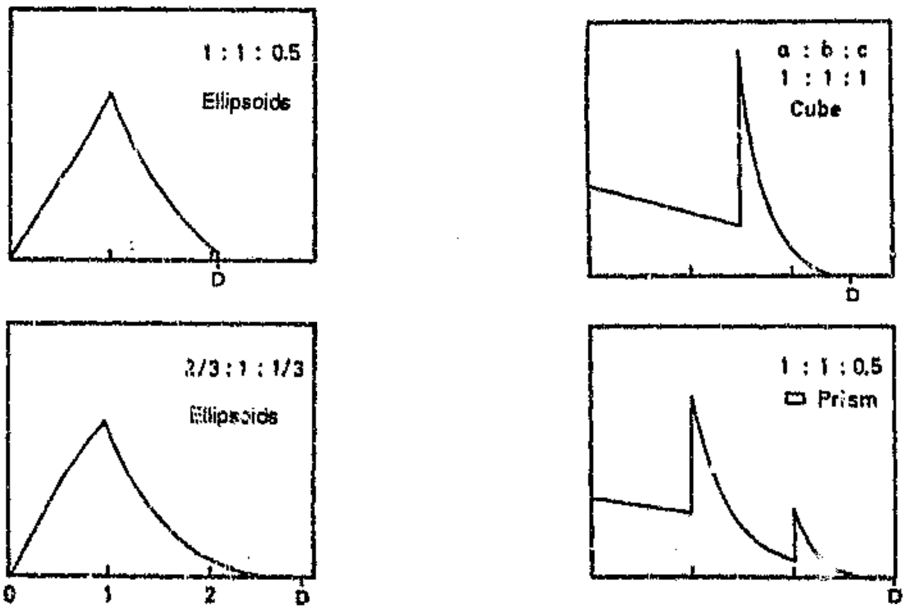

Figure 3.15. Linear intercept distributions of ellipsoids, cube and prism after Nuamovich and Warren (1978). The axes ratios for the ellipsoids are given for each distribution.

The following observation can be made with regard to the shape of the distributions and the particles shape. For both linear and area distributions, rounded particles without any sharp corners or edges, eg spheres, produce a peak near the maximum diameter of the particle which tails off towards the shorter lengths. As the particles become more angular, the number of short chords and small areas intercepts measured becomes larger. Particles with a number of (parallel) facets result in peaks in middle of the distribution, which holds for both linear and area intercepts. The reader is referred to Naumovich et al (1978), Paul (1980), Naumovich (1982), and Warren (1987), for more details concerning the dependence of the functional form of $p(M \mid D)$ on particle shape.

The rocks as found on the conveyor belt reflect *all* the above rock-shape characteristics. It is thus predicted that the chord distributions for these rocks should be complex. However as will be shown in sub section 3.6.2 the large variation of the rock shapes and hence linear-intercept distribution tend to average out to a relatively simple functional shape, given a large enough number of intercept length samples.

Because the chord or areal distributions for a single size class of particles tend to spread themselves out from the origin to some maximum value which is related to the maximum diameter and/or areal section, distributions of data originating from the smaller particles tend to merge with the data of the larger rocks. This is shown in figure 3.16 in which two hypothetical size distribution of two size classes of particles which are *homothetic* are combined. Observations of the resultant distribution in fig. 3.16 show that chords belonging to the smaller particles become "lost' in the smaller chords resulting from the larger particles. It is thus obvious that the *unfolding* process which attempts to separate the populations of the chords contributed by each particle size class according to their number of mass, is inherently ambiguous.

From the problem shown in figure 3.16 with regard to the smaller chord lengths, it is concluded that the recognition and unfolding of the smaller-sized particles could be a major problem, especially where the function form of $p(L \mid D)$ is irregular or unknown. In chapter 7 it is shown that resolving the smaller sized particles is a significant problem as predicted here, and that resolving smaller sizes of run-of-mine rock material is exacerbated because the functional form of the *measured* linear-intercepts is distorted by image processing and segmentation errors.

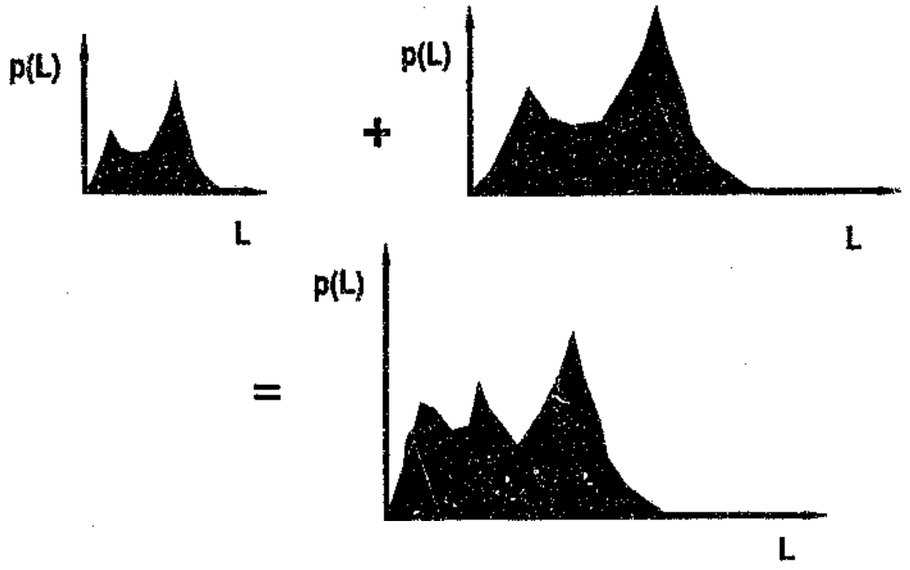

Figure 3.16. A hypothetical resultant chord length distribution of two classes of deformed cubes, where the one class is twice the size of the other and that there are equal quantities of particles in each class.

3.6.2 Linear intercept distributions of Arbitrary Shaped Particles.

In this subsection we present linear-intercept distributions $p(L)$ which can be assumed to be the chord-length density distributions $p(L \mid D)$ of irregularly shaped particles in a given narrow size range. Chapter 6 provides a full description of the experimental rigs and procedures employed to derive these results.

The rock samples used for deriving $p(L \mid D)$ consist of dry quartzite taken off a feed belt to an autogenous mill in a gold plant. The rock was classified into size classes by hand sieving. The chord-length distributions were measured from scenes of rocks "randomly" laid out by hand on a dark surface which contrasts with the lighter colour of the rocks. The rocks were laid out so that they did not *touch* each other allowing for global thresholding to be used for unambiguous and fast rock identification and segmentation. The static[3.3] image of the rock scene of non-touching rocks was captured and transferred to a frame-grabber and globally threshold (chapter 4) to give a binary representation of each rock against the background. Adjacent chord-lengths were then measured in a direction parallel to the image horizontal axis. This process was repeated for a number of image

---

[3.3] Static as opposed to dynamic or moving images as found on moving conveyor belts.

scenes (20-40) where for each scene new rocks are introduced and jumbled around to random orientations with the only unnatural interference being the separation of touching rocks by hand. After the ensemble of the chord distributions per size groups was measured, they were averaged to produce an average distribution

The ideal IUR linear sampling probe to perform the above chord-length measurements should be selected by randomly chosing a point in the image plane, and then constructing a line through this point with an angle which is also randomly chosen. The probability of both the co-ordinates of the point chosen as well as the angle of the probe line must be uniformly distributed, ie must be equally likely, otherwise a bias will manifest itself in the distribution. Care was thus taken to orientate the rocks as "randomly" as possible, with all possible orientations of rocks occurring with equal probability which should emulate the IUR linear probe. However this procedure does not rule out any possibility of bias. For example, all the rocks rest in their most stable positions thus presenting their largest surface projection to the viewer or camera, thus biasing the populations of projected areas and chord-lengths to larger values.

Fig 3.17 shows the chord-length distributions for sized groups of *non-touching* rocks where each rock X_i can be unambiguously identified. Fig. 3.18 shows the linear intercept distributions from the same rocks except they have now been pushed together and are *touching*, ie the trace of each rock X_i has merged with a number of its neighbours. The reason for allowing the rocks to touch is to illustrate the influence of erroneous rock identification on the intercept distributions, which is more realistic as well. These errors manifest themselves as a smearing out of the chord distribution across a broader size spectrum, which can be considered to be analogous to the sampling effect in the Fourier domain where impulses are smeared out due to sampling and windowing effects. In other words combining a number of particles of different size into a conglomeration can be likened convolving the size distribution of rocks $f(D)$ with the impulse response of the each size class effectively $p(M \mid D)$ which has an overlapping effect in the size domain.

Examination of figures 3.17 - 3.18 shows that the basic functional form of the unit distributions $p(L \mid D)$ does change a little with small changes in rocksize. The ratio of the centre peak to the "width" of the distribution changes with rocksize which can cause problems in stereological models where $p(L \mid D)$ is assumed to remain constant with rocksize.

Figure 3.19 also shows how the mixing of two different sized group of rocks creates a mixed chord-length distribution, which is difficult to reconcile unambiguously back to the original and separate chord-length distributions.

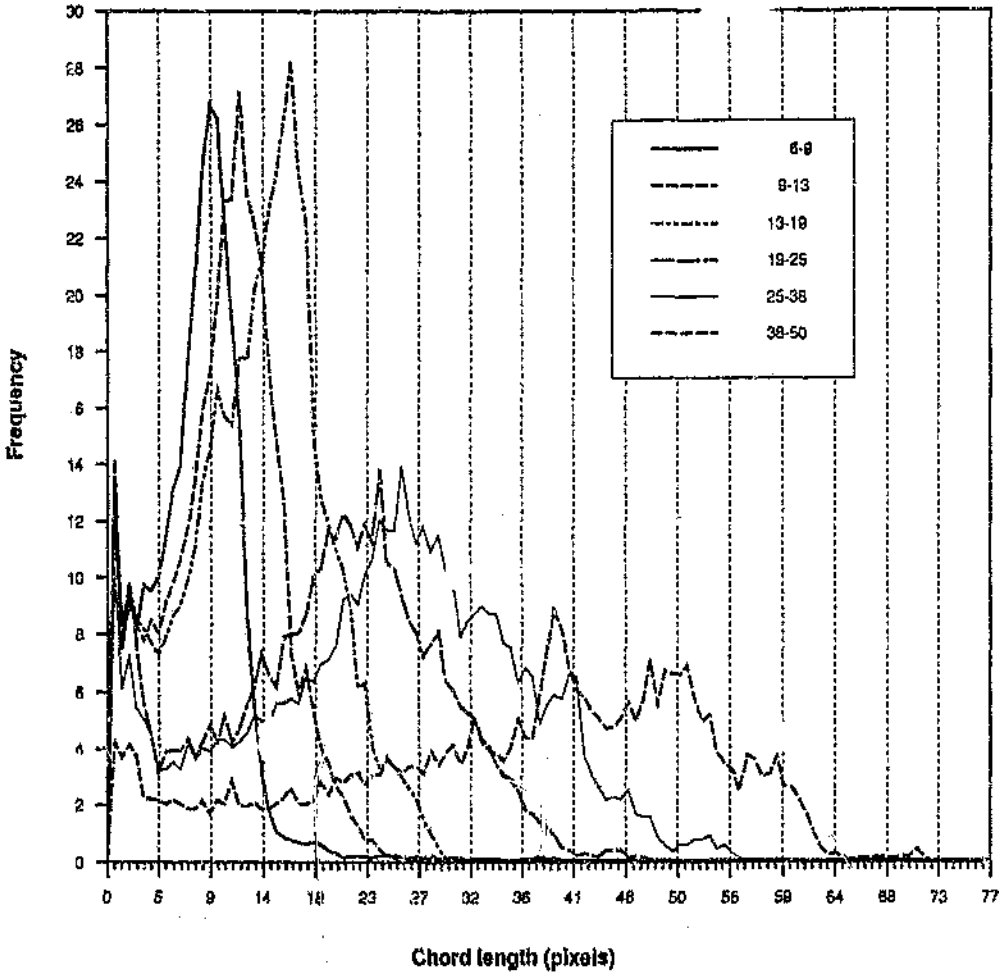

Figure 3.17. Linear intercept distributions of irregular shaped particles that have been separated. Each distribution is an average of between 20-40 distributions measured. (Note 1 pixel = 1mm in the *x* direction, ie across the belt.)

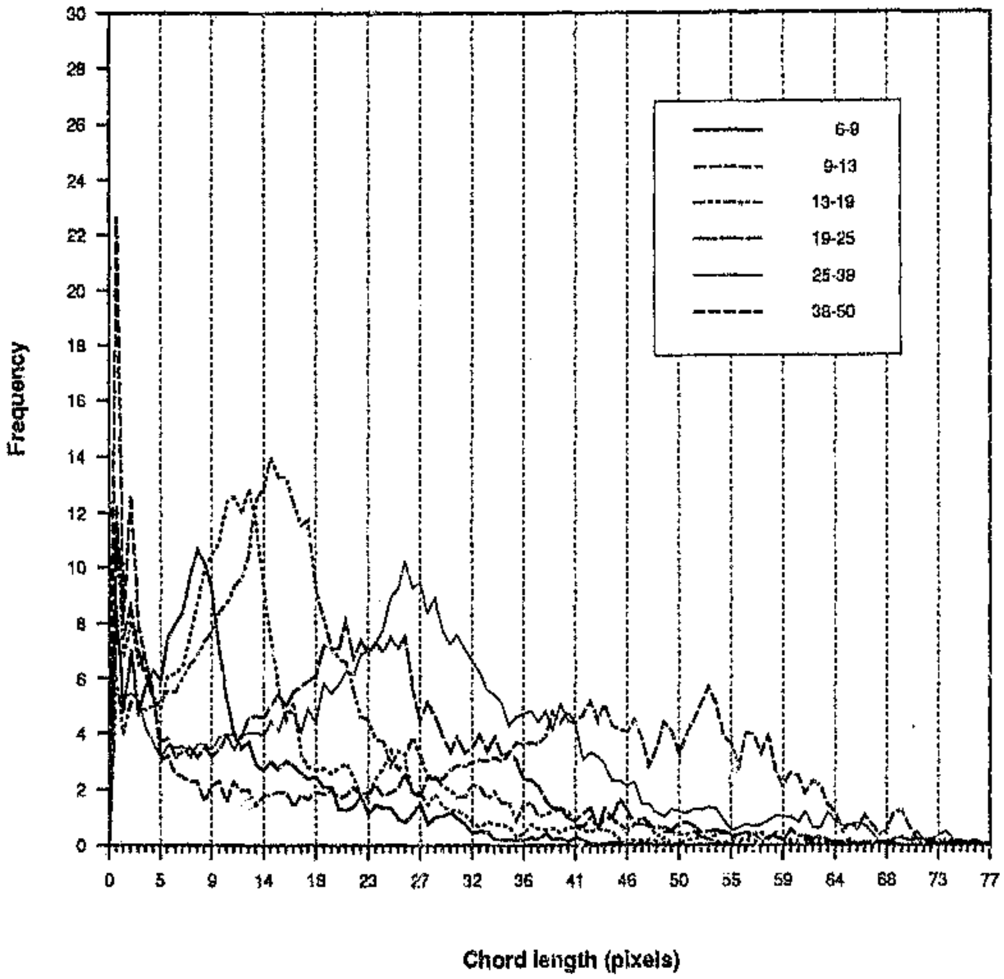

Figure 3.18. Linear intercept distributions of the same irregular shaped particles except they have been left touching. Each distribution is an average of between 20-40 distributions measured. (Note 1 pixel ≈ 1mm in the *x* direction, ie across the belt.)

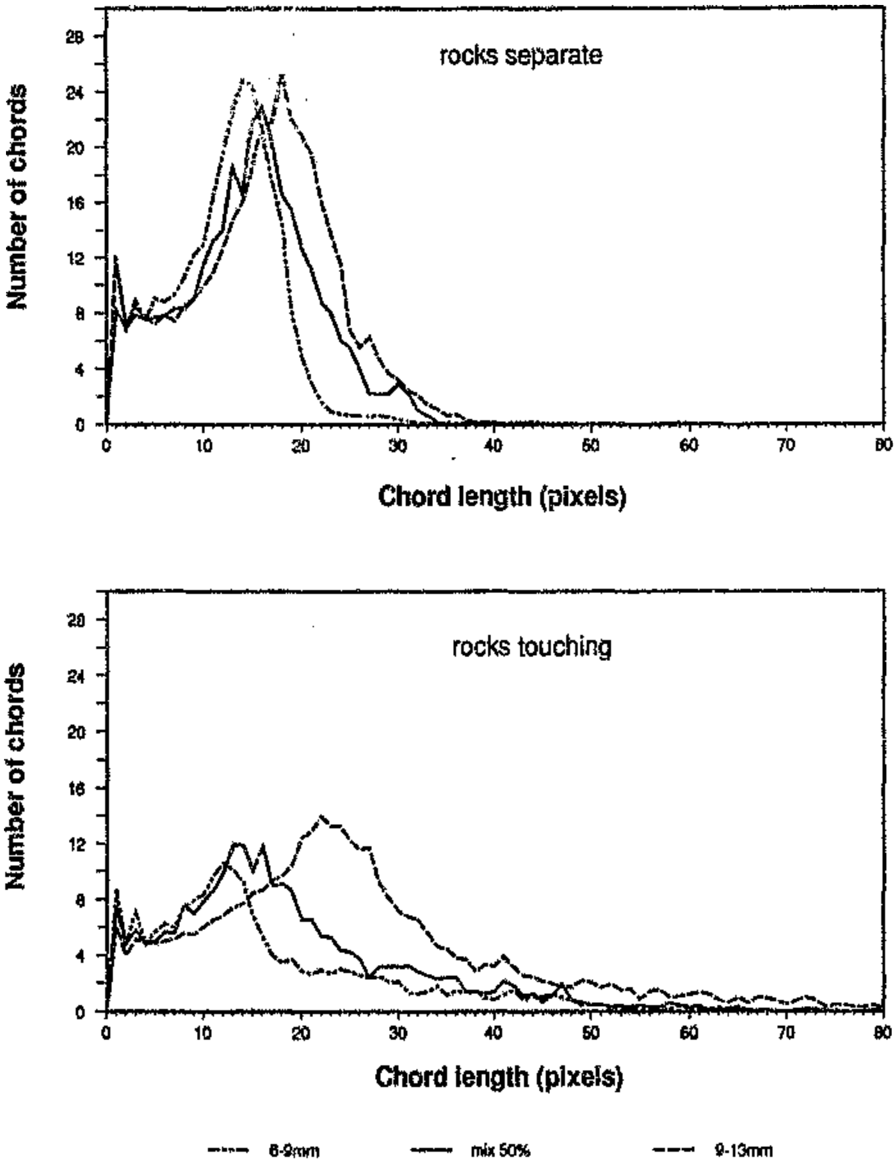

Figure 3.19. Linear intercept distributions resulting from the mixing of equal portions of rock of size 6-9m and 9-13mm, for non-touching and touching situations.

3.7 DERIVING AN ANALYTICAL MODEL FOR THE ROCKSTREAM

3.7.1 Introduction

In section 3.3.3 a stereological model (equation [3.6]) based on geometric probability theory was derived which relates the distribution of parameters measured on section profiles to size distributions. In section 3.4 and 3.5 this model is reduced to analytical expressions for *spherical*, and *irregular shaped* particles. All these models assume some form of ideal world, far removed from the situation on the conveyor belt. Significant assumptions are that the particles are uniformly and randomly dispersed throughout the volume. In addition it is also assumed that the particles are sparsely distributed so that there is no overlapping, and the probes used, planes T_2 or lines T_1, are IUR probes and infinitesimally thin.

Although these assumptions render these models unsuitable for the conveyor belt rockstreams, they serve a critical purpose in that they prove that *lower-dimensional measurements can be used explicitly to estimate higher-dimensional properties, subject to certain assumptions or limitations.*

However the use of the spherical or King's model (equations [3.22] [3.32] and [3.40]) are restricted because a vital component of these expressions is the unit conditional distribution $p(M \mid D)$ is difficult to derive. In addition experimental data is presented (section 3.6) which shows that the functional shape of $p(M \mid D)$ for conveyor belt rocks is very different for *separated* or *touching* rocks, and as will be shown in chapters 4 and 5, very prone to error because of rock identification problems in the images. It is also shown (section 3.6) that unfolding and resolving the *lower* sized particles is a difficult problem because of the functional shape of $p(L \mid D)$.

These points raise some fundamental questions, which in a way form part of the research objective.

1) Can the stereological problem for rocks on a conveyor belt be solved for the totally general case of arbitrary conglomerates of irregular shaped particles ?

2) Are models needed for estimating size distribution ?

Considering the complex mathematics, and the assumptions made, is it not more prudent to disregard a rigorous analytical or statistical description of these stereological mapping, and rather formulate empirical models through experimentation that fulfil the application requirement ? In particular can simple models such as those derived from spheres be used ?

DeHoff (1982) comments that the use of the spherical model as an ***approximation*** to the real structure is open to serious question in the absence of independent procedures for assessing the spherical models. Thus a more realistic model or closed analytical solution to the rocksize problem based on much fewer assumptions is required.

In addition, because no stereological model has been found in the literature which relates $f(D)$ to $p(L)$ without any assumptions, and in an attempt to answer the above questions, this section formalizes the events and requirements for a complete and totally realistic stereological model which links chord-length distributions $p(L)$ measured from processed images of ***conveyor-belt*** rockscenes, to rocksize distribution $f(D)$.

3.7.2 Modelling the measurement process

The model, whose function is to link the measurement of a chord length in the range $L, L+dL$ to a rock of size $D, D+dD$, is based on a probabilistic approach and methodology borrowed from King (1978). Conceptually the model can be broken down into two parts. The first is the link between the image I and the rockstream Ω, where the image is considered to be the result of projecting the top of the rockstream Ω_{top} onto a plane T_2. The second part of the model is the linking of measurements from the linear-intercept probes T_1 to the projections in projected plane image. Thus in terms of set theory, a chord-length measured by the probe is given by

$$L = L[(\Omega_{f(D)} \cap T_2) \cap T_1] \qquad 3.41$$

where the rockstream Ω is a function of the size distribution $f(D)$ of the rocks X and L is the measurement function. The measurement L can only take place once certain events have taken place. For example the linear probe T_1 can only intersect a areal projection of a rock X_2 if and only if X_2 is hit by the probe, ie $T_1 \uparrow X_2$.

To model the rocksize problem is to reduce equation 3.41 to a function of $f(D)$, which has to be derived in terms of *probability theory* because only the *probability* of a rock of size D being detected and measured can be estimated. As given in chapter 2, the measurement of the size distribution of the rockstream passing a point is considered a *stochastic process* where it is assumed that the statistics of the rockstream can be determined.

In order for a chord length measurement to occur, the following events must take place.

A. A rock in the size range $D, D+dD$ must be present in the population of rocks in Ω.

B. The test plane T_2 must intersect the rocks, or the rocks must be projected onto the test plane.

C. The resultant areal section of a rock in the test plane must have a "diameter" in the size range $D_c, D_c + dD_c$.

E. A test line must intersect this rock's section.

F. The intercept length must fall in the size range $L, L + dL$.

These series of events are similar to the those presented by King (1978), (1982). However there are differences to some of these events which result in the unique problem in this research[3.4].

Given all the above events it could be possible to calculate the probability of a chord of length L being measured given that rock of size D is present. However as mentioned in chapter 3 every point on the chord length distribution has some probability function associated with it, and similarly for the rocksize distribution. Thus the continuous rock-size distribution $f(D)$ and chord-length distribution $p(L)$ each have an infinite set of probability distributions which are related in some way. This modelling exercise attempts to relate only *one* chord length to *one* rocksize through probability theory, which then should be extendible to more points in the size distribution.

Splitting the probability of events into dependent probabilities

The final objective to this model is to fit all the above events together to derive the probability of measuring a chord-length in the range $L, L + dL$ ie $Pr\{\mathbf{F}\}$ which is given by

$$p(L)dL = Pr\{\mathbf{F}\} = Pr\{L < \text{ chord length measured } < L + dL\} \qquad 3.42$$

The probability of measuring a chord-length in the range $L, L + dL$ is *dependent* on the other events **A**,**B**,**C** and **E** occurring. So that summing over all the probabilities of **A**,**B**,**C**, and **E** gives

$$Pr\{\mathbf{F}\} = \int_{\mathbf{E}} \int_{\mathbf{C}} \int_{\mathbf{B}} \int_{\mathbf{A}} Pr\{\mathbf{FECBA}\}\ d\mathbf{A}d\mathbf{B}d\mathbf{C}d\mathbf{E} \qquad 3.43$$

Now

$$Pr\{\mathbf{FECBA}\} = Pr\{\mathbf{F} \mid \mathbf{ECBA}\}\, Pr\{\mathbf{E} \mid \mathbf{CBA}\}\, Pr\{\mathbf{C} \mid \mathbf{BA}\}\, Pr\{\mathbf{B} \mid \mathbf{A}\}\, Pr\{\mathbf{A}\} \qquad 3.44$$

where

$Pr\{\mathbf{A}\} = f(D)dD$ is the size distribution.

[3.4] In order not to confuse, D has not been used to label an event, because D represents rocksize (sieve size).

$Pr\{B\,|\,A\}=$ is the probability that the rock in size range $D,D+dD$ is intersected by thick section T_2 or projection onto the plane T_2.

$Pr\{C\,|\,BA\}=$ is the probability that the size of areal projection of the rock in size range $D,D+dD$ is D_c,D_c+dD_c.

$Pr\{E\,|\,CBA\}=$ is the probability that test line T_1intersects the areal projection given that all the above events take place.

$Pr\{F\,|\,ECBA\}=$ is the probability that the test line measures a chord in the size range $L,L+dL$ given all the above events take place.

The final model relating chord length to the size distribution is given by

$$p(L)dL=Pr\{\mathrm{F}\}$$

$$=\int_{\mathrm{F}}\int_{\mathrm{C}}\int_{\mathrm{B}}\int_{\mathrm{A}}Pr\{\mathrm{F}\,|\,\mathrm{ECBA}\}\,Pr\{\mathrm{E}\,|\,\mathrm{CBA}\}\,Pr\{\mathrm{C}\,|\,\mathrm{BA}\}\,Pr\{\mathrm{B}\,|\,\mathrm{A}\}\,Pr\{\mathrm{A}\}\,d\mathrm{A}\,d\mathrm{B}\,d\mathrm{C}\,d\mathrm{E} \qquad 3.45$$

The final step is to substitute expressions for all the conditional probability distributions in equation [3.45], and then to evaluate equation [3.45] for all the possible outcomes of events A,B,C and E.

Deriving explicit expressions for the conditional distributions in [3.45] is non-trivial task and is discussed in the next subsections.

Event A : A rock of a certain size exists in the rockstream.

Event A that a rock in the size range $D,D+dD$ must be present, is dependent on the size distribution and time. ie

$$Pr(\mathrm{A})=f(D)dD \qquad 3.46$$

where $f(D)$ is the size distribution density which is random and a function of time too. With $f(D)=f(D,t)$ implies that the *instantaneous* measurement of a size distribution $f(D,t)$ at time t cannot be considered a valid indication of size, but is only one of an infinite number of samples of $f(D)$. It is only the statistics of $f(D,t)$ such as $\bar{f}(D,t)$ or $\sigma_{f(D(t))}$ which are acceptable assuming that the infinite number of probability distributions associated with $f(D)$ can be evaluated in the first place.

Event B : The plane section intersects the rock.

In event B the test plane must intersect the particle of size $D, D+dD$, or in the case of an image captured by a video camera the particle in the size range $D, D+dD$ must be projected onto the plane T_2. This projection plane for the rock stream is peculiar in that it is certain that it will sample *all rocks* on the *surface* of the rockstream irrespective of the height and position of the individual rocks above the conveyor belt. This test plane is thus very different from the test plane as used by other researchers, because the "plane" is a *thick* section of width τ which is dependent on the vertical caliper diameters of all the rocks in the image, as well as their height in the rockstream above the conveyor belt. If for example, only one rock is captured in the image then the section is the height of this rock above the conveyor belt surface, the caliper diameter H of this rock lying in its most stable position in a direction perpendicular to the belt surface, see figure 3.20. If however many rocks are piled on portion of the belt, then the projection has a *levelling* effect which tends to "pull" all rocks in the image into a plane with thickness a function of the vertical caliper diameter H_V and the physical arrangement of the rocks as shown in figure 3.21.

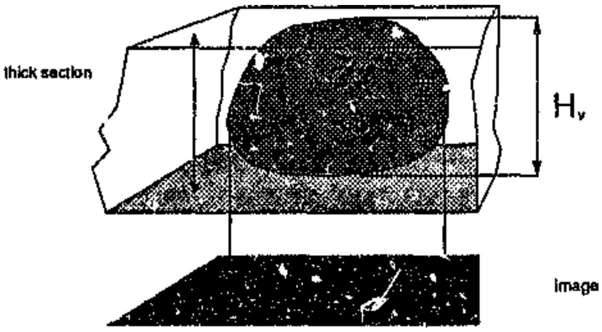

Figure 3.20. A conceptual thick section for a single rock.

Thus the outcome of event B is dependent on the probability of a rock in the size range $D, D+dD$ being present on the *surface* of the rockstream determines, and the position of image frame over the rockstream. If the rocks have their centres uniformly and sparsely distributed over the surface of the conveyor belt, ie a homogeneous distribution, then the probability of rocks of a certain size being observed is 1, assuming the whole surface of Ω is sampled. Note that the definition of homogeneity of the rockstream is open to question because homogeneity must be defined and measured and is a function of the scope of observation (Wiencek and Hougardy, 1985).

However the *distribution of rocks* on the conveyor belt is *neither sparse, nor uniform* and the spatial distribution of the rocks on the surface of Ω is *dependent* on many factors. These factors influence several classification mechanisms which separate the rocks spatially. These factors include rock shape and size D, the

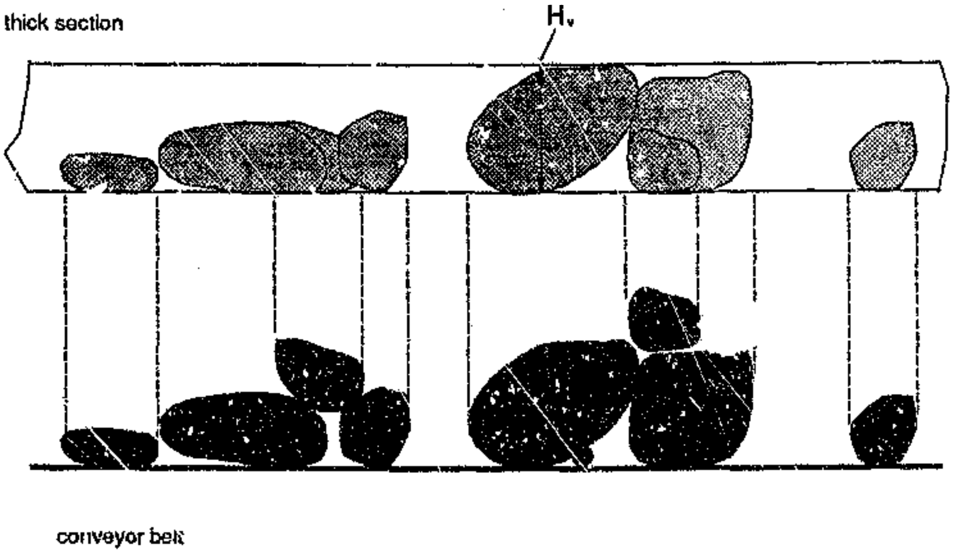

Figure 3.21. A thick section for piled rocks showing how the image tends to sample only surface rocks and pull them into a thick section.

size, shape and speed v_{belt} of the conveyor belt, the mass flow $\dot{m}_{\Omega}$ of the rock from the hoppers onto the conveyor belt, and the geometry and physical arrangement Ξ of the load chutes relative to the conveyor belt. Thus the probability of rocks being cut by the test plane T_ξ or alternatively being seen in the image is given by

$$Pr\{\mathbf{B}\} = 1 \qquad \text{for uniformily distributed rocks}$$

$$\text{or} \qquad Pr\{\mathbf{B}\} = \Theta(D, \Xi, \dot{m}_{\Omega}, v_{belt}, \ldots) \qquad \text{for other distributions} \qquad 3.47$$

where Θ is a function of all the above factors and a number of other factors, for example the viscosity of the slurry covering the rocks.

The loading configuration of the belt is an important factor. Two common loading configurations which influence the distribution of rocks on the conveyor belt are shown in figure 3.22. In 3.22(a) the rocks are loaded from a vertical hopper resulting in the smaller rocks rolling to the sides and the larger rocks being deposited in the middle. In figure 3.22(b) the rocks are loaded from the side, resulting in a classification process due to the rocks inertia and momentum. The larger rocks fall near the chute while the smaller ones fall away. Another important mechanism which influences the arrangement of the rocks on the belt are the belt vibrations which result in a *jigging* effect which causes small rocks to percolate to the bottom of the rockstream. This process is also assisted to a limited extent by the impacts caused by large rocks falling onto the belt from the chute.

In addition to the size and shape of the rocks, other properties such as moisture content, or the amount of slurry which covers the rocks, also plays an important role in determining the spatial arrangement of the rocks. Slime and slurry cause the rocks to stick together or to conglomerate to form what looks like large rocks. The more angular and non-spherical the shape of the rocks, the more interlocking that occurs between neighbouring rocks. A large amount of interlocking implies that the rocks will not re-orientate themselves easily into stable positions, resulting in possibly large voids which can be filled by the fines or smaller rocks.

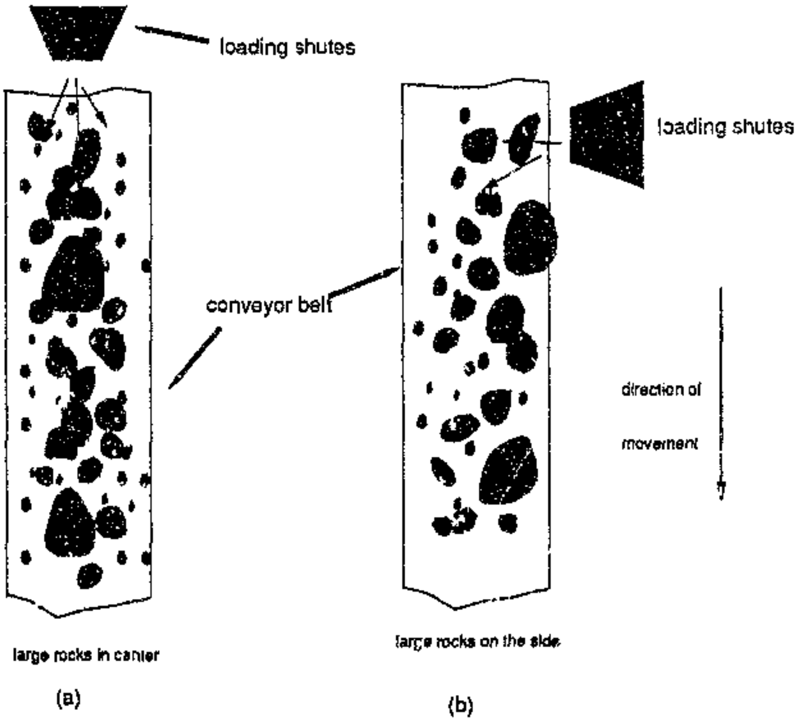

Figure 3.22. Influence of the physical arrangement of a loading chutes relative to the conveyor belt of the spatial distribution of rocks on the conveyor belt. (a) Vertical loading, (b) Side loading.

Thus an expression for $Pr\{B\}$ based on the above factors is difficult to determine, because some factors such as $\dot{m}_\Omega$ are random variables as well and the derivation of analytical expressions for the sorting mechanisms on the belt are beyond the scope of this thesis.

However instead of deriving analytical descriptions for deriving the distribution of rocks on the belt, it can be assumed that the rocks have some deterministic spatial distributions over the belt. For example, observations of the rocks show that the size distribution of rocks can be assumed (i) to vary parabolically with the width y of the belt, (ii) vary linearly with height z, and (iii) be on average constant with the length ie $x = x(t)$ for a fixed $f(D)$. See figure 3.23 and equation [3.27] where Θ' is some function.

$$\begin{aligned} Pr\{B\} &= \Theta'[x_D, y_D, Z_D] \\ &= \frac{D}{D_m}(ay^2+by+c)(a'z+b') \end{aligned} \qquad 3.48$$

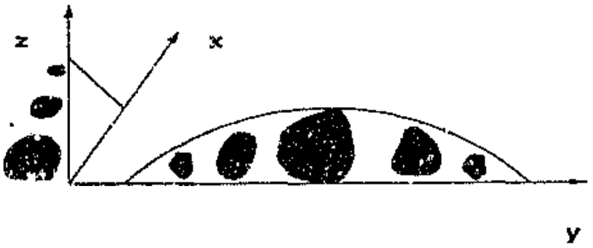

Figure 3.23. Assuming a spatial distribution of rocks over the conveyor belt.

This assumption of a spatial distribution (not necessarily the above functions) can be assumed to hold for rockstreams which are evenly laden and consist of a "narrow" size range. However this assumption will in general not hold for most autogenous-feed streams because the randomness of the rockstream flow totally precludes the use of such assumptions.

This difficulty in modelling the classification process on the belt again reinforces the concept that an *empirical or experimental* approach may be better suited for certain engineering applications than an analytical approach.

Event C : The rock section has a certain diameter.

The probability that a rock section profile captured in the test plane (image) has a certain size or equivalent diameter in the range $D_c, D_c + dD_c$, is dependent on the *shape* of the rock sampled, the amount of *overlapping* from neighbouring rocks. Overlapping in turn is dependent upon the density of the particle distribution as well as the relative size of neighbouring rocks and their spatial arrangement.

In the next few paragraphs it will be shown that overlapping is one of the most inhibiting factors to be dealt with in this model and makes the determination of $Pr\{C\}$ almost impossible.

The *umbra U* of an 2-D object or curve $f(x)$ in space defined as $U(f) = \{(x, y, t) \in D \times R: f(x, y) > t\}$, Maragos (1985), and the domain of support is shown in figure 3.24. Thus the projection of a particle onto a plane for a given orientation (θ, ϕ)[3.5] is assumed to be equal to the ***domain of support*** *S* of the ***umbra*** of the particle. This is equivalent to the area of a cross section of rock with a very thick section where for a given orientation the thickness of the section is greater than the caliper diameter $H(X)_{max}$ in the direction (θ, ψ) see figure 3.28.

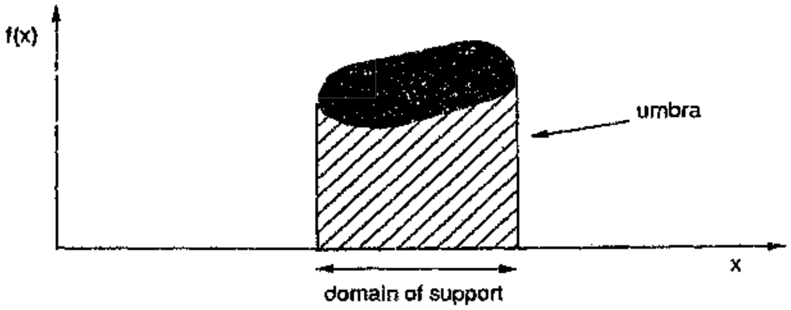

Figure 3.24. The umbra and domain of support of an object or function in one-dimension. .

Figure 3.25(a) shows the projection a number of sparsely distributed particles. For densely distributed particles the areal projections become the ***domain of support*** *S* for the union of the umbras of a number of particles, figure 3.25(b). In the limit the projection of a pile of rocks as found with the rockstream is the union of the domain of support of the umbras of all the particles. Because of overlapping or touching the resultant projection of a pile of rocks is a single area with no means for distinguishing between umbras contributed by individual rocks. See figure 3.25(c). From figure 3.25(b) and (c) it can be seen that the derivation of $Pr\{C\}$ is thus heavily dependent on the *correct identification* of combined profiles which depends largely on the image processing. However from chapters 4 and 5 it was shown that the identifying and extracting each umbra correctly is an exceedingly suspect process and prone to errors.

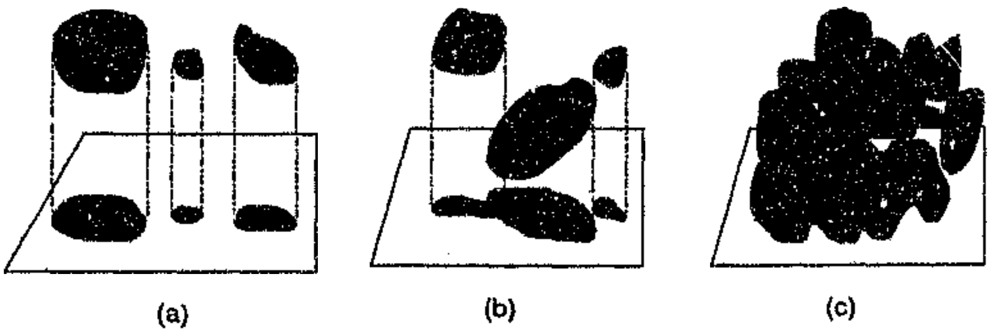

Figure 3.25. The result of projections of (a) sparsely distributed particles, (b) overlapping particle, and (c) piled rocks. .

[3.5] Spherical co-ordinates

Thus, because in the first place it is difficult to identify unambiguously the areal section of *irregularly shaped* rocks, the derivation of algorithms for compensating for overlapping with thick sections of irregular shaped rocks is assumed to be a futile exercise. The effect of overlapping and thick sections is discussed in the literature by Hillard (1962), Underwood (1967), Underwood (1970), Exner (1972), and Cruz-Orive (1983). Underwood (1970) comments that overlapping of only the simplest of particle shapes within the subset of convex particles can be considered. He adds further that when the number of overlaps extends beyond two, the mathematics becomes intractable. In conclusion no analytically correct expression for $Pr\{C\}$ can be derived.

Event E : The test line must intersect the areal section.

Assuming that areal projections in the size range $D_c, D_c + dD_c$ are available, then the linear probe T_1 must intersect this areal section. This is dependent on the relative *spacing* or distribution of the linear probe lines on the image as well as the *size* and *shape* of the areal projection.

The probe lines chosen are usually parallel probes regularly distributed across the test plane or image. However there are other methods for distributing the probes T_1 on the test plane T_2, which gives rise to different types of randomness and thus different probabilities of $Pr\{E\}$. In general only convex particles are considered because the occurrence of non-convex rock particles is highly unlikely, but nevertheless possible. Observations of the rocks on the conveyor belts feeding autogenous mills have shown that the very large rocks have higher probabilities of having a *concave* surface.

As an example consider a probe intercept arrangement of a grid of equidistant parallel probes as shown in figure 3.26. If the window is of size W and the probes are spaced a distance $d > H(X)_{max}$ where $H(X)_{max}$ is the maximum caliper diameter of any possible areal section, then the probe line can only intercept the section once (figure 3.26(a)), and

$$Pr\{E\} = \frac{H(X)}{d} \qquad 3.49$$

See Underwood (1970), Weibel (1979) and Weibel (1990). However the scheme shown in figure 8.7(b) of closely spaced probe lines is the one required to obtain a sufficiently large number of intercept measurements. Thus the probability of a test line intersecting the rock is one, $Pr\{E\} = Pr\{T_1 \uparrow X_{D_c}\} = 1$.

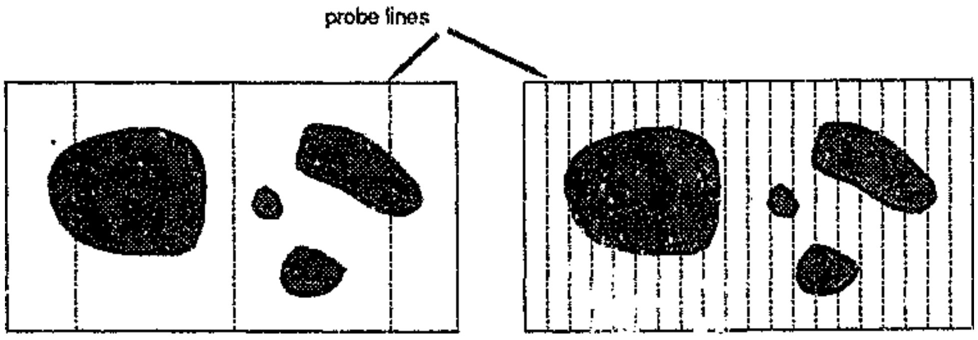

(a) (b)

Figure 3.26. (a) The correct spacing of probe lines for a rockscene. (b) Closely spaced probe lines used to obtain more intercepts..

Event F : The intercept length is of a certain size.

$Pr\{F\}$ is the probability that the resultant chord length measured is in the range $L, L+dL$. $Pr\{F\}$ is dependent on the shape and size of the areal cross-section intersected by T_1, and generally is difficult to determine.

In section 3.6 these distributions were evaluated for a single linear probe intercepting a given sphere, which gives rise to a distribution $p(L\,|\,D)$. These distributions have been worked out analytically for objects of simple shape such as spheres and cubes, (Wicksell, 1925), (Underwood, 1970), (King, 1978), (Weibel, 1980). Intercept distributions for other irregularly shaped objects have also been measured experimentally or by Monte Carlo simulations, (Naumovich et al, 1980), and (Naumovich et al, 1982).

Sampling the rock more than once

However with this work adjacent-linear probes have been used which results in a given section profile being intercepted more than once, and the resultant chord-length distribution $p(L)$ must be modified to take into account this *over-sampling*. The effect of oversampling is that $p(L)$ is influenced by the full range of possible chord lengths that can be measured in a given direction on a single rock. We must thus introduce a new event G which is that a rock can be linearly sampled n times. Thus the final output distribution is not simply $p(L)$ but a modified chord-length distribution which is a function of its maximum caliper diameter of the rock (profile) in a direction perpendicular to the direction of the probe, ie $H(X)_{\max,l}$ and the shape of the rock ie $p(L\,|\,D)$. $H(X)_{\max,l}$ is also a function of the size and shape of the rock relative to the probe direction, as shown in figure 3.27.

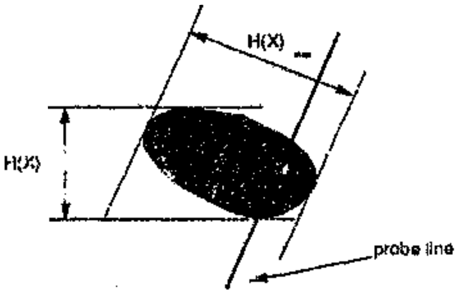

Figure 3.27. The number of chord measured per rock is a function of its maximum caliper diameter $H(X)_{max,1}$ in a direction perpendicular to the direction of the probes T_1.

Thus the final chord-length distribution $p_f(L)$ is given by equation [3.50] where $Pr\{G\}$ is function of the width of the image window W, the linear probe spacing T_1, as well as $H(X_{D_e})_{max,1}$ and other shape factors such as $p(L \mid D)$.

$$p_f(L) = \int_G Pr\{G\} dG \qquad 3.50$$

3.7.3 Deriving a final expression

The final stage to derive this model is to combine all the above conditional probability distributions equations into equation [3.5]. However the probabilities for events **B**, **C** and **E** are very difficult to evaluate without making any major assumptions, and in the case of event **F** the expression has to be determined experimentally (King, 1982, 1984). In particular, the probability distributions **B** and **C**, require a rigorous understanding of the packing and arrangement mechanisms of the rocks on the conveyor belt, which is a formidable task beyond the scope of this thesis. Thus to reduce the equation [3.46] to an analytical equation which is solely a function of D without any assumptions is near to impossible.

Compounding the above difficulties with deriving a final expression are the realities of image processing which are naturally error prone, (discussed in chapters 4 and 5.)

3.8 CONCLUSION

In this chapter stereological methods for estimating populations of 3-D parameters such as size from populations of 2-D parameters were discussed. In particular, in section 3.7, the problems associated with trying to develop a stereological model without any assumptions were shown to be extremely difficult if not impossible. The complexity of such methods tend to suggest that the answers to the questions at the end of *section 3.6 should be that an alternative method or philosophy should be explored* to derive rocksize. This ***empirical*** and experimental approach is presented in the remainder of the thesis.

Thus in the absence of realistic analytical models, the philosophy embraced has been to experiment in a logical and scientific manner, exploiting the stereological techniques to test *sizing* hypotheses based on established techniques without first developing a model. Thus the development a complete model linking the rockstream, images and chord-lengths measured to rock size is ***not a prerequisite*** of this measurement process. However the development of such a model could possibly provide the means of verifying the empirical process developed in the rest of this thesis and highlighting stereological errors or omissions, thus improving the measurement.

On a more practical note it is finally concluded that in order to measure any parameter of a rock, either the ***boundaries*** of X denoted ∂X, or the ***segmented regions*** $\overset{o}{X}$ of the projected images the rocks of Ω_R, be extracted. Thus the objective of the image processing and analysis stages of the instrument should aim to extract either ∂X or $\overset{o}{X}$. Recognition processes for these purposes are described in detail in chapters 4 and 5.

4 IMAGE PROCESSING I : ROCK BOUNDARY DETECTION

4.1 INTRODUCTION

In chapter 3 stereological relationships for measuring the size distribution of spherical particles were developed, where it was shown that the size distributions of the spheres can be estimated from measurements on their sections. The measurements are for example areas or linear-intercepts measured from projections or areal intercepts of the spheroids, also known as traces. It was then assumed that these stereological methods can be extrapolated to particles of arbitrary shape, eg King's method. Common to all these stereological techniques is the need for undistorted and error-free *traces*. It was concluded that the *traces* for rocksize estimation should be particle-*boundaries* ∂X, or the *projected-areas* (interiors) $\overset{o}{X}$ of the particles (rocks) X.

The objective of the image processing and analysis stage Ψ is thus to focus the contents of the raw image I into useful entities and symbolic objects which form an image of the rock boundaries $E_{\partial X}$, or projected areas $E_{\overset{o}{X}}$, via the transformation $E_{\partial X} = \Psi(I)$, or $E_{\overset{o}{X}} = \Psi(I)$, namely *trace* images.

In general there is a wide gap between the raw image and the required trace image. To bridge this gap there is need for a range of intermediate steps which simplifies the transformation into manageable steps. For this rocksize application, the transformation Ψ is broken up into two main sequential stages Ψ_1 and Ψ_2 where $\Psi = \Psi_1[\Psi_2]$. The objective of the preliminary stage Ψ_1 is to perform *primary* rock-boundary detection and object extraction which is developed in this chapter. In chapter 5 post-processing methods Ψ_2 are developed, which modify and *correct* the incomplete primitive-patterns derived in this chapter which are then combined into the final output, which can either be $E_{\partial X}$ or $E_{\overset{o}{X}}$.

4.1.1 Image Processing Terminology

The goal of the transformation Ψ which employs *computer vision* techniques, is to generate *scene descriptions* for *image understanding*. *Image understanding* is the automatic processing and interpretation of imagery or natural scenes from which knowledge is inferred. This chapter together with chapter 5 discusses the *computer-vision* techniques incorporating *image processing* and *image-analysis* for deriving scene descriptions which are the boundaries ∂X or the projected areas $\overset{o}{X}$ of the rocks. A vital part of this image processing is the *identification* of each individual rock and *extraction* of their properties (traces) which requires *image understanding*. In this research the measurements made on the traces in order to derive size distribution can be considered an extension of image understanding.

4.1.2 Notation and Convention for Image Processing

The image processing stage Ψ requires digitized images for numerical processing as opposed to the continuous image as defined in chapter 2. We thus define the discretized image I as captured by the frame-grabber, denoted $I(i,j)$ to be a matrix of samples in the continuous three dimensional Euclidian space $\Re$, where the 2-D domain is given by $(i,j) \in Z \times Z$ which are the co-ordinates of the centre of the elements (pixels) in the matrix. For convenience it is assumed that the image is square and of dimension NxN, ie contains NxN pixels[4.1]. Each pixel is assumed to be a sample of the continuous image at the co-ordinates (i,j) where each element (pixel) within the image denoted $I(i,j)$ can take on the values of $0,1,2..K \in Z$ where K is the maximum[4.2] gray level (brightness) in the image. Each pixel is assumed to be square[4.3] as well, with the gray level within each pixel representing an intensity sample of the real image corresponding to the position of the centre of the pixel.

The convention used in this document is that the horizontal direction of the image is represented by distance x and the index i, and the vertical by y and the index j. See figure 4.1. We also define the histogram of $I(i,j)$ to be $h(g)$ which is the number of pixels of brightness $g = I(i,j)$ $0 \le g \le K$ and where $0 \le i \le N-1$ and $0 \le j \le N-1$.

Each rockstream is denoted Ω_q, and provides a series of rockscenes which are captured as a series of images where the p'th image is denoted $I_{p,q}$ where $p \in Z, q \in Z$, $\infty < p < \infty, q = 1, 2, \ldots n$. See figure 4.1 (b).

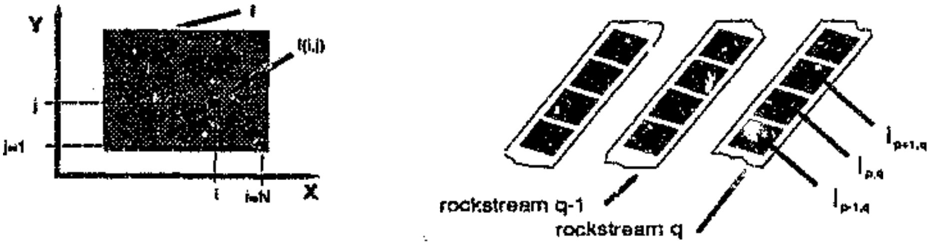

Figure 4.1: (a) Discretized representation of the image with address conventions of the pixels. (b) Rockstream q providing a stream of images $I_{p,q}$.

[4.1] This is not necessary and the image may be of dimension $N \times M$ where $N \neq M$.

[4.2] For the hardware used during this research each pixel was represented by a byte thus the gray levels ranged from 0 to 255.

[4.3] Due to the nature of the hardware used for experimentation, the aspect ratio of the pixels was not square. The significance of this is discussed in chapter 6.

4.2 SEGMENTATION OF ROCKSCENES

4.2.1 A conflicting requirement for "generic" and "custom" algorithms.

The measurement procedure consists of capturing, transforming and analyzing a number of sequential images $I_{p,q}$ of the rockstream q, from which a a series of discrete-size distributions $f_{p,q}(D) = \Psi_c[\mu\Psi[I_{p,q}]] \quad -\infty, p < \infty$, is to be estimated. Each different rockstream Ω_q presents a large variety of image scenes to the observer, with image characteristics such as texture and gray level statistics varying with time and space. The *image processing* Ψ must cater for these changing rockstream characteristics which are unique and differ substantially from other scenes processed in many other applications. In particular with these scenes,

1) The objects (rocks) to be identified, *touch* one another.
2) Many of the objects (rocks) *overlap* and *occlude* (obscure) one another.
3) There is often no discernible background (conveyor belt), but sometimes large areas of background are visible in the image.
4) The varied angles of the rocks' surface normals caused by their rough surfaces results in a large range of intensities to be reflected from a single area that should be classified as one object. The effect of such reflections from the whole image results in broad and generally unimodal gray-level histograms which are undesirable. Most industrial imaging applications rely on bi- or multi-modal histograms which ease the task of object recognition. The functional form of these gray-level histograms also changes with time, which complicates matters further.
5) The rock scenes are scenes of "natural" objects which exclude all regular geometric shapes. Although the shape of these objects (rocks) do fall within certain broad shape groups, they do vary a great deal.
6) The sieve size range of the objects (rocks) can vary from a narrow range of 19 to 25mm, to a range varying from less than a metre to tens of microns.
7) A positive point is that the group rock features although random, are unique, ie do not have straight lines or smooth curves, and are generally convex.

The above points together with the fact that existing imaging techniques are generally unsuited for rock images, implies that the extraction of either ∂X or $\overset{o}{X}$ will be based on heuristic and ***application-specific*** pattern-recognition algorithms. The argument for ***custom*** image-processing techniques is strengthened further by the fact that no generic computer-vision system has been developed that can handle any image (Rigaut, 1989) and in particular the rockstream images.

From observation, the characteristics of images of a rockstream q from a particular mine or mill will generally differ from another. Thus each rockstream forms its own *class* of images, and an algorithm developed for one class of images generally does not work for another, (Hartley, 1982). This again implies the customization of imaging strategies on an ad-hoc basis, where the software must be tuned or customized to the particular rockstream (Ω_q).

The rockscene characteristics change randomly with time and space. Thus a sequence of images captured from a given rockstream Ω_q can be considered a unique but *broadband* signal from a stochastic process. It is important therefore that the rock-edge detection algorithm be ***generic*** or ***broadband*** to ideally allow for the processing of a ***wide range*** of images from a given rockstream, so that all the traces in each image may be extracted successfully. Unfortunately this is not possible because of the limited power of computers and relatively primitive state of image-processing technology. The ideal requirement for perfect object extraction over a large range of images, can be likened to the quality factor Q of an electric circuit (fig. 4.2) where we have a trade-off between accurate object-extraction (gain), and rockscene-variations (bandwidth). Generally only a custom algorithm can perform perfect image-processing, thus a conflict exists between the requirement for "generic" and "custom" algorithms. Therefore in this thesis a compromise is sought in which the edge detection algorithms developed, perform "*acceptable*" segmentation for *all* rock images, of a given rockstream Ω_q .

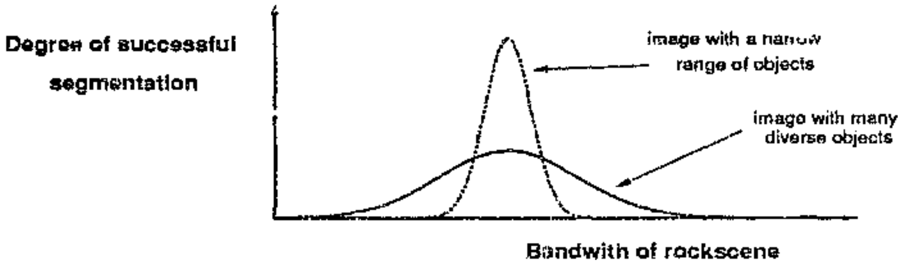

Figure 4.2: Q filter analogy for segmentation performance versus the variety of scenes to be segmented.

Associated with the development of image-processing strategies for this project are a number of other inherent limitations or problems. Firstly algorithms developed for a given rockstream will *not* be generic, because the development of the algorithm for practical reasons must be undertaken on a relatively *small* number of image samples, thus *biasing* the algorithm towards these images. Secondly, the suitability or success of an algorithm for size measurement cannot be predicted on the basis of the outcome of processing a finite number of images, but rather only after long-term testing on a real conveyor belt, where a *large* range of images can be processed. A positive note is that a myriad of image processing and analysis techniques exist which are available for use and customization, and which will be reviewed briefly in the next subsection for possible use in this research.

4.2.2 Review and Introduction to Segmentation techniques

Before a possible structure for a rock-edge detection system is proposed, it is necessary to review existing-imaging techniques in anticipation of the need for a *broadband* system, ie a system which can provide "*acceptable*" segmentation of *a wide range* of rockscenes for a given rockstream Ω_q . In agreement with Chassery and Garbay (1984), it must be noted that the widespread proliferation of segmentation techniques precludes a comprehensive survey of all such techniques.

One objective of the image-analysis or machine vision is to perform *object-recognition*, which in this research is ***rock*** and the ***rock-edge*** detection. Common to most object-recognition systems are the ***segmentation*** or *image-partitioning* processes which concentrate the contents of the raw image into entities for *understanding* by higher-level processes (Dunn, 1989). The development of segmentation processes is still a major problem in machine vision, and the lack of progress in image segmentation is retarding the application of automated image-processing. As a result Riguat (1989) emphasizes that "new ideas or a significant breakthrough in automated image segmentation" is a major objective in the field of machine vision. Although he was talking specifically about applications in biological microscopy, his comments do apply to most other segmentation applications, including conveyor-belt rockscenes.

In this research the author classifies segmentation methods as being either "classical" or morphological. Strong links exist between morphological and classical imaging techniques (Maragos, 1985). Classical segmentation methods can be sorted into three classes, namely (i) characteristic feature extraction, (ii) edge detection and (iii), region extraction, see Fu and Mui (1981). Pratt (1978), Farag (1978), Nakagawa and Rosenfeld (1978), Hartley et al (1982), Garbay (1986), and Beaulieu and Goldberg (1989), are amongst the many authors who discuss various segmentation algorithms. Most segmentation algorithms are designed for only one class of image, whilst others are more broadly based to handle a larger variety of input signals. Many algorithms employ feedback from high to low level processes, are iterative or adaptive (Kelly, 1988), or are statistically or spatially based (Rosenfeld, 1979). A number of segmentation techniques should, and do, make use of *a-priori* knowledge of the characteristics of a given class of scenes to be processed (Rosenfeld, 1979) which results in *application-specific algorithms*. *A-priori* knowledge is also often used to control the convergence of iterative techniques (Garbay, 1986), which can take a long time to process.

A-priori segmentation algorithms can generally only be developed if the objects can be modelled. The extraction of man-made and regularly-shaped objects lend themselves to model-based object extraction processes because the objects can be described. Easy object description results for example. in template matching imaging systems, which are utilized in quality-control or industrial-inspection systems where bottle caps or labels are checked on-line. However *natural scenes* which are exceedingly complex, impose a key constraint on the development of algorithms based on explicit models or a-priori knowledge, because common objects such as trees, clouds and rocks are difficult to describe in a formal manner suitable for machine recognition (Firschen, 1988) (Mandelbrot, 1990). A possible solution is to use fractals (Mandelbrot, 1983). Even the analysis and modelling of what appears to be conceptually simple scenes may be exceedingly difficult because they contain a vast amount of detail, (Bergholm, 1987). If however predicates or conditions of, for example, the convexity or circularity of naturally occurring objects can be established, then control strategies can be developed for the segmentation process of complex scenes (Chassery and Garbay, 1984).

Man, through experience and inference can deduce and understand the contents of an image. This, together with the diversity of control mechanisms and other factors affecting image segmentation, as well as the reliance on heuristic procedural algorithms, has led to the development of knowledge and rule-based segmentation systems encompassing artificial intelligence and expert systems which ultimately try to emulate the human, Nazif (1984) and Stansfield (1986). Nazif (1984) comments that rule-based segmentation techniques produce partitions that simultaneously maximize the many aspects of the segmented image, whereas specialized techniques maximize one property at the expense of another.

For this rocksize problem it is very difficult to create an expert or rule-based system that can take cognizance of the many possible rock patterns and still process the image within a reasonable time-frame, (Berger, 1985), (Wigeson, 1987). However Wigeson (1987) developed rule-based systems to analyze and segment rock scenes using some *a-priori* knowledge which processed rock images in much less time than Berger's system. This is a positive indicator of the viability of rockscene segmentation, where a prudent choice of rules incorporating a variety of modified classical techniques, can provide a solution.

What becomes apparent with many segmentation techniques discussed in the literature, is that (i) they often strive for near-perfect segmentation, for example edge detection to sub-pixel accuracy (Tabatabai and Mitchell, 1984), and (ii) the variety or number of images processed by the algorithm is small, contrary to the requirement of the rockscene segmentation algorithms. Striving for good and accurate segmentation, as well as *details* such as the precise location of an object is still important to this application. However the *stochastic* nature of the rockstream implies that a stochastic approach to rock recognition and segmentation algorithms can also be considered. A stochastic approach is useful in that such methods suggest defining a tolerance for errors rather than eliminating them completely.

A significantly large number of images with different characteristics can be generated from a single rock scene, although rock scenes form a very tiny subset of the universal set of image scenes. This, together with the stochastic nature of Ω implies that *uncertainty is an integral part of the measurement and cannot be eliminated* (section 4.3). Thus the philosophy adopted with regard to the development of rock-edge detection algorithms is,

(a) to utilize the many useful segmentation and image-processing techniques *available*, avoiding the need for laborious fundamental algorithmic development, and

(b) not to attempt the development of the perfect system, but rather to find out how *ba .y* classical or existing methods perform, with the objective of selecting a *combination* of these techniques which work at an acceptable level of uncertainty. The minimisation of this uncertainty is a long term goal to be pursued after the establishment of the acceptable system.

4.2.3 Combining Image Processing Processes

Examination of past work (Berger, 1985), as well as experimentation with a number of classical and well-established segmentation techniques as applied to a series of conveyor belt rockscenes, shows that *in isolation* no single segmentation algorithm can perform satisfactory segmentation. this is a result of the fact that most imaging techniques are *not* being designed for the peculiarities of rockscenes, see section 4.5 for specific examples. Brink and De Jager (1987) also similarly conclude that in general, no single algorithm is likely to provide the best result for all applications. This has led to the conclusion that instead of developing an intricate custom algorithm for accurate rock-recognition (Berger, 1985), a *combined* system utilizing a number of relevant techniques should be used for rock-edge recognition and extraction (Malik and Maydan, 1989). A combined system will allow for the best features in each method to be used to support or refute the presence and location of a rock edge, ie " a democratic system". The architecture of such an image processing structure is shown below in fig. 4.3.

Each branch of the structure given in figure 4.3 can be considered a modified classical pattern-recognition strategy as discussed in the literature. These strategies usually consists of a number of well defined sequential processing stages (Coleman and Andrews, 1979), usually called the low and high level processes, or as Farag

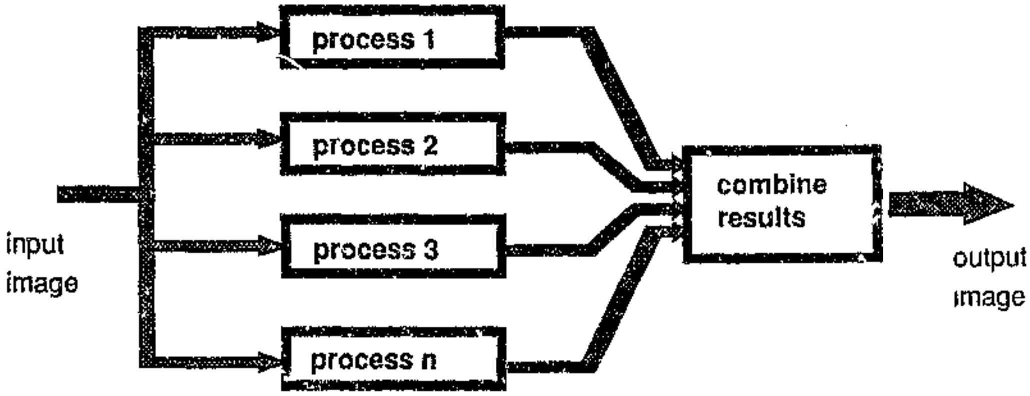

Figure 4.3: Block diagram of a simple parallel image processing architecture.

(1978) discusses, the extraction of *micro* and *macro* information. The first part of these strategies (after image acquisition), consists of the low-level processes which extract local features of the image in a non-semantic way. Following this are a number of high level processes which group or classify these local features (entities) into meaningful relationships or sets, which could consist of homogeneous regions of defined shapes (segmentation).

For the global strategy advocated here, the image pattern from each parallel branch is then fed to a final combining stage, the control of which is still an area for concern because it involves *contextual understanding* of the contents of an image, a critical area still to be researched (Chassery and Garbay, 1984).

There are many other models in the literature other than the those in figure 4.3 for dealing with image understanding, most which have been developed for a specific application. The question of which low-level feature extraction and higher-level segmentation algorithms should be used for rock-scene analysis will be discussed in section 4.3.

4.3 ROCK BOUNDARY DETECTION OR ROCK EDGE DETECTION - ASSOCIATED ERRORS

The 2-D boundary or projected area of each rock is assumed to be all that is necessary for rock size detection (chapter 3), which implies that segmentation algorithms should be geared towards *rock-region* or *rock-boundary* identification and analysis. Object-boundary detection is based on the analysis of discontinuities in the image gray levels, whilst region analysis can be based on a number of criteria, one of the most common being the homogeneity of groups of pixels (Fu and Mui, 1981). Both methods can be used and the decision of whether to use region or boundary analysis is dependant upon

(i) which pattern (edge or areal) contains the most *reliable* and *useful* information ?

(ii) the *complexity* of the algorithms required to process the entities, which affects the speed of the measurement. ie which pattern is the easiest to generate in the shortest possible time ?

(iii) the relative amount of segmentation errors produced by each method per image and the cumulative effect of these errors on the final size measurement. This is related to the complexity of a technique, which unfortunately has been found (subjectively) to increase exponentially with the decrease in errors.

(iv) which pattern requires the least amount of correction and how quickly can this be achieved ?

Boundary and *region* analysis are very closely related because boundaries can be considered *edges* of segmented *regions*. Thus both boundary and segmented-area data should ultimately provide the *same* information with regard to size although it appears intuitively that areal patterns are the correct patterns to use, see fig. 4.4. It is assumed further that a segmented image can be converted to an edge pattern, and vice-versa. What is common to both patterns in the end is that the traces for each rock must be *unambiguously* identified and *separated* from its neighbour. (For convenience and clarity X_i refers to the interior $\left(\overset{o}{X}\right)_i$ of the 2-D projection of the i'th rock X_i .)

The two possible image patterns E that can be derived from the input image via Ψ are shown in figure 4.4, which are either *projected areal patterns* $\overset{o}{X}$ or *boundary patterns* ∂X . With *projected areal patterns* $\overset{o}{X} = \sum_i \left(\overset{o}{X}_i\right) = \sum_i (X_i)$, the rock areas are of phase $\alpha \in X$,, and the background of phase $\beta \in X'$. The total rock area is given by the set of subsets $X = \{X_1, X_2, \ldots X_i \ldots X_n\}$ where the *i'th rock* X_i is uniquely labelled (Berger, 1985) λ_i and where n is the number of rocks in the image, thus giving an image ***function***. ***Edge or boundary patterns*** $\partial X = \sum_i (\partial X)_i$, are connected together to form a ***binary*** set where α represents the edges and β non-edges. Ideally $\alpha \in (X \cap X' = \partial X = \partial X')$ and $\beta \in (X \cup X')$, ie β includes the interiors of the rocks as well as any exposed surfaces of the conveyor belt. Note that if the rocks are not touching or overlapping then ∂X can consist of uncoupled binary sets. However with overlapping rocks the edge patterns interlock and all the boundaries can have the same label.

For areal patterns the *transition*[4.4] $\alpha \rightarrow \beta$ or $X_i \hookrightarrow X_j \quad i \neq j$ and vice-versa, indicates the edge of a rock section. Therefore a chord length for example, can be measured as the distance between the two transitions $\beta \rightarrow X_{\lambda_i} \rightarrow \beta$ or $X_{\lambda_j} \rightarrow X_{\lambda_i} \rightarrow X_{\lambda_k}$ see fig. 4.5(b). The area is measured by counting pixels of phase α of a unique label λ_i, where the boundaries are given by the above transitions.

[4.4] A spatial transition (or displacement) across the image is denoted $\rightarrow$.

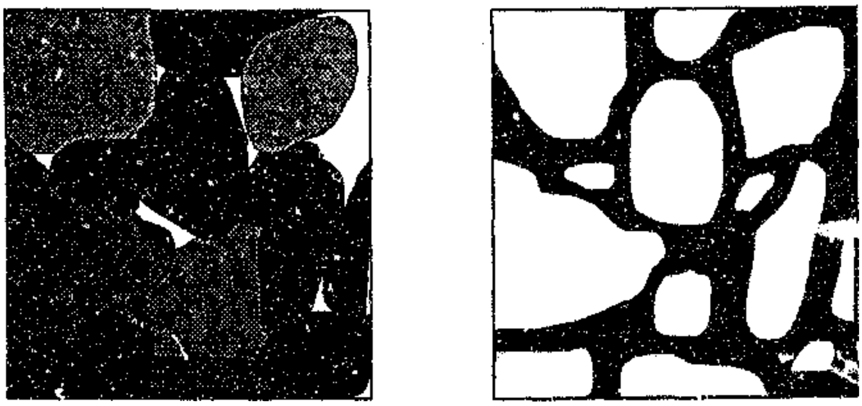
(a) (b)

Figure 4.4: Example of synthetic entities from which size is to be measured. (a) Segmented regions of the rocks where each rock-region is given a label. (b) Edges or the boundaries of the rocks.

With edge patterns, chord lengths are measured as the distance between the two adjacent transitions $\beta \rightarrow \alpha \rightarrow \beta$, whereas areas of traces would be measured by counting pixels of phase β provided that $\alpha \in X$. See figure 4.5.

The fact that edge patterns are binary is a major advantage over segmented patterns which are essentially functions because of the labels λ_i, where $\lambda_i > 1$ and $\lambda_i \in Z$, and consequently require more memory and take longer to process. However edge patterns do have a disadvantage, this being the finite width of the edges ∂X where $\partial X \subset X$ or $\partial X \subset X'$, which distorts the measurement. Figure 4.6 (a) shows how edges of finite thickness affect the measurement of chord-length resulting in errors L_e ranging from $L_e = L_{true} - L_{inner}$ to $L_e = L_{outer} - L_{true}$. Labelled areal patterns on the other hand are less ambiguous with regard to the definition of boundaries, because labelled regions can lie next to one another with conceptually infinitesimals thin edges, fig 4.6(b). See Serra (1982) Chap. 1 B.4 for more on boundaries and their definitions.

A segmented area of a rock or rock boundary should define a closed homogeneous area. However definition of a *closed* homogeneous area with respect to pixel groupings on the discretized plane and its associated edges is a problem. This is essentially a problem of *connectivity*, where on a rectangular discretized plane a pixel can be connected to 4- or 8- neighbours see fig. 4.7. (See Serra, 1982 for more on hexagonal grids.) Connectivity is significant because the edge or areal patterns derived will be erroneous with, (i) "holes" in areas, figure 4.8(b), (ii) gaps in edges, figure 4.8(db), and (iii) bridges or connections between areas, figure, 4.8(a), or edges caused by noise components. The connectivity of a group of pixels defines these errors and the methods required to repair them.

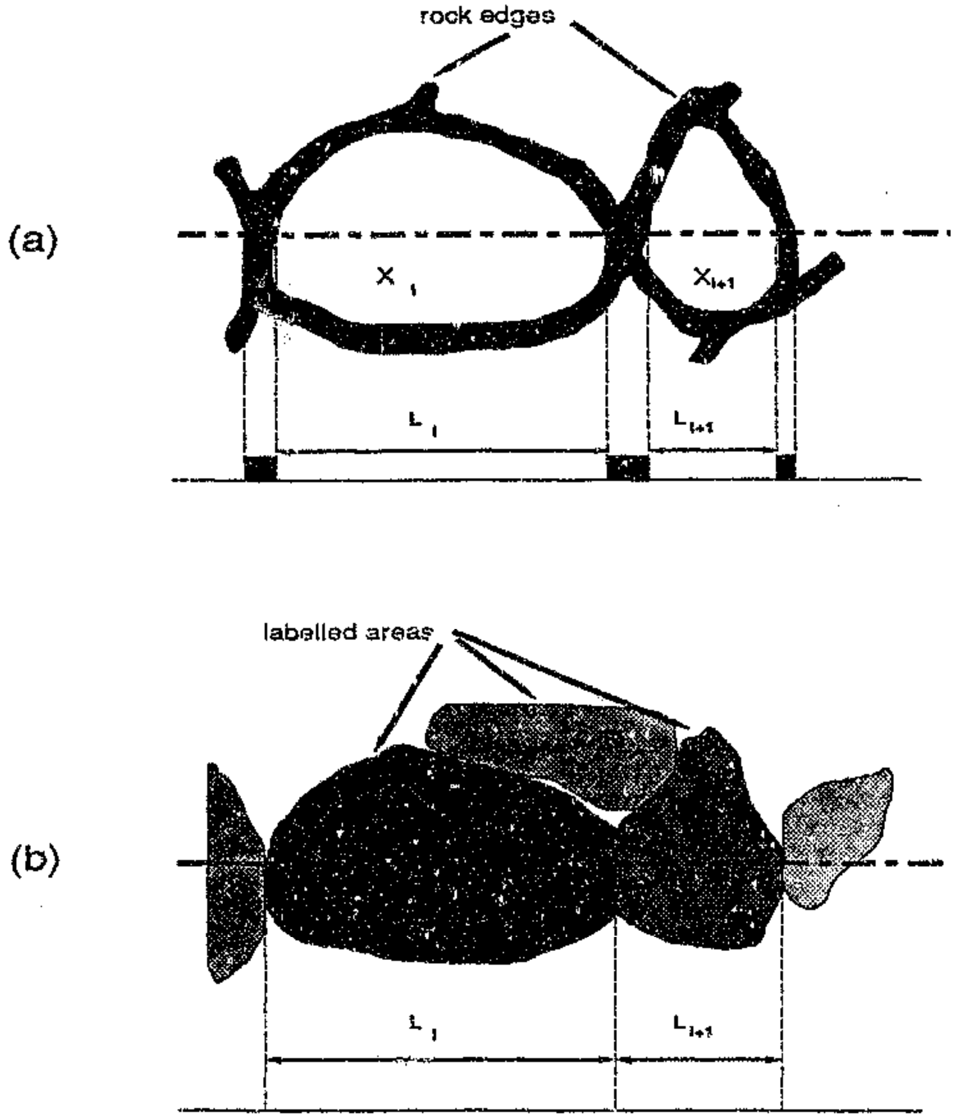

Figure 4.5: Schematic diagram of portion of (a) an edge pattern, and (b) a segmented areal pattern of rocks (synthetic), showing how chord-length measurements may be made on both types of patterns.

For ***labelled area patterns***, errors stem from (i) merged adjacent areas (ii) isolated islands and (iii) broken up areas. *Merged* areas result in a measured area A^* and chord length L^* being larger than the true value A and L, ie

$$A^* = A\{X_i \cup X_j\} > A\{X_i\} \qquad 4.1$$

$$L^* = L\{X_i \cup X_j\} > L\{X_i\} \qquad 4.2$$

"Holes" or islands on the other hand result in for example

$$A^* = A\{X_i - Y_i\} < A\{X_i\} \qquad 4.3$$

$$L^* = L\{X_i - Y_i\} < L\{X_i\} \qquad 4.4$$

where Y_j is a island in X_i. *Splitting*, figure 4.8(c), results in the same error as given in [4.3] and [4.4] except that the hole Y_i is replaced with a valid rock X_j. The problem of merging is the more significant error for larger rocks, whilst smaller rocks are affected more by holes and spurious noise.

With ***edge patterns,*** the similar errors as shown above will occur, with merging resulting from gaps in the edges, and false edges causing holes or islands. However a third type of error also occurs with edge patterns, and these are caused by the finite width of the edges. These errors are more significant for short chord length and area measurements when $L(\partial X) \approx L(X)$ and $A(\partial X) \approx A(X)$. The measured chord length and areas are given by equations [4.5] and [4.6] where Y_j is a false edge or island. See figure 4.8(d).

$$L^* = L\{X\} - L\left\{\sum_j Y_j\right\} - L\{\partial X\} \qquad 4.5$$

$$A^* = A\{X\} - A\left\{\sum_j Y_j\right\} - A\{\partial X\} \qquad 4.6$$

In the next subsections we continue to discuss various segmentation techniques for extracting the projected areas or edges of the rocks in the images, in the anticipation that both sets of information will not be error free, but together could provide some redundancy which can help to reduce errors for rock recognition.

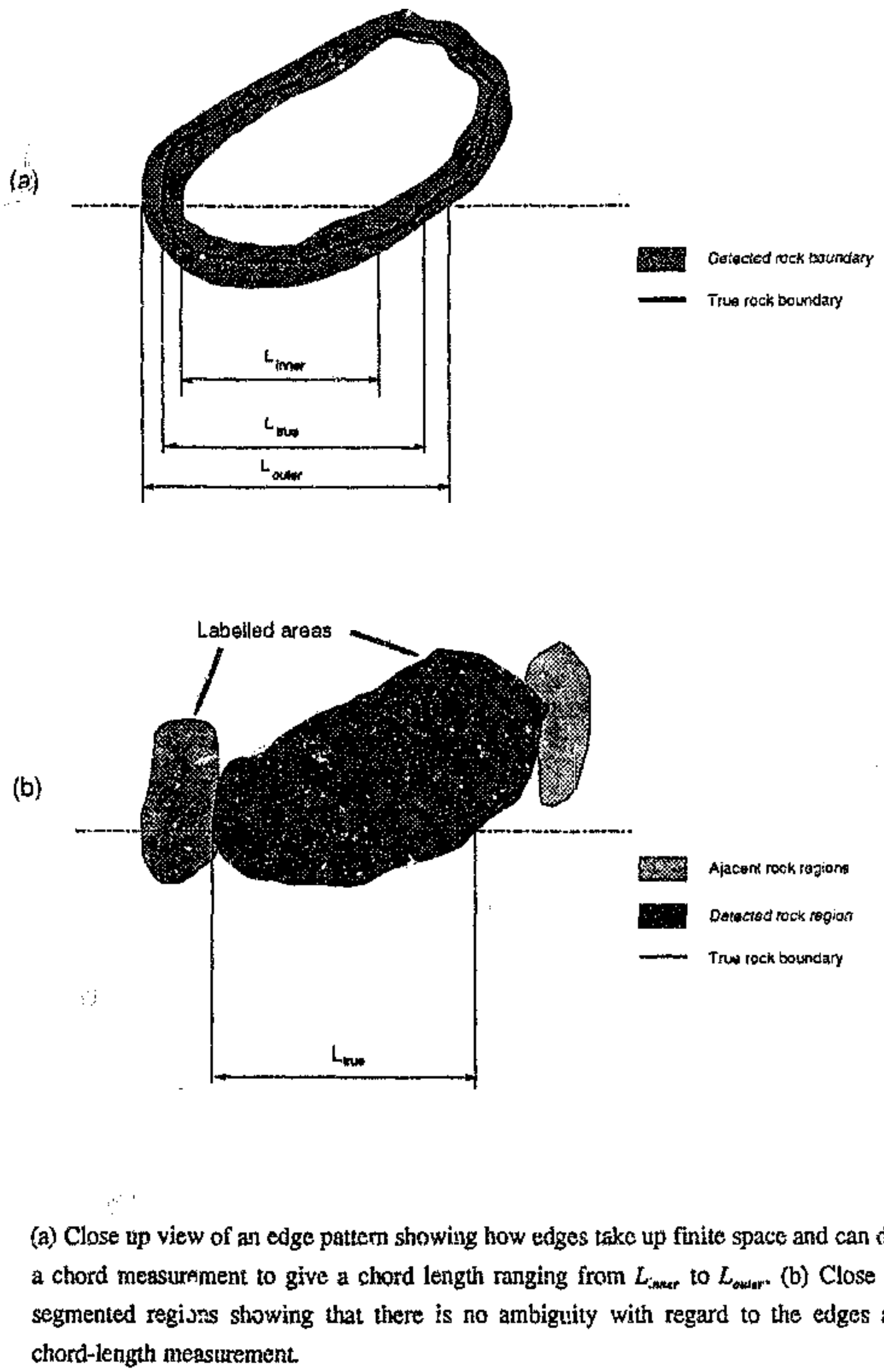

Figure 4.6: (a) Close up view of an edge pattern showing how edges take up finite space and can distort a chord measurement to give a chord length ranging from L_{inner} to L_{outer}. (b) Close up of segmented regions showing that there is no ambiguity with regard to the edges and a chord-length measurement.

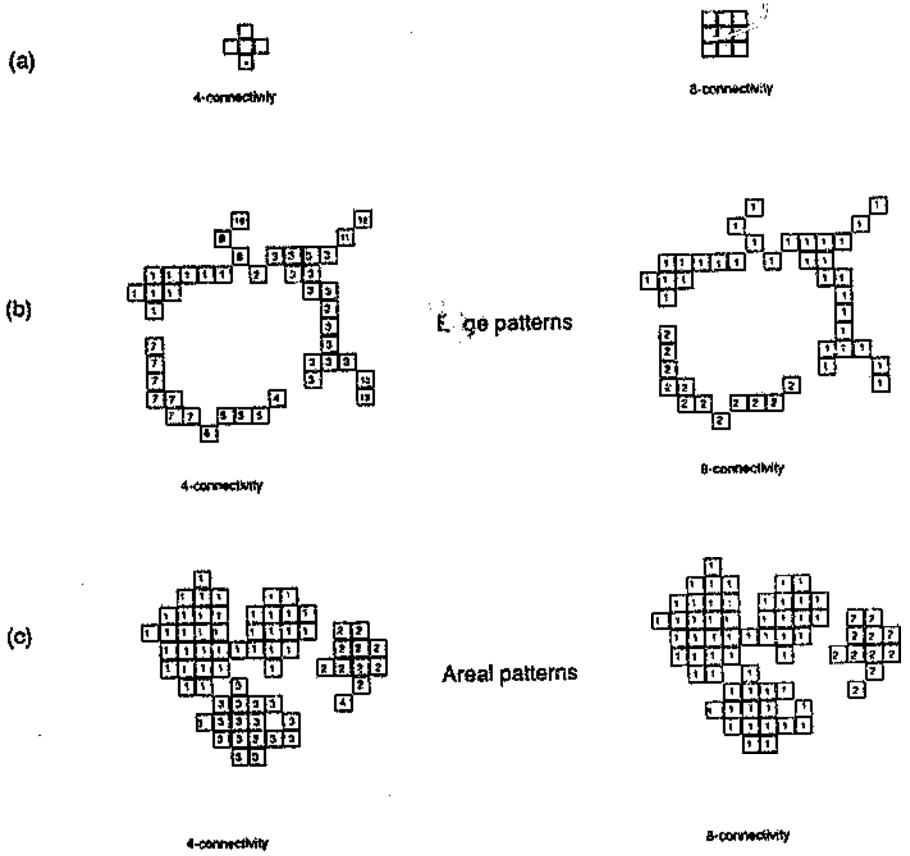

Figure 4.7: (a) 4- or 8- connectivity on a rectangular grid. (b) Example of a string of pixels forming an edge in 4- or 8- connectivity. (c) Example of pixels forming a closed region with 4- or 8- connectivity.

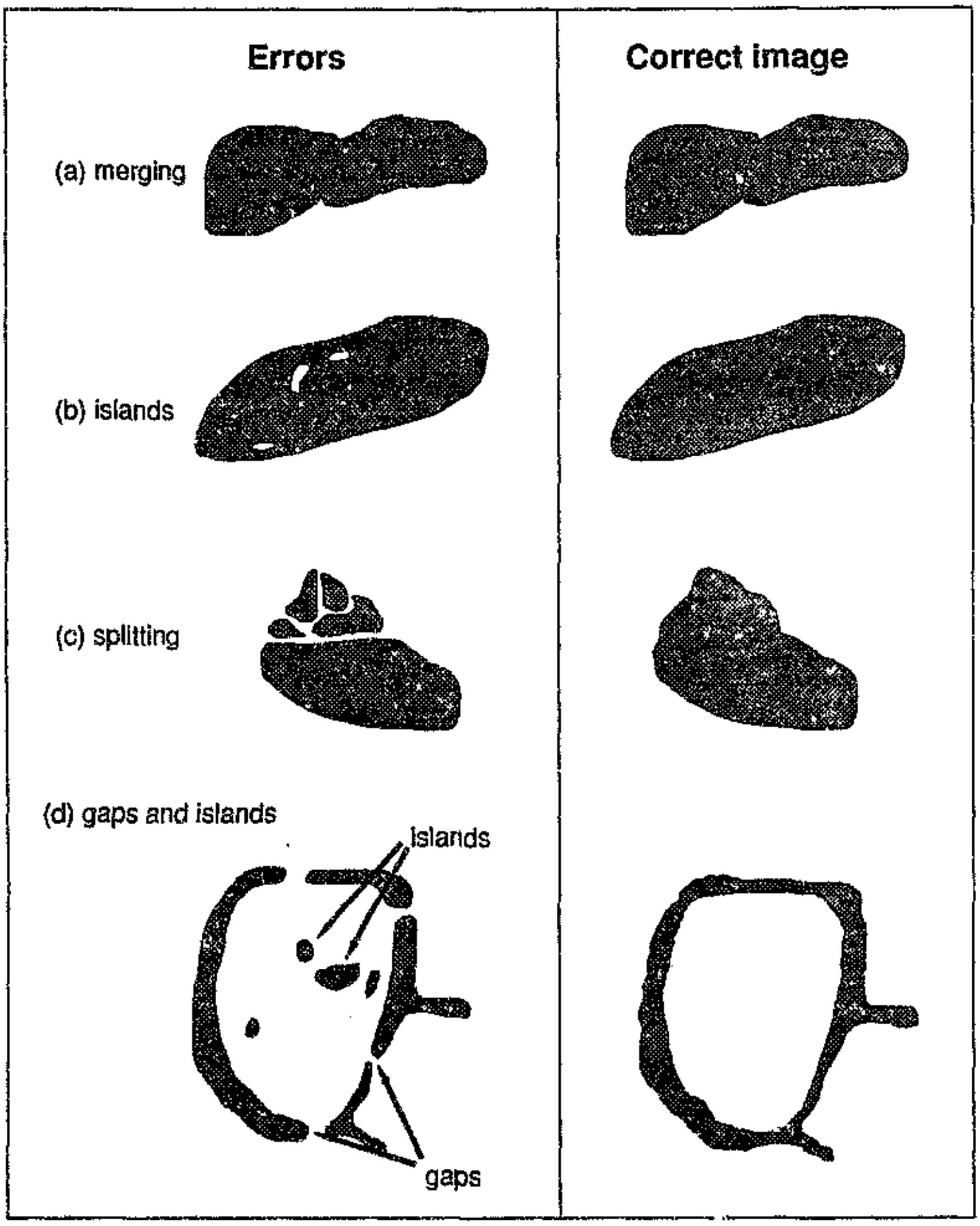

Figure 4.8: Errors in size measurements on labelled area patterns due to (a) merging, (b) islands, (c) splitting, and (d) gaps and islands, in an edge image.

4.4 THRESHOLDING FOR ROCK REGION EXTRACTION

The *rock-identification* task can be thought of as classifying each area of the image as belonging to a unique rock which can be labelled unambiguously, ie a *segmentation* process. There are many methods that have been devised for segmentation, one of the most common being thresholding.

4.4.1 Global and local thresholding

Thresholding is conceptually the easiest and simplest segmentation method to implement, and is thus the first method to be investigated for primary rock segmentation. ***Binary*** thresholding is the transformation of the gray level image $F(x,y)$ to the binary image $G(x,y)$ where object (rock) pixels, and background pixels are relegated to one of two classes. ***Global*** binary-thresholding is performed over the *whole* image and is given by

$$G(x,y)=\begin{Bmatrix} a & \quad if \quad F(x,y)\geq T \\ b & \quad if \quad F(x,y)<T \end{Bmatrix} \qquad 4.7$$

where T is the threshold value chosen and a and b are any values, traditionally 1 and 0. Thresholding in general can be extended to produce $G(x,y)$ consisting of *more* than two classes, eg Berger (1985).

There are many different types of thresholding algorithms depending on, methods for selecting T and the number of classes required, (Rosenfeld and Smith, 1981), (Weszka, 1978), (Weszka et al, 1974), (Ridler and Calvard, 1978). Lee and Jurkevich (1989) remark that not all images can be successfully segmented because the image does not always contain distinctive classes. Most segmentation techniques based on thresholding assume that the images have a histogram $h(g)$ with two or more distinctive peaks (bimodal or multimodal). The background usually consists of one peak, and the objects the other peaks, and the threshold values are typically selected from the valleys. However many images, including most of the conveyor-belt rock images have broad and "near-unimodal" gray-level histograms, with which it is very difficult to distinguish unambiguously between different peaks and hence segment the images, see figure 4.10. The problem associated with images having unimodal distributions is discussed by Bhanu and Faugeras (1982), where a relaxation process for segmenting this class of image is presented. However this technique is not suitable for this application, because of the large amount of computation required and the unpredictable convergence rate for relaxation schemes which are a problem for realtime processing. Lee and Jurkevich (1989) have also developed an unsupervised method for segmenting the unique speckled SAR images with unimodal histograms.

Although much effort has been spent in developing algorithms which artificially reclassify and redistribute the pixels so as to form distinctive peaks in the gray-level histogram, these thresholding techniques do not work very well with rock images as found on conveyor belts, where the rocks are *overlapping* and *touching* (occluding). This problem confirms what has been discovered in practice with instruments based on thresholding (eg MSD-95 which is a one dimensional thresholding system), in that the gray levels in an image I do not necessarily represent the topology of the physical scene from which the image was created, although it is closely related, (sometimes but not always $I \sim z_{\Omega}$, see chapter 2).

However, thresholding of rockscenes consisting of a mono-layer of separate rocks does produce acceptable segmentation. A separate arrangement of rocks forms an image of gray or *light-coloured objects* on a *darker background*, which results in a bimodal histogram as shown in fig. 4.9(b). Figure 4.9(c) shows the unambiguous pattern of areas of rock X and non-rock Y resulting from the global thresholding of the rockscenes in fig. 4.9(a).

On the other hand consider figure 4.10(a) which shows a rockscene of overlapping rocks, the gray-level histogram in figure 4.10(b) and the result of global thresholding in figure 4.10(c). The histogram in fig. 4.10(b) is not bimodal and the segmented image does not consist of unambiguously segmented rock projections. There are three main reasons for the merging and splitting of the rocks as shown in fig. 4.10(c).

1) The intensity valley between two individual rocks becomes more shallow as the two rocks are brought closer together causing merging. Similarly and in an opposite sense, ridges or irregularities on the rock surface cause shadows which splits up a rock's area into separated individual rocks.

2) Except for the background and shadows between rocks, there are no features in piled rockscenes which produce homogeneous areas that can be relegated unambiguously to a particular object.

3) The facets on the surface of the rocks have a relatively wide distribution of surface normals which reflect light "uniformly" over a wide intensity range.

The above factors combine and result in a unimodal histogram with broad peak which creates difficulties in selecting threshold values for unambiguous or error free segmentation. As a result, global thresholding requires time-consuming post-analysis in order to separate merged regions, (Berger, 1985).

Another reason for global thresholding not segmenting rock scenes properly is that the average gray level often varies across the captured image because of the practical difficulty of illuminating a relatively large scene area[4.5] evenly. However local-thresholding techniques can be used to compensate for uneven illumination where the threshold values $T(i,j)$ in different parts of the image are adaptively adjusted in sympathy with the local increase or decrease in gray-level and hence illumination. The local threshold value $T(i,j)$ for each pixel is calculated by comparing both the global gray level statistics, to the gray-level statistics of a local window $W \subset I$ of N elements surrounding the pixel to be threshold. The principle behind using windows on an image is that the group of pixels within a window is usually spatially correlated and that the illumination can be considered to be constant within that window. For example given an image $F(i,j)$, $T(i,j)$ can be calculated by comparing the local average gray value $\overline{F}(i,j)$ to the global average gray value $\overline{\overline{F}}$, as shown in equation [4.8] and [4.9][4.6].

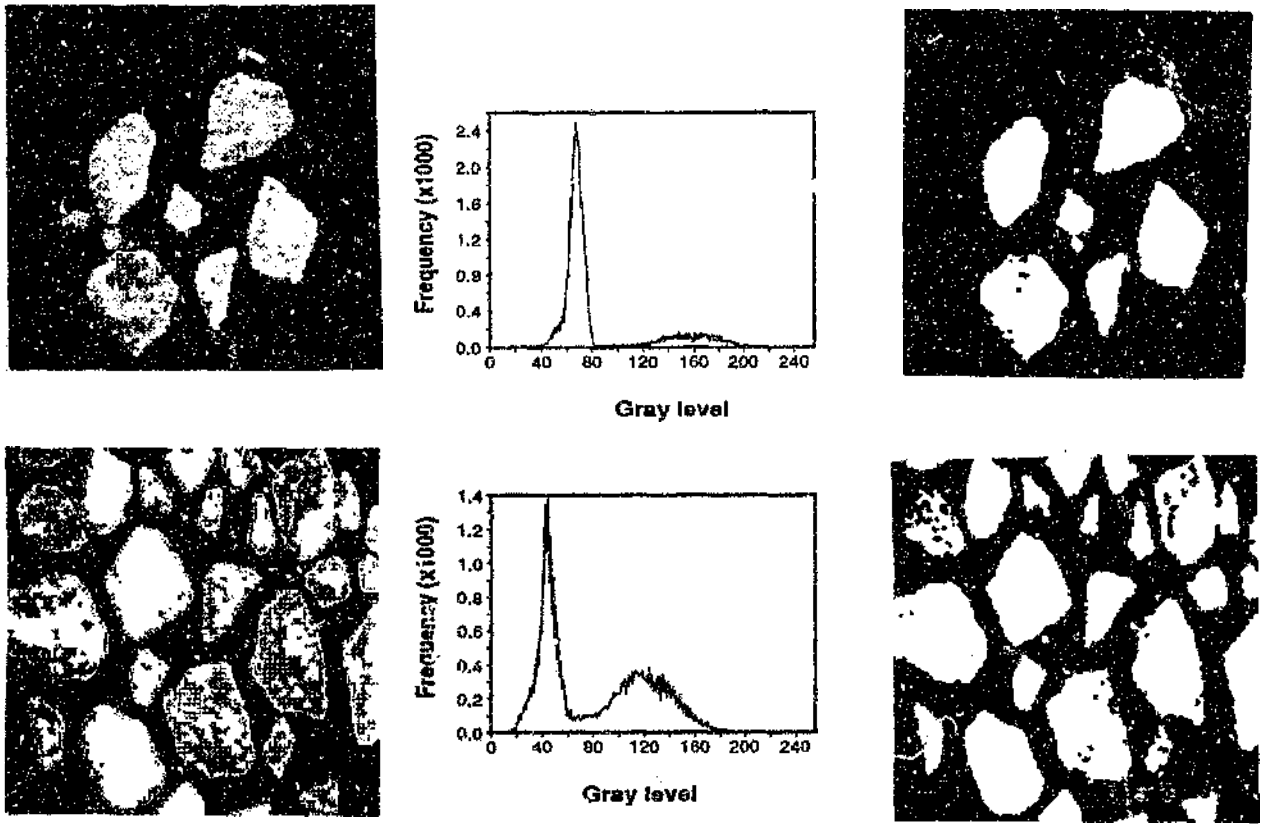

(a) (b) (c)

Figure 4.9: (a) Example of an image of a *mono-layer* of *separated* rocks. (b) Gray level histogram of (a). (c) The rockscenes after global thresholding at $T = 90$.

[4.5] Typical areas covered by a camera vary from 0.2 m ^{2} to 1 m^2.

[4.6] There other schemes that may be used instead of equation [4.8] and [4.9].

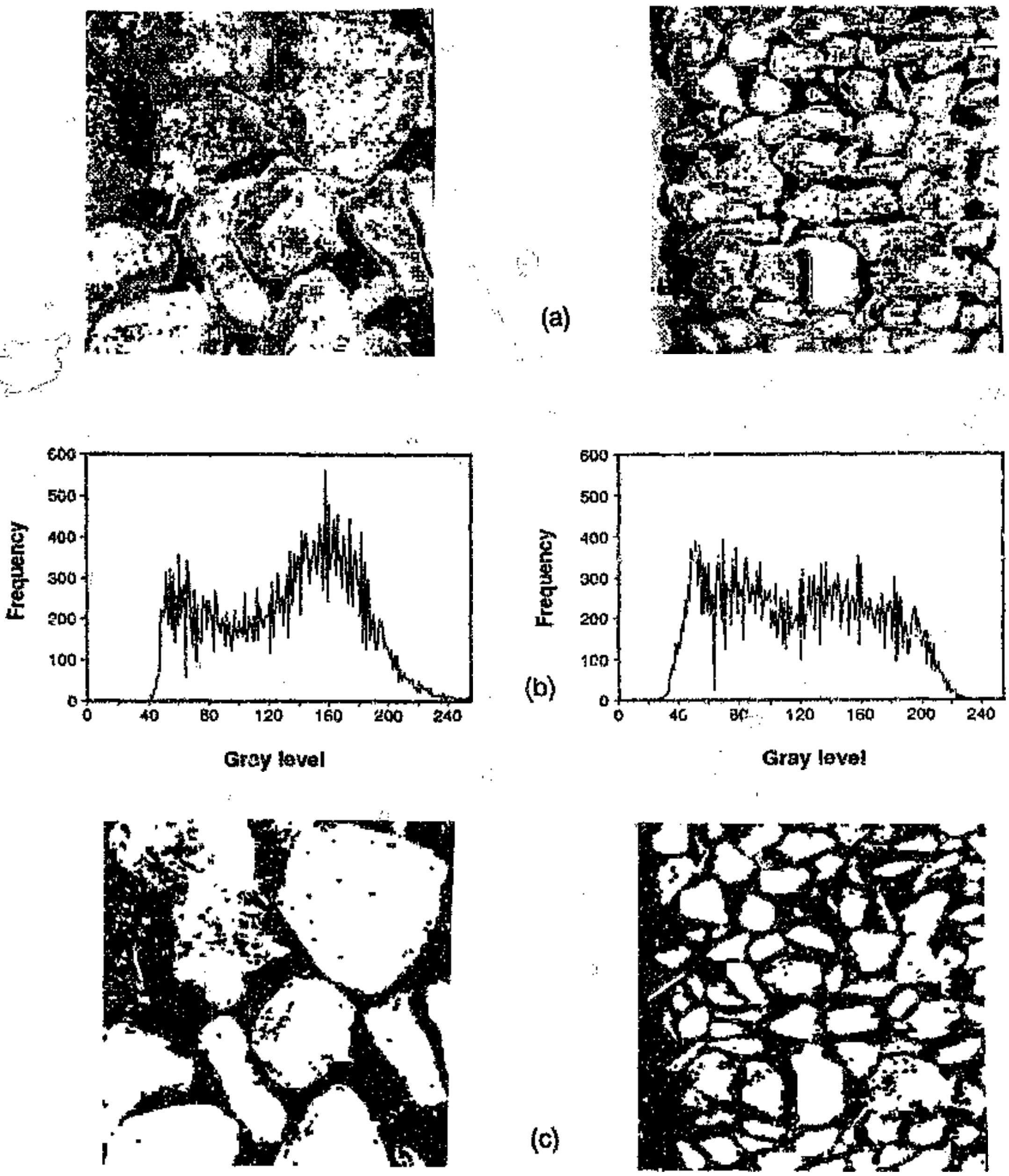

Figure 4.10: (a) Two examples of images of overlapping and occluding rocks from Ω . (b) Histogram of the images. (c) Resultant segmented images, with threshold at $T = 120$ for both images.

$$\overline{F} = \frac{1}{N} \sum_{i,j \in W} F(i,j) \tag{4.8}$$

$$T(i,j) = T_g + k\{\overline{F} - F(i,j)\} \tag{4.9}$$

The problem with local thresholding as with many other similar algorithms employing windows, is the choice of window *shape* and *size*, as well as the large amount of computation[4.7] required to calculate $\overline{F}(i,j)$. The shape of the window over which $\overline{F}(i,j)$ is calculated in this research was made *rectangular* instead of *circular* in order to ease the processing time, However rectangular windows introduce a certain amount of *directional* bias, because pixels at the corners of the rectangle at a distance d_W are "consulted", while pixels vertically or horizontally placed a similar distance d_W away from the central pixel of interest are ignored.

An alternative to local thresholding is to optimize the lighting to give a relatively constant illumination over the rockscene to be analyzed thus eliminating the need for costly software compensation such as local thresholding and analysis. The optimization of lighting and other hardware to avoid software overheads (section 2.6.5), is an obvious and recurring theme in this research which is usually restricted by hardware costs and the practicalities of installing the equipment in a rough environment.

Figure 4.11(c) and (d) shows an example of *local* thresholding over a 20 by 20 window (image is 200 by 200 pixels) which can be compared against *global* thresholding figure 4.11(b). For all threshold images $T = T_g = 100$. From figure 4.11 it is obvious that local thresholding provides a much better segmentation pattern with less merging although more splitting and islands but on a micro scale. The only reason why such methods were not finally used is the extremely large computation time.

[4.7] The calculation of local-average gray levels in a window of 20x20 in a 200x200 image using a non-optimized algorithm takes approximately 1.5 to 2 minutes on a 20MHz 80386 machine with an 80387 with a 64Kbyte cache.

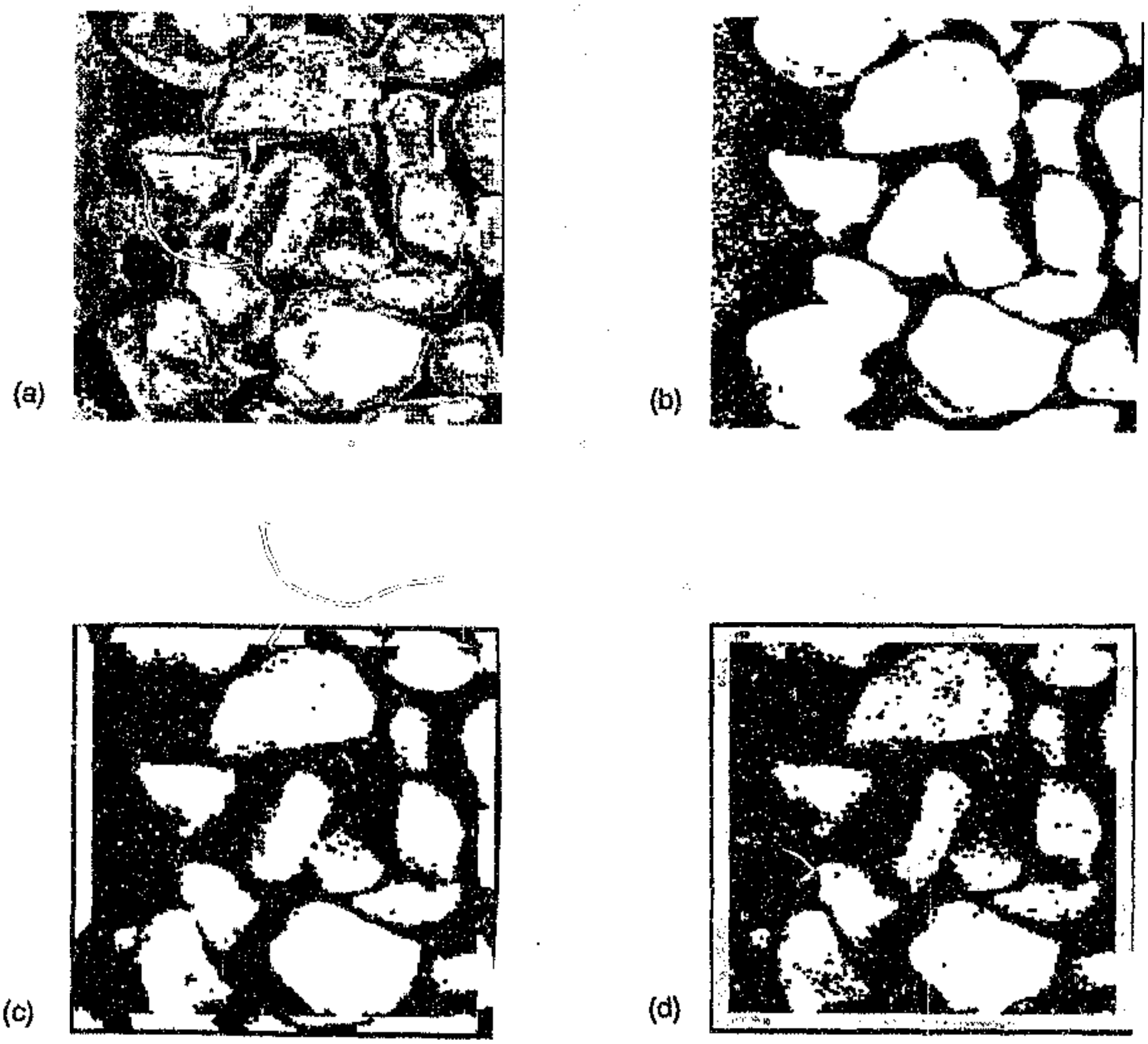

Figure 4.11: Example of using local thresholding to segment rock images, equations 4.8 and 4.9. (a) Original image. (b) Global thresholding at $T = 100$. Segmented images using local thresholding with T_g=100 and (c) k=0.1, (d) k=0.5.

4.4.2 Histogram-tail thresholding

Although the gray-level histogram of belt-scene images are near unimodal as shown in figure 4.10(b), they still contain valuable information. As observed in fig. 4.10(c), global thresholding still provides a *reasonable first estimate* of the locations of areas rock and non-rock, despite the merging and hole errors which vary tremendously from image to image.

It is thus prudent to try and exploit thresholding, in particular, global thresholding, despite the errors generated. From observation of hundreds of rock images, it is hypothesized that the pixels belonging to the *high* and *low end tails* of the histogram have a high probability of belonging to either *rock* or *non-rock* respectively. Very dark pixels are highly likely to be conveyor-belt rubber or the shadows between the rocks. Similarly very bright areas are highly likely to be rocks. Between the tails is the "gray area" which consists of roughly 80% of all pixels. The decision as to whether these pixels belongs to X or X' is relatively uncertain and as a first approximation depends on the position of the gray level of the pixel in relation to the rest of the histogram. This classification scheme of global thresholding at two values at the tails to provide *initial* estimates (seeds) for rock and non-rock areas, and has been incorporated as part of the overall processing strategy (chapter 5), although it must be kept in mind that such techniques cannot be used alone and that other techniques must be used to correct the errors resulting from such thresholding[4.8].

Tail thresholding is thus performed at two gray levels T_{low} and T_{high} (fig. 4.12) which segments an image into the following three areas :

I) Areas with a low probability of being rock, $F(x,y) \leq T_{low}$

II) Areas which do not a have a very high or low probability of being rock. $T_{low} < F(x,y) < T_{high}$

III) Areas with a high probability of being rock. $F(x,y) \geq T_{high}$

The values of T_{low} and T_{high} must adapt to the changing images and corresponding histograms; thus a heuristic method was developed to which adapts T_{low} and T_{high} to the changing statistics of the gray level histogram $h_I(g)$ of each image I . T_{low} and T_{high} is calculated by

$$T_{high} = k_{high} \cdot g_{\max(h(g))} \qquad 4.10$$

$$T_{low} = k_{low} \cdot g_{H_p(g)} \qquad 4.11$$

[4.8] In chapter 5 segmentation through thresholding will be used to *correct* edge errors, which is opposite to this scheme of other techniques being used to correct thresholding errors.

where k_{low} and k_{high} are some constants selected through experimentation. $g_{\max h(g)}$ is the gray level at the peak of the histogram, and $g_{H_p(g)}$ is the gray level at the p'th percentile of the cumulative histogram where $H_p(g') = \sum_{g}^{g'} h(g)$ (see figure 4.13). Figure 4.14 shows a typical result of tail thresholding.

Note that in many cases during experimentation it has been observed that this classification scheme (*tail thresholding*) often renders false segmentation. For example, areas of belt covered with a thin film of water often reflect light very strongly to give bright areas in the image, whilst shadows on dark rocks formed by indentations on the rock's surface are not part of the belt.

Instead of the ad-hoc method described above, other *non-heuristic* threshold selection methods based on, for example, criteria such as *maximum separability*, Otsu (1979), and *second-order gray level statistics*, Ahuja and Rosenfeld (1978), can be selected. Brink and De Jager (1987) provide a good discussion on various other threshold selection techniques and conclude that the selection is application specific, as is the case with rock images. This scheme of assigning probabilities to pixels (whether or not they belong to a certain segmentation group) can be extended further to more than two classifications using *relaxation* methods which are iterative in nature, and which require large amounts of processing time, which is not entirely deterministic. Berger (1985) used a multi-class classification scheme using thresholding techniques to reduce the gray levels in the image to 6 classes.

In summary it has been shown that thresholding rocks, although ambiguous, can produce useful thresholding results on piled rocks. Although the final rock identification process is to be based on edges detection, which is still to be discussed in section 4.5, tail thresholding can complement the rock recognition and extraction process.

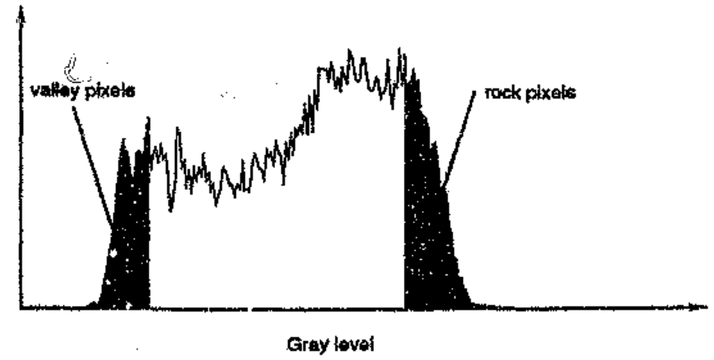

Figure 4.12: Classifying pixels at the tails of the gray level histogram.

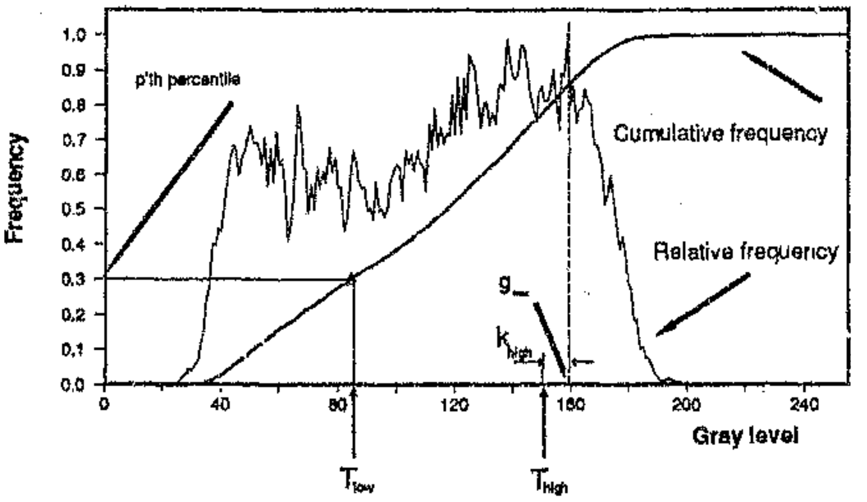

Figure 4.13: Example of selecting of T_{low} and T_{high} from the gray level histogram.

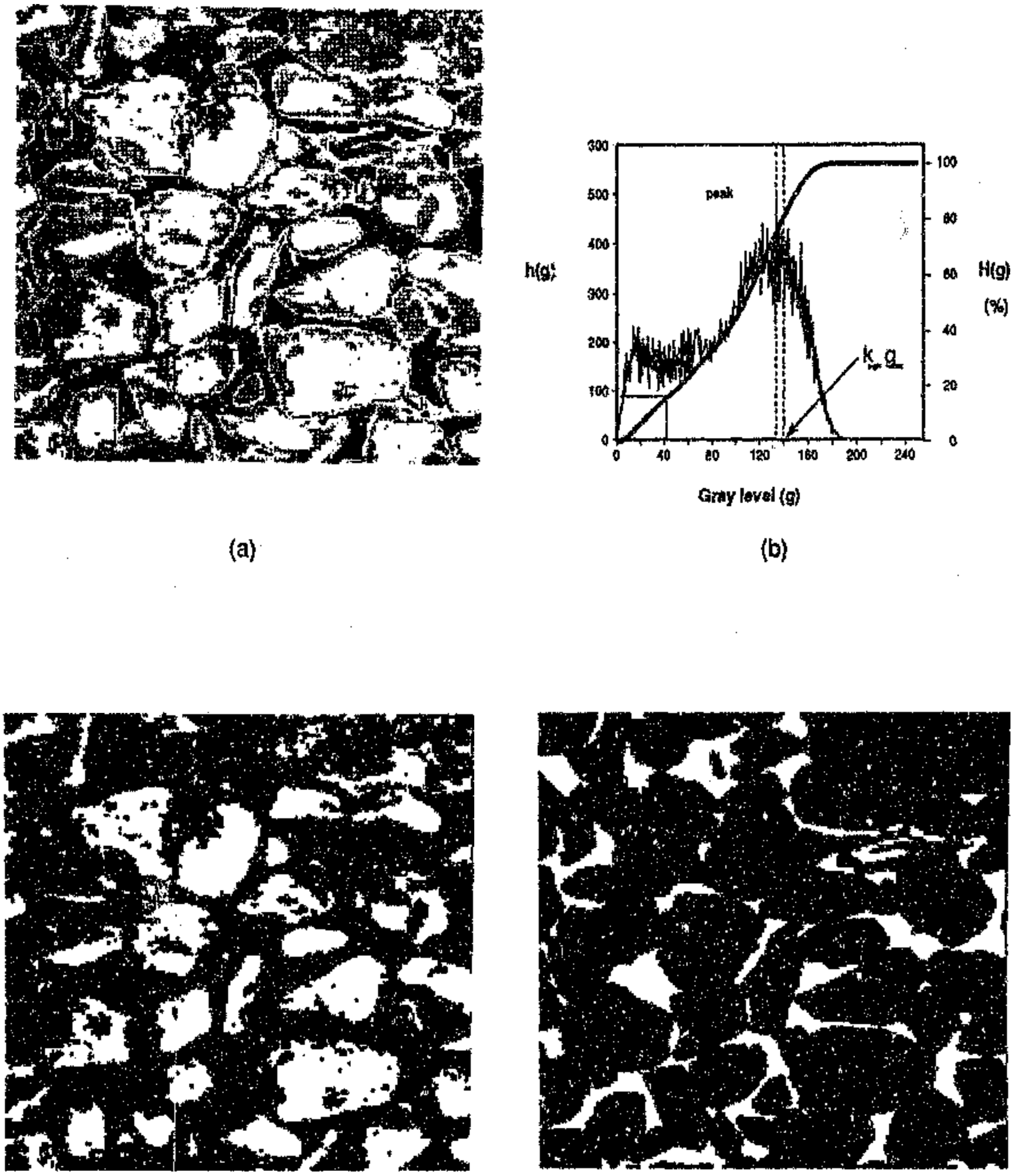

(a)

(b)

(c)

(d)

Figure 4.14: Example of thresholding a rockscene to obtain a *first estimate* of the location of areas rock and non-rock. (a) Original image, (b) histogram, (c) threshold at $T = 130$, (d) threshold at $T = 40$ and the image inverted to give non-rock as white areas.

4.5 ROCK EDGE DETECTION USING CLASSICAL EDGE DETECTION METHODS

4.5.1 Using Edge detection to Complement Thresholding

In the previous subsection it was shown that thresholding can provide initial estimates of the location of rock X and non-rock Y . However these "projected areas" produced by thresholding are not very accurate, with merging of adjacent rock-projections being a major source of errors. There is thus a need for additional information on the rocks in order to *merge* or *split* these projected areas. For example, consider the merged projections of two rocks in figure 4.15(b) resulting from a thresholding operation on the image 4.15(a). The application of a sensitive ***edge detector*** should reveal a valley between these two blobs shown in 4.15(c), allowing the merged regions to be split[4.9].

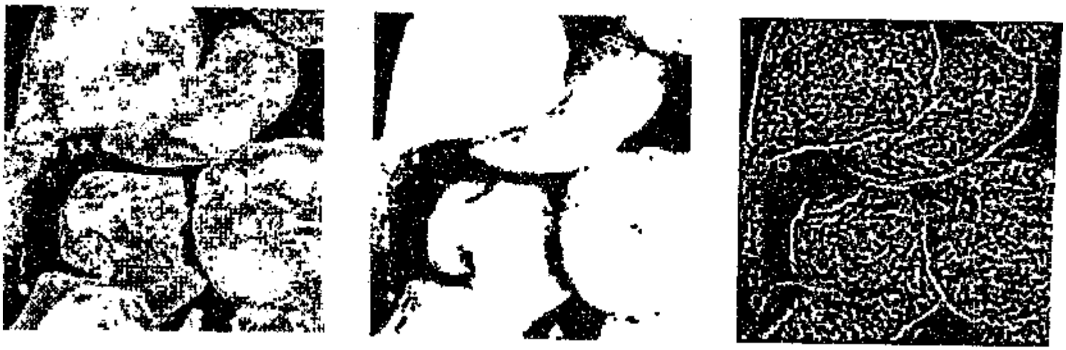
(a) (b) (c)

Figure 4.15: (a) Original image of rocks. (b) Threshold image of the image $T = 100$. (c) Result of a Laplacian edge detector (section 4.5.5) on image (a).

Originally edge detection was to be used as a support for thresholding which would be the primary operator, ie to divide over-merged areas as shown above[4.10]. However with time and experimentation the roles of thresholding and edge detection were reversed, with thresholding being used as a support for edge detection. This sub-section thus discusses edge detection as the primary segmentation technique.

4.5.2 Edge Detection and Image Filtering

An edge is defined in the Concise Oxford dictionary as (i) the crest of a narrow ridge, (ii) a sharp dividing line with which two surfaces meet abruptly, or (iii) a relatively thin terminating border, all which define features as

---

[4.9] The are other methods such as mathematical morphology for performing these split and joining corrections. The application of morphological methods in *addition to the more traditional ones will be discussed later in this chapter 5.*

[4.10] Correction of threshold images can be performed by other processes for example, curvature analysis of the boundaries of the objects in the threshold image (Berger, 1985). This is a costly process in terms of processing time and requires many rules to cater for the large variety of shapes to be expected.

as found in rockscenes. In computer vision an edge usually refers to a point between two regions (Lu and Jain, 1989). Therefore depending on the objectives, an edge can have many different interpretations. An interpretation of edges which describes their essence is that edges should form part of the *primal sketch* of line drawings (Marr and Hildreth, 1980), which is easier to work with than a full image because it contains less data, but which conveys almost all the information that a full image would, and which means something to the observer, (Charniak and McDermott, 1985).

Technically *edge detection* attempts to characterize all the intensity changes in the image in terms of the physical processes that originated them (Torre and Poggio, 1986). In the context of this research the purpose of the edge detection is to locate entities related to ∂X and to output a binary image pattern $E_{\partial X}$ which should be a primal sketch of the rockscene. The edge detection procedure is thus a *filtering* process from which details of *input signal I* not related to the rock edges ∂X must be filtered out. This edge detection or filtering process is however a complex and virtually impossible task to perform on a computer, whereas for own vision systems coupled to the brain with its knowledge and inference powers, this recognition is carried out quite correctly and very efficiently.

An image I is characterized by *bandwidth* and *dynamic range*, where bandwidth and dynamic range refer to the spatial frequencies and image intensity respectively. An image with a *large* size range of very angularly shaped rocks is considered to have a *large bandwidth*, whilst an image of spheres of a *single* size, is a *narrowband* signal. It is advantageous to try and reduce the bandwidth of an image which implies reducing the image content and classes of objects to be processed. However no steps can be taken with the rock scenes to reduce the bandwidth and in fact, ***the pursuit of rocksize is an attempt to measure a form of "bandwidth" of the image.***

Dynamic range or contrast refers to the range of brightness in an image. Part of the objective of the image processing is to ensure that the images are of sufficient contrast to ensure that the filtering or edge detection can be carried out efficiently, ie it is difficult to see in the dark ! However, contrast in a rock image depends on *how* the rocks cover the belt, and their colour, which is affected very strongly by moisture or water content as well as lighting or illumination. Observation of the numerous rockscenes shows that low contrast is a serious problem, (consider processing images of coal).

There are, however, many methods available for coping with low contrast, the simplest which is to increase the power of the lighting and increase the sensitivity of the camera hardware. There are also image enhancement techniques (section 4.5) which usually precede the edge detection process which can be used to increase contrast. Image enhancement techniques such as histogram modification (Rosenfeld and Davis, 1978) and equalization, as well as a number of other enhancement algorithms (Pratt, 1978) can be used, but are avoided because of the processing cost[4.11]. In general image *enhancement* techniques only provide for the *subjective* improvement of images as viewed by man, and methods for exploiting the subjectiveness of image enhancement procedures in computer vision have yet to be developed.

4.5.3 Two stage Rock Edge Detection Algorithms

There is a traditional belief in computational vision that edge-detection cannot be reached in a single step and at least two separate sequential stages are required for edge detection (Torre and Poggio, 1986). The first is the low level characterization of the intensity changes, and the second is the evaluation of these low-level entities *with knowledge in order to combine the output from the low-level edge detection processes into meaningful* regions or objects for the application in mind. Hence the requirement for the two stages Ψ_1 and Ψ_2 as discussed in section 4.1.

For this rocksize application, the *first stage* detects a set of edges E_d, which is the response of the edge detector to all characteristics of a particular image function. E_d thus contains *parts* $E^{*}_{\partial\chi}$ of the true rock edges $E_{\partial\chi}$ as well as unwanted edges E_n often construed as noise. This is because features which trigger the detector are not necessarily only rock perimeter edges, and conversely not all rock-edge features trigger the detector either. In summary we have

$$E_d = \Psi_1(I) \qquad 4.12$$

$$\text{and} \qquad E_d = E^{*}_{\partial\chi} \cup E_n \qquad 4.13$$

$$\text{where} \qquad E^{*}_{\partial\chi} \subset E_{\partial\chi} \qquad 4.14$$

The *second stage* Ψ_2 attempts to ***correct*** the edge pattern E_d in order to recover $E_{\partial\chi}$. This edge correction requires the classification of the valid rock edges $E^{*}_{\partial\chi}$ and noise E_n so that E_n can be removed leaving only $E^{*}_{\partial\chi}$. However there are still missing perimeter edges E_Δ ie gaps, where

$$E_\Delta = E_{\partial\chi} - E^{*}_{\partial\chi} \qquad 4.15$$

Thus the final estimate of the edges $E^{**}_{\partial\chi}$ is given by

---

[4.11] The DT2851 *frame-grabber amongst others*, usually allows for some form of histogram modification in (video) realtime through the use of the input-lookup -tables, ie LUTS.

$$E_{\partial x}^{**} = \Psi_2\{E_d\} = \Psi_2\{E_{\partial x}^{*}, E_n\} \qquad 4.16$$

where $$E_{\partial x}^{**} = E_{\partial x}^{*} \cup E_{\Delta}^{*} \qquad 4.17$$

where E_{Δ}^{*} is an estimate of E_{Δ} derived through the use of a-priori knowledge because $E_{\partial x}$ is not known. See figure 4.16 for a block diagram of the two stage edge detection scheme required to derive the rock boundaries

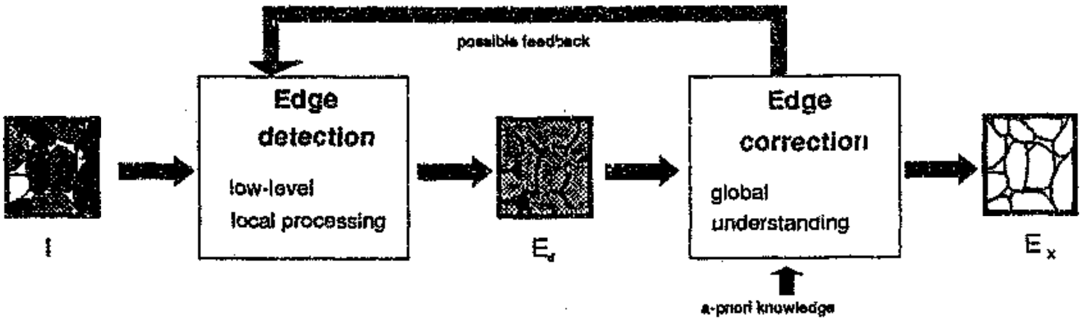

Figure 4.16: The edge detection process consisting of low level edge detection with a subsequent edge analysis and correction stage.

Although the literature generally treats these two stages of (I) edge *detection*, and (II) edge *correction* separately they are inextricably linked with the analysis steering the detection in a direction optimal for the detection of a particular type of edge. Looping back between stages I and II can take place because of the need to use the original image data to re-evaluate the correctness of an edge in terms of the original picture. The estimation of $E_{\partial x}$, E_n and E_{Δ} is an iterative procedure which can converge to an incorrect solution because of the fundamental uncertainty associated with the estimation of rock edges, discussed in section 4.5.3. As shown in figure 4.16 above, there is a need for some form of intervention with *a-priori* knowledge to ensure that the edges detected are sensible.

There is no established method of choosing a suitable algorithms from the many which are available, eg (Pratt, 1978), (Holyer and Peckinpaugh, 1989), for the edge detection scheme developed above. For most edge detection problems the solutions devised encapsulate specialist knowledge of the edges resulting in an application specific algorithm based on :

1. *Definitions* of the "edge" for that particular application. This is dependent on what the objects are and what information the user requires.
2. Philosophies and *criteria* for edge detection,

3. *Mathematical techniques* to be used for implementing the algorithm selected,
5. Processing time, which includes hardware considerations.

For example, the edges between different areas of vegetation in a satellite photograph are texture based, transitional, and not orientated in a particular direction, and accuracy may not be vital. However the edges of tracks on a silicon wafer are sharp and usually orientated in a vertical or horizontal direction, and accurate positioning may be very important.

Most edge detection algorithms can be grouped into the following (overlapping) classes: local, regional, global, heuristic, dynamic and relaxation, (Levialdi, 1980). All these different types of edge detection techniques have various advantages and disadvantages and the author proposes and will show that a union of certain "classical" as well "morphological" techniques yield an acceptable methodology for the treatment of rock images. Similar sentiment is expressed by Lee et al (1986) who state that morphological operations as well as all other techniques available should be combined as shown in figure 4.3, because of the increased complexity of images to be processed. This concept is proposed for rock images because, in general, no single edge detection algorithm is sufficient to cope with the large bandwidth of rock images, and not all algorithms may be tried because of limited time and processing power. This approach of combined techniques has been explored to a certain extent in the literature but constitutes a rich and largely unexplored area for further research. This includes parallel filter or image processing structures, as well as feedback and adaptive type algorithms. Some of these algorithms unfortunately are not totally deterministic because of the stochastic nature of the signals (rock images), which is undesirable for process control. In addition the complexity of the establishment of rules for combining the results of each parallel process to give one final result, is another area of research beyond the scope of this thesis.

4.5.4 The Uncertainty Principle

Before continuing with edge detection algorithms a formal statement regarding the uncertainty of detection of edges must be made.

According to Wilson and Granlund (1984) the key task in vision problems is to move from a pointwise description "the pixel at location X has magnitude m", to a description in terms of elementary events "an event of class C is located at position X". The classification of these events should *not* depend on *position*, thus some degree of *localization* is required. In addition these events should also be *independent of magnitude* because the magnitude varies with lighting conditions. Thus only *relative* distributions of energy can help with this classification. This implies that the signals to be classified should not be of arbitrary wide bandwidth, since such signals would tend to excite all classes equally, and in addition, they cannot have arbitrary large spatial extent, since no spatial localization is then possible.

These points lead directly to the ***uncertainty principle*** where signals are being used to infer the existence and location of certain classes of objects in vision systems as well as in quantum mechanics. The consequence of this principle in a vision system is, for example, that the application of a filter which increases the certainty of an object belonging to a certain class, does so at the expense of a loss of positional information. This fundamental difficulty with visual processing is most succinctly and precisely stated in the uncertainty principle which states that "a signal cannot be arbitrarily highly concentrated in both the spatial and [illegible] frequency domains"[4.12], a problem which is discussed by Wilson and Knutsson (1988), and which is generally the case with the rock images dealt with in this research. Thus a natural contradiction exists for the requirement of the simultaneous and accurate determination of both the *description* and *location* of objects in an image.

Therefore the objective of edge detection, which is to *identify* and *locate* edges related to the real rock edges, is inherently problematic, because algorithms which help to identify and separate one rock from another will obscure the rocks' positions, and vice-versa.

4.5.5 Rock Edge detection using Shadows

The assumption that an area of rock and non-rock is closely related to the image intensity was used initially together with *enhanced shadows* for edge detection. The motivation behind this use of shadows was that it was desirable to reduce actual image processing in order to achieve realtime performance. Angled lighting improves the definition of a rock edge, which implies that simple edge detection can be used to locate these shadows which should delineate the rock boundaries. However, as was discussed in chapter 2, enhancing the rocks' edges through the use of low angled light also enhances all other rock edges which are not necessarily part of the rocks' perimeters.

Static experiments were set up in a laboratory where the rock scene was illuminated with lights arranged in the five directions as shown in figure 4.17(a). These lights were termed the *north, south, east, west* and *top*. The principle was to capture images with illumination from each one of the light directions thus creating a set of five images of the *same* scene namely $I_n(x,y)$, $I_s(x,y)$, $I_e(x,y)$ and $I_w(x,y)$ from the four lights illuminating the scenes from the sides, and $I_V(x,y)$ which is image of the scene illuminated from vertically above. In this

---

[4.12] For example an impulse in the time domain has an infinite frequency spectrum, and [illegible] (1975).

way positional edge information is obtained which should allow for the creation of a continuous and closed edge pattern for each rock by combining the edge patterns together like a jigsaw puzzle. (Using angled light in this manner is similar in concept to the reconstruction methods discussed in chapter 2 which use structured light.)

The edge images can be combined in a number of ways to give the final shadow edge pattern $I_{sh}(x, y)$. The simplest method is to add arithmetically the images together as shown in equation [4.18] below where α, β, γ and ε are some scalar factors. For this application it is assumed that $\alpha = \beta = \gamma = \varepsilon$ for *equal* illumination from all sides. Other methods are to combine the images logically using OR or AND operations.

$$I_{sh} = \alpha I_N + \beta I_S + \gamma I_E + \delta I_W + \varepsilon I_V \qquad 4.18$$

The shadow method was implemented in the laboratory on static images where $I(t) = I(t + \tau)$ and where t, τ is time, thus allowing for each image to captured one *after* another, instead of simultaneously, as will have to done with an actual plant instrument. The segmentation of static [illegible] scenes resulting from the combination of shadow enhanced images with global *thresholding*, equation [4.18], is shown in figure 4.18(g). [illegible] produced better segmentation when compared with simple global thresholding, figure 4.18(h).

However these methods of shadow enhancement are rejected for a number of reasons.

(i) The scene is moving and it is impossible to capture the *same scene* at *different positions* on the belt without some change taking place to the scene. The time to capture a frame is typically 1/30s and with a belt moving at typically 0.5ms^{-1}, a rock on the belt would be displaced 17mm, thus not allowing for the capture of the *same* rocks in the camera's field of view. In order to overcome this problem multiple camera and frame grabber systems, or a fast and accurately-moving camera would have to be used in order to facilitate the capture of the same scene, which is a costly and undesirable solution as far as reliability and maintenance is concerned.

In addition to the rocks in the scene changing position relative to the camera's field of view, the rocks will also rearrange their relative positions due to shaking and jigging effects of the belt. If $I_{\Omega(t)}$ is the image of a number of specific rocks captured in a scene at a point on the conveyor belt at time t , then in general $I_{\Omega(t)} \neq I_{\Omega(t+\tau)}$ where τ is time delay between successive image capture, and the rocks X as found in $I_{\Omega(t)}$ are the same as those in $I_{\Omega(t+\tau)}$. There are correlation and re-alignment algorithms which can re-align images together based on common features. However these algorithms are time-consuming, and the resultant rock edges are blurred because the rock patterns have changed. These blurring effects (which are not due to shutter speed), can be minimized by decreasing the capture time τ between images

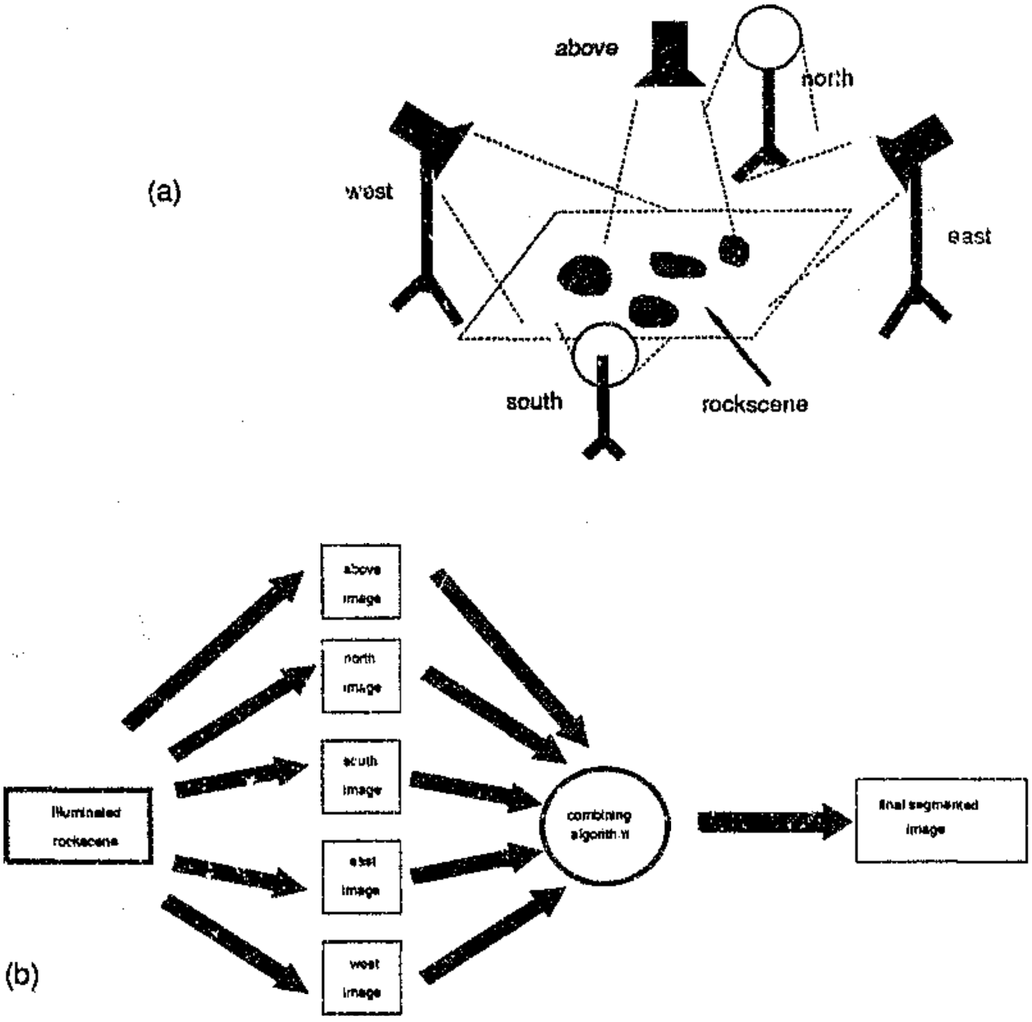

Figure 4.17: (a) Schematic diagram of experimental setup to enhance shadows for quick edge-detection. (b) Combining shadow images to detect a continuous rock-boundary.

through the use of strobe lights and faster frame grabbers, which leaves less time for the rocks to shift. However the short life and high cost of strobe lights, as well as the high cost of faster hardware makes this system impractical and uneconomical.

(ii) Angled light amplifies unwanted edges E_u by emphasizing shadows caused by rock-surface ridges which increases the difficulty of determining E_{3x} in numerous, but not all rockscenes.

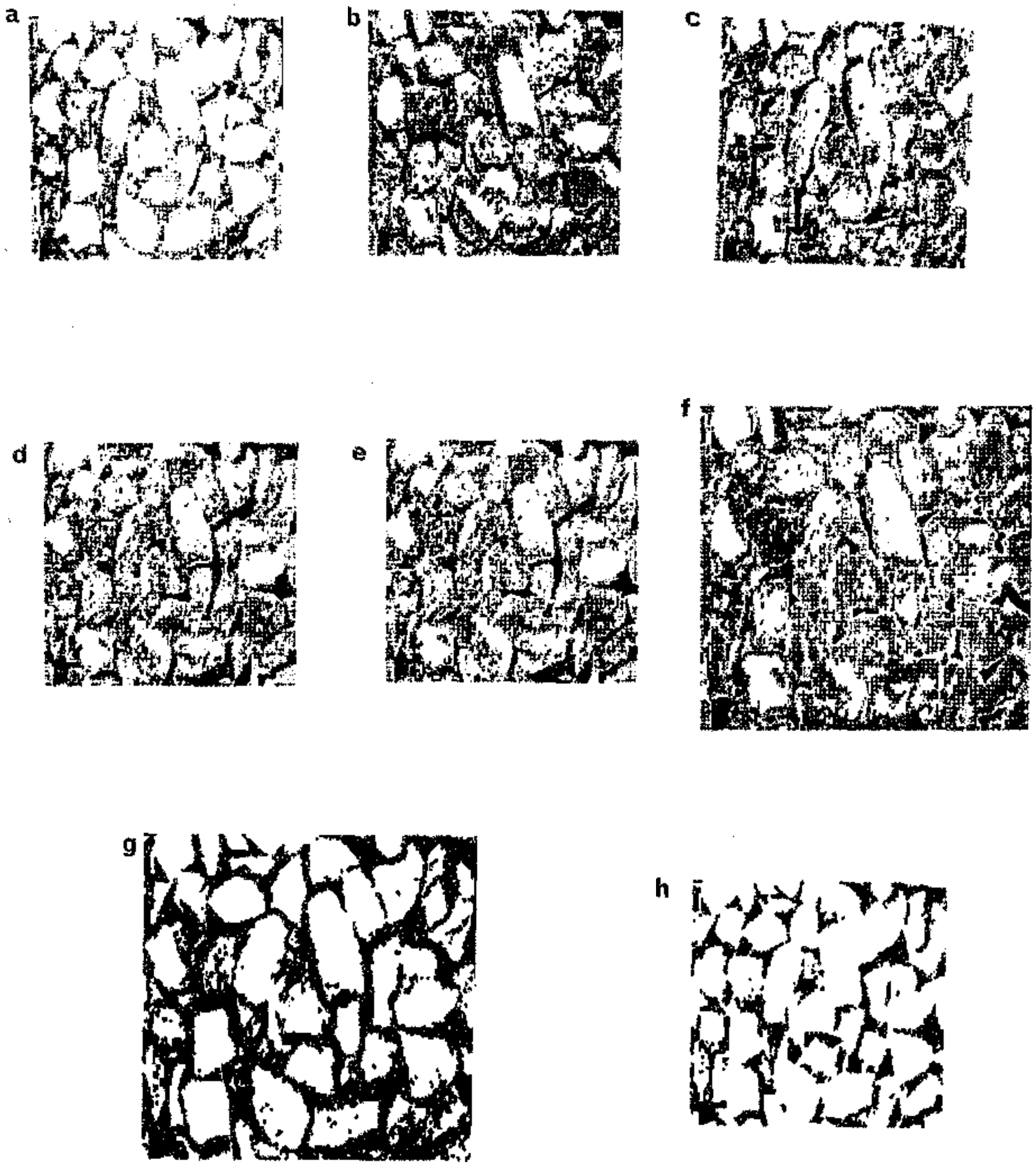

Figure 4.18: (a) Rock scene illuminated from above I_v , (b) north I_n , (c) east I_e , (d) south I_s , and (e) west I_w . (f) Result of summing all images together I_{sh} as given by equation [4.18] with the exception that $\varepsilon = 0$. (g) Global thresholding of the resultant combined shadow image I_{sh} . (h) Global thresholding of the above image I_v .

4.5.6 Rock Edge detection using Differential Techniques

In this subsection *differential*-edge detection methods are discussed as an alternative to thresholding and shadow edge detection (section 3.5.5) for primary rock detection.

The basic tool for most of these *differential*-edge detection methods is the two dimensional *convolution*, a linear operation where a kernel or mask H_p is convolved with input image F to produce output gradient functions G_p $p = 1...n$ where n is the number of function masks, as shown in equation [4.19] and [4.20]. See Abdou and Pratt (1979), Pratt (1978).

$$G_p(x,y) = F(x,y) * H_p(x,y) \qquad 4.19$$

$$\Leftrightarrow G_p(x,y) = \int_u \int_v F(x+u, y+v) H_p(u,v) du dv \qquad 4.20$$

At each pixel, the n gradient functions G_p are combined with a linear or non-linear operator $\Theta\{\cdot\}$ to create an edge pattern or enhanced version of F where

$$G(x,y) = \Theta\{G_p(x,y)\} \qquad \text{for} \quad p = 1...n \qquad 4.21$$

The different edge detectors or filters are designed by selecting various masks $H(x,y)$ and functions Θ which can, for example, be a point magnitude, or rms value. To illustrate this consider two masks H_1 and H_2 applied separately to image F to give G_1 and G_2; a *rms* operator is given by

$$G = \Theta\{G_1, G_2\} = \sqrt{G_1^2 + G_2^2} \qquad 4.22$$

For a discretized image, a convolution is performed by passing a window of dimension M,N over the image where each element of the image within the window is multiplied by the corresponding window coefficient and summed to produce the output image $G(i,j)$ as shown in equation. [4.23].

$$G(i,j) = \sum_{k=-\frac{M}{2}}^{\frac{M}{2}} \sum_{l=\frac{N}{2}}^{\frac{N}{2}} H(k,l) F(j+k, i+l) \qquad 4.23$$

$H(k,l)$ are the coefficients of the convolution window, and M and N are the dimensions of window MxN. The design parameters required are the size and shape of the window and the values of $H(k,l)$.

According to Abdou and Pratt (1979) convolution edge-detector operators can be classified into two groups, namely *differential* and *template-matching* operators. Micheli et al (1989), however, classify edge detectors as being either *extrema* or *zero-crossing* schemes, which are the first or second order differential operators respectively, where the n'th operator is denoted $\frac{d^n}{d^n x} f(x) = D^n f(x)$ for some continuous image function $f(x)$.

In chapter 2 it was shown that edges of objects in a scene are related to the image gray level and its *derivatives*, equations [2.2 -2.4]. There is thus a strong motivation for evaluating $D^1I(x,y)$ or $D^2I(x,y)$. Amongst the numerous *differential* operators are the Roberts, Prewitt and Sobel operators whose masks are given in figure 4.19, (Pratt, 1978). Figure 4.20 shows a number of *template* operators, which are effectively first derivative operators.

$$H_1=\begin{bmatrix}1 & 0 & -1\\ c & 0 & c\\ 1 & 0 & -1\end{bmatrix}\qquad H_2=\begin{bmatrix}-1 & -c & -1\\ 0 & 0 & 0\\ 1 & c & 1\end{bmatrix}\qquad H_1=\begin{bmatrix}0 & 1\\ -1 & 0\end{bmatrix}\qquad H_2=\begin{bmatrix}0 & 1\\ 0 & -1\end{bmatrix}$$

(a) (b) (c)

Figure 4.19: Masks (a) and (b) are for the Prewitt (c=1) and Sobel (c=2) operator. (c) is the Roberts operator.

$$\begin{bmatrix}3 & 3 & -5\\ 3 & 0 & -5\\ 3 & 3 & -5\end{bmatrix}\qquad \begin{bmatrix}3 & -5 & -5\\ 3 & 0 & -5\\ 3 & 3 & 3\end{bmatrix}\qquad \begin{bmatrix}1 & 0 & -1\\ 1 & 0 & -1\\ 1 & 0 & -1\end{bmatrix}\qquad \begin{bmatrix}1 & 1 & 1\\ 0 & 0 & 0\\ -1 & -1 & -1\end{bmatrix}$$

Kirsch Kirsch 3-level 3-level

Figure 4.20: Template matching operator masks (a) Kirsch (b) 3- level

Of particular interest is the Laplacian operator ∇^2 which is a second order operator, see equation [4.24], the mask which is shown in figure 4.21.

$$\nabla^2 I(x,y)=\frac{\partial^2 I}{\partial x^2}+\frac{\partial^2 I}{\partial y^2} \qquad 4.24$$

$$\begin{bmatrix}1 & 1 & 1\\ 1 & -8 & 1\\ 1 & 1 & 1\end{bmatrix}$$

Figure 4.21: Laplacian operator mask.

The criterion for the selection of the best edge detector is dependent upon the ability of the selected operator to detect only rock edges at all locations where these rock edges are supposed to exist without introducing noise into the edge image. This must hold for rock of all shape and size under all conditions as found on the conveyor belt to be instrumented. In addition the set of pixels representing the edge must be continuous and connected as defined in figure 4.6 and must be as thin as possible thus establishing a primal sketch of *lines* as shown in figure 4.22.

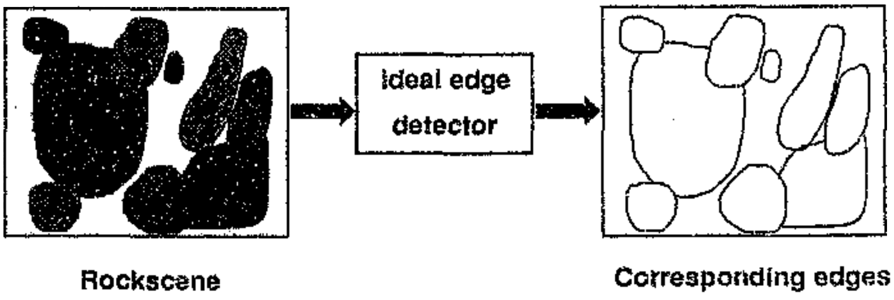

Figure 4.22: The ideal edge detector.

Figures 4.23, and 4.24 present edge patterns E_d resulting from the application of a number of differential edge-detection filters to rock scenes of large and small rocks[4.13]. From the resulting edge patterns E_d it is observed that:

i) Each method detects a *similar* edge pattern of the rock edges, which are easily understood and interpreted by the observer.

ii) Most rocks are identifiable by means of closed edge rings which are generally *complete* and *convex*.

iii) In comparison with the original image, each method detects a large proportion of the conceived true edge pattern $E_{\partial X}$. However parts of the true boundary pattern $E_{\partial X}$ are missing and noise E_n is introduced into the patterns in varying amounts. In summary $E_d \neq E_{\partial X}$ but $E_d = E^*_{\partial X} \cup E_n$.

iv) Many noise edgelets E_n which do not contribute to the estimation of rocksize, are nevertheless valid as they do correspond to real surface irregularities of the rocks such as ridges and valleys. The generation of this superfluous information, not related to size, makes the unambiguous recognition and extraction of the edge patterns $E_{\partial X}$ very difficult.

[4.13] These rockscenes were captured from a closed-loop conveyor-belt system circulating quartzite material from a gold mine. Belt speed was $0.5 ms^{-1}$.

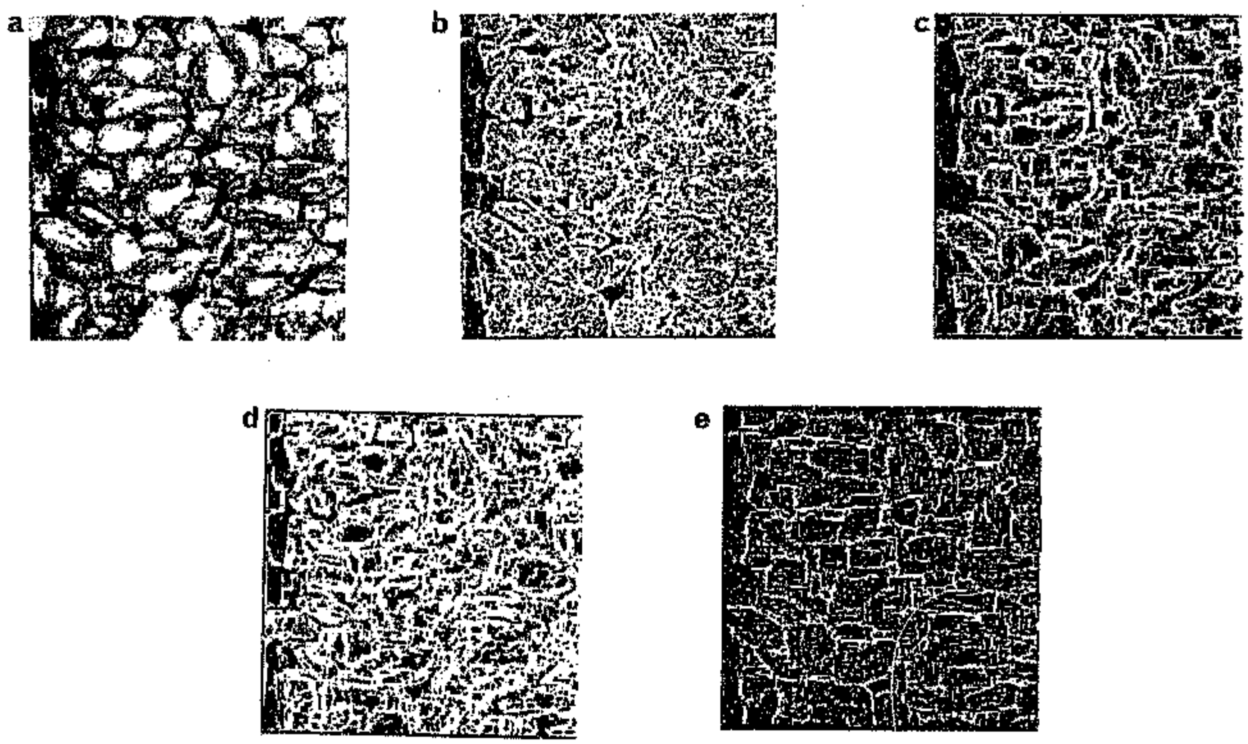

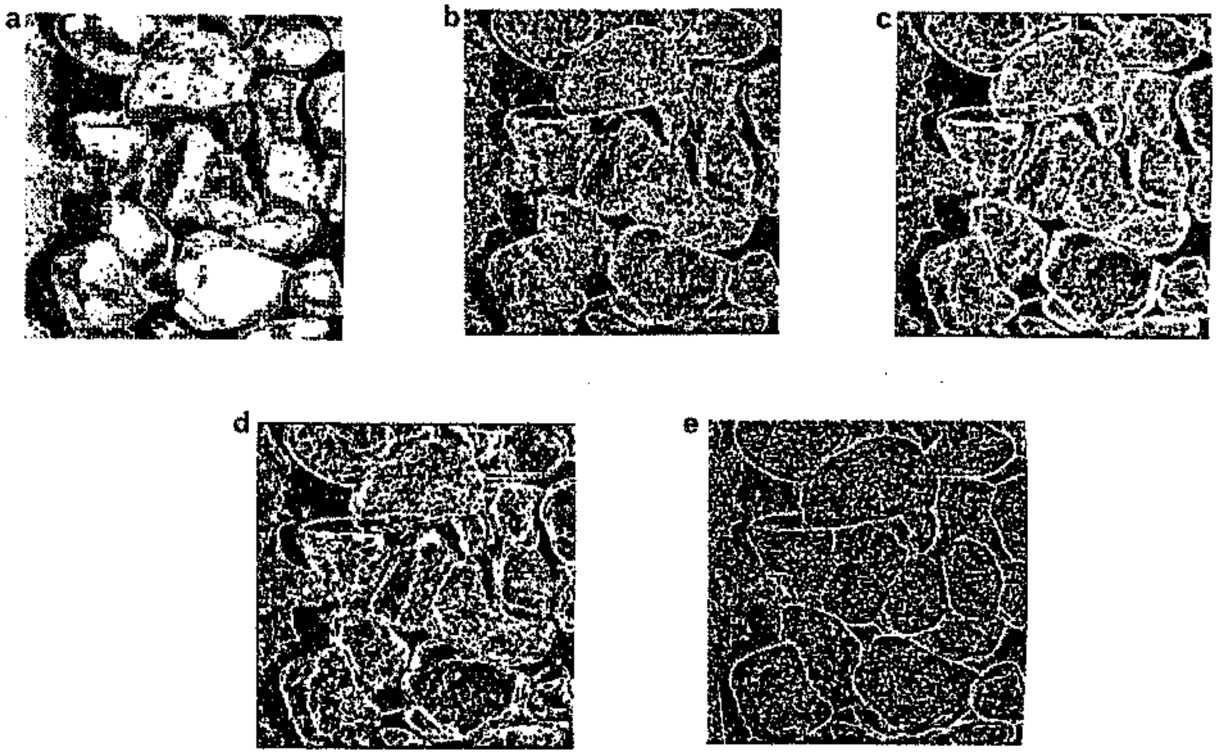

Figure 4.23: (a) Original. Results of the application of (b) *Prewitt* (c) *Roberts* (d) *Sobel* and (e) *Laplacian* edge detectors on a scene of large and small rocks.

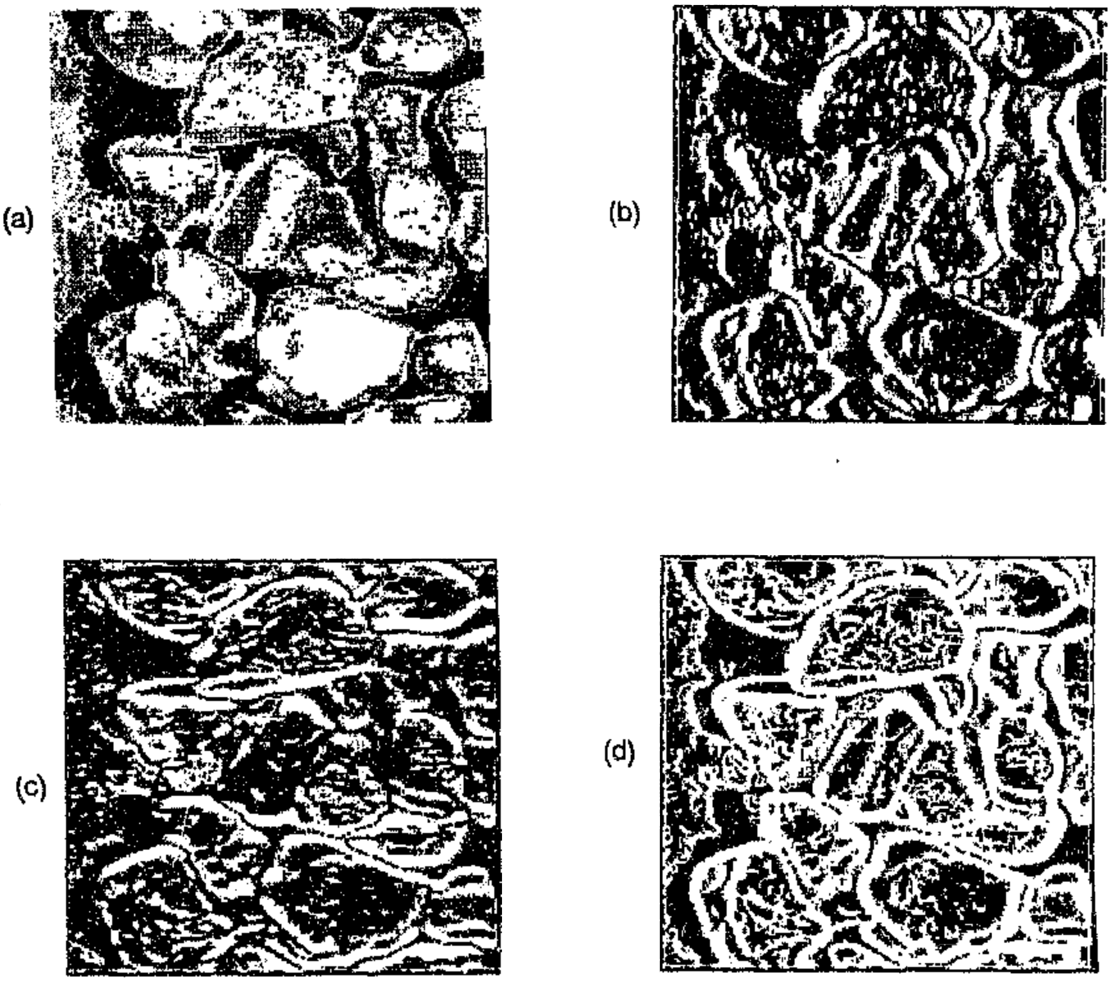

Figure 4.24: (a) Original image. Results of the application of the (b) *vertical* and (c) horizontal gradient operators to a scene of large rocks. (d) Result of combining the output from the vertical and horizontal gradient operators using the rms operator as given in equation [4.22].

From examination of the results of the edge detectors as shown in figure 4.23 and 4.24 it can be observed that the piling and packing of rocks complicates the identification of the true rock edges E_{ax} because of the effects of *occlusion* and shadows. Consider the edge patterns generated with the Laplacian edge detector as shown in figure 4.25. Figure 4.25(a) was derived from scene of a number of *separate* rocks in a *monolayer*, while figure 4.25(b) was derived from the same rocks except they are now pushed together to *touch* and *overlap* which forms a complex scene. As a consequence shape recognition algorithms based solely on the convexity of particle edge patterns must be excluded because small areas of rocks may be missing due to the protrusion of neighbouring rocks which result in non-convex boundary patterns. The randomness of the occurrence of these non-convex as well as convex rings implies that shape analysis to identify a single rock must be carried out simultaneously with *all* neighbouring rocks on a global and syntactic basis in order to recognize occlusion given a-priori knowledge of the basic rock shapes, a somewhat daunting, if not almost impossible, task. This latter statement implies that local analysis for identifying rocks is *not sufficient*, and that *global* as well as *local* image analysis for object extraction is required. *Simultaneous global* and *local* analysis is analogous to observing a painting close up to see details and then gradually moving further away so as to understand the overall picture better. In the same way one would repetitively move back and forth to understand and interpret a painting, so the same mechanism should be applied to the rock image and the edge patterns in order to identify the rocks correctly. These types of algorithms include *multi-resolution* and *pyramidal hierarchical* methodologies (Ichikawa, 1981), (Hong and Schneier, 1984), and were not considered here because of the large computing and memory storage capabilities required. In addition the ability to correlate and combine information at different scales is still a new area of fundamental research.

Observation of the different types of edge detectors (figure 4.23 and 4.24) shows that the Laplacian ∇^2 operator appears subjectively to provide the best edge patterns for both large and small rocks. However the Laplacian patterns E_{∇^2} are far more noisy because the Laplacian operator is a rotationally symmetric operator (Torre and Poggio, 1986) which is not sensitive to edges orientated in any particular direction, as are the vertical and horizontal edge detectors shown in figure 4.24. The Laplacian thus detects most undulations in gray-level image function especially impulse or spot noise which is characteristic of rock surfaces. In addition to the noise edges, second-order edge detectors can produce phantom or spurious edges which have no correlation to significant changes in image intensity, but rather points of inflection (Clark, 1989).

These noise or unwanted edge components imply that some post processing must be applied in order to clean up the edge patterns which are unacceptable for chord measurements as defined in section 4.3. In the next section it will be shown that pre-filters can *reduce* the amount of false edges by removing the high frequency impulse noise, thus reducing the amount of edge correction processing required for actual chord or area measurements to be made, (stage Ψ_2).

If the processing time for a very good edge detector Ψ_1 which removes the need for a edge-correction stage Ψ_2, is less than the time required for a mediocre Ψ_1 such as the Laplacian, which requires a substantial edge-correction Ψ_2 , then the use of an edge detector such as the Laplacian is not justified.

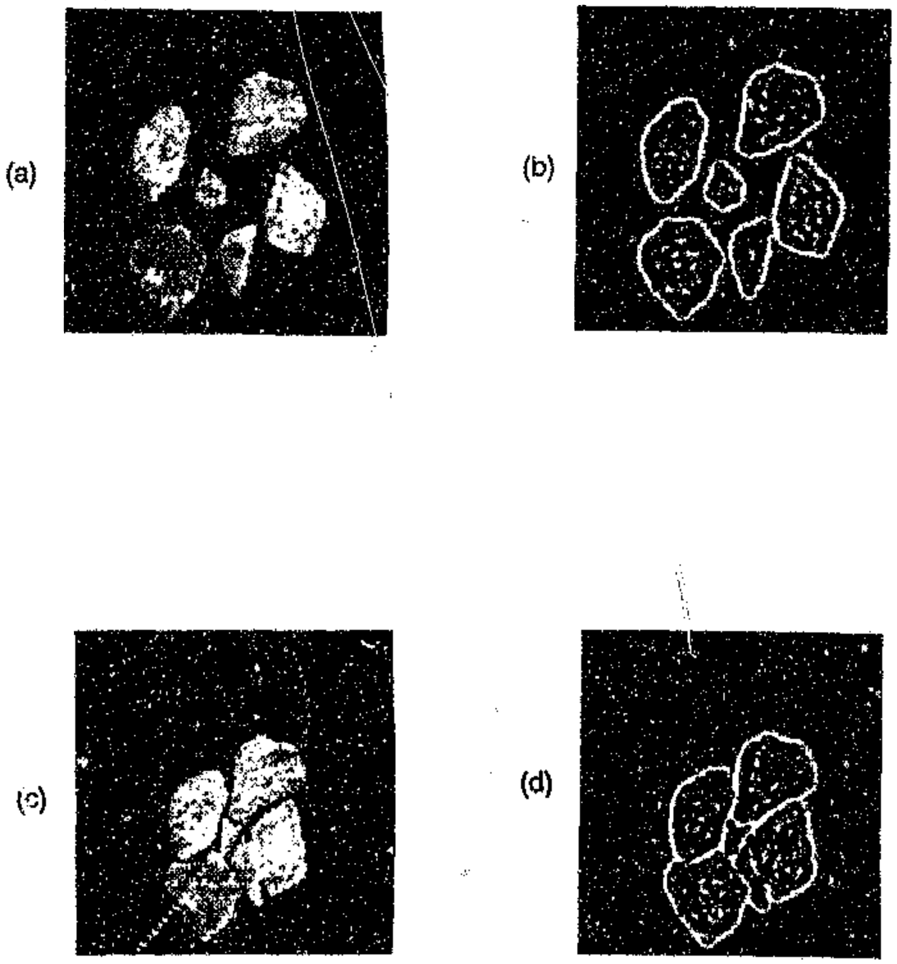

Figure 4.25: (a) A scene of separate rocks. (b) Edge patterns of separate rock scene after application of the Laplacian. (c) Scene of the same rocks in figure 4.25(a) except they have been pushed together. (d) Edge pattern of the touching rocks shown in (c) after application of the Laplacian operator.

4.6 PRE-FILTERS

Edge detection is essentially a problem of numerical differentiation (Torre and Poggio, 1986) and differentiation amplifies high-frequency noise, resulting in the loss of stability or continuity from the original image. This problem is emphasized in the section 4.4.5 where it was shown that the impulsive nature of the gray-level function of a rock scene results in a saturation of edgelets in the edge image which are not part of the rocks' edges.

The problem of edge detection is ill-posed in the classical sense because of noise (Torre and Poggio, 1986), (Micheli et al, 1989), but can be transformed into a well-posed problem by methods which *bandlimit* the image by ***lowpass filtering*** . Filtering prior to edge detection is shown schematically in figure 4.26.

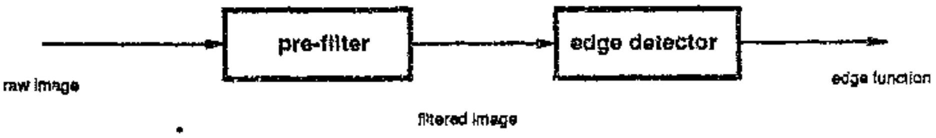

Figure 4.26: Block diagram showing a prefilter being applied to an image before edge detection in order to reduce the amount of noise resulting from differential operators.

Lowpass filtering can be achieved in the (i) spatial, (ii) spatial frequency, or (iii) time domain, using linear or non-linear filters. For example, time domain filtering is used in astronomy, where images are captured one after another sequentially and averaged to reduce spurious impulse noise. This method cannot be applied here because of the invariant and stochastic nature of the signals of interest. In the spatial domain, function fitting, including *interpolation* (Haralick, 1984), (Narwal, 1987), as well as *convolution* with band-limiting functions (Marr and Poggio, 1979), (Marr and Hildreth, 1980) are widely used lowpass-filtering techniques. Gaussian, Hermite and prolate are some of the functions used by many authors to achieve this filtering using convolution. The Gaussian in particular is very popular. However the filtering effect of the different functions becomes very similar when the masks are small and consist of a small number of elements. Filtering in the Fourier domain through the use of the Fast Fourier Transform (FFT) is very useful for removing cyclic noise, but is inappropriate for these rockscenes because the image impulse noise is randomly distributed.

Lowpass filtering, in general, has a disadvantage in that the edges of the image features are smeared out, which is agreement with the *uncertainty principle* discussed in section 4.4.3. Figure 4.27 shows the typical distortion caused by a lowpass filter as applied to an (a) clean and (b) noisy 1-D step edge. The effect of the filtering on 1-D edge detector is shown in figures 4.27(c) and (d) respectively where the filtered edge in 4.27(d) results in a less precise localization of the edge after application with a Laplacian.

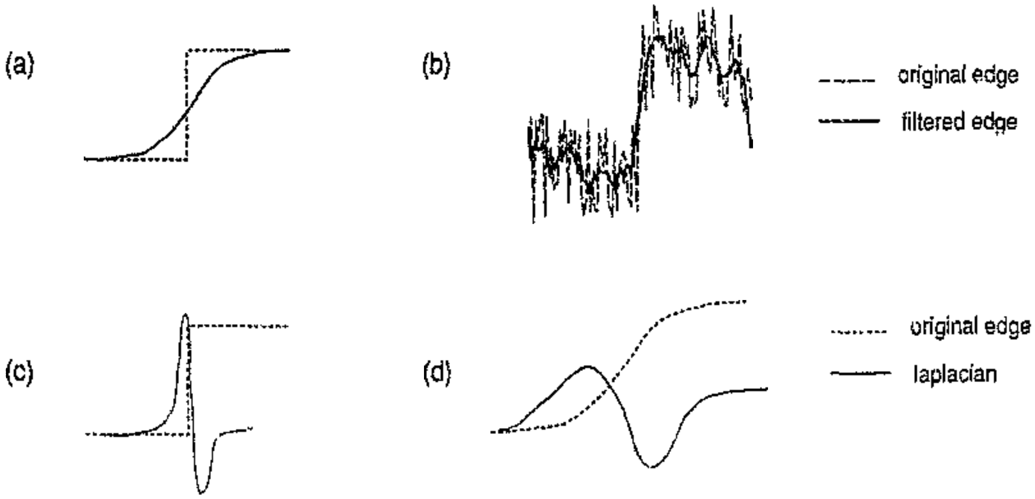

Figure 4.27: Example of the smearing caused by a filter on an (a) clean and (b) noisy 1-D step edge. Figure (c) shows the result of applying a Laplacian edge detector to a clean edge and (d) shows the result of applying the Laplacian edge detector to a filtered edge.

There are a large number of digital filtering techniques in the literature which can be applied to digitized images in which the windows of operation vary in size and shape as well as in character, (Pratt, 1978), (Kuan et al, 1985) and (Hu and Rabiner, 1972). The filters include 2-D infinite impulse response (IIR), and finite impulse response (FIR), which are generally difficult to design in 2-D especially as far as stability is concerned, (Shanks et al, 1972). With all these filters, the objective is reduce this smearing effect, whilst reducing impulse noise and concentrating the energy of the image signal into *valid* features, ie the rocks.

The next subsection shows the results of prefiltering with various filters before edge detection. The resultant edge patterns show that the incorrect choice of filters can corrupt the image instead of improving edge detection, and that different filters have different effects on the output edge patterns. Note that for all filters, the ease and speed of implementation is as important as the quality of filtering.

4.6.1 Nearest Neighbourhood Averaging Filters

The nearest neighbourhood averaging (NNA) filter is implemented by using the convolution operation given in equation [4.23], see Davis and Rosenfeld (1978), Pratt (1978). These filters are based on the assumption that the gray levels of K [illegible] belonging to the same population within a $(2k+1)\times(2k+1)$ window are *highly* *correlated*. According to Davis and Rosenfeld (1978), the images are composed of compact regions of essentially constant gray level, i.e., that underlying the observed image is an ideal image consisting of regions of *constant* gray level, but that the observed image has been corrupted by white noise.

The NNA filter functions by replacing the pixel at the centre of the window with the *average* of the K neighbours. Averaging over a large window produces a large amount of smoothing and attenuation of noise, whilst averaging with a small window, leads to a lower attenuation of noise and a higher preservation of detail. Thus the size of the rocks and the size of the filter are interlinked and small filters (windows) are required for scenes of small rocks, and large filters for large rocks. Thus there is a requirement to adapt the scale of the filter to the scale of the objects being detected, which will allow for the detection of objects at different levels of detail without too much edge blurring.

This adaptive filtering according to the scale or size of the objects leads to multi-frequency analysis of images, where for example, the $\nabla^2 G$ edge operator has proved very effective for detecting edges or intensity changes at different spatial frequencies. The $\nabla^2 G$ operator results from the unification of a Gaussian filter with the Laplacian edge detector to form one operator. Thus by controlling σ, which is the width of the Gaussian filter, one can detect edges that relate to edges of objects of different size.

Most images of autogenous rockfeed consist of rocks whose size range (bandwidth) is large. Such scenes, which contain different sized features in different parts of the same image, require multi-resolution filters (a parallel processing structure) which can be applied to a number of copies of the *same* image so that various edge sets belonging to different sized features may be identified. In addition, there is a great deal of potential in this method to *track* edges of rocks in a single image in order to establish closed boundaries. However, multi-frequency filtering was not adopted for the working algorithms in this study because of processing time and computer memory limitations. In addition, this approach does not quite fit in with the edge detection strategy (one of many) which can be developed for rock-edge detection. Although multi-frequency analysis is one of many viable approaches to the rock-edge detection problem, such techniques were not pursued any further, with the exception of laboratory experimentation to gauge the maximum size of a filter to remove impulse noise without affecting the small rocks. See Hearn (1988), Lu and Jain (1989), Yuille and Poggio (1986) for further details on multi-frequency filtering and edge detection.

For rock edge detection using the Laplacian operator, pre-filtering is a very important operation because the Laplacian is sensitive to impulse noise. A simple 3x3 averaging filter (mask given in figure 4.28) has been applied *twice* in sequence to the raw rock images of figure 4.29(a) and (b), and the results of this pre-filtering are shown in figure 4.29(c) and 4.29(d). It is observed that the resultant rock patterns are far cleaner and softer.

This filtering effect can also be observed in figure 4.30 in which we present a 3-D views of the gray-level *function* of the *raw* 4.30(a) and *filtered* 4.30(b) image. The effect of the pre-filtering on the various edge patterns is shown in figure 4.31 and 4.32 where the edge patterns for a scene of large and small rocks are pres[illegible] the edge patterns of the filtered images are *very much cleaner* with *less false edges* , compare with imag[illegible] figure 4.23. The effect is particularly dramatic for the Laplacian edge detector because the filter has effectively removed much of the impulse of spot noise from the image.

$$\frac{1}{9}\begin{bmatrix} 1 & 1 & 1 \\ 1 & 1 & 1 \\ 1 & 1 & 1 \end{bmatrix}$$

Figure 4.28: The mask for a 3x3 nearest neighbour averaging (NNA) mask

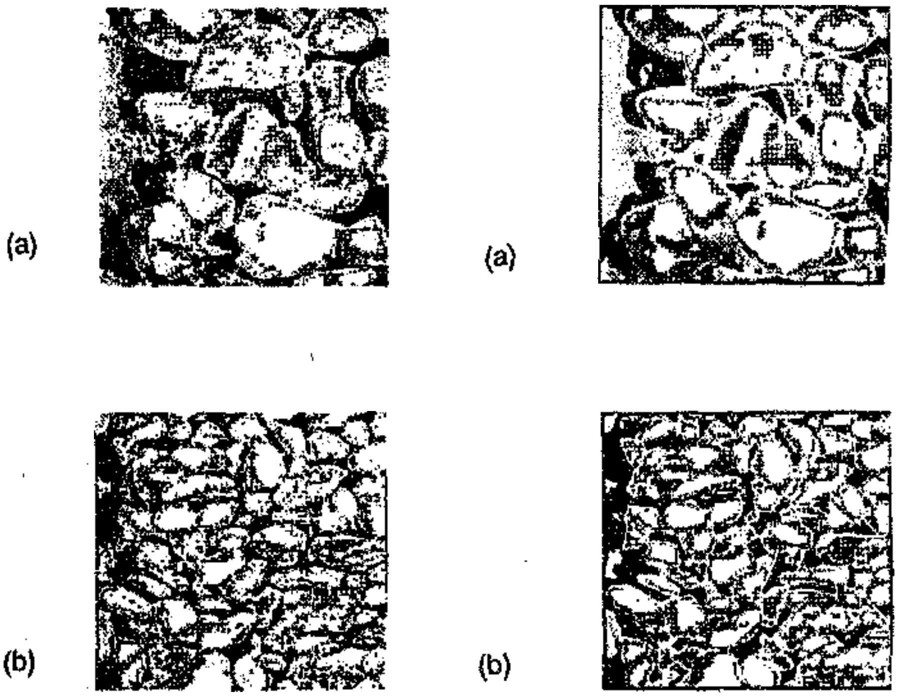

Figure 4.29: Example of applying the nearest neighbourhood averaging (NNA) filter to images of large (a) and small (b) rocks.

The results of all edge detection convolutions are functions themselves. Thus in order to derive a binary-edge pattern E_d, the resultant edge images $G = G(x, y)$ as given in equation [4.25],

$$G = \Psi_{\nabla^2}\Psi_{NNA}\{I\} \qquad 4.25$$

must be threshold further in order to derive the binary edge pattern E_d as discussed in section 4.3. Ψ_{NAA} denotes the NAA filter, and Ψ_{∇^2} denotes the Laplacian edge detector. In order to threshold G its histogram $h_G(g)$ is determined and the global threshold T is determined by calculating p_e'th percentile from the cumulative histogram $H_e(g)$.

For display purposes, the resultant edge functions in figure 4.31 and 3.32 from the different edge detectors and rpe-filter are displayed at three different thresholds to give a pseudo 3-D effect. The thresholds are for the Laplacian T=1,2,3, Roberts T=10,25,40, Prewitt T=30,50,70, and Sobel T=50,70,90.

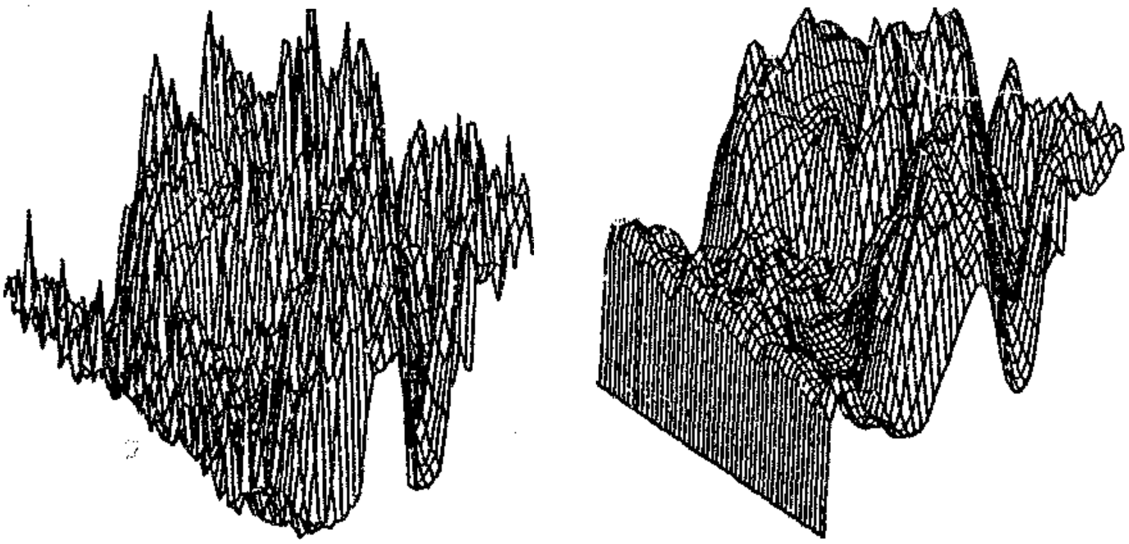

Figure 4.30: (a) Three-dimensional view of the gray level function from part of the image of a rock scene. (b) Three dimensional view of the same image function after application of the nearest-neighbourhood averaging filter three times, showing how the edges have been smoothed and "smeared out", and the images cleared of sharp impulses.

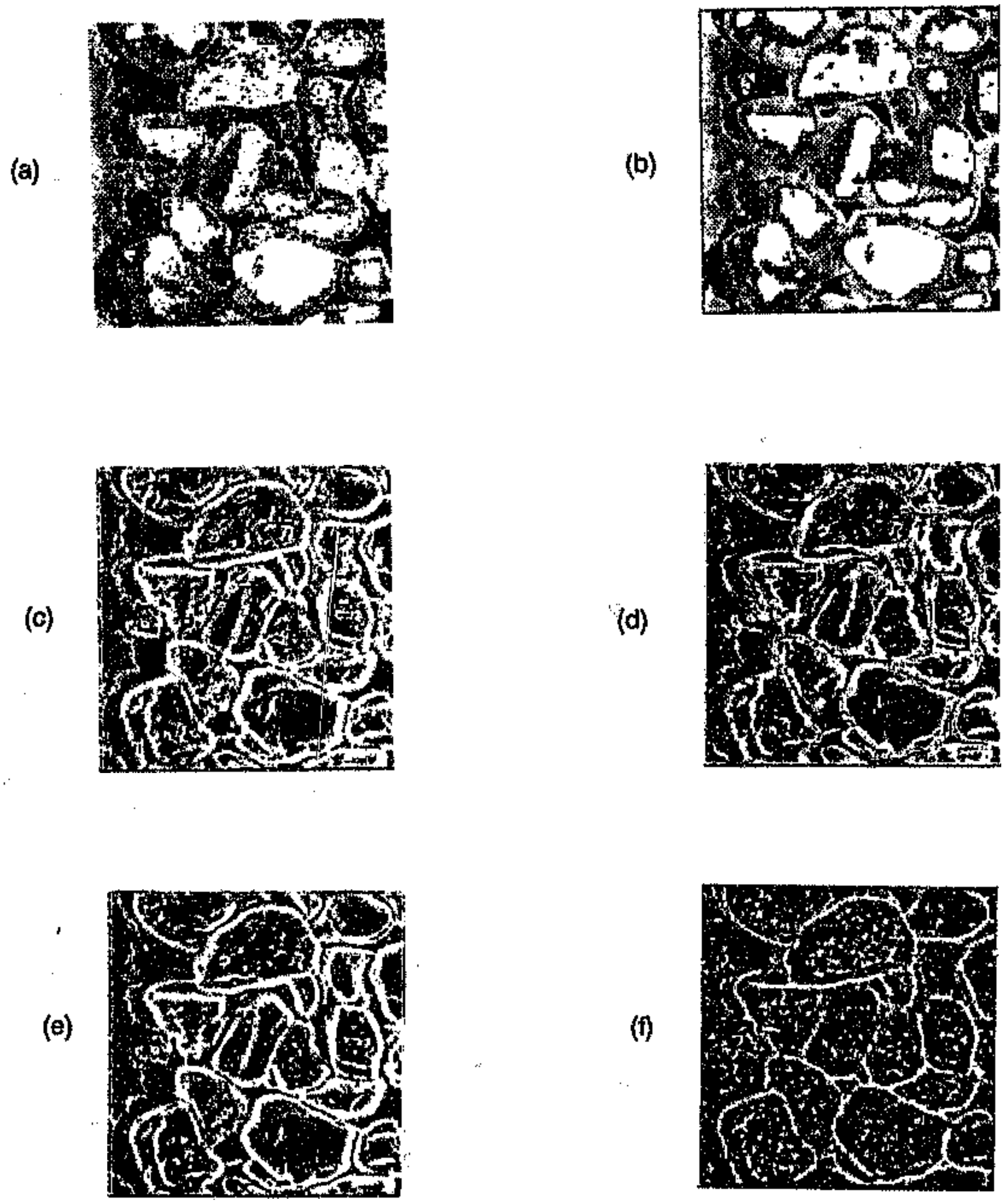

Figure 4.31: (a) Raw image. (b) Image (a) after lowpass filtering with a 3x3 NNA filter. Results of the application of (c) Prewitt, (d) Roberts, (e) Sobel, and (f) Laplacian edge detectors to *large* rocks.

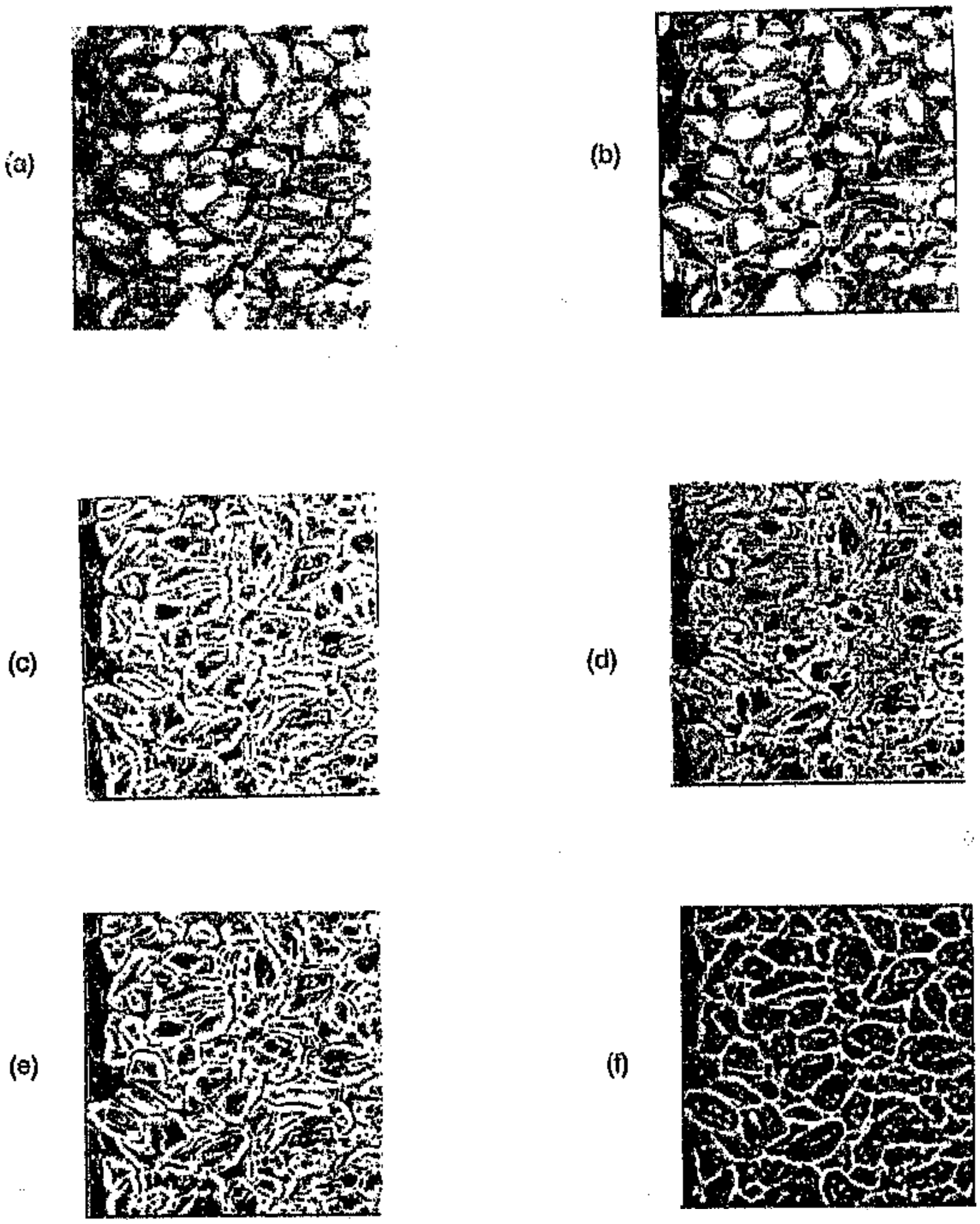

Figure 4.32. (a) Raw image. (b) Image (a) after lowpass filtering with a 3x3 NNA filter. Results of the application of (c) Prewitt, (d) Roberts, (e) Sobel, and (f) Laplacian edge detectors to *small* rocks.

4.6.2 Median filters

The median filter is part of the group of non-linear *rank order statistical (OS) filters*, (Bovik et al, 1983), (Nodes and Gallagher, 1983), (Maragos, 1985). These filters have the basic property of preserving edges whilst eliminating spot or impulse noise by behaving as low-pass filters. Thus median filters are theoretically ideal pre-filters to the Laplacian for rock edge detection because they simultaneously lowpass-filter whilst preserving the rock edges, thus satisfying a conflicting requirement. With a noise free signal the impulse response of a median filter is zero, and the step response is the step.

Median filters operate on a selected window of a certain shape and size which is passed over the image. For a 1-D signal with a window *W* of *2*m+1* elements the output is defined to be

$$\hat{x}_j(m) = median(x_{j-m}, \ldots, x_j, \ldots, x_{j+m}) \qquad 4.25$$

For 2-D signals (images) and a window *W* centred around (i,j), the median filter is defined to be

$$\hat{G}(i,j) = \underset{(u,v \in W)}{median}\{F(i+u, j+v)\} \qquad 4.26$$

The shape and size of the filter's window affects its performance and an analysis of this effect on various types of images is given by Bovik et al (1987). Nodes and Gallagher (1983) comment that although median filters are easy to implement, they are non-linear with memory and difficult to design correctly, and that in general, most past designs have been ad-hoc in nature. The problem with the median filter is the lengthy time to run the filter, which is approximately 5 minutes for a 3x3 cross filter on a 200 by 200 image on a 20MHz 80386 based PC. However there are many software and hardware architectures being designed specially to ease the processing burden (Arce and Stevenson, 1987, (Nieminen et al, 1987). For example, faster 1-D separable median filters can be used instead of 2-D filters. OS filters are linked to morphological filters (Maragos, 1985) which will be discussed in chapter 5.

Figure 4.33 shows the result of applying median filtering to rock images before edge detection and the resultant edge patterns. What is apparent, is that median filter distorts the image entities by stretching the rock shapes in sympathy to the shape of the filtering window.

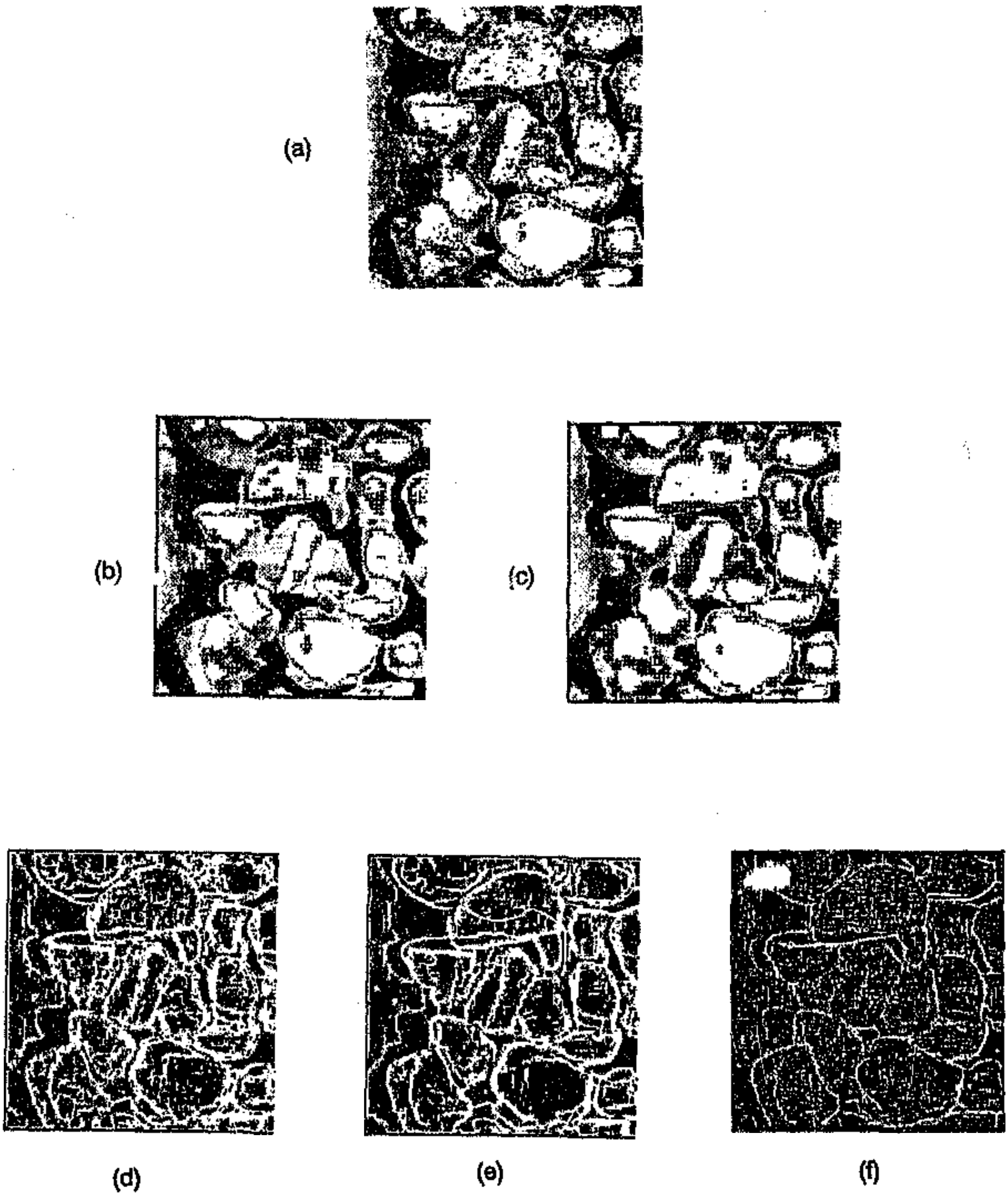

Figure 4.33: Result of median filtering to an image of large rocks. (a) Original (b) Original after image median filtered with a cross 3x3 window. (c) Original Image median filtered with a square 7x7 window. (d) Laplacian (e) Prewitt and (f) Sobel edge pattern of filtered image in (b).

4.6.3 Summary

From experimentation with the various filters mentioned above as well as other digital filters, it is concluded that the most appropriate filter to use with the *Laplacian* edge detector, is the *nearest neighbourhood averaging* (NAA) filter, because it complements the Laplacian in removing mainly impulse noise to which the Laplacian is susceptible, and consolidates the edges E^{*}_{ax} as shown in figure 4.30 and 4.31. This assumes that the Laplacian is the best edge detector to use in the first place. A positive point with regard to the implementation of the Laplacian is that, in practice, the 3x3 Laplacian operator take less than second to operate on 200x200 sized image in a 386 based microcomputer[4.14]. This compares very favourably with the speed of other operators which range from 5 to 15 seconds, and supports the realtime goal of achieving an image processing time of approximately one second. Experiments with median filters showed that, although the median filter suppresses impulse noise very well, the edge patterns are generally distorted by the shape of the median filter window, which led to the median filter being discarded. This is shown in figure 4.33 in which the edge patterns appear noisier and have a larger number of horizontal and vertical components, which indicate a distortion of the rock shapes in the raw image.

Other possible filters which may be used for pre-filtering are the FFT filters, morphological-filters (Nakagawa and Rosenfeld, 1978b) and (Serra, 1988), and 2-D digital filters such as infinite-impulse-response (IIR) filters. FFT filters are very useful for removing periodic noise but are not used because the rock images are not subject to any periodic noise, with the exception of alternating bands in the line-scan images caused by AC lighting, solved by the use of DC lighting (see chapter 6). Morphological filters which are non-linear have some extremely useful properties, (Haralick et al, 1987), (Maragos, 1985), (Maragos and Schafer, 1986), although morphological filtering operations such as stripping the image of peaks or troughs are not necessary. Morphological filtering as an alternative to edge detection will be discussed in chapter 5.

Other digital filters such as recursive filters can be used because they allow the filter frequency response to be tailored exactly to a specification. However, the large spatial bandwidth of the image, together with the difficulty of correlating undesirable image features with a frequency response, specification led to these filters being abandoned. Other disadvantages of such filters include instability, and a large computing capacity.

However the above conclusions are based on experimental work and the subjective analysis of the results produced by various combinations of pre-filters, edge-detectors, and post-filters, used to produce the best edge pattern. The advantages various filters versus the processing time and memory requirements also played a role

---

[4.14] The computer is based on a 80386 with 80387 co-processor running at 20MHz with a 64kbyte cache. The operator is written in Microsoft C v5.1 optimized for 80286 code.

in determining which filters to use. However, a more thorough and objective evaluation of the effect of various filters on the final boundary pattern as well as the possible design of a custom filter and edge detector combination, with multi-resolution capabilities, is required. Such an investigation is beyond the scope of the thesis because of time limits, and a fundamental inability to relate real objects and knowledge to a functional specification as required by conventional computers.

4.7 CLOSURE

In this chapter several methods have been developed for either *segmenting* images of rock scenes, or extracting *rock edges* in accordance with the conclusions reached in chapter 3. It is shown that, although, accurate rock boundary and region location is desirable, it is unattainable, especially after taking into consideration the real-time and cost restraints for the rocksize instrument (Chapter 1.2). A major problem encountered is that the images can only be transformed by ad-hoc image-processing algorithms which are evaluated subjectively, ie by visual inspection, where a visually pleasing or acceptable image of extracted rocks, as perceived by humans, is not necessarily the correct one for quantitative analysis or rocksize measurement.

Furthermore despite the various types of tools used to derive the edge or segmented patterns, the results derived in this chapter show that the processed images of rockscenes are inherently noisy and error prone. This supports the move to the hypothesis put forward in section 3.7 that because analytical solutions to the rocksize problem cannot be derived, and that the nature of the images from which populations of parameters are to be measured, are error prone, an empirical approach to the rocksize measurement problem should be adopted.

It is finally concluded that *post-edge correction* is required, because missing edges and noise in the edge patterns render such patterns useless for quantitative measurements. Edge correction, and the combining of the various techniques to obtain a better estimate of the rock boundaries from the simple edge detection and segmentation data as developed in this chapter, is discussed in chapter 5.

5 IMAGE PROCESSING II : EDGE CORRECTION AND THE FINAL ALGORITHM

5.1 INTRODUCTION

In chapter 4 an edge pattern E_d was derived by using an edge operator preceded by a filter on a raw image I. In particular the *Laplacian* operator preceded by a *neighbourhood-averaging* filter results in an acceptable the rock-boundary set $E_{\nabla^2} = E_d = \Psi_1(I)$. The image edge image E_d in general contains a number of ***entities*** E_i also referred to as "islands", which are the numerous subsets or segmented regions of the binary edge image E_d produced by the edge detector, where $E_i \subset E_d$ and $\bigcup_i E_i = E_d$ figure 5.1(b). Each entity E_i of the edge pattern E_d is defined as a set of pixels that is connected according to the 8-neighbour rule, where $E_i = \{e \mid e_8, e \in E_d\}$, and e_8 is pixel connected according to the 8-neighbourhood rule, see figure 5.1(a).

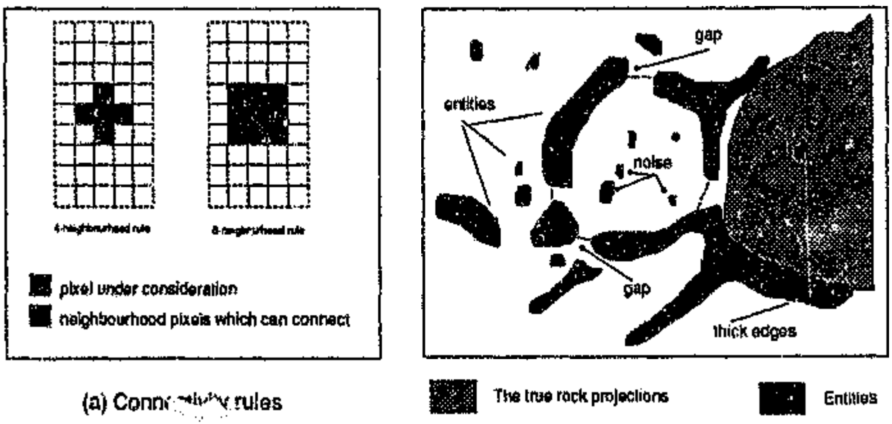

(a) Connectivity rules

Figure 5.1: (a) A rectangular grid showing which pixels can be connected to the central pixel according to the 4 and 8 neighbourhood rule. (b) Definition of the entities or islands E_i in the edge image E_d according to the 8-neighbourhood rule.

The resultant set of edges E_d (E_{∇^2} as detected by the Laplacian) is unsuitable for the direct application of linear or areal probes. Ideally, each rock in the edge pattern E_{∇^2} should be represented by a *closed* thin perimeter ∂X_i, not necessarily convex, which is free of any gaps or breaks, and which represents the edges of the projection of each rock $\overset{o}{X}_i$. Unfortunately this not the case because the edge patterns generally have a number of defects as shown in figure 5.1(b). These defects are :

(i) The edges are unusually *thick* in many places where they should be much thinner.

(ii) The edges are *broken* or have *gaps* where in fact they should be *continuous*. It is assumed *a-priori* and logically that the perimeter ∂X should be a closed and continuous perimeter.

(iii) Many undesirable edges E_n are detected in the perceived interior of each rock $\overset{o}{X}$, which are often fused with a number of perimeter edges.

Thus the objective of the second stage of image processing Ψ_2 is to correct edge patterns by *removing the noise* edgelets, *closing the gaps* and *thinning very thick edges*. This chapter discusses the development of such edge correction strategies which ultimately form the second image-processing stage Ψ_2.

Two main classes of algorithms have been developed for Ψ_2. These are the *"joining"* and *"morphological"* algorithms. The *joining* algorithm is based on "traditional" image processing strategies, whilst the morphological algorithm is based on the "newer" mathematical morphology (Serra, 1982). Morphological techniques look at the image in terms of *shape* and *geometrical* content, whereas traditional imaging techniques (eg Pratt, 1978) are based on the *functional* and *mathematical manipulation* of an image. Although the final algorithm implemented is based mainly on morphological techniques, the joining algorithm is presented because it is a typical example of the traditional (and initial) approach used to detect rock boundaries. It is the difficulty of implementing certain functions using traditional methods which led to the adoption of morphological techniques.

At the end of this chapter a final algorithm is presented for rock-edge detection which is based on a combination of a number of different image-processing methodologies, including traditional and morphological techniques. For example, it is shown in chapter 4 that *thresholding* can be useful for segmenting rock images, thus thresholding together with morphological techniques have been incorporated into the final algorithm. This combined approach is not a mixing of "oil and water", because thresholding and mathematical morphology can be unified into single theory, (Maragos, 1985).

5.2 THE "JOINING" ALGORITHM FOR EDGE CORRECTION

The joining algorithm has two main objectives which are (i) to close the gaps in genuine edges, and (ii) to remove spot noise, in order to construct complete edge patterns free of errors, see figure 5.2. There is a third objective of thinning the edges to form primal sketches. However this objective was not pursued because the high processing cost of thinning does not justify the slight improvement in chord-length or areal measurements which will be swamped by other larger errors in segmentation. The two objectives of closing gaps and removing noise are not independent of one another, and finding a balance between these two objectives, which provides an optimum edge pattern, is a subjective and difficult problem. The subjectiveness arises from the necessity of classifying each entity $E_i \subset E_{v2}$ as belonging to either noise E_n , or parts of the rock perimeter E_{ax} .

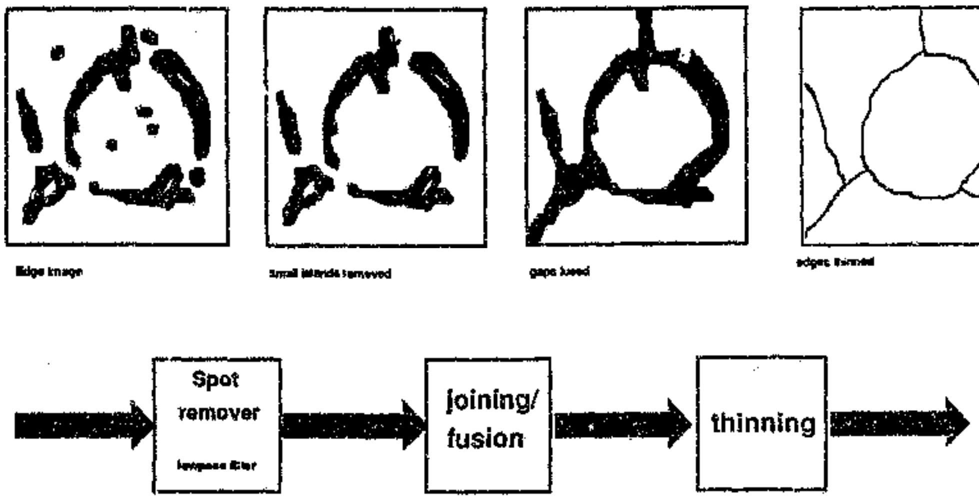

Figure 5.2: Schematic diagram showing the sequential operations to be performed by the joining algorithm.

The joining algorithm is structured around the *a-priori* knowledge of the *shape* of the rocks and the *anticipated* or *expected* shape of their boundary patterns. This knowledge is used to try and identify parts of the *true* rock edges E_{ax} hence allowing for the removal of the remaining noise entities, and the joining together of the remaining edges to eliminate gaps.

Figure 5.2 shows the block diagram for the joining algorithm. The algorithm consists of the following sequential steps, (i) labelling, (ii) noise removal, followed by (iii) joining the gaps. In practice these algorithms may employ feedback as is shown in figure 5.3. The reasons for these steps and their execution are discussed in the following subsections.

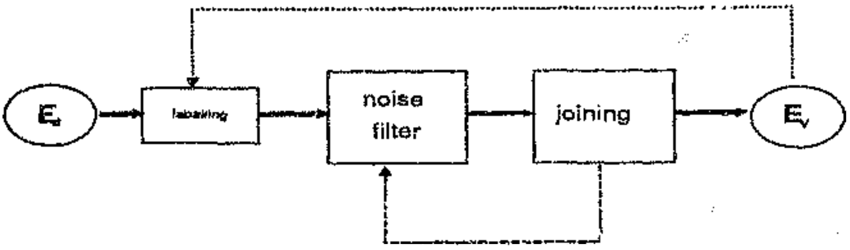

Figure 5.3: Block diagram of the joining algorithm.

5.2.1 Labelling

The first step to this edge correction scheme is to identify unambiguously and label each entity E_i so that they can be manipulated in a logical and intelligent manner. The edge image E_d or in particularE_{∇^2} is scanned and each entity E_i is labelled by giving each pixel $e \in E_i$ a label λ_i depending on whether it is connected to a neighbouring pixel or not, see figure 5.4. The connectivity of the pixels determines how the entities are labelled which can be quite a complex process, because the convoluted shapes of the entities implies custom "flood-filling" algorithms.

When labelling, the "area" of each entity $A_i = A[E_i]$ is calculated automatically by *counting* the number of pixels which are given the same label λ_i . If the counting operation is given by N then

$$A_i = N\{ e \in E_i \mid e = \lambda_i, E_i \subset E_{\nabla^2}\} \qquad 5.1$$

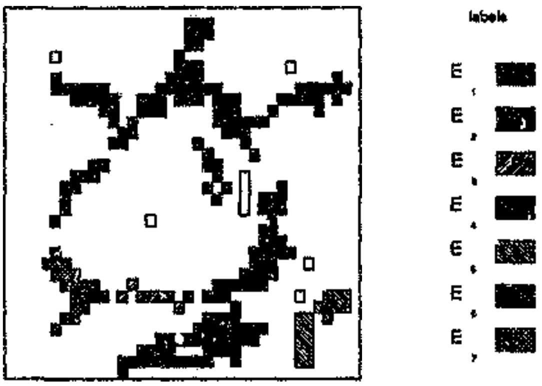

Figure 5.4: Example of labelled entities from which their size can be calculated.

5.2.2 The Noise Filter or Spot Remover Ψ_f

In anticipation of joining entities together to close gaps, it is important to remove those entities which do not form part of the true set of rock edges $E_{\partial X}$, because the joining together of *all* islands in the image will result in a useless mass. Thus there is a need for a noise filter. The problem in implementing this noise filter is to classify which islands are noise and which are valid edges.

Observation of most rock images show that on average the *large entities* form part of the edges, while most of the *smaller entities* are the noise components. We define the size of the entities to be its area A_i. Thus as a first approximation it is assumed that for a given image the *small* islands can be removed because they are noise. To remove these small entities requires eliminating those labelled entities with a pixel count less than a chosen value A_n. The classification process of entities into noise E_n or edges belonging to $E_{\partial X}$ is given by

$$E_n = E_{<A_n} = \{ e \in E_{\nabla^2} \mid A[E_i] < A_n \} \qquad 5.2$$

$$E_f = E_{\geq A_n} = \{ e \in E_{\nabla^2} \mid A[E_i] \geq A_n \} \qquad 5.3$$

The filtered image containing estimated rock edges is denoted E_f and e is a pixel element of edge entity E_i. Because this classification process is not perfect, the filtered edges in E_f will in general not be complete and will not represent the true rock boundary $E_{\partial X}$ exactly, so that we have

$$E_f = E_{\nabla^2} - E_n \qquad \text{but} \qquad E_f \neq E_{\partial X} \qquad 5.4$$

The results of applying the spot remover equations [5.2] and [5.3] are fairly satisfactory because most of the noise is removed, as shown in figure 5.5. However the assumption, *small islands are noise*, is not totally correct because certain small islands with $A_i < A_n$ which do form part of the rocks' perimeter $E_{\partial X}$, are removed, while some entities with $A_i > A_n$ which according to our perception are noise, are not removed, eg edges resulting from ridges on the rocks' surface. Nevertheless removing small islands does improve the image for stereological measurements and thus this noise filter (spot remover) where $E_f = \Psi_f(E_d)$ is a necessary step where E_d can be the result of any edge detection process.

Experimentation with the *Laplacian* edge detector shows that the resulting edge patterns E_{∇^2} of scenes of small rocks have entities of large area, while scenes of large rocks result in many entities of small area, see figure

5.7. Thus the spot remover algorithm must adapt to the *size* of the rocks in the image (not known) in order to remove the correct noise entities. Figure 5.6 shows the application of Ψ_f to the same scene of rocks with different values of A_s showing how incorrect values of A_s result in distorted edge patterns.

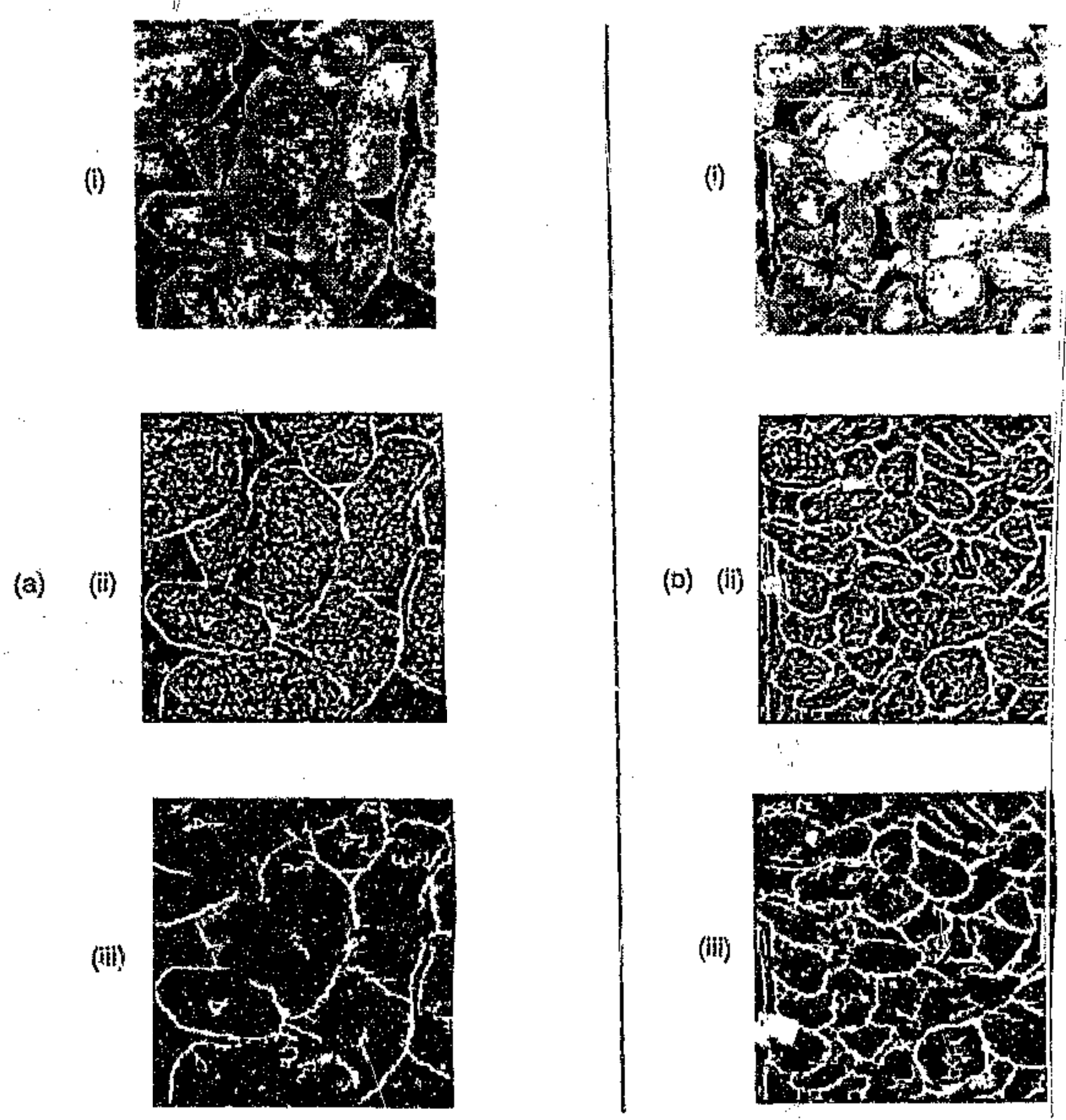

Figure 5.5: Examples of applying the spot remover to edge patterns E_{∇^2}, resulting from the application of the Laplacian operator ∇^2 to quartzite rockscenes of size range (a) -50+38mm (b) -25+19mm. (i) original, (ii) result of the Laplacian, (iii) result of spot remover.

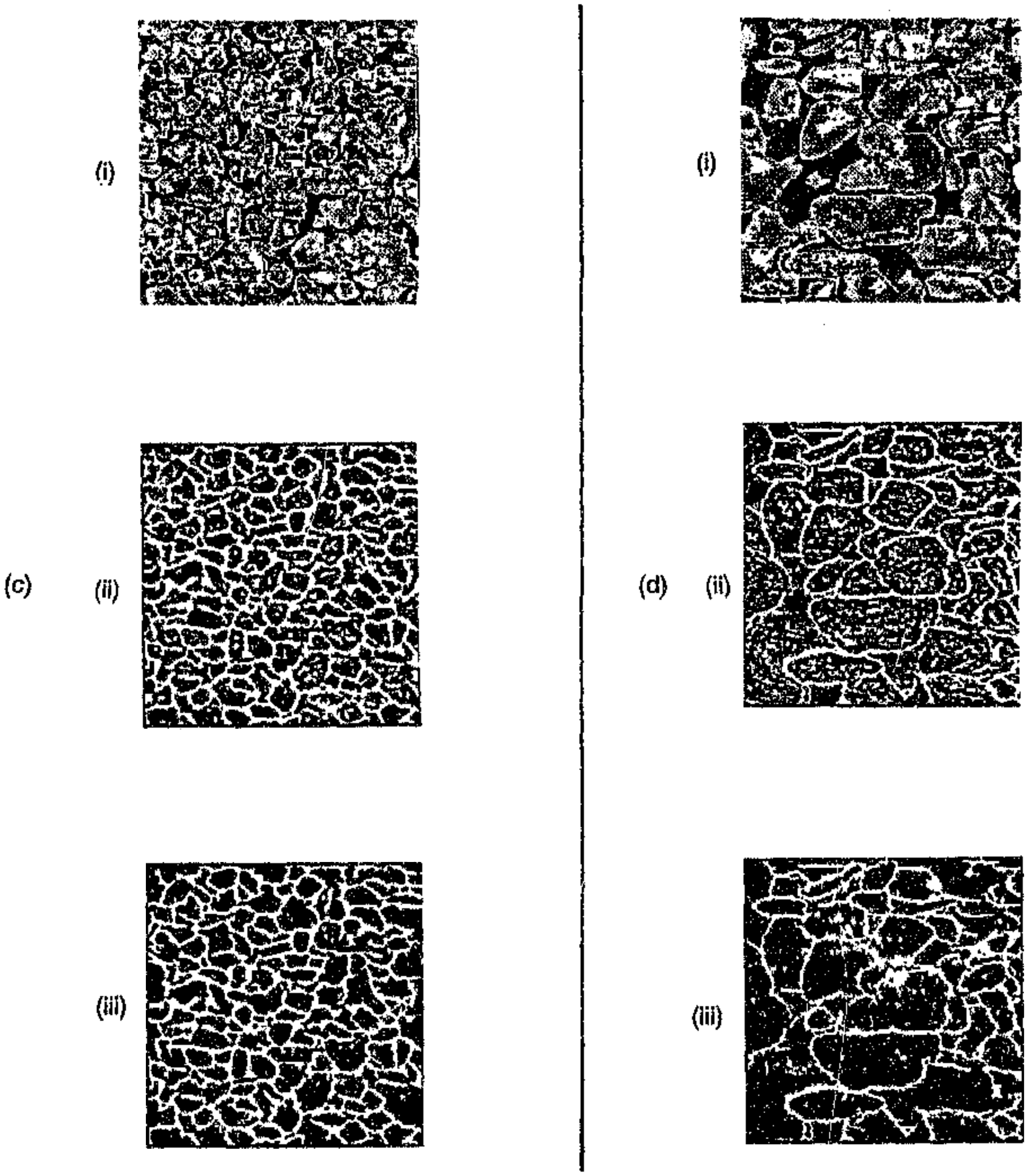

Figure 5.5 continued : Examples of applying the spot remover to edge patterns E_{∇^2} , resulting from the application of the Laplacian operator ∇^2 to quartzite rockscenes. (c) -13.5+9.7mm, (d) -50+13.5mm. (i) original, (ii) result of the Laplacian, (iii) result of spot remover.

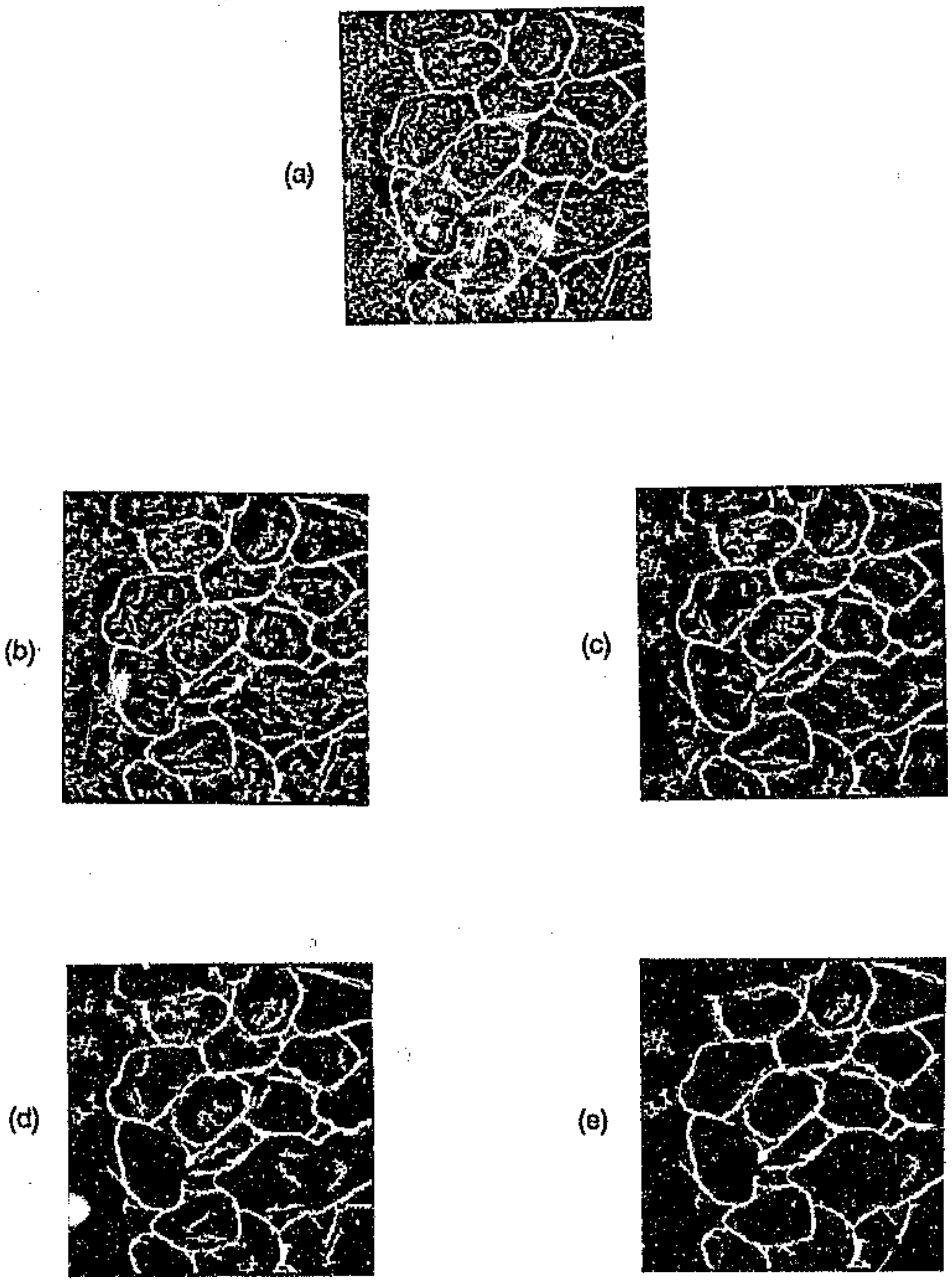

Figure 5.6: Results of varying A_n to achieve different amounts of filtering, (a) original, (b) $A_n = 10$, (c) $A_n = 20$, (d) $A_n = 40$, (e) $A_n = 80$.

It has been discovered from experiments that the average area of the edge entities $\overline{A}_{E_i}$ is roughly *inversely* proportional to the average rocksize $\overline{f}(D)$ as shown in equation [5.5]. This effect is also evident from inspection the images shown in figure 5.7. A measured relationship between entity size and rocksize [5.5] is shown in figure 5.8.

$$\overline{A}_{E_i} \approx \frac{1}{\overline{f}_D} \qquad 5.5$$

where $$\overline{A}_{E_i} = \frac{1}{N}\sum_{i=1}^{N} A[E_i] \qquad 5.6$$

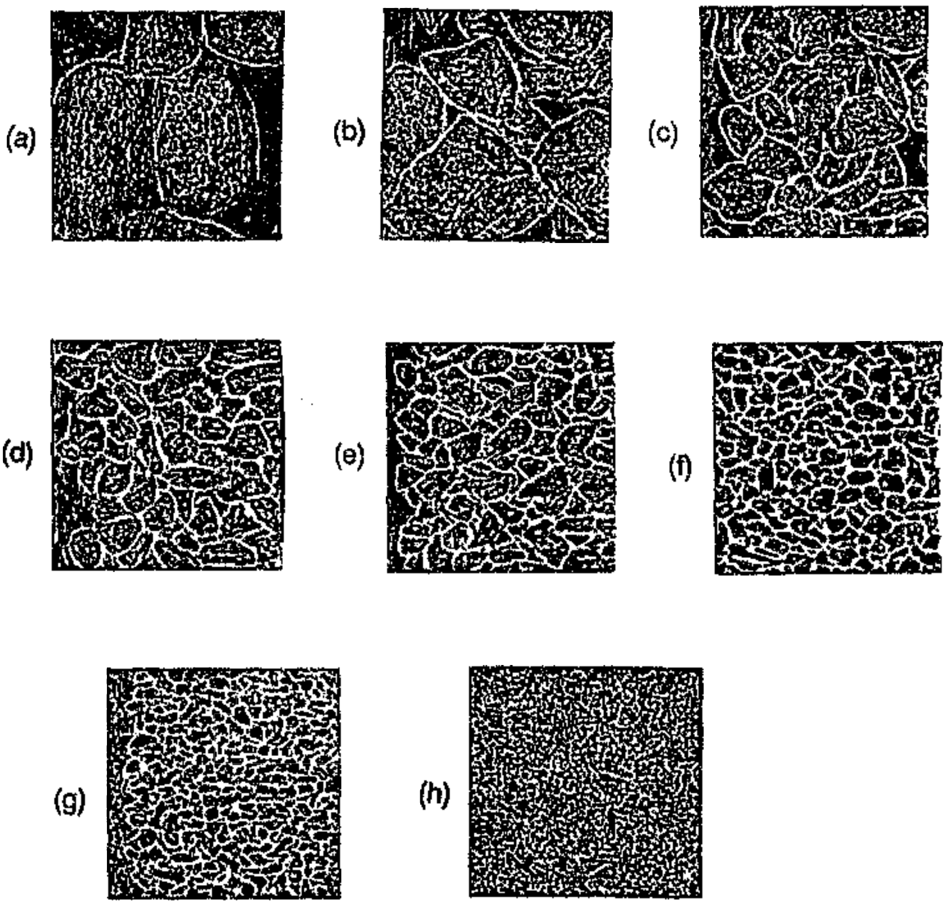

Figure 5.7: Images showing how the size of the entities in E_{∇^2} change with average rock size. (a) -75+50mm, (b) -50+38mm, (c) -38+25mm, (d) -25+19mm (e) -19+12.7mm (f) -12.7+9.35mm, (g) -9.35+6.15mm, and (h) -6.15mm.

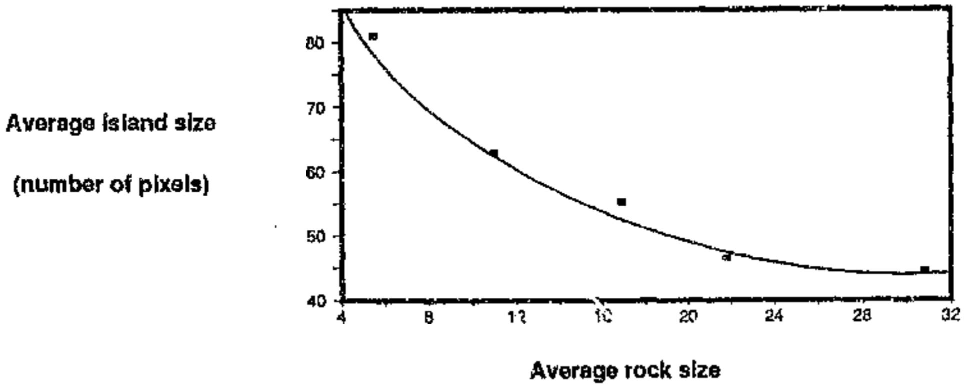

Figure 5.8: Graph of $\overline{A}(E_i)$ versus $\bar{f}_D$. Data is derived from static images of scenes of piled sieved granite.

The relationship shown in figure 5.8 or equation [5.5] is useful because it allows for a preliminary but *not* reliable average size estimation to made. Relationship [5.5] also indicates that use of $\overline{A}_{E_i}$ to control the spot filtering Ψ_f which is dependent on the size of the rocks, is partially justified. However $\overline{A}_{E_i}$ is an unreliable indicator of $\bar{f}_D$ because the average size of the entities is also dependant on how *broken* the entities are, which is a function of many other factors including the rock shape and not only rocksize. For example, objects of simple and rounded shape result in contiguous edge patterns which only give a few islands of very large size, irrespective of particle size and hence a large and erroneous estimate of $\bar{f}_D$. However the rough estimate of $\bar{f}(D)$ from equation [5.5] allows for A_n, on average, to be varied adaptively with rocksize, allowing for the removal of small noise components from images of small rocks, and large noise components from images of large rocks, thus minimizing possible errors induced by an incorrect A_n as shown in figure 5.6.

With scenes of rocks of *wide*-size distributions, the implementation of Ψ_f with a global A_n over the whole image will remove small islands corresponding to valid parts of the edges of small rocks, thus creating edge errors and biasing the measurements. We will now present one of many possible strategies to counter the noise identification errors due to a *global* filter factor A_n , the solution to which is to use *local* criteria to classify entities as noise.

Inspection of the edge patterns shows that *relatively* large entities in a local area can be assumed to be part of E_{ax} . Thus it is highly probable that small islands near to a large one could be part of E_{ax} . Thus a classifying criterion could be an estimation of the *relative position* of the suspected noise entity with respect to (i) ***large neighbouring*** islands, or (ii) to an *estimated centre* of the rock. This classification strategy thus requires the calculation of the following probabilities $Pr(E_i \subset E_{ax})$ or $Pr(E_i \subset E_n)$ where $Pr(E_i \subset E_{ax}) + Pr(E_i \subset E_n) = 1$.

For example if the centre of gravity of the rocks and entities are C_X and C_{E_i} respectively, then $d = d[C_X, C_{E_i}] = \| C_X - C_{E_i} \|$ can be used as criteria to calculate the probability $Pr(E_i \subset E_n)$.

As an example of a strategy, assume the rocks and small entities can be approximated as spheres with the radius of the rocks and small entities being $r_{\partial X}$ and r_{E_i}. Then equation [5.7] and [5.8] can be used as a first estimation to the classification of these edges as shown in figure 5.9, where d_r and d_R are some cutoff distance defining an *edge zone* which could be derived from experimentation, ie

$$d_r < d\left[C_X, C_{E_i}\right] > d_R \quad \Rightarrow \quad Pr(E_i \subset E_n) = 1 \quad \Rightarrow \quad E_i \subset E_n \qquad 5.7$$

else if $$d_r \le d\left[C_X, C_{E_i}\right] \le d_R \quad \Rightarrow \quad Pr(E_i \subset E_{\partial X}) = 1 \quad \Rightarrow \quad E_i \subset E_{\partial X} \qquad 5.8$$

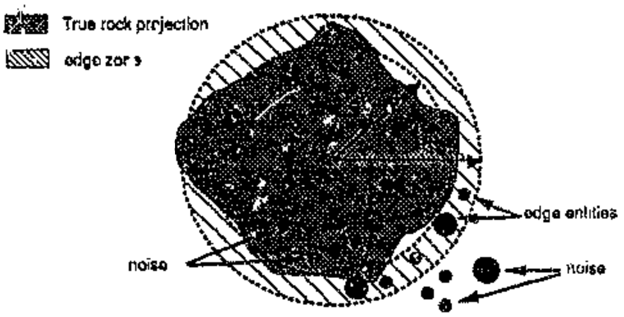

Figure 5.9: Schematic diagram showing a scheme to for classifying the entities E_i as either $E_{\partial X}$ and E_n.

The above classification scheme is one of many possible schemes that can developed for entity classification. However strategies for determining A_n similar to above were rejected because of the need for too many invalid *assumptions*, and the difficulties in formulating *rules* which govern the classification process, ie equation [5.7] and [5.8], which can determine the values of d_r and d_R.

More importantly the islands have *irregular non-convex* shapes, often causing the centre of gravity of the entity to fall outside its boundary which totally invalidates the above scheme. In addition these strategies require a great deal of costly processing and are difficult to code efficiently. In summary the results obtained by these local methods are too unreliable to justify the costly processing, hence the use of a "global" A_R for spot removal. Note that examination of the spatial relationships between different sized entities as above could be further investigated by looking at the image *covariance*, see Serra (1982) chapter IX.

5.2.3 Closing the Gaps and Joining Ψ_V

After application of the spot remover Ψ_f it is necessary to close the gaps in the remaining edge patterns to produce an estimated edge pattern E^*_{ax} from Ψ_f where theoretically $E_f \subset E_{ax}$. However in addition to E_f missing edge elements E_Δ that should be part of E_{ax} , ie $E_\Delta = E_{ax} - E_f$, E_f still contains elements that are not part of E_{ax} ie $\{E_i \subset E^*_{ax}\} \not\subseteq E_{ax}$. This situation can be observed in figure 5.10 which shows an edge pattern with *gaps* as well as some *unnecessary edges* that were not removed by Ψ_V.

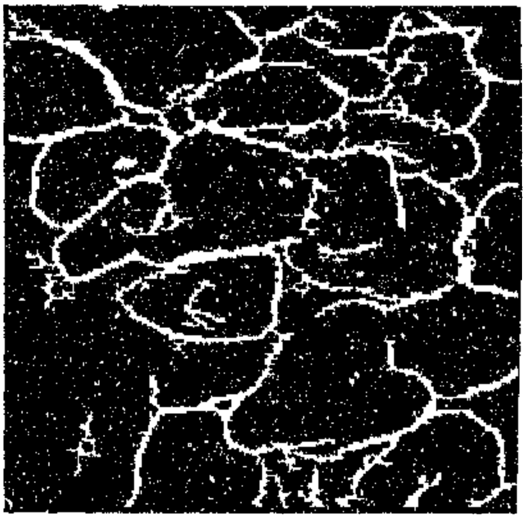

Figure 5.10: Example of a filtered edge patterns E_f showing *gaps* that need closing as well as a number of *unnecessary edge elements*. The image was captured from dynamic quartzite rock scenes on the conveyor belt test-rig (See chapter 6).

In order to close the gaps in filtered images E_f such those shown in figure 5.10, rules have to formulated so that *legitimate* gaps can be *identified* and *fused together* according to *our perceptions* of what a closed edge pattern should look like, ie a rule-base or expert system. As mentioned in chapter 4 it is difficult to build up a complete set of rules to cater for all the various edge entities because of the many different rock shapes and sizes which give rise to an infinite number or classes of edge patterns. However the following is known with regard to the general rock edge pattern,

(i) Ignoring the effects of occlusion and assuming the rocks are convex in shape, the rocks perimeters should form *closed-convex* perimeters.

(ii) It is highly unlikely that rocks have holes, or that there are significant and deep indentations on the surface of the each rock forming narrow isthmuses or bays.

(iii) The possibility of small rocks lying on top of larger rocks is small, thus all edges in the centre of the rock are undesirable as was discussed in subsection 5.2.2.

It is assumed that the only error generated by the "spot remover" Ψ_f is that some of the small entities belonging to $E_{\partial X}$ have been removed, but that all the remaining entities are part of the valid edges, ie $E_f \subseteq E_{\partial X}$. Therefore allowing all remaining entities to be fused together should give a reasonably good estimation of ∂X . The joining up of all these entities E_i to form one complete structure is carried out in the following procedure in accordance with a number of rules, because without rules an uncontrolled joining would result in a totally useless image. The procedure rules briefly are that

(i) Entities greater than a minimum size A_{min} , ie $A\{E_i\} \geq A_{min}$ are identified and assumed to be large islands which are part of $E_{\partial X}$.

(ii) The ***extremities*** (figure 5.11) of these large entities are located because it is assumed that the points of contact between entities should only take place from *extremities* of islands.

(iii) A controlled search is then propagated from certain extremities of the *large* or *source* island to find the *closest neighbouring* island. The search area is defined according to the *type* of extremity from which the search is taking place. As an initial investigation only four types of extremities were defined. These were the *north, south, east,* and *west* extremities, which are identified by those parts of the island that touch its smallest enclosing rectangle aligned parallel to the edges of the image. Figure 5.11 shows how the search area from the extremities are defined, which is a 180° sector extending outwards in a direction parallel to the directional label given to the extremity from which the search is propogating. Two constraints are placed on the search for neighbours. Firstly the distance to a neighbour has to be less than d_{max} , and secondly the neighbour had to be of a minimum size A_{n-min} .

The above model for locating the extremities is extremely limited. For example, two extremities may exist in the "south" of which only one will be found. In addition *the neighbourhood search* pattern should rather be biased in the direction of curvature of the entity. However, how is the curvature of an entity defined ? For example, a straight entity with an end hook should have a search area extending parallel to it, but the continuation of the rock border may be at right angles, ie, in the direction of the hook. Thus in order to reduce the computation and coding required, only the four search patterns as defined above are used, where any neighbour entity within a fixed distance away from the main extremity can be linked up.

(iv) Once a suitable neighbour is identified within the control restraints, a *link is constructed* from the extremity of the *main* island to the *neighbouring* island. Record is then made to the effect that both islands and the respective entities have been involved in a fusion or joining operation. This is to stop the propagation of too many links to too many islands from the same extremity which has the effect shown in figure 5.12.

The links and islands should be joined to form a *continuous curve* with a curvature similar to that of the larger islands. However only *linear* bridges are constructed because the computation required for calculating *curved* links is too costly considering the fact that the links are only *estimates* to the shape of the rocks in the first place, and that most of the required link distances d_{link} are short relative to the size of the entities involved and can be approximated with *straight* links. However provision is made for the construction of long links with 90° or 45° bends.

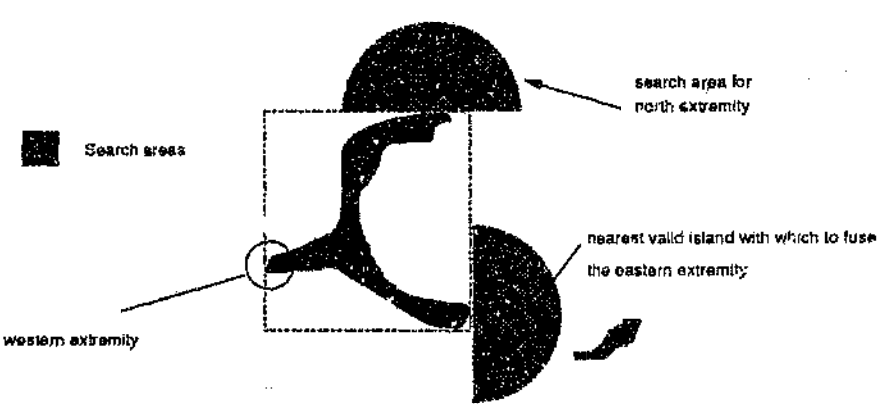

Figure 5.11: Example of the search pattern from a Northern extremity.

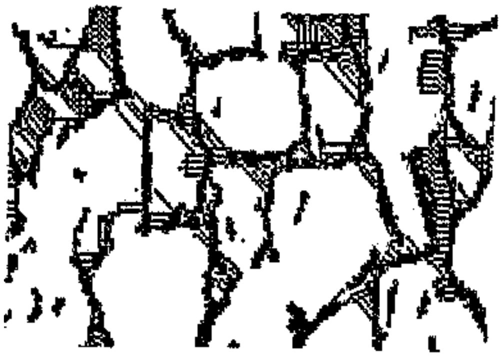

Figure 5.12: A typical result of over-joining.

5.2.4 [illegible] of Experimentation with Rock Piles

The joining algorithm Ψ_V as described above was applied to numerous static and dynamic images of various sizes and size distributions. Arbitrary samples of resulting estimated rock boundary patterns $E^{*}_{\partial x} = \Psi_V\Psi_f(E_d)$ are shown in figures 5.13 and 5.14.

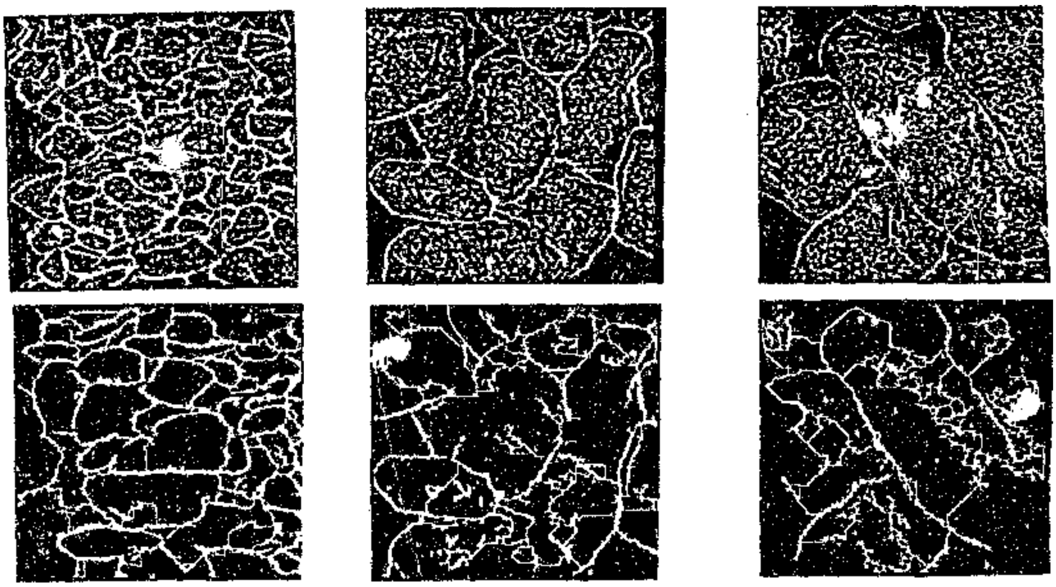

(a) (b) (c)

Figure 5.13: Results of applying the joining algorithm to (a) small (b) medium (c) large rocks.

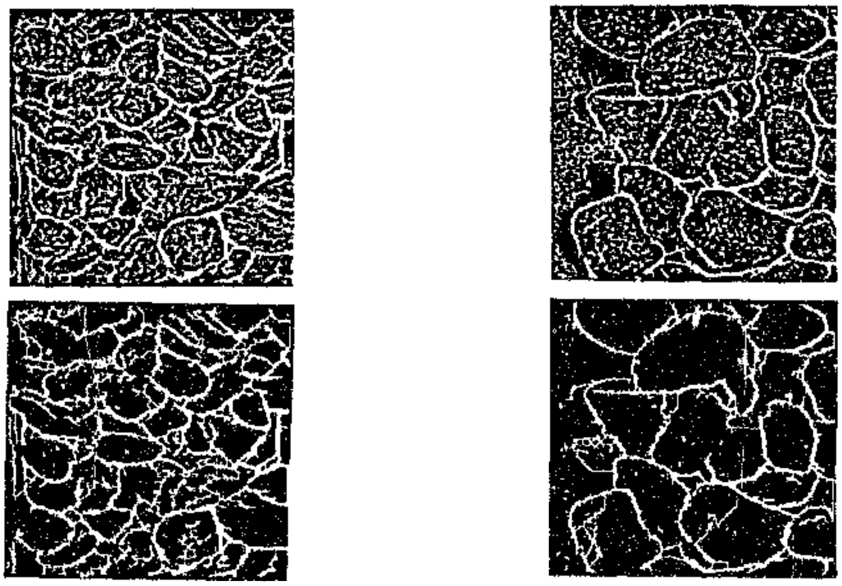

Figure 5.14: Results of applying the joining algorithm to piles of rock of wide (mixed) size distribution[5.1].

[5.1] The scale for all images shown in figures 5.13 and 5.14 is the same.

5.2.5 Summary

The development of the *joining* algorithm raises the following points. From a qualitative point of view, size data is inherent in the edge pattern E_d despite the noise and erroneous edges, and the joining algorithm is a valid method of improving the edge patterns according to our perceptions. More importantly, quantitatively chord distributions measured from E_{3x}^{*} derived from the joining algorithm, do varying sensibly to the changes in rock distributions, see figure 5.15. However the simple suite of rules incorporated into the algorithm as described above, is crude, and relies on too many assumptions. However the implementation of a more accurate and valid strategy taking into account a more realistic model of the rock scene incorporating shape and spatial distribution factors is impractical because it can only be done at the expense of a large increase in processing time and the generation of large and unwieldy algorithms. Experience in designing this joining algorithm also showed that selecting the correct control parameters to control the joining requires extensive *experimentation* in order to establish the heuristic control strategies to adapt the algorithm automatically to changing conditions in the image. In view of the fact that the joining strategy is one of a large number of algorithms that can be postulated for joining edge gaps, the cost of investigating such algorithms is not really justified in the light of the overall objective of an online rocksize measurement.

The conclusion thus reached is that a *simpler* method with less control parameters or criteria is required. As will be shown in the next section, the techniques of mathematical morphology are simple, and can perform the required edge correction transformations within a reasonable time

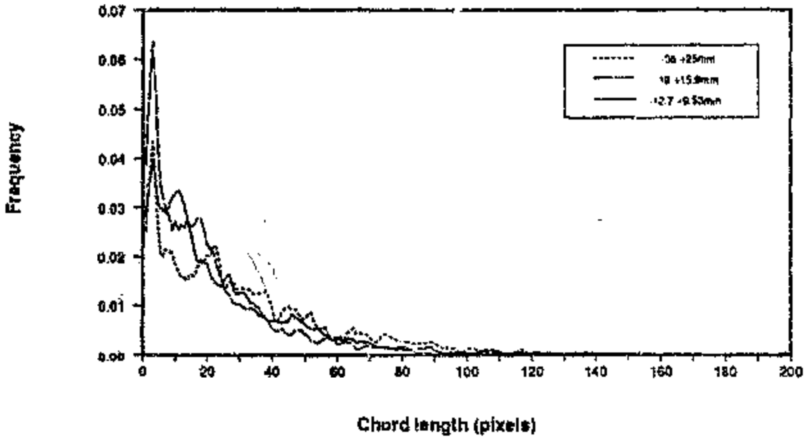

Figure 5.15: Examples of chord-length distributions measured from rock boundary patterns constructed by the joining algorithm. The images processed were of static images of granite, (see chapter 6).

5.3 MATHEMATICAL MORPHOLOGY FOR EDGE CORRECTION

5.3.1 Why use Mathematical Morphology ?

The development of the joining algorithm shows that an edge-correction algorithm based on our interpretations of what the edge patterns should be, can be designed. However there are natural limitations to our ability to interpret such images and to formulate rules based on shape to modify these images. There is thus a need for alternative techniques which operate both locally and globally on the *shape content* of the image, in the knowledge that the image content is not error free and has to be considered statistically. In addition these alternative techniques must be independent as possible of the rock characteristics so that intractable and complex rules with too many unrealistic assumptions such as those discussed in section 5.2 can be avoided.

The requirement for simpler techniques which requires less complex algorithms as concluded in section 5.2, can be satisfied to large extent by the techniques of *mathematical morphology*. It will be shown in this sub-section that mathematical morphology provides a replacement to the joining and other classical edge correction algorithms, as well as an alternative to the Laplacian for edge detection. Morphological techniques use mainly logical or Boolean operations which are easy to implement in hardware and which thus provide the potential for realtime response, an important consideration as far this rocksize measurement is concerned.

5.3.2 Introduction to Mathematical Morphology.

Mathematical morphology is based on set-theoretic concepts in which a probe of suitable shape (structuring element) is used to transform the *spatial* nature of the image under analysis. These transformations are non-linear and are based on tools such as set theory, integral geometry, convex analysis, and fuzzy set theory in multilevel signals, as opposed to classical tools such as linear filters, Fourier transforms and statistical or syntactic patterns analysis (as attempted in section 5.2).

Mathematical morphology was first investigated by Matheron (1975) and was extended by others, in particular Serra (1982). Haralick and Sternberg (1987), and Maragos (1987) provide excellent tutorials on mathematical morphology. Important links between mathematical morphology and signal processing are discussed by Maragos (1984, 1985, 1986, 1989a, 1989b) and Giardina and Dougherty (1988). Many other theoretical results concerning mathematical morphology have been developed by Serra (1982), Serra and co-workers (1988), Lantejoul and Serra (1982)[5.2].

[5.2] A complete survey of mathematical morphology and its applications is beyond the scope of this paper.

Morphological methods are more suited to *shape* analysis than linear filters (Maragos, 1987), and morphological filters avoid the shifting and blurring of linear filters (Maragos, 1989a, 1989b). Lantuejoul and Serra (1982) comment that mathematical morphology provides an alternative to classical filtering methods such as convolution. Image processing is often concerned with shape, and mathematical morphological operations tend to simplify image data while preserving their essential shape characteristics and eliminating irrelevancies, which is directly compatible with the objectives of the image processing stage Ψ.

5.3.3 Definitions of Morphological Operations

The origin and definitions of mathematical morphology are covered quite extensively in the references given above. However it is important to define the basic morphological operations of *erosion, dilation, opening* and *closing* which are used extensively for the detection (Ψ_1) and correction (Ψ_2) of size features in rockscenes[5.3]. Both *binary* and *gray level* morphology is used in this work where binary images can be considered "subsets" of gray level images through the "umbra transform" (Haralick et al, 1987), (Maragos, 1985).

Let E^N be the set of all points in the N-dimensional Euclidean space. Let A and B be subsets of E^N in particular Z^2, $a \in A$ and $b \in B$, where by convention A and B represent an image and a structuring element respectively. We will now consider binary images only. The translate of the set $A = \{a \in Z^2 \times D\}$ where D is the domain, by the vector b is given by $A_b = \{a + b \mid a \in A\}$. The *erosion* $A \ominus B$ and *dilation* $A \oplus B$ of an object A by a probe B is defined by equation [5.9] and [5.10] respectively.

$$A \oplus B = \{c \in E^N \mid c = a + b \quad , \quad a \in A, b \in B\} = \bigcup_{b \in B} A_b \qquad 5.9$$

$$A \ominus B = \{x \in E^N \mid x + b = \in A \quad for \quad every \quad b \in B\} = (A^c \oplus B)^c = \bigcap_{b \in B} A_b \qquad 5.10$$

The operations of *erosion* and *dilation* can be thought of as transformations which *shrink* or *expand* a set. Figure 5.16 below shows in detail how a dilation and erosion operates with an horizontal probe structure B and image A. Note that the results of the operation are very dependent on the position of the origin of the structuring element B as shown in figure 5.16.

[5.3] Note that various authors do tend to give different definitions of morphological operations depending on their frame of reference etc.

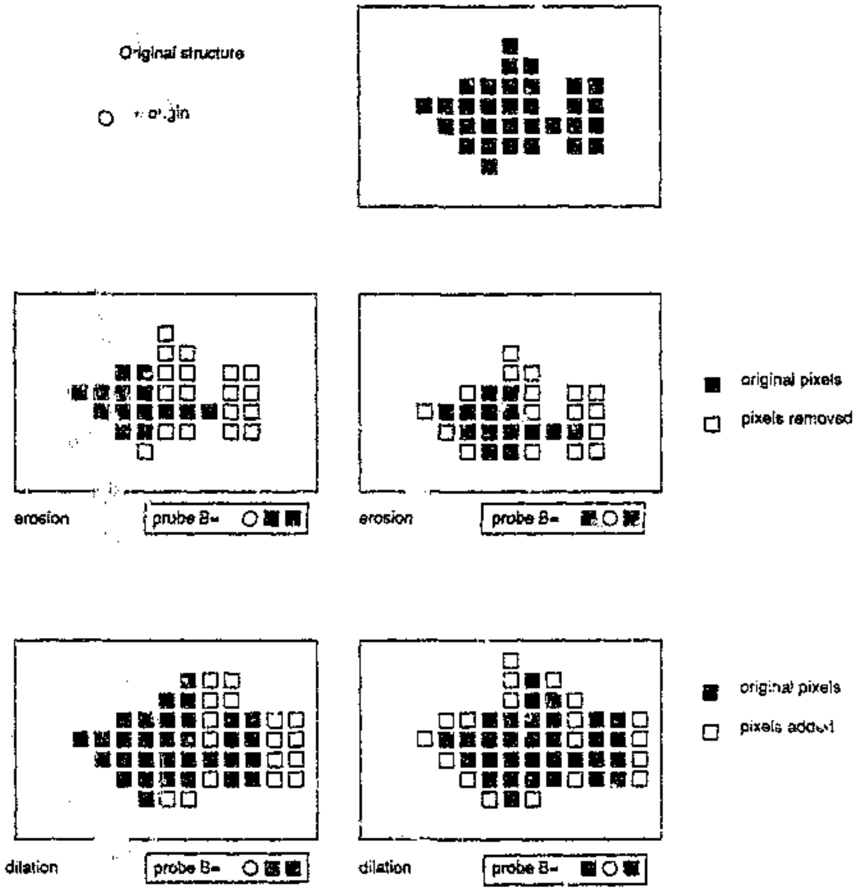

Figure 5.16: Detailed example of erosion and dilation of a structure *A* by horizontal probe *B*

For the rectangular grid dealt with in this research structuring element *B* can take up the shapes as shown in figure 5.17

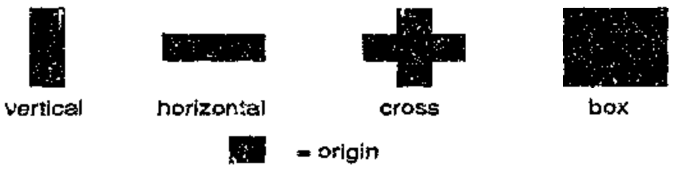

Figure 5.17: Examples of structuring elements used for morphological operations on rectangular grids.

Figure 5.18 and 5.19 give further examples of the effect of erosion and dilation. Erosion tends to break up an object, whilst dilation tends to close any gaps. Note that the effect of these transformations depends on the size of the probe which will be discussed in subsection 5.3.4.

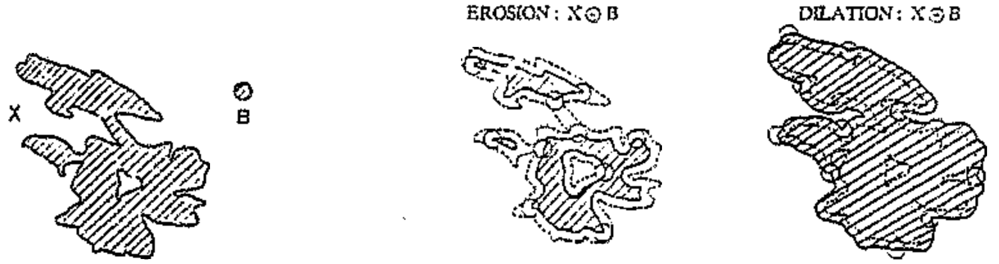

Figure 5.18: Example of erosion and dilation using a circular probe, after (Maragos, 1985).

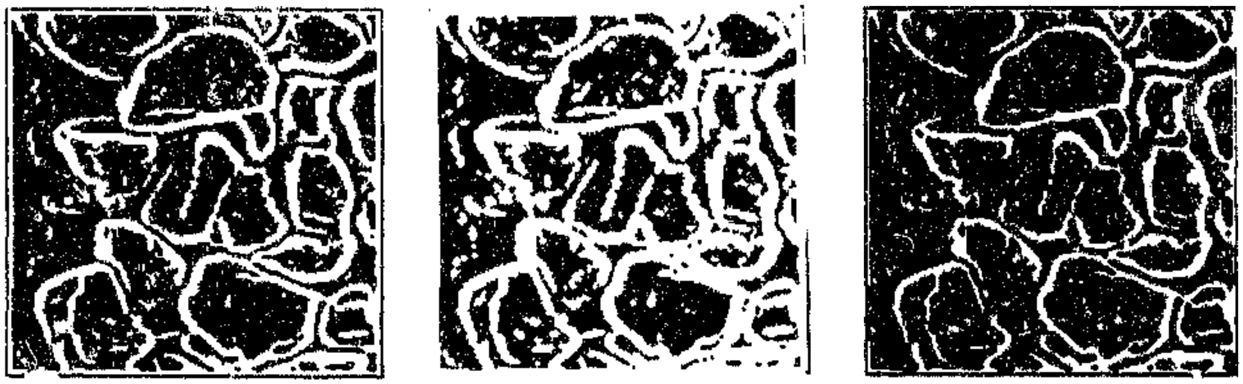

(a) (b) (c)

Figure 5.19: Examples of (b) dilation and (c) erosion of (a) a rock boundary pattern $E_{\nabla t}$ using a 3x3 cross-probe as shown in figure 5.17.

It is the combination of these erosion and dilation operations which are very useful for image processing work. The morphological operations of *opening* and *closing* are defined as $A \circ B$ and $A \circ B$ respectively where

$$AOB = A_B = (A \ominus B) \oplus B \qquad 5.11$$

$$A \bullet B = A^B = (A \oplus B) \ominus B \qquad 5.12$$

Figure 5.20 shows an example of *opening* and *closing* operations. Further examples are given in subsection 5.3.5 and 5.3.6.

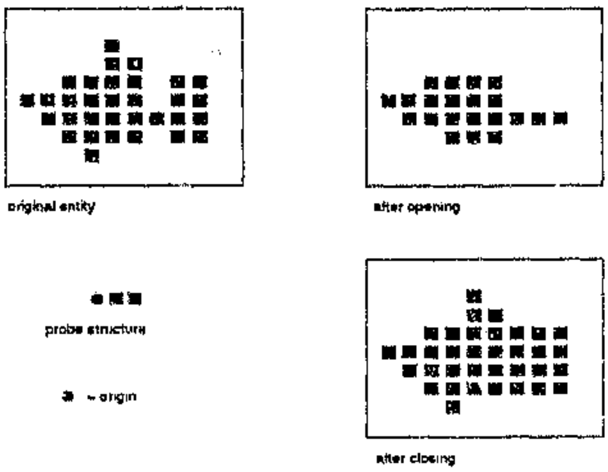

Figure 5.20: Examples of morphological opening and closing operations with a horizontal 3x1 structure.

All morphological operations can be extended to gray level images where functions instead of sets are transformed. The dilation and erosion of a grayscale function *f* by a gray scale structuring element *g* is defined by equations [5.13] [5.15] (Haralick et al, 1987), or by equations [5.17] and [5.18] (Lee et al, 1986), ie

$$f \oplus g = T[U[f] \oplus U[g] \qquad 5.13$$

$$= \max_{k,l} \{f(i-k, j-l) + g(k,l)\} \qquad 5.14$$

$$f \ominus g = T[U[f] \ominus U[g]] \qquad 5.15$$

$$= \min_{k,l} \{f(i-k, j-l) - g(k,l)\} \qquad 5.16$$

T[*f*] is defined as the *top* of *f*, and *U*[*f*] is the *umbra* of *f*, see figure 5.21 for definitions. Note that the definitions in equations [5.14] and [5.16] use the *max* and *min* operations (Maragos, 1985).

The opening and closing of a function are similar to those given in equation [5.11] and [5.12] for a binary image and are defined in equations [5.17] and [5.18].

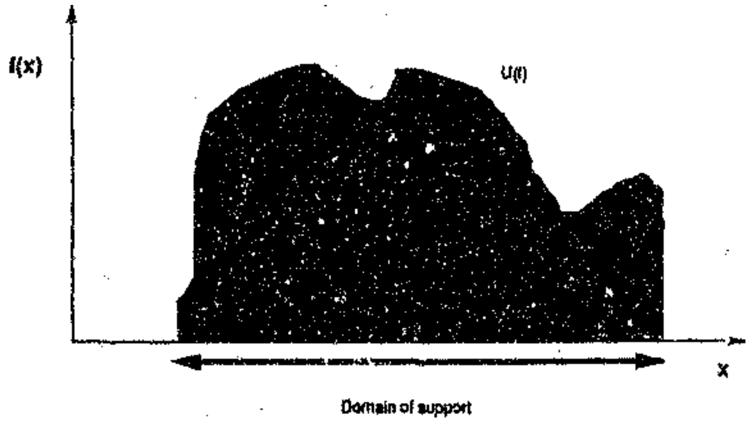

Figure 5.21: Definition of the *top* and *umbra* for a 1-D signal.

$$f \circ g = (f \ominus g) \oplus g \tag{5.17}$$

$$f \bullet g = (f \oplus g) \ominus g \tag{5.18}$$

Although the morphological operators as described above are simple to implement, they form the foundation for a large variety of image processing operations composed of combinations of erosions, dilations, openings and closings, which can have very complex results. In the next few sections morphological operations will be developed which perform *filtering* (spot-removal), *gap-fusion* and *edge-detection* of rock images.

5.3.4 Spot removal

Morphological ***opening*** with, for example, a disk-shaped probe smooths contours, breaks narrow isthmuses and eliminates small islands and sharp peaks or capes but leaves the underlying geometrical structure untouched. This is because the opening operation consists of (i) an erosion which shrinks all objects and eliminates features smaller than and similar in shape to the probe, which is then followed by (ii) a dilation which restores all remaining objects ***almost*** back to their original state. Thus generally small entities less than size A_x in an edge image E_d can be removed by the following operation

$$E_f = E_{<A_x} = [E_d]_B = (E_d \ominus B) \oplus B \tag{5.19}$$

where B is some structuring element of size A_x, and $E_{<A_x}$ is the edge image with all entities of shape similar to B and less than size A_x removed.

The opening operation is *antiextensive* because $A \circ B \subseteq A$, ie the set resulting from of opening will always be less than or equal to the original set. Figure 5.22 and 5.23 shows how opening an edge image E_d gives a filtered image E_f .


(a) (b) (c)

Figure 5.22: (a) Edge pattern E_d . Opening E_d with a (b) 3x3 *cross* and (c) *circle* structure of size 1. Figure 5.27 gives the definition of the circle structure.


(a) (b) (c)

Figure 5.23: (a) Edge pattern E_d . (b) After opening E_d with a 3x3 *cross* structure of size 2. (c) After opening E_d with a *circle* structure of size 2.

5.3.5 Fusing gaps

The morphological *closing* operation is the converse of opening because instead of removing small islands it removes small holes. This is very useful because the gaps in edge patterns could be thought of as partial holes, and closing should fuse the gaps between sets of entities as given in equation [5.20].

$$E_{\vee} = [E_f]_B = E_f \bullet B = (E_d^{\wedge} \oplus B) \ominus B \qquad 5.20$$

where $E_{\vee}$ is the fused edge image. For example consider figure 5.24 where an image is closed with a 3x3 cross shaped element. Initially all entities are dilated so that any entities separated by a gap smaller than the size of the structure are joined. The erosion which follows will then almost restore the dilated entities to their original state except that gaps between entities with a size less than the probe will remain joined depending on the original shape of those entities on either side of the gaps. The fusion occurs because of the *extensivity* property of closing ie that $A \subseteq A \bullet B$. In figure 5.25 and 5.26, the closing operation is applied to examples of edge patterns E_{∇^2} which fuses gaps to give $E_{\vee}$.


(a) (b)

Figure 5.24: Example of closing gaps between entities in an edge image E_{∇^2} with a 3x3 *cross* structuring element (size 1) to produce fused edge images $E_{\vee}$. Rock is -38+25mm quartzite. (a) Edge image, (b) $E_{\vee} = E_{\nabla^2} \bullet B$.

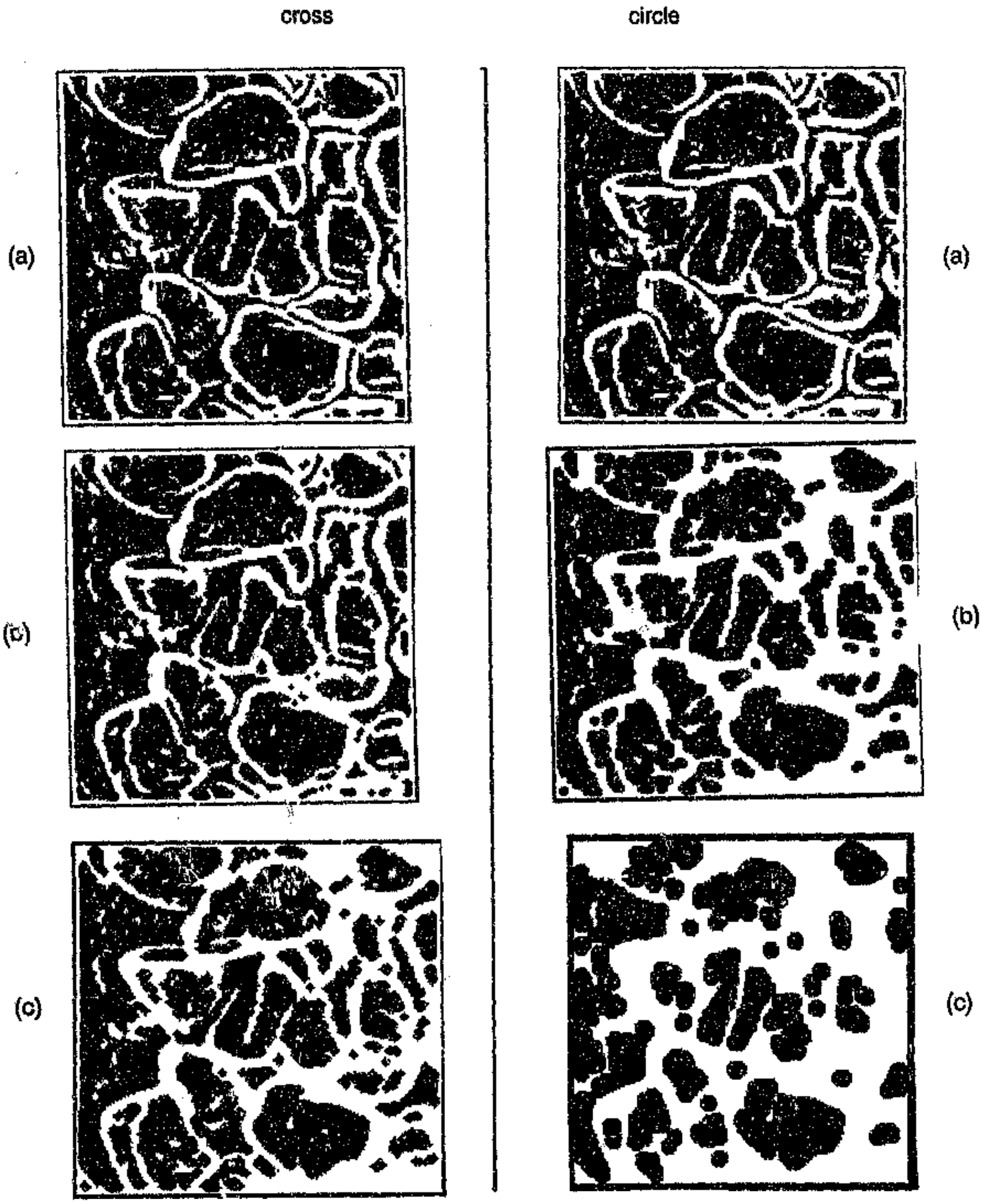

Figure 5.25: Example of closing gaps between entities in an edge image E_{v1} with a 3x3 *cross* and *circle* structuring element (size 1 and 2) to produce fused edge images E_v. (a) Edge image, (b) $E_v = E_{v1} \bullet B$, (c) $E_v = E_{v1} \bullet 2B$. Rockscene is dolomite (-38+25mm) captured from the conveyor belt.

5.3.6 Removing holes

It was suggested in chapter 4 that *thresholding* could be used to aid in the edge correction. In particular thresholding can be used to reinforce the classification of parts of an image as rock X or non-rock $Y = X'$. However one of the problems of thresholding are the holes in the segmented areas resulting from thresholding.

In addition to fusing gaps (subsection 5.3.5) the morphological operation of *closing* can also be used to remove the holes in segmented areas of rock X. If the set of rocks at threshold t is given by $E_X = X_t$ then the closed threshold image is given by $E_X^\bullet$, as shown in equation [5.21]. See figure 5.26 which shows how the holes are filled in.

$$E_X^\bullet = [X_t]_B = X_t \bullet B = (X_t \oplus B) \ominus B \qquad 5.21$$

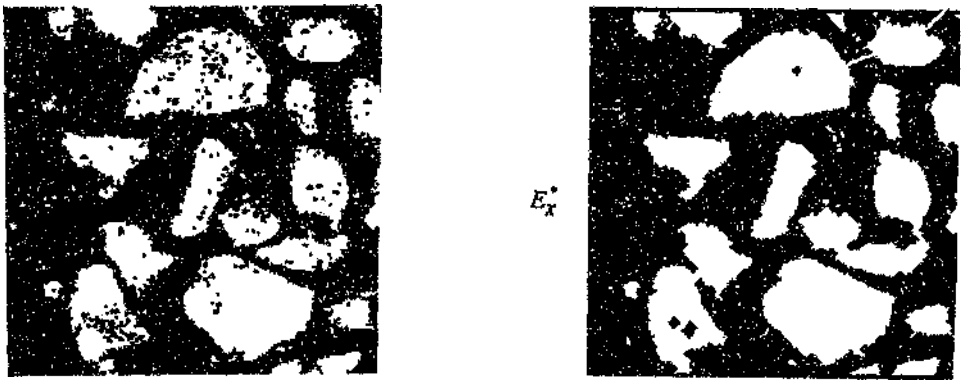

Figure 5.26: Example of closing holes in segmented areas resulting from thresholding using a cross probe of size 2.

5.3.7 Varying the size of structural elements

In the previous section we gave examples showing how opening and closing can remove small islands and close small gaps respectively. However it may be required to remove bigger islands or close larger gaps, which requires a larger structure of a suitable shape. This can be done by either using one large structuring element as has been demonstrated above, or by using multiple passes with a small element because a large structuring element can be decomposed into sets of smaller ones. Equation 5.22 shows how a large element B_{large} can be decomposed in smaller elements.

$$B_{large} = B_1 \oplus B_2 \oplus \ldots B_n \qquad 5.22$$

If $B_i = B_j$ then $B_{large} = nB$ and

$$\begin{aligned} A \oplus B_{large} &= A \oplus nB \\ &= (((A \oplus B) \oplus B) \ldots \oplus B) \qquad \text{n times} \end{aligned} \qquad 5.23$$

Thus opening or closing with a structure of any large size can be implemented by just repeating the erosions or dilations a number of times with a small structure. Morphological transformations using multiple passes with smaller structures is often desirable because of the processing speed advantages when coding the algorithm in a certain way (Maragos, 1985). Decomposition rules similar to [5.22] are also useful for constructing probes of different shapes to those elementary ones shown in figure 5.19. Figure 5.27 shows how the *box* and *circle* structure can be constructed by dilating a vertical and horizontal, and a cross and box structure together respectively.

Figure 5.27: (a) A *Box* shaped probe can be decomposed into a *vertical* and *horizontal* probes of smaller size. (b) A *cross* and *box* probe can be used to compose a *circle* probe.

5.3.8 Morphological Edge detection

In chapter 4 the Laplacian operator (∇^2) was described as the primary edge detector because most other edge detectors tested were generally unsuited for rock edge detection because of poor edge detection as required for stereological measurements. Although the Laplacian outputs acceptable edge patterns, they are contaminated with impulse noise because the Laplacian-edge detector is a differential process which amplifies high frequency noise and especially impulse noise. An alternative to using linear edge detectors such as the (∇^2) operator is to use morphological edge detection.

Morphological edge detection forms part of the set of morphological filters. The opening an image effectively removes small entities which is similar to the operation of a low pass filter. Thus by calculating the differences or residue between sets or functions that have been eroded or dilated *different amounts*, one can effectively perform a bandpass filtering operation, (Maragos, 1985), (Serra, 1988). The morphological-edge detection scheme has been found to be more robust than most other edge detection schemes for these rock images. Lee et al (1986) also found that a combination of morphological edge detectors gave comparable performance to second derivative zero-crossing edge detectors, ie ∇^2.

As an example consider the fig. 5.28(a) which shows an original binary image X. Fig 5.28(b) is the same object after erosion by a spherical structure B to give $X \ominus B$. Fig. 5.28(c) shows the difference between image (a) and (b) ie $X-(X \ominus B)$ which is essentially the edge of the object.

Figure 5.28: Example of the morphological edge detector as applied to a binary entity. (a) Original image X. (b) $X \ominus B$. (c) The difference $X-(X \ominus B)$.

The morphological edge detection scheme can be extended to gray-scale images f, where the generic filter function $g_{m,n}$ is given by

$$g_{m,n} = (f \ominus mB) - (f \ominus nB) \qquad \text{where} \quad m < n \tag{5.24}$$

and nB is the n-fold Minkowski sum of B with itself, and m and n are scalars, and where the $\ominus$ can be replaced with a $\oplus$ for $m > n$. The values of and difference between m and n controls the bandwidth of the filter, or the thickness of the edges in an edge detection operation. For the algorithms developed in this work m was made 1 and n=0 to give the edge detector as shown in equation 5.25, which gives thin edges for reasons discussed in chapter 4.5.2.

$$g_{1,0} = (f \oplus B) - f \tag{5.25}$$

The orientation of B controls the orientation of the edges detected, but is of no consequence if *symmetric* structuring elements are used. For gray level images the probe B does not necessarily have to be a set but can also be a function k .

Figure 5.29 and 5.30 show the result of applying the morphological edge detector to some rock images. It is observed that the morphological edge detector produces far less unwanted edges than Laplacian, if some form of prefiltering is used, see figure 5.29.

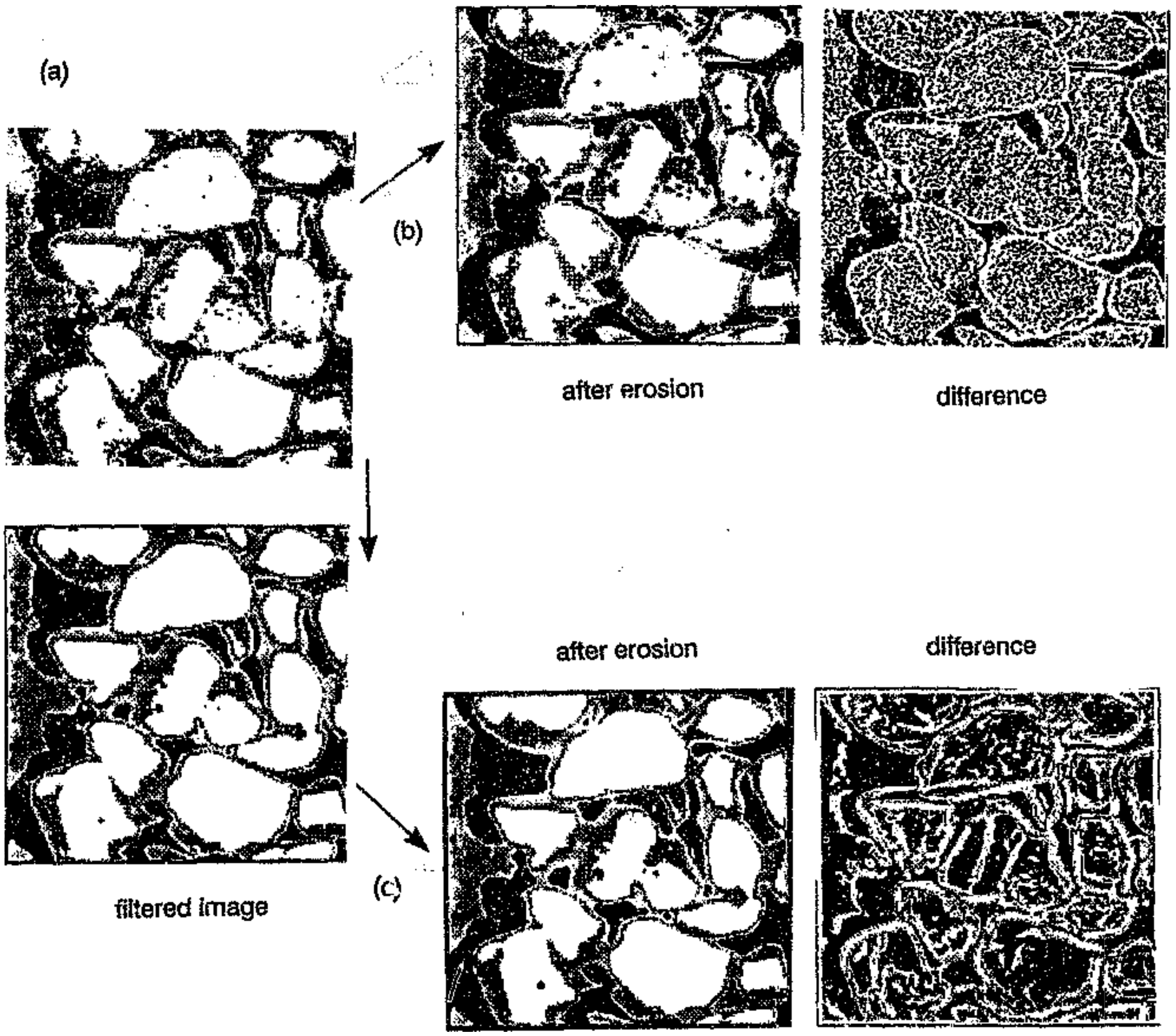

Figure 5.29: Morphological edge detection applied to a scene of large rocks (-38 [illegible] mm). (a) Original image. (b) Morphological edge detection with no pre-filtering. (c) Morphological edge detection with *NAA* pre-filtering. Probe structure used is a 3x3 cross.

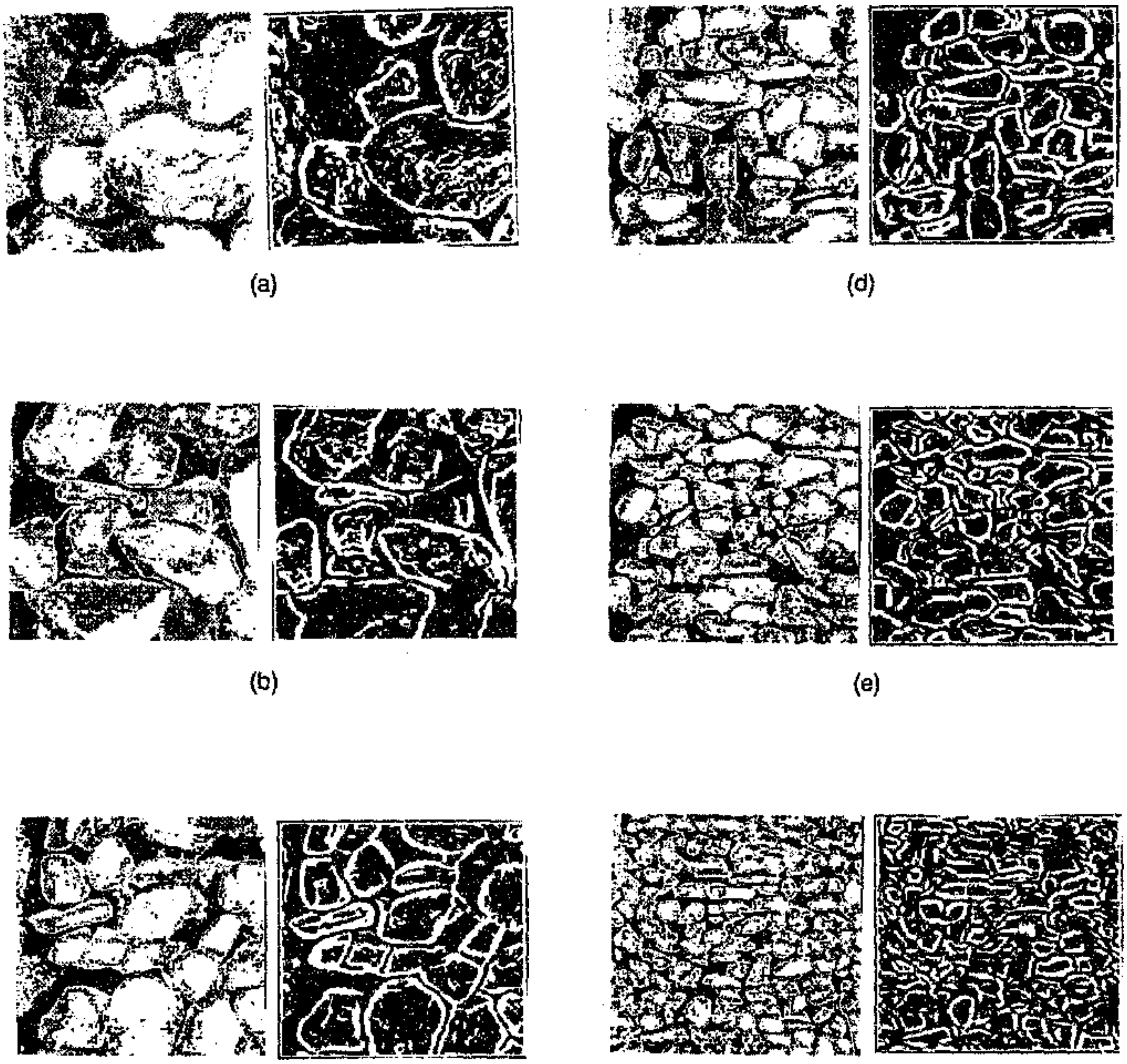

Figure 5.30: Examples of morphological edge detection applied to rock edges. The raw images shown have been prefiltered using the *NAA* filter. The probe used is a circle. The above figures show pairs consisting of the original image and the result of the morphological edge detection for (a) -50+38mm, (b) -38+25mm, (c) -25+19mm, (d) -19+13.7mm, (e) -13+9.35mm, and (f) -9.35+6.15mm size distributions.

5.4 THE FINAL ALGORITHM

5.4.1 Introduction

The final algorithm for rock edge detection should fulfil the following requirements.

(i) The algorithm must be as *simple* as possible so that it does not take too long to process a single image.

(ii) The algorithm must be *generic*, in the sense that it should be able to handle as many rock scenes of a given rockstream as possible, without having to resort to major modifications when the characteristics change.

(iii) The rock scenes do change and the algorithm must be able to automatically adapt to changing image and environmental conditions, ie the algorithm must be independent of the user.

In the previous subsection various techniques or tools for improving edge patterns at various stages of completion have been discussed and developed. In addition the morphological edge detector is deemed a viable alternative to the linear edge detectors as discussed in chapter 4. It now remains to exploit the best features of certain of these techniques and *combine* them into one image-processing system. In this section a complete algorithm for rock boundary detection based on extensive experimentation, is described together with the strategies for combining these various tools and methodologies.

5.4.2 The Total System

The final objective of the image processing is to derive an ideal image of the rock boundaries E_{ax} from the raw image I. However because the algorithm is not perfect the output is denoted E_{ax}^{*} where

$$E_{ax}^{*} = \Psi[I] \qquad 5.26$$

and $$E_{ax}^{*} = \Psi_2[\Psi_1[I]] \qquad 5.27$$

The flow diagram of the final algorithm, (figure 5.31), shows sequential stages of *primary feature detection* or *extraction* Ψ_1, and *edge correction* Ψ_2. Ψ_1 can be broken down into two parallel[5.4] branches of *segmentation (thresholding)* and *edge detection*. A more detailed algorithm is shown in figure 5.32.

The data (image) flow is as follows : The raw image I is fed into the primary stage Ψ_1 where it is filtered to produce I_f . I_f is then fed into the two parallel stages which are the ***primary-edge detection*** and the ***tail-thre-***

[5.4] The stages are only conceptually thought of as being parallel. In practice they were executed on a sequential computer.

sholding stages, which produce three sets of image data. This includes the edge pattern E_d, an estimate of the rocks E_X and an estimate of non-rock E_Y. Both E_X and E_Y are results of the tail thresholding as discussed in chapter 4.4. The edge and threshold data sets are then fed into Ψ_2 in which the three data sets E_d, E_X, and E_Y are processed and subsequently combined to give the final estimate of the rock outlines $E^*_{\partial X}$. As has been discussed in section 5.1, 5.2 and 5.3 the edge data E_d has many errors and has to be corrected. The edge correction can be performed by either or both the *joining* Ψ_V or *morphological* Ψ_{morph} correction schemes which are assisted by the data in the threshold data sets E_X and E_Y. For the pilot plant tests described in chapter 6 and 7, the morphological processes were selected.

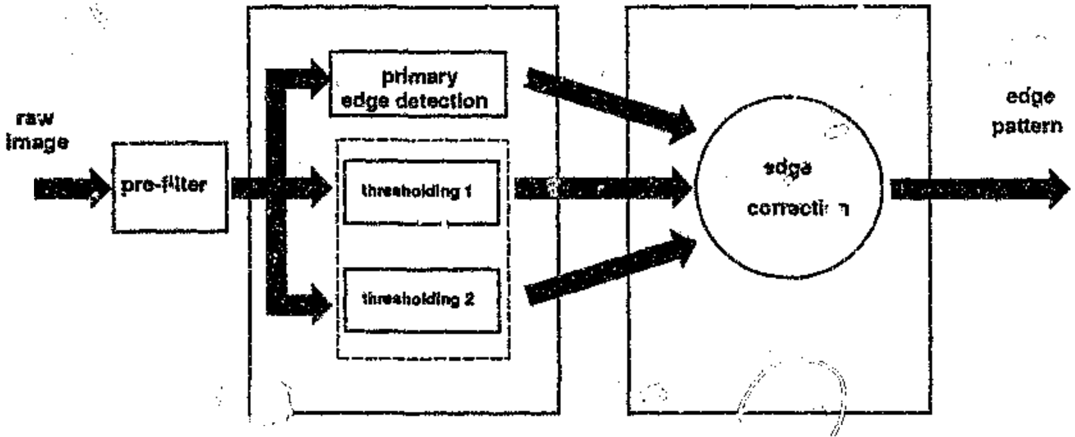

Figure 5.31: Simplified block diagram of the final algorithm Ψ showing the two main blocks of (i) primary parameter detection, and (ii) edge correction and the combining stage.

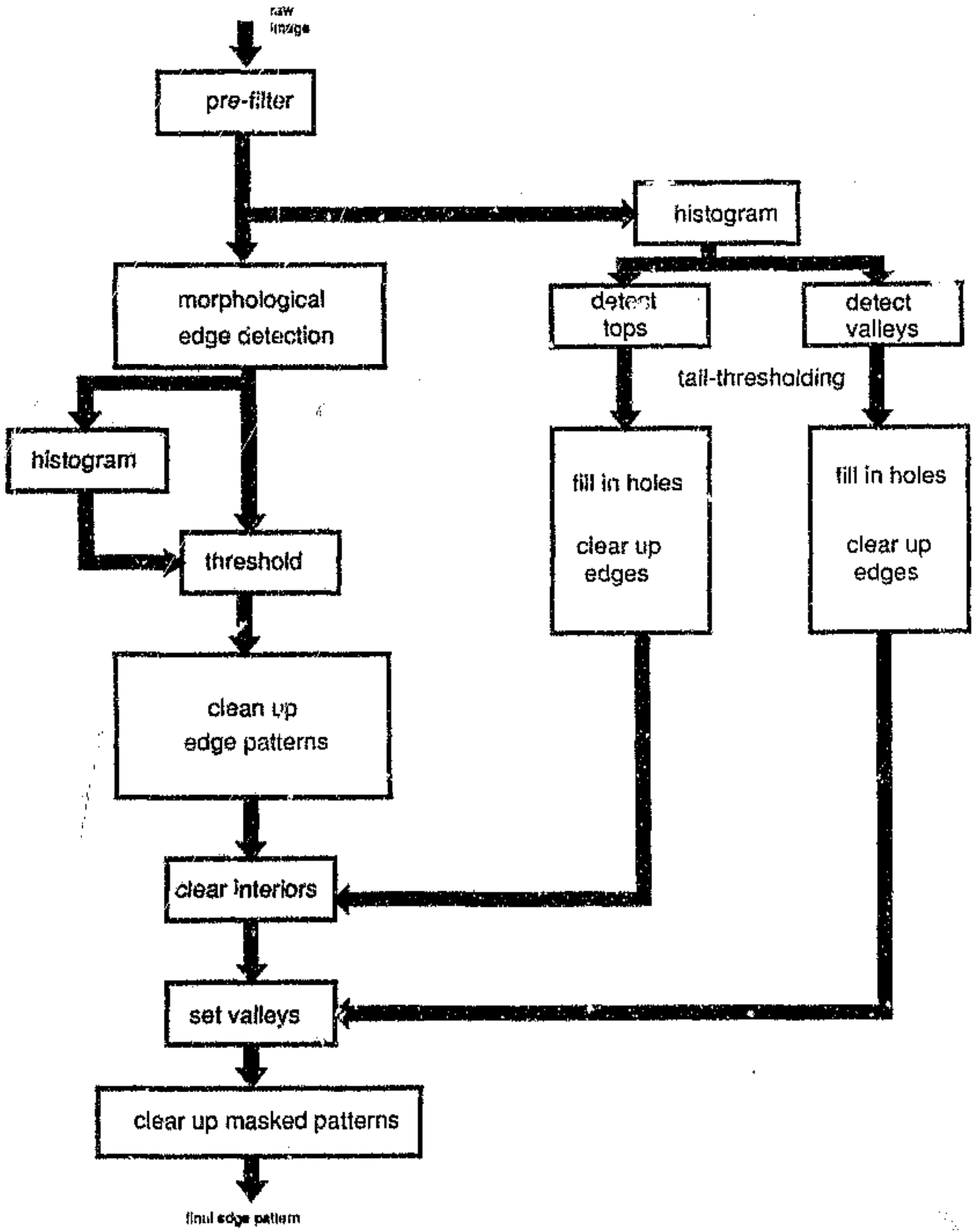

Figure 5.32: Detailed block diagram of the processes in Ψ as implemented in pilot plant conveyor-belt tests.

5.4.3 Primary operations Ψ_1

The raw image I as digitized by the frame grabber is filtered by a *nearest neighbourhood averaging* (NAA) filter which smooths the raw image I and removes most of the impulse noise to produce the image *function* I_f. For this research the image is filtered consecutively three times.

The filtered image I_f is then fed to two 'parallel' processes. The first process is the morphological-edge detection which produces a gray level image $g_{1,0}$ pattern. The edge image $g_{1,0}$ must be converted to a binary image which requires the thresholding of $g_{1,0}$ to produce the binary set E_d . The threshold value is selected from the histogram of $g_{1,0}$, $h_{g_{1,0}}$ which has a decaying exponential shape. The method of selecting the threshold $t_{g_{1,0}}$ is ad-hoc and the p'th percentile of the cumulative histogram $H_{g_{1,0}} = \int H_{g_{1,0}}(x)dx$ is the method chosen. Note that an alternative edge-detection algorithm such as the ∇^2 operator can be used in place of the morphological-edge detector.

The other parallel processing stage is the "tail thresholding" algorithm which produces the two binary images E_X and E_Y , which represent areas in the image of high and low probability of being rocks respectively. The algorithm is developed in chapter 4.4 and relies on the histogram $h(g)$ of I_f to select the threshold values.

5.4.4 Correction and Combining operations Ψ_2

In the correction and combining stage Ψ_2 three fundamental operations are performed on the edge pattern using all three data sets derived in Ψ_1. The first operation is the removal of noise or small islands $E_n \subset E_d$ which is performed by filter Ψ_f which uses *opening* to remove the small entities $E_{<A_n}$. The second stage is the fusing together of the remaining edges by estimating and constructing missing edges $E_\Delta = E_{\partial X} - E^*_{\partial X}$. This fusion operation is performed by *closing* the remaining entities $E_f = E_{\geq A_n}$ together. These two transformations are shown in equations [5.28], [5.29] and [5.30], where B_f and $B_\vee$ are the different probes used for Ψ_f and $\Psi_\vee$ respectively.

$$E_f = \Psi_f(E_d) = [E_d]_B \qquad 5.28$$

and $$E_v = \Psi_\vee(E_f) = [E_f]^B \qquad 5.29$$

$$\Rightarrow \quad E_\vee = \Psi_\vee \Psi_f\{E_d\} = ([E_d]OB_f)OB_\vee \qquad 5.30$$

However the fused edge pattern E_V still contains a number of large fused entities which are not part of the rock boundaries ∂X because they lie in the perceived interior of the projected rocks. In addition some of these noise islands have merged with the rock boundary entities because of the fusing operation Ψ_V. These merged islands have to be removed and this is done with the help of the E_X which is an estimate of the location of the interiors of rocks.

E_X is used as a *mask* to *clear* the interior of the projected rock areas, where all entities falling within the mask area are eliminated by logically ANDing the edge image with the inverse of E_X as given in equation [5.31].

$$E_{mask} = [E_V] \quad \text{AND} \quad [E_X^*]' \tag{5.31}$$

where $[E_X^*]'$ is the binary inverse of E_X^*. E_X^* is a transformed version of E_X where the transformation on E_X has filled up holes and cleaned up the edges of the entities in E_X. The transformation on E_X is performed with morphological closing and openings.

After the masking transformation, the set E_Y is used *to fill in* certain areas of the image that are *definitely not rock* ie Y to produce $E_{\partial X,Y}$, for example parts of the conveyor belt, or small areas between rocks which may be part of occluded rocks but are partially or fully in shadow, and have been assumed to be too distorted to provide any real indication of the size of the underlying rocks. Only the edges of these void areas are detected so E_Y fills in these voids so that the chord-length probe does not measure in these areas when applied. This operation is performed by ORing E_Y with the masked edge image as shown in equation [5.32]. Note that E_Y is also preprocessed with morphological operators to give E_Y^*.

$$E_{\partial X,Y} = [E_{mask}] \quad \text{OR} \quad E_Y^* \tag{5.32}$$

5.4.5 Discussion

$E_{\partial X,Y}$ is conceptually the final output of the image processing stage Ψ_2 thus $E_{\partial X}^* = E_{\partial X,Y}$. However the details of data flow as presented in this section are not exactly the same as the data flow implemented in experiments and in tests. The basic structure of combining edge detection, thresholding and morphological operations for filtering and closing gaps is essentially still the same. However other stages are inserted where necessary depending on the type of rocks and images to be processed in order to improve the overall results of the rock boundary detection for a particular type of rockstream. For example, erosion of the edge pattern (ie *thinning*) E_d may be necessary because the threshold value T_{high} used by the tail thresholding algorithm may result in which thick edges which would have to thinned.

The choice of a particular edge detector, pre-filter or other operator, is not fixed to the morphological or NAA filter, but can be any operator that fulfils the requirements stated in subsection 5.4.1 and which when put together detects valid and accurate edge perimeters in the shortest possible time.

There is still a universal need to tune this system (or any other edge detection system) to the particular characteristics of the rockscenes being processed. Parameters to be tuned include for example the size and shape of the morphological probe structures, as well criteria for thresholding. It is possible that *neural networks* hold the key to future rocksize systems where the system can learn to adapt to the characteristics of a given rockstream.

5.4.6 Examples of the resultant Edge patterns

In figures 5.31 to 5.33 we shows some results of the edge patterns produced by this algorithm.

Figure 5.33: Edge E^*_{ax} patterns for scenes of large rocks.

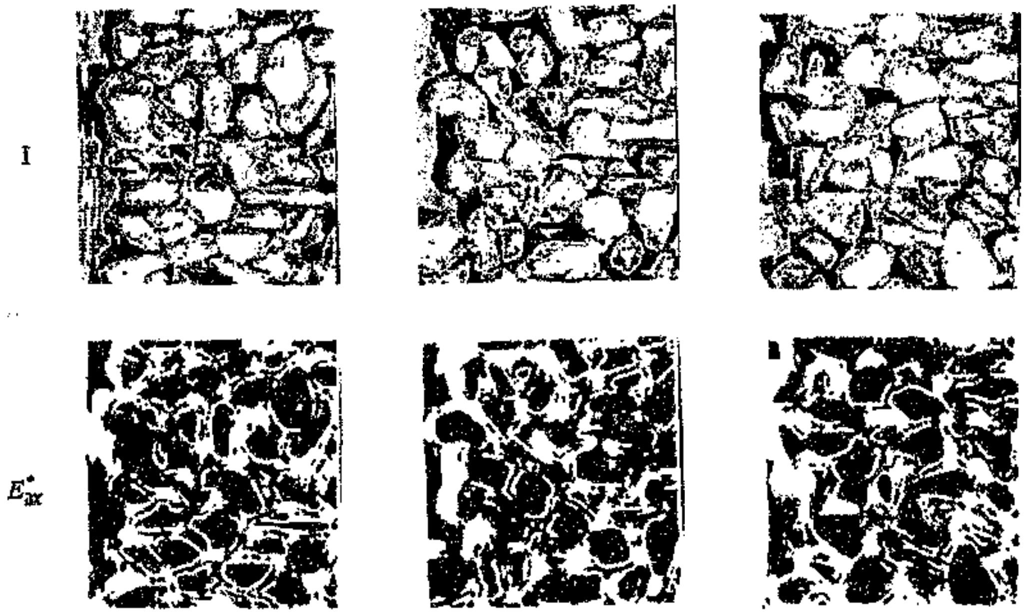

Figure 5.34: Edge patterns E^*_{ax} for scenes of small rocks.

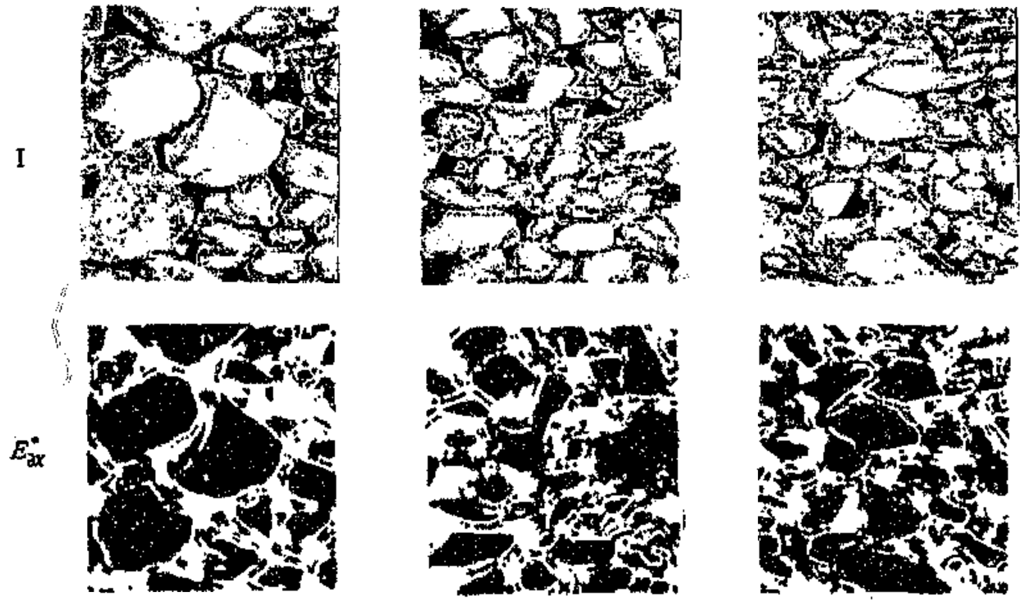

Figure 5.35: Edge patterns E^*_{ax} for scenes of mixed rocks.

5.5 CONCLUSION

In this chapter the second part to the global rock-edge detection strategy Ψ_2 was developed, the main tasks being the removal of unwanted edges and closing of gaps. This corrective action is required because primary edge-detector or thresholding algorithms generally cannot produce an image of rock edges or areas on which useful stereological measurements can be made.

The final algorithms developed in this chapter make extensive use of mathematical morphology and these techniques have proved to invaluable as far as image transformations are concerned. In particular they provide a simpler alternative to the more complex "joining" type algorithm which follows the traditional approach to image processing.

The only way in which the success or usefulness of the algorithms developed in this chapter can be verified, is by implementing these algorithms and measuring rock size. The experimental setup for such tests, and the resulting measurements and transformations are discussed in chapter 6 and 7 respectively.

In conclusion it must be emphasized that the algorithm developed for Ψ (chapters 4 and 5) is only one interpretation of how the problem can be solved. There is the possibility that in time many other algorithms or image processing techniques may be developed which given faster and more powerful hardware, could result in better rock segmentation. This emphasizes the philosophy adopted with regard to the development of the image processing algorithms in this research, that these algorithms are only stepping stones proving that measurements of rocksize on a conveyor belt can be made.

6 EXPERIMENTS AND TESTS TO DERIVE CHORD-LENGTH DISTRIBUTIONS

6.1 INTRODUCTION

This chapter presents the apparatus and experimental procedure developed for testing the techniques and algorithms described in chapters 3, 4 and 5. The measured outcome of these experiments are raw chord-length distributions $g(L)$[6.1] from which size distributions are to be determined, in particular *sieve* or *mesh size* distributions $f(D)$. The conversion $f(D)=\Psi_z\{g(L)\}$ is discussed in chapter 7.

Two groups of rocksize tests were conducted, namely *static* and *dynamic* tests. Static tests were undertaken in the laboratory, and *dynamic* tests were carried out on a pilot-plant conveyor-belt system. The group of static tests consists of two classes of experiments which were carried out on *separate* and *piled* rocks, which can be viewed as *sparsely* and *densely* distributed particle systems respectively. On the conveyor-belt, dynamic tests were only carried out on piled rocks which formed dense rockstreams, high N_V.

6.2 THE OBJECTIVE OF THE ROCKSIZE TESTS

The purpose of these tests and experiments is to provide experimental data so that,

1. The hypothesis, that the size of rocks under *ideal* conditions can be measured using machine-vision, can be tested. Ideal conditions includes *separated* rocks *uniformly randomly* distributed in space. The fundamental principles associated with deriving sizing parameters using machine-vision under these conditions to a large extent have already been tackled and proved by other researchers on microscopic applications in the biological and metallurgical fields respectively (Weibel, 1979, 1980), (King, 1982, 1984). However no work other than what has been mentioned in chapter 1 has been performed on rocks and in particular conveyor belt applications.
2. The hypothesis, that the size of rocks under *non-ideal conditions* can be measured using machine-vision, can be tested. Non-ideal conditions includes *piled* rocks on a *moving* conveyor belt, where most rocks are hidden or cannot be seen. Associated with this hypothesis is the need to fulfil the requirements for a practical *instrument* system which can process moving images in realtime without resorting to supercomputers.

[6.1] The measured chord length distribution is $g(L)$ which when converted to density function becomes $p(L)$.

3. The instrument can be tested for consistency with the basic principles of any instrumentation system; ie that the measurements are *repeatable*, and actually represent the physical property required.

The last point concerning the representation of the *physical property* to be measured, is difficult to fulfil because size is not unambiguously defined, and is dependent on the form of measurement (chapter 1). Because of the lack of an alternative standard for rocksize, *sieve size* (Allen, 1981) has been selected as the *physical property* against which this measurement system is to be evaluated.

Points 2 and 3 above form the basic part of the original work done in this thesis. Except for Yacher et al (1985) no reports could be found in the literature on rocksize measurements on moving rockstreams, and the report of Yacher et al does not include sufficient detail on the rock material, ie shape, and the type of processing used to compare its performance with the system developed here.

6.3 THE ROCK MATERIAL

In order to perform comprehensive tests of the robustness of the instrument in terms of hardware and software, as many different types of rockstreams as possible should be tested. However as a result of time constraints, bulk handling, crusher and sieving problems, only a few varieties of rock could be tested, the main groups being granite and quartzite. Both rock groups were used for static tests in the laboratory, whilst only quartzite was used for dynamic testing.

Granite which was only used for initial tests, has a rough texture and a spotty appearance, and varies from dark gray to white. Quartzite on the other hand has a smoother texture and is a more homogeneous colouring of light gray. The colour of quartzite changes significantly with the amount of water, and when wet or damp becomes dark gray as opposed to a white gray.

In order to test the instrument system's response to various sizes of rocks it was decided to sieve the rock material into "narrow" size classes from which artificial distributions (wide band signals) could be mixed. Measurements by the instrument of a *single* size class could be likened to testing the response of a system to a "single" frequency or narrowband signal. The quartzite was initially available as a mixed distribution and was hand sieved to produce rock size groups as shown in table 6.1. The granite which was only available in 25mm size range had to be successively crushed and sieved to produce the size ranges as shown in table 6.2. The fractions for the quartzite and granite tests are different because the granite material was prepared for Wigeson (1987) using a combined crusher and sieving system, whilst the quartzite was prepared for conveyor belt tests

Table 6.1 **Table of size classes used for testing quartzite rock material.**

Size Group	Sieve Size (mm)
1	-6.3mm
2	-9.35mm + 6.3mm
3	-12.7mm + 9.35mm
4	-19mm + 12.7mm
5	-25mm + 19mm
6	-38mm + 25mm
7	-75 + 50mm
8	+75mm

Table 6.2 **Table of size classes used for testing granite rock material.**

Size Group	Sieve Size (mm)
1	-0.212mm
2	-1.00mm + 0.212mm
3	-2.36mm + 1.00mm
4	-3.35mm + 2.36mm
5	-4.8mm + 3.35mm
6	-6.3mm + 4.8mm
7	-7.94mm + 6.3mm
8	-9.35mm + 7.94mm
9	-12.7mm+ 9.35mm
10	-15.9mm + 12.7mm
11	-25 + 15.9mm

by hand sieving with a limited selection of sieves where the larger size factions were of interest. On average, over 150 kg of each fraction of each rock was prepared and sieved. The accuracy of the manual sieving procedure is not ideal because *time* and the *amount* of material on a sieve determines the quantity of material that passes through the sieve (Allen, 1981). In addition the mass handling problem with the larger rock fractions of quartzite made the sieving procedure very labour intensive and subject to human errors.

6.4 EXPERIMENTAL RIGS

Two experimental rigs were set up for the rocksize experiments. One was for processing scenes of *stationary* rock piles, the other for processing scenes *moving* rockstreams on the conveyor-belt system.

THE STATIC RIG

For *stationary* rock piles, an image capturing system was setup in a "rock lab" where different illumination systems and image capturing hardware and software was developed and tested. Figure 6.1 shows schematically the image capturing system which is based on an Intel 80286 based microcomputer and the Data Translation frame grabber DT2851 which plugs into the AT bus of the microcomputer. Figure 6.3 shows a photograph of the "rock-lab" setup. PAL colour-video cameras as well as various black and white cameras were used to capture the images of stationary rockscenes.

The images of rockscenes to be processed were captured and digitized by the DT2851 frame grabber which stored the image in the frame grabber's RAM as a gray scale (black and white) image. The size of image stored was 512 by 512 pixels; however only the centre portion of this image (200 by 200 pixels) was transferred to the computer's memory for further processing by versions of the software described in chapters 4 and 5. Not all the available image is used because of memory limitations imposed by the operating system MS-DOS used on the microcomputer as well as processing time.

THE DYNAMIC TEST RIG

A *closed-loop conveyor-belt* system was constructed to test the rock size system on moving rock images. The conveyor belt system consists of two separate belts lying alongside one another and moving in opposite directions. At the end of each belt, a chute channels rock material falling off the one belt onto the other belt lying alongside. Both belts were driven by variable speed DC-motors with independent variable speed controls. This systems simulates to a certain extent the rockstreams as found on conveyor belts feeding autogenous mills. However it is important to note that each rockstream being fed to a mill has its own unique characteristics which is impossible to reproduce accurately on the test rig.

Moving rock scenes introduce special problems such as image *blurring* and *interlacing* which can render the whole measurement process useless. Blurring is caused by a point in the scene reflecting light onto more than one part of the image sensor by virtue of its movement and the sensor being "on" for part of the duration of the movement. Blurring can be solved by estimating *point spread functions* and reversing the effect of the blurring mechanism, (Du Toit, 1987). The *interlacing* problem is also brought about by scene movement, which causes the adjacent "even" and "odd" sequential fields of standard television signals to contain displaced copies of the same scene. Thus when a full frame which is made up of both an even or odd field is digitized, the image appears grossly distorted. To remove the interlacing problem one could, for example, resort to single field image-digitizers or software which realigns the fields. However edge detection on these single field or realigned images was too susceptible to noise generated by missing lines and slight misalignments respectively. Thus in order to solve the blurring and interlacing problem a custom *line-scan* image capturing system was designed and developed.

THE LINE-SCAN CAMERA SYSTEM

The line-scan camera system which eliminates all interlacing operates as follows. The line-scan camera captures a *line-image* of the conveyor belt in a direction perpendicular to the direction of movement. This image line is then digitized and stored sequentially together with a number of similar lines captured one after another in the frame grabber, essentially allowing an image to be built up line by line. Blurring is also reduced by capturing each line-image in a very short exposure-time. The speed of operation of the line-scan camera system developed is variable and typical line exposure times are 1/5000 of a second. A schematic diagram of the hardware system developed for dynamic image capture is shown in figure 6.2. A custom wide-band video amplifier (100Hz - 10MHz, -3dB) was also developed which interfaces the inverted line-scan camera video-signal to the format required by the frame-grabber. The camera and associated hardware were installed in a protective control room adjacent to a closed-loop conveyor belt system. Figure 6.4 shows a photograph of the conveyor belt system, and figure 6.5 shows schematically the experimental setup of the camera system, conveyor belt and lighting.

The lighting for the conveyor-belt system consists of four 500 Watt halogen lamps driven by 240V DC because the sinusoidal variations in AC power (and hence lighting) is picked up by the image capturing system. With the line-scan camera system this AC lighting interference manifests itself as alternating horizontal bands of dark and light. The AC lighting problem was also noticeable with normal video cameras used for static tests where two images captured one after another of the same scene were generally not exactly the same.

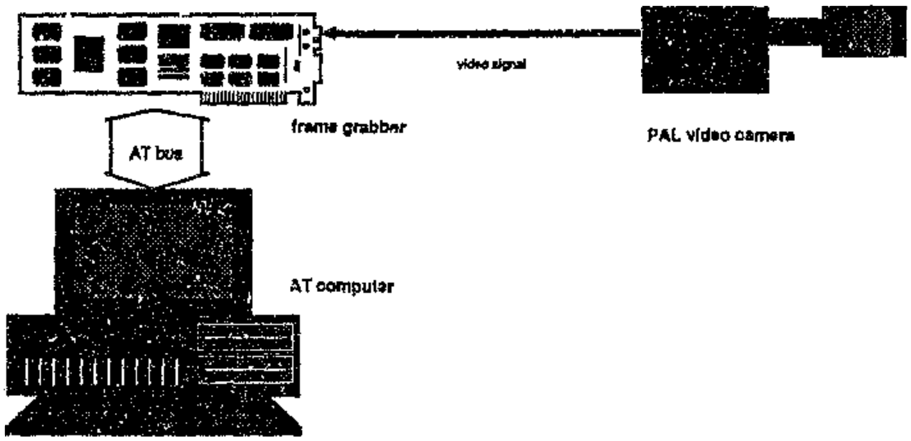

Figure 6.1: Schematic diagram of the image processing system in the "rock lab".

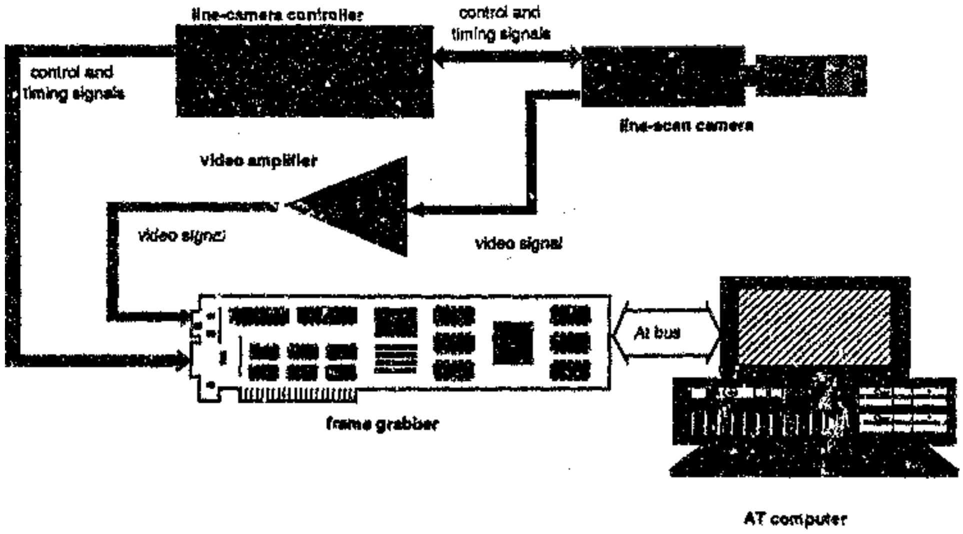

Figure 6.2: Schematic diagram of the image processing system used for dynamic image capture on the closed-loop conveyor belt system.

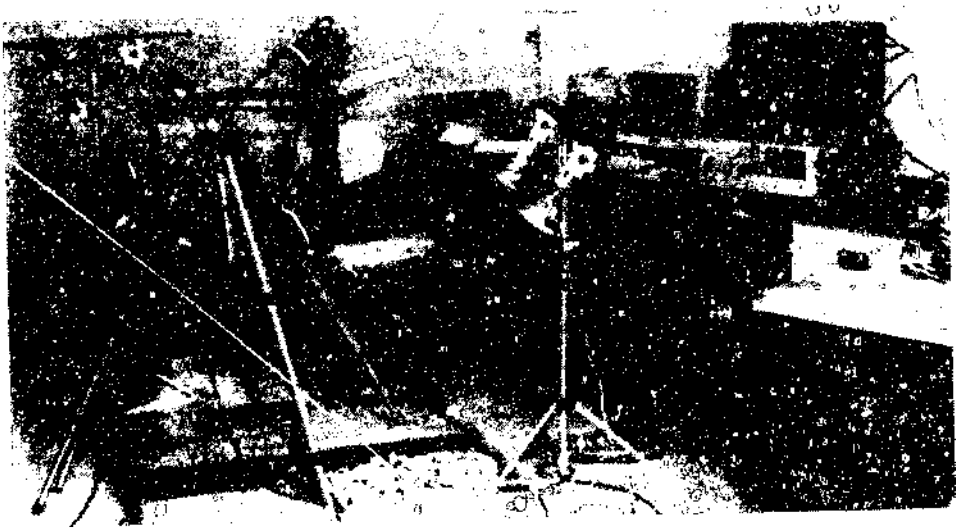

Figure 6.3: Photograph of the image capture system as used in the rock lab.

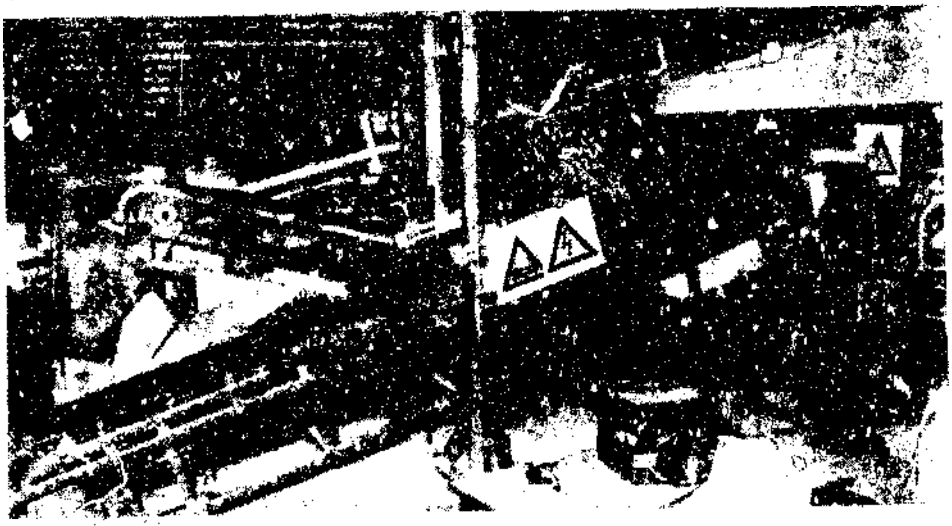

Figure 6.4: Photograph of the closed loop conveyor belt system used for dynamic image capture.

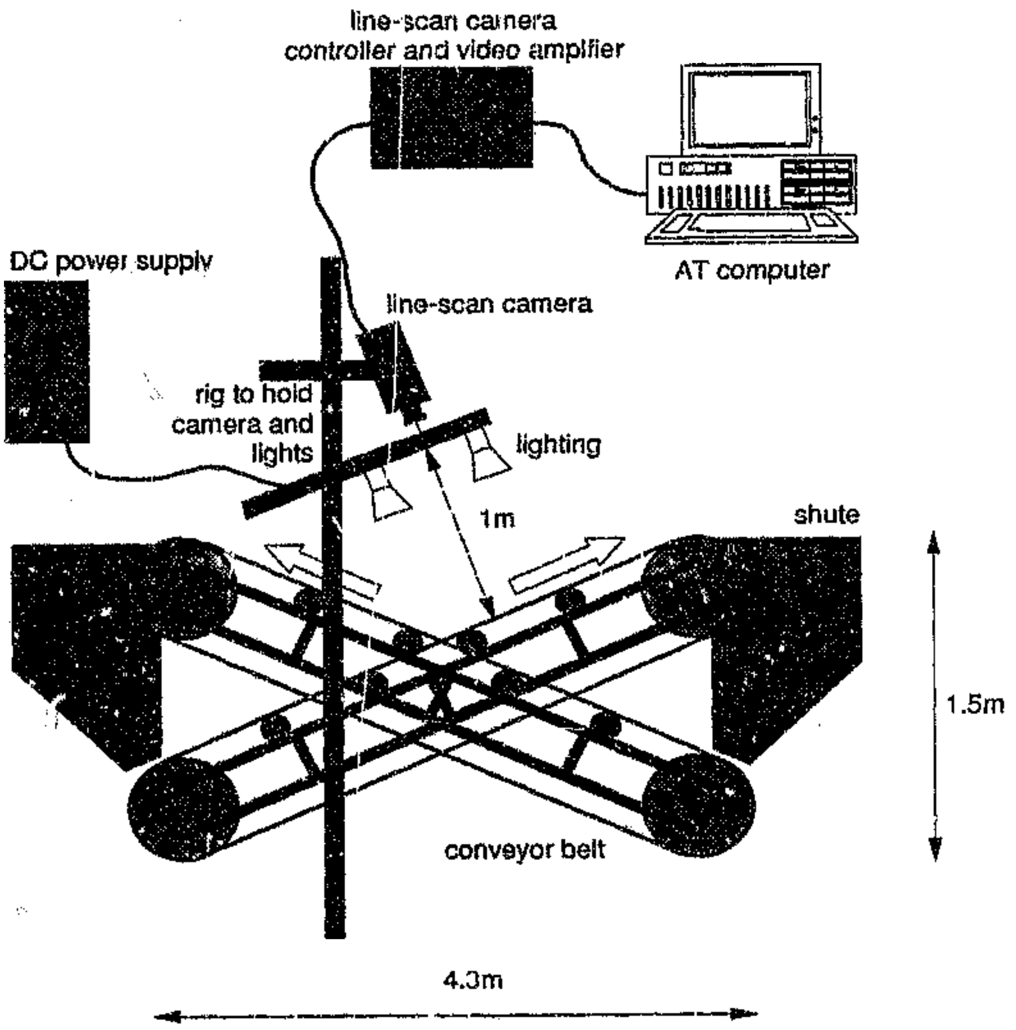

Figure 6.5: Schematic diagram of the experimental rig used for dynamic rock-size measurement tests.

6.5 CHORD-LENGTH DISTRIBUTIONS FROM STATIONARY ROCK PILES

6.5.1 Separate rocks - Quartzite

Static tests were conducted in the "rock-lab" on ***separated*** granite and quartzite rock material in order to investigate the use of chord-length measurements on ideal rock projections. The software used was neither the joining nor morphological algorithms because, as discussed in chapter 2, the segmentation and identification of separate rocks is simple. To aid rock segmentation, the rocks were placed on a matt-black background which effectively rendered the image into two areas of dark background and light-coloured rocks, which results in a bimodal gray-level histogram and makes simple global thresholding a perfect candidate for rock segmentation. Uniform neon lighting provided the illumination. Examples of these images are shown in figure 6.6.

The size groups of rocks used for these separate tests are given in table 6.2. The measurement procedure consisted of pouring the rocks randomly onto the black surface and separating the rocks by hand so that they did not touch each other. Note that the rocks were not selected individually from a pile. The image scene was inspected relative to a reference grid on a monitor and all rocks cutting the frame or image border removed. The scene was then captured, globally threshold, and the chord-length distribution measured. A PAL video camera was used for image capture, and lighting consisted of uniform AC neon lighting.

The resultant *average* chord-length density distributions $\overline{p}(L)$ for different piles of quartzite rocks and probe spacing are shown in figures 6.10 and 6.11 where separate and touching rocks are compared. If a measured chord-length distribution is given by the $g_i(L)$ the average chord-length *density* distributions $\overline{p}(L)$ is calculated by equation [6.1]. Because the above procedure for setting up the rocks is very labour intensive, the average chord-length distribution is derived from measurements made on between n=20 to 40 images only.

$$\overline{p}(L) = \frac{\overline{g}(L)}{\sum\limits_{L} \overline{g}(L)} \qquad \textit{where} \qquad \overline{g}(L) = \frac{1}{n}\sum_{i=1}^{n} g_i(L) \qquad 6.1$$

The chord-length distributions should be measured by probe lines spaced a distance apart that is greater than the maximum caliper diameter of the rocks being measured (Weibel, 1979). However the chord-length measurements in this research were made with *adjacent* probes which allows many more samples to be collected than with properly spaced probe lines. Correctly spaced probe lines result in chord-length distribution curves that are discontinuous and difficult to interpret and compare because of the small number of samples. Note that although adjacent probing produces better looking distributions, the rocks are being oversampled, thus biasing the measurement. Figure 6.7 shows how probe spacing affects the chord-length distribution.

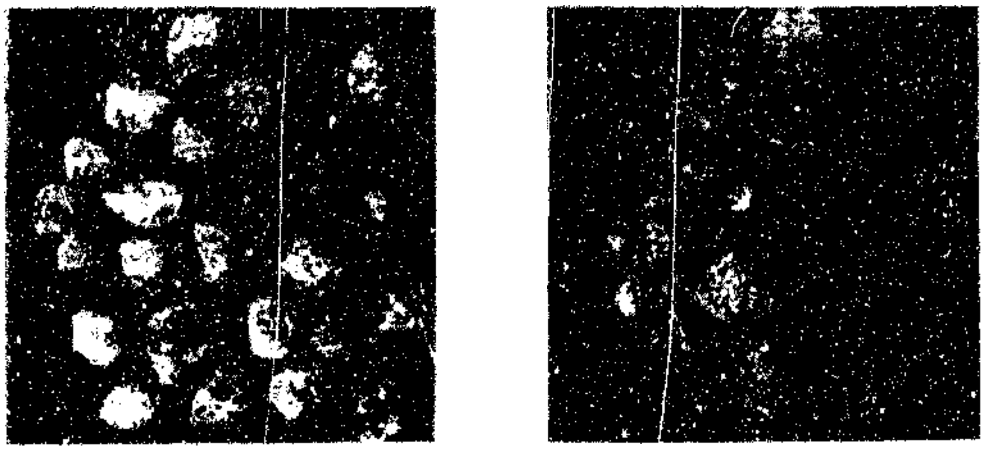

Figure 6.6: Examples of rock images of separated quartzite rock

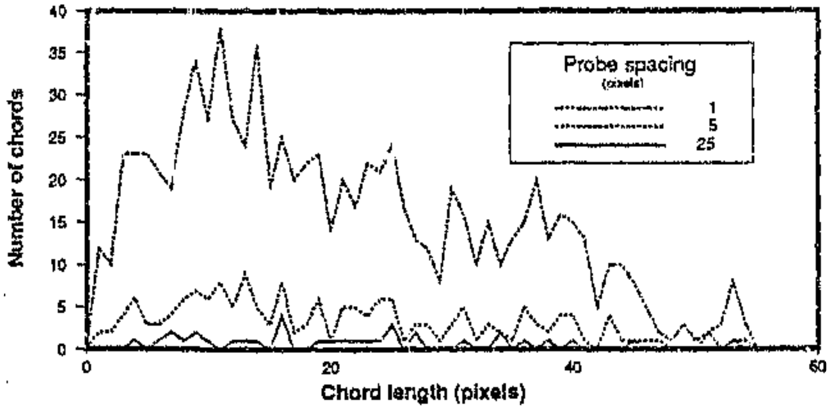

Figure 6.7: Typical example of resultant chord-length distribution measured with chord probes spaced 25, 5 and 1 pixel(s) apart. Image is 200x200 pixels.

The graphs of chord-length distributions are plots of the *number* frequency of chords of a certain length L being measured. For convenience the x-axis shows chord length measured in units of ***pixels*** instead of meters. It is possible to convert these pixel units to meters, where pixels and meters are linearly related in the x and y co-ordinates of the image. It must be noted that many sets of tests and chord lengths were measured at different focal distances covering different areas, thus care has been taken to compare only those sets of data which covered the *same* scene area.

It must also be noted that the frame grabber used does not digitize square pixels, although the DT2851 in particular has a frame size of 512 by 512 pixels. Therefore in order to allow for a square image to be displayed on a non-square television tube, the approximate pixel aspect ratio is $1{:}\sqrt{2}$. This is an undesirable situation because it is possible that chord-length distributions in both the x and y directions can be combined to give further size data. Because of the non-square pixel aspect ratio, all linear probes applied during the course of this research, were in the x direction only. The difference in data from row or column probes is shown in figure 6.8 in which the chord distribution of adjacent probes measured from the same image in orthogonal directions, is presented.

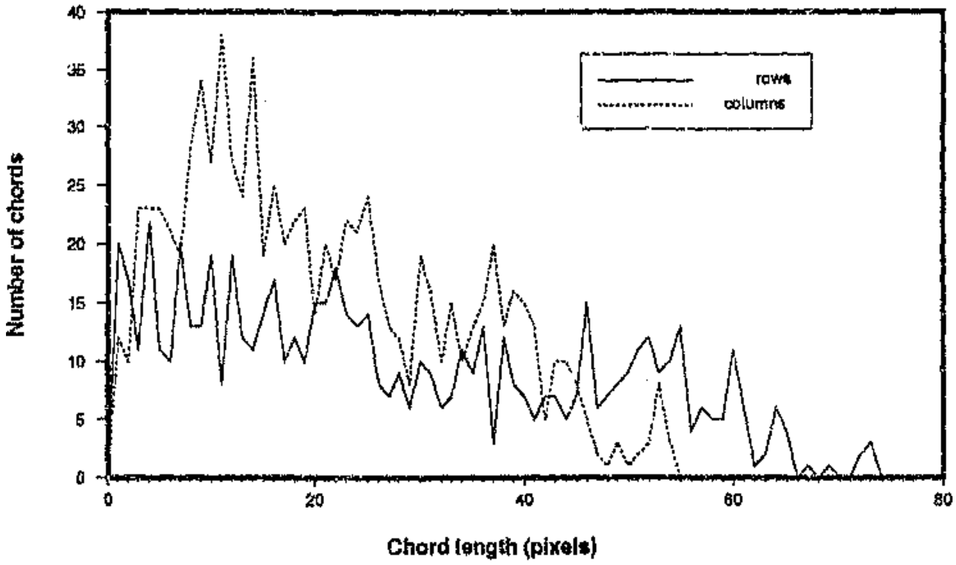

Figure 6.8: Example of chord-length distributions measured on the same image of separated quartzite rocks taken in the x (row) and y (column) direction.

6.5.2 Touching rocks - Quartzite

These chord-length measurements were made on the same rocks as those used in section 6.5.1, except that these rocks were pushed together so that they were touching, but not occluding one another. Figures 6.9 and 6.10 show the chord-length distributions $p(L)$ measured from these images of touching rocks, which are compared to $p(L)$ of separate rocks, which are calculated in the same manner as described in section 6.5.1.

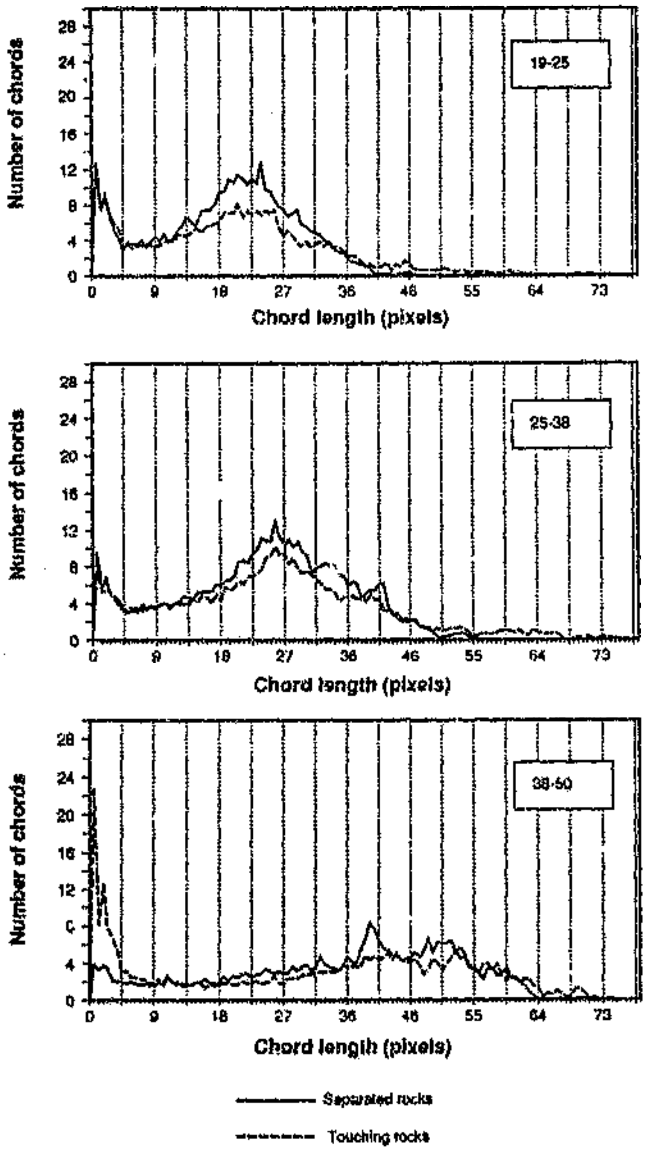

Figure 6.9: Comparison of chord-length distributions measured from scenes of separate and touching quartzite rocks.

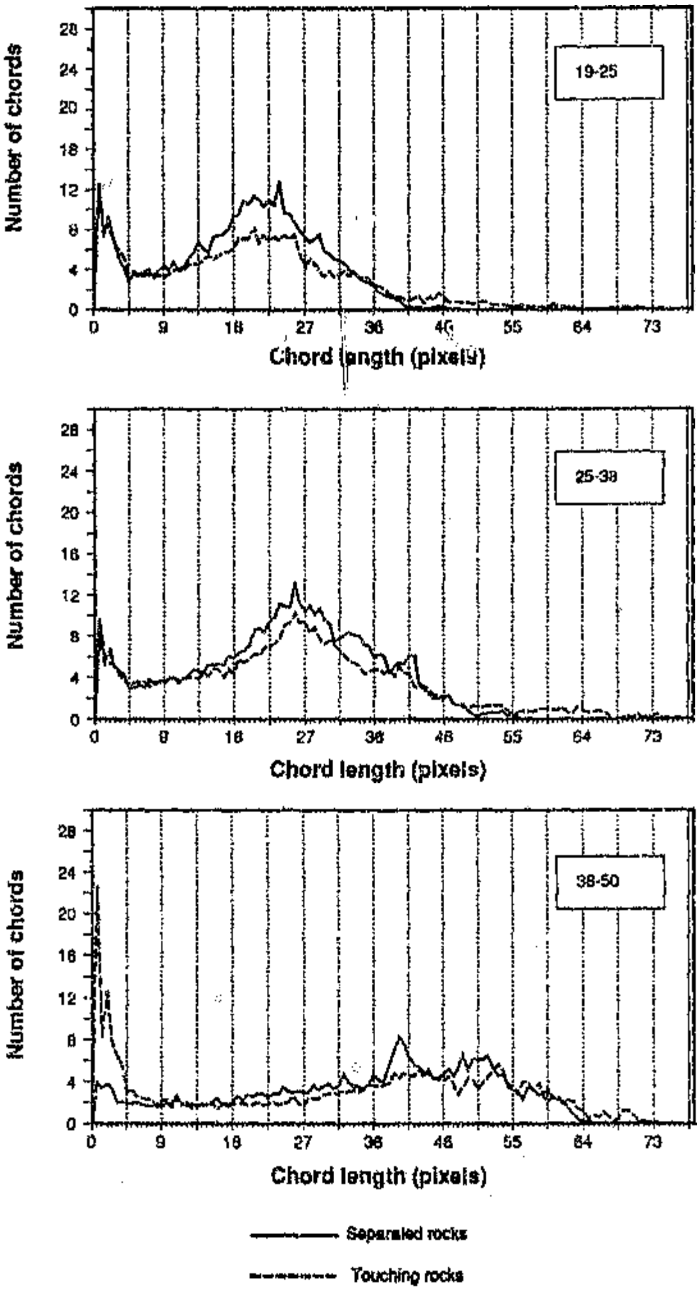

Figure 6.10: Comparison of chord-length distributions measured from scenes of separate and touching quartzite rocks.

6.5.3 Piled rocks - Granite

In this section chord-length distributions are presented (figure 6.12) which have been measured from piled *granite* rock scenes (figure 6.11). The rock scenes were illuminated by uniform neon lighting over the whole image scene. These image scenes were processed by the joining algorithm as described in chapter 5.2. The joining control parameters for this scenes where, Maximum neighbour island =20, Minimum main island size =20, and maximum link distance =25. (All figures are in units of pixels, and the image is 200 by 200 pixels.)

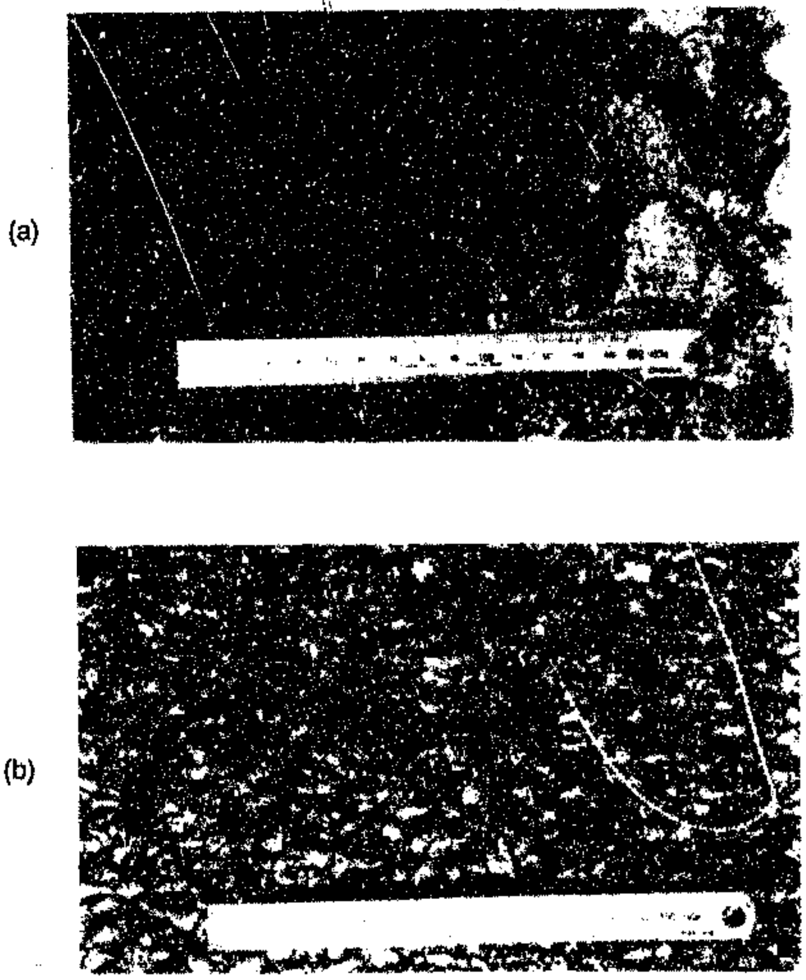

Figure 6.11: Examples of images of piled granite rocks. (a) -38+25mm, (b) -12.7+9.35mm.

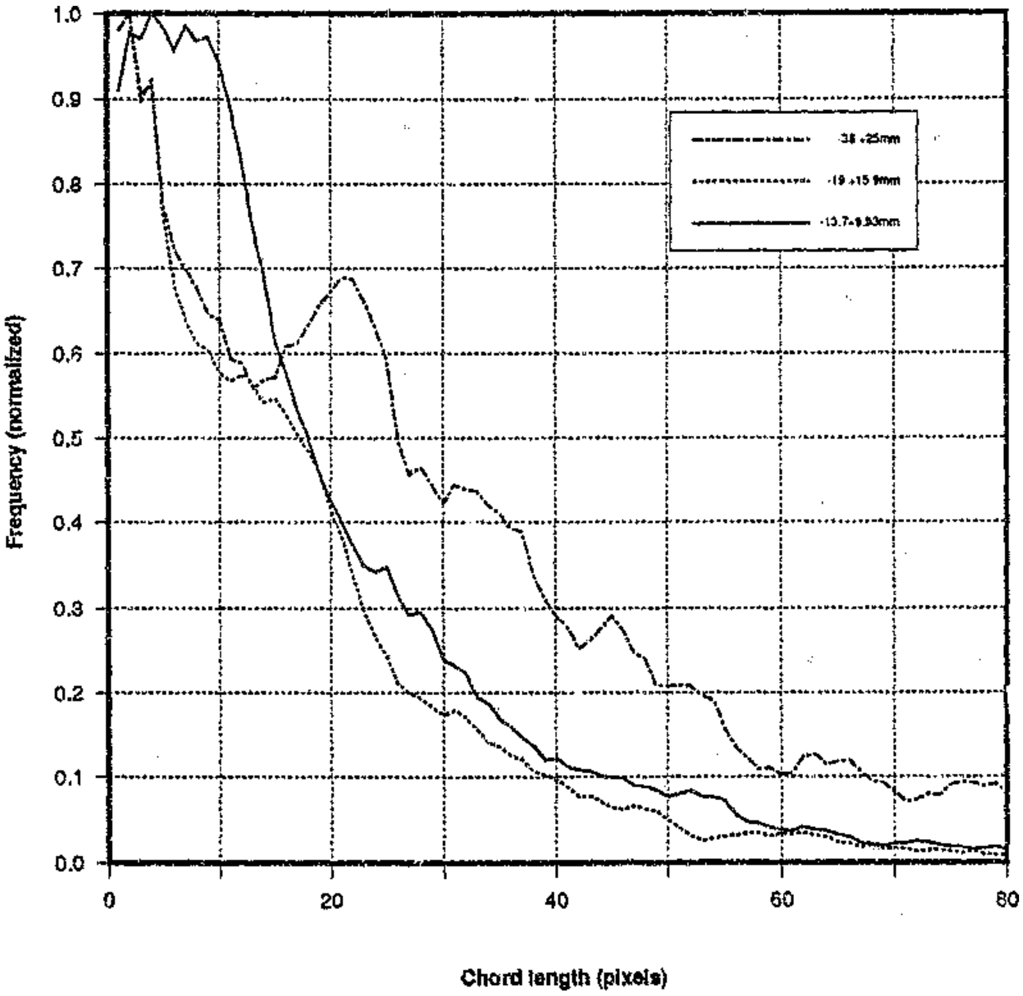

Figure 6.12: Resultant chord length distribution as measured using the joining algorithm on piled granite rock scenes.

6.5.4 Piled rocks - *Granite* - Rosin Rammler distributions

To test further the ability of the system to measure and differentiate between different rock-size *distributions*, a number of rock-size distributions were set up according to the Rosin Rammler distribution equation. The mixed rock or "mud" piles (granite) were created by Wigeson (1987). He describes in his dissertation how these distributions were mixed. The resultant rock piles of different distributions of rock are labelled by the controlling parameter *n* in the rosin Rammler characteristic equation, given in equation [7.33]. Examples of these rock piles are given in figure 6.13 and the results of applying these algorithms are shown in figure 6.14. The distributions presented in figure 6.14 are averaged distributions taken from different 8 rockscenes of the same distribution.

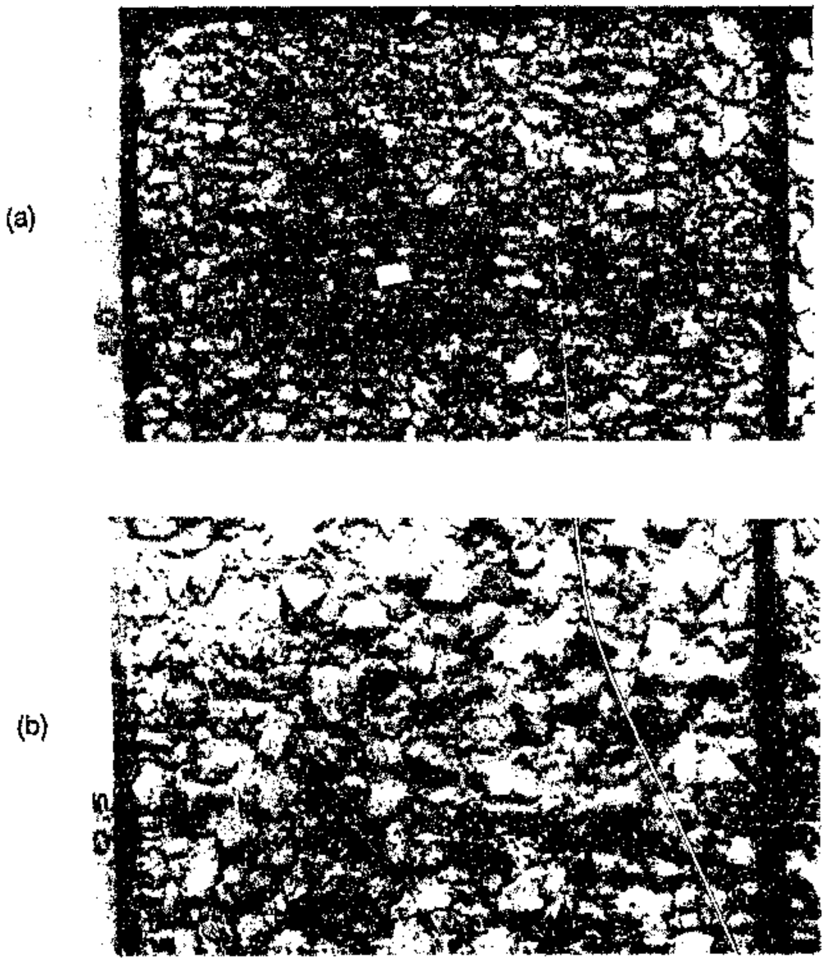

Figure 6.13: Examples of rock piles mixed according to the Rosin Rammler distribution function. (a) n=2.0, (b) n=0.5.

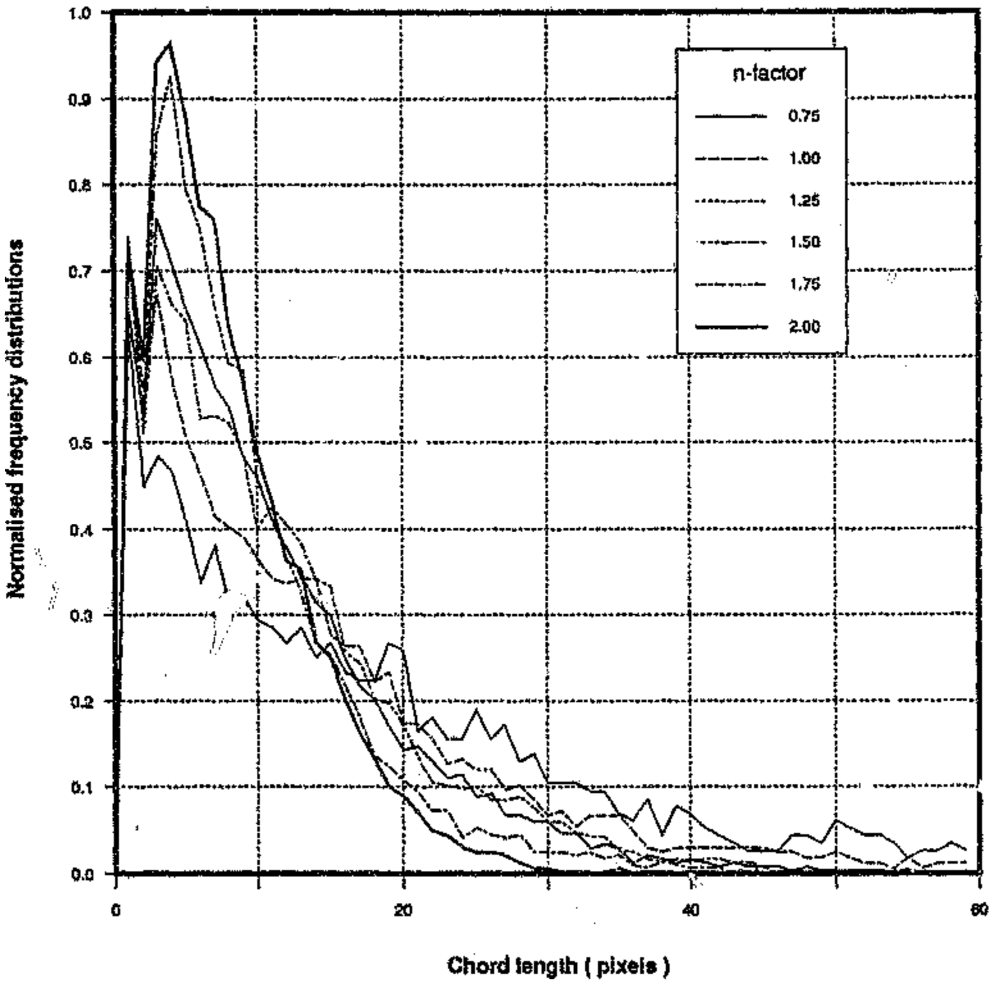

Figure 6.14: Chord-length distributions resulting from the application of the joining algorithm to rock size distributions of granite mixed according to the Rosin Rammler distribution.

6.5.5 Observations and Comments

The following observations and conclusions can be made with regard to the chord-length measurements on stationary rocks.

If the rocks are *separated* and arranged in a *monolayer*[6.2] then the measurement of rocksize can be made with the minimum of processing and the peaks of the chord-length distributions show a good correlation to the actual *average* sieve size. However if the rocks *touch* then the chord-length distributions become flatter with smaller peaks appearing in the chord-length distributions. These peaks occur in the area of the larger chord lengths and are attributed to *merging* errors as discussed in chapter 4.

A feature common to all chord-length distributions measured are the spikes in the region of the very short chord lengths. These peaks are attributed to the sharp and angular shape of the rocks as well as the image processing, which results in shapes and image features that are sharp and angular and which cause a large number of short chords to be measured.

With piled rocks the distributions appear have a dominant peak in the range of the very short chord lengths with a far less discernible peak corresponding to their average in the centre of the chord-length distributions. In fact the distributions tend to take on a decaying exponential form which is fairly different from the more peaky type distributions displayed in figures 6.10 and 6.11.

The results of the Rosin-Rammler experiment appear encouraging as the distributions measured vary sensibly for various n-factors. However these distributions also have a decaying exponential form, similar to those in figure 6.12. Note again the peak at the very short chord-lengths.

Another observation to be made is that for small rocks the peaks of the chord-distributions are very high, indicating large numbers of samples, whilst with the larger rocks the peaks are lower indicating smaller samples. This observation is in agreement with the predictions made in chapter 3 where the *size* of the rocks (spheres) affects the linear intercept distribution.

It must be emphasized that all the above results are for static images, and the next section presents chord-length distributions as measured from dynamic images.

[6.2] A monolayer is a layer of rocks where no rocks lie on top of each thus obscuring part of one another.

6.6 CHORD-LENGTH DISTRIBUTIONS FROM CONVEYOR BELT ROCKSTREAMS

The chord-length distributions derived from the tests on the conveyor belt constitute the main part of the experimentation performed during this research.

These tests were carried out on quartzite material (table 6.1) from a gold mine. The tests were separated into two groups. The first group of tests was carried out on *single* size groups of rocks. For example a single size group might consist of material par [illegible] the 25mm sieve and caught by the 38mm sieve. The second set of tests was carried out on *mixed* or wider size distributions of rocks. For example a mixed test might consist of rocks where half the total rock mass circulated on the conveyor belt consisted of rocks of size 19 to 25mm, and the other half of rocks of size 25 to 38mm. All mixed distributions were synthesized according to weight or mass, and not volume or number. Table 3 gives a summary of some of the mixed distributions tested, which were mixed to form *uniform* sieve distributions according to mass. The letters are labels given to each size distributions prepared.

Table 6.3 Table of mixed size classes used for testing quartzite rock material on the conveyor belt.

<table>
<tr><th>Size component</th><th colspan="8">Fraction of single size group added to total mass.</th></tr>
<tr><td></td><td>100%</td><td colspan="2">50%</td><td colspan="2">33 %</td><td colspan="3">25%</td></tr>
<tr><td>0-6.15mm</td><td>H</td><td rowspan="2">I</td><td></td><td rowspan="3">O</td><td></td><td rowspan="4">S</td><td></td><td></td></tr>
<tr><td>6.15-9,35mm</td><td>G</td><td rowspan="2">J</td><td rowspan="3">P</td><td></td><td></td></tr>
<tr><td>9.35-12.7mm</td><td>F</td><td rowspan="2">K</td><td></td><td rowspan="4">U</td></tr>
<tr><td>12.7-19mm</td><td>E</td><td rowspan="2">L</td><td rowspan="3">Q</td><td rowspan="4">T</td></tr>
<tr><td>19-25mm</td><td>D</td><td rowspan="2">M</td><td rowspan="3">R</td><td></td></tr>
<tr><td>25-38mm</td><td>C</td><td rowspan="2">N</td><td></td></tr>
<tr><td>38-50mm</td><td>B</td><td></td><td></td><td></td><td></td></tr>
<tr><td>50-75mm</td><td>A</td><td></td><td></td><td></td><td></td><td></td><td></td><td></td></tr>
</table>

Figure 6.15 shows some typical dynamic rock scenes as captured from the conveyor-belt. Figures 6.16 show typical chord-length distributions measured from scenes of groups of rocks circulating on the conveyor-belt and segmented according to the final global strategy presented in chapter 5.4. In figure 6.17 single distributions from a few size groups are compared.

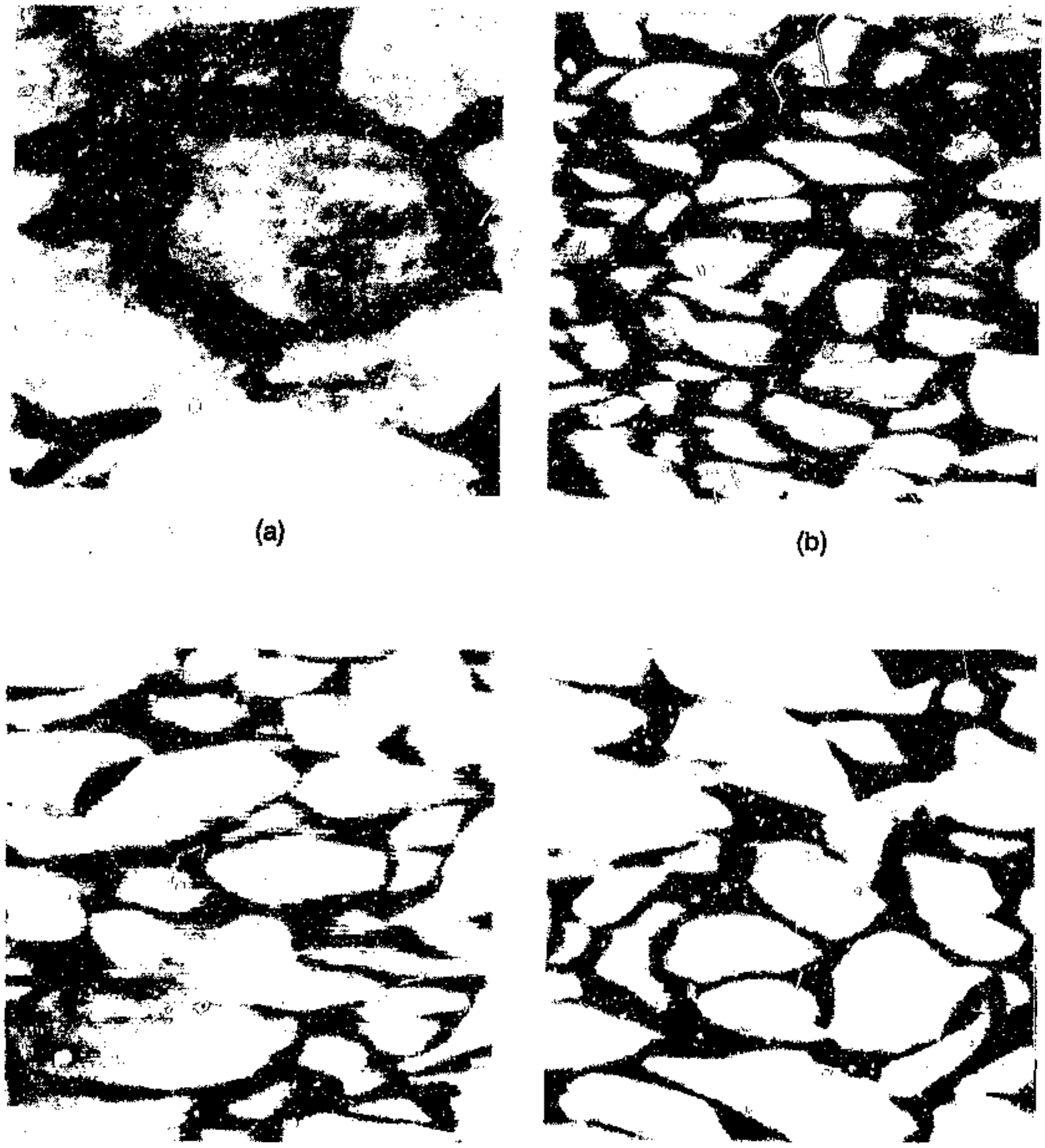

(a) (b)

(c) (d)

Figure 6.15: Examples of dynamic images of piled rock scenes as captured from the pilot-plant conveyor belt using the line-scan camera. (The photographs presented are 35mm stills of the video monitor.) Belt speed was 0.5ms^{-1} and material is gold bearing quartzite. (a) -50+38mm, (b) -19+12.7mm, (c) -50+12.7mm, (d) -38+12.7mm.

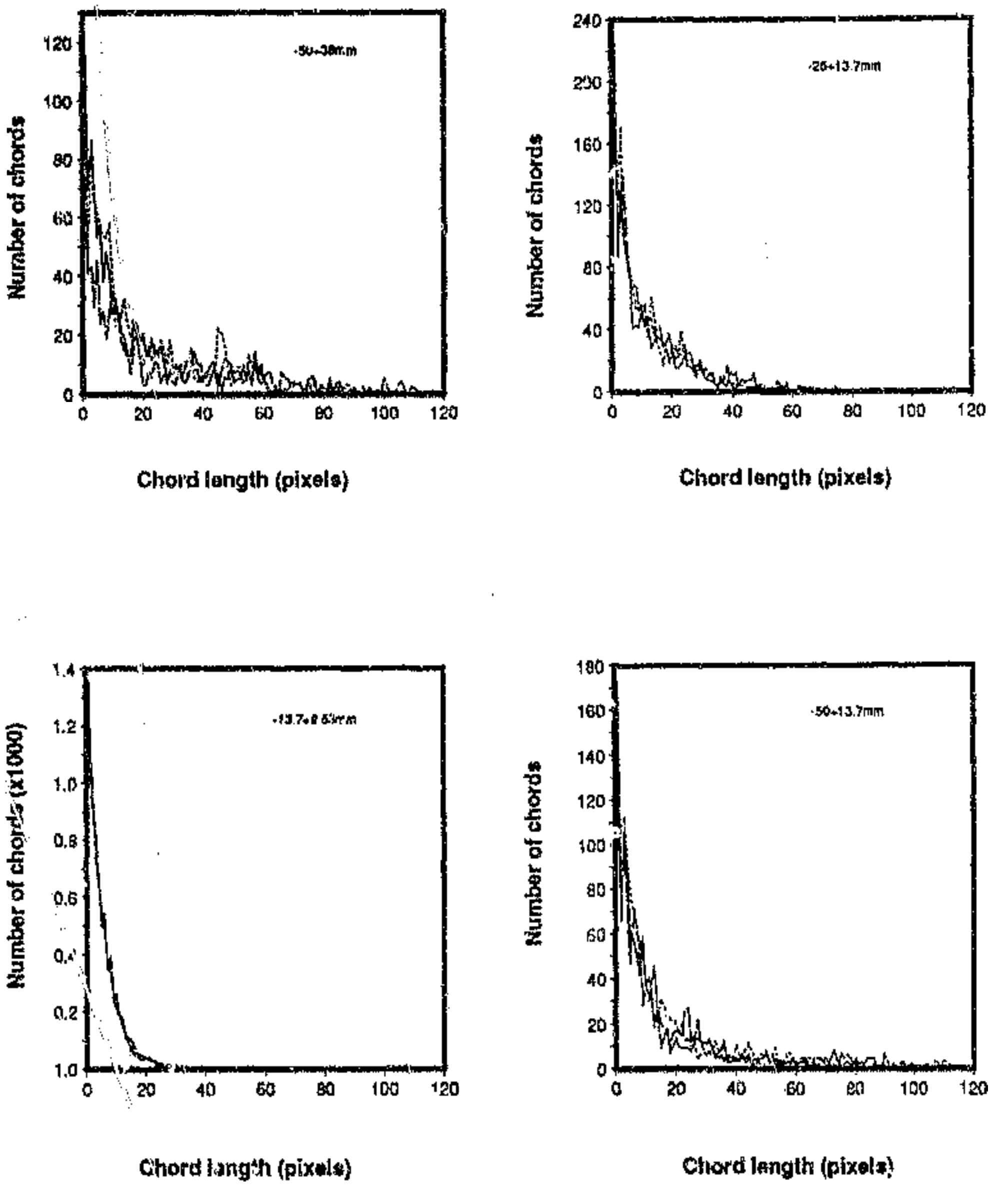

Figure 6.16: Chord-length distributions resulting from the application of the morphological algorithms to size groups of rocks. In each of the above four graphs, three chord-length distributions are presented. Each chord-length distribution is measured from a different image captured at random from the rockstream of given size.

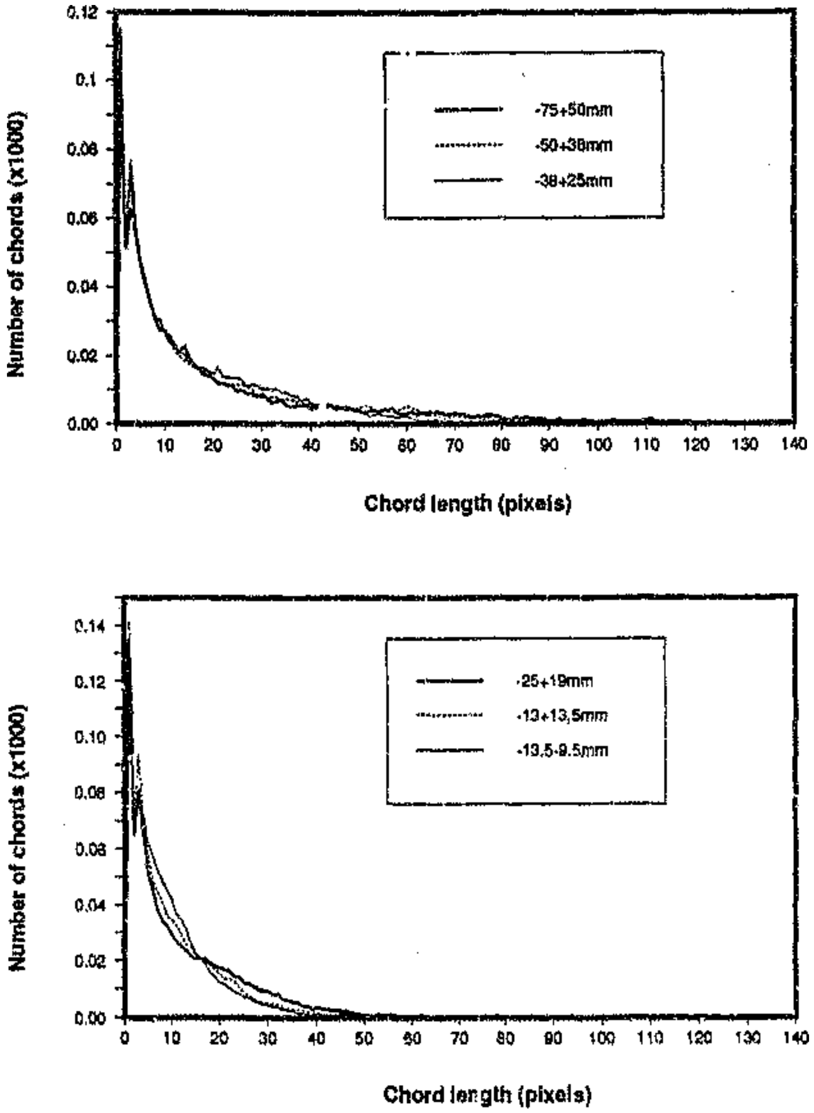

Figure 6.17: Comparison of chord-length distributions resulting from the application of morphological algorithms to various size groups of rocks.

6.6.1 Practical problems with the conveyor belts

A valid and reliable instrument should make *repeatable* measurements for constant conditions. However a number of *practical* problems manifested themselves on the conveyor belt during tests, which varied certain parameters which affect image characteristics and hence chord-length distributions measured. A number of steps were taken to try and minimize these disturbances, however these disturbances could not be eradicated totally ,and cognizance should thus be taken when evaluating the data produced by the imaging system on the conveyor-belt test rig. These problems were :

1) During testing the material was kept moist as is generally found on the mines. However due to a natural drying out process, as well as the heat emitted by the lighting, the moisture content and hence colour and reflectivity properties of the rocks changed with time. This resulted in a number of rocks being partially dried out which gave a speckled appearance of white and dark gray areas causing a great number of errors in the segmentation process.

2) To combat the above problem of varying moisture content, the material was sprayed continuously with a fine mist of water. However too strong a spray effectively washed the rocks clean of fines and mud making them appear darker thus decreasing the contrast of the image. (On actual plants, the rocks being fed to the mills are not washed, thus this situation is artificial.) On the other hand spraying the rocks too finely results in an uneven dampening effect which also increases the speckled appearance of the rocks and causes errors in the segmentation.

3) Spraying water on the rocks also leaves a thin film of water on the rocks' surface which behaves like a mirror. This has the undesirable effect of reflecting light directly into the camera which saturated and created very bright spots. This again induces errors into the segmentation process.

4) The rocks circulating on the closed loop conveyor belt system tend to break up with time due to *grinding* and *fracture* mechanisms whilst falling in the chutes. This causes the size distribution of the rocks to change with time. In addition after the rocks have circulated on the belt for an hour or more, their shapes change from being highly angular and square to being more rounded, which essentially made them too different from the original angular rocks to be used for direct comparison. This implied that a "fresh" set of rocks should be sieved and used, but this created a problem considering the limited quantity of material and time available. A given pile of rocks could thus only be used on the belt for a limited period (30 to 60 minutes) before having to be discarded.

Rock breakage and grinding on the belt also results in the generation of a great amount of *slurry* or mud which coats the rocks and again changes their colour, reflection characteristics and hence the chord-length distributions measured.

5) Surging in the chutes, ie a sporadic mass flowrate, causes parts of the belt to be covered heavily with rocks, whilst other parts of the belt were only partially covered with rock. The surging is caused by blockages in the chutes resulting from the high viscosity and sticky nature of the slurry resulting from grinding, as well as the interlocking mechanisms between the rocks due their highly angular and irregular shapes.

6.7 SUMMARY

In this chapter the experimental setup for static and dynamic images were described briefly . Typical chord-length distributions resulting from the application of image processing techniques as developed in chapters 4 and 5 were also presented. From observation of these chord-length distributions it can be seen that there are properties in the chord-length distribution which vary sensibly with the sieve size of the rocks. In particular the peaks of chord-length distributions measured from rock scenes of *separated* rocks in a *monolayer* correspond very well to the average rock size.

However for *piled* or *touching* rocks, the chord-length distributions are more difficult to interpret and the distributions look very similar to each other irrespective of the technique used. For image captured from dynamic rockstreams the chord-length distributions take on a decaying exponential form from which it is difficult to distinguish any size information. It is thus obvious that further processing is required to extract useful information from these measured chord-length distributions. However despite these problems, the chord-length distribution derived from dynamic images are useful because they do vary with rocksize and rocksize distributions.

The task that remains is to convert these chord-length distributions to size distributions, or alternatively reveal *useful* differences between the various chord-length distributions for analysis of sizing trends. These objectives are covered in chapter 7.

7 CONVERTING CHORD-LENGTH TO SIZE

7.1 INTRODUCTION

In chapter 6 experiments were described from which discrete chord-length distributions $p(L_k)$ were measured which varied meaningfully with rocksize and rocksize distribution $f(D)$ but which were difficult to interpret. In this chapter we undertake to convert these chord-length distributions to a measurement which relates to "*size*" and which is *useful* to the metallurgist and the mining industry. The process to convert $p(L_k)$ to some useful size measurement, namely Ψ_c , is the third and last stage of the rocksize measurement process, (section 2.8).

Qualitative information such as "there are more larger rocks now than before", is deemed a useful starting point for such a measurement given that it has just not been available. However *quantitative* measurements which can be logged against mill performance or which can be fed into control systems are preferable. For historical reasons (as discussed in chapter 1) an accurate and reliable ***sieve-size*** distribution in the cumulative form where $F(D)=\int_0^D f(D')dD'$, is the ideal measurement preferred by the mining industry.

The conversion of chord-length distribution to rock-size distributions is one of the many *ambiguous* physical-inversion problems to be solved which does not posses a unique solution (Twomey, 1977). Twomey comments that although there have been many advances in mathematical procedures for solving such inversion problems, these advances do not remove this fundamental ambiguity and in some instances only hide it. He *remarks further that the techniques he discusses* for solving inversion problems only *reduce* the number of possible solutions from infinity to a lesser, but still *infinite* selection of possibilities.

In this chapter, a number of methods to estimate rocksize distributions explicitly from chord-length distributions are discussed. The *first* group of estimation methods use inversion techniques. The problems and difficulties with inversion methods are highlighted and consequently modified in order to overcome these problems. However the problems with explicit inversion methods are not totally solved and a new philosophy is proposed, that *perhaps such direct inversion is not necessaryto solve for sieve size distribution.* This philosophy stems from the hypothesis that the ambiguous conversion of $p(L)$ to an equivalent size distribution such as sieve size, is perhaps not the best approach for this conveyor-belt sizing application. The chord-length density distribution $p(L)$ does contain *generic size* information and sieve size is only one approach to describing this information.

As part of the objective of this thesis, evidence is presented to show that size information *related* to sieve size can be extracted from the chord-length distributions using established and modified inversion techniques. However because these inversion techniques are unstable and unreliable, other techniques such as moment and morphological techniques which do not estimate sieve size are also developed and it is shown that such techniques do provide useful *size* information.

7.2 EXPLICIT INVERSION METHODS

The original objective is to convert chord-length distribution to sieve-size distribution which is not a trivial problem (Lin et al, 1987). Depending upon the circumstances, this conversion can be accomplished via many different ***inversion*** techniques, each of which has advantages and disadvantages depending on the application and the nature of the data (chord-length distribution) measured. Inversion techniques investigated in this subsection include analytical solutions, linear numerical solutions, as well a unique solution by King (1982).

With regard to *linear* methods, it is shown that with the exception of *constrained linear inversion*, most of these methods do not work properly for the data in this particular sizing application, because of the randomness and errors in the measurement data, as well as the *inherent ambiguity* of the inversion problem, (Twomey, 1977), (Lin et al, 1987). Although the poor results obtained with these methods led to development of a new approach to this measurement (sections 7.3, 7.4, and 7.5), the basic hypothesis that rocksize can be measured using machine vision is validated because the size measurements obtained from certain inversion techniques although not accurate, are shown to *relate* to sieve size. The principles underlying these established inversion methods is not original work, although the application, modification, and analysis of these techniques to rockscenes from conveyor belts is new, as well as the new methodologies developed for rocksize measurement in section 7.3 7.5.

7.2.1 Deriving explicit analytical solutions

The explicit mathematical inversion of the working equation which relates the continuous chord-length distribution measured $p(L)$ to the continuous sieve size distribution $f(D)$, has been the first and most popular method used for calculating particle size distribution from section measurements. This equation, which has been thoroughly discussed by authors such as Wicksell (1925), Underwood (1970), Weibel (1980), King (1982), is derived in chapter 3 [3.36] for the particular case of spherical particles and is reproduced again in equation [7.1].

$$p(L)=\overline{L}\int_{kL}^{\infty}p(L\mid D)\frac{f(D)}{\overline{L}_D}\,dD \qquad 7.1$$

$$\Rightarrow p(L)=\Phi\{f(D),p(L\mid D),\overline{L}_D,\overline{L}\} \qquad 7.2$$

Equations [7.1] and [7.2] show that the measured chord-length density distribution $p(L)$ is a function Φ of sieve size distribution $f(D)$, and $\overline{L}$, $\overline{L}_D$, and $p(L\mid D)$ defined in chapter 3. The objective of the third stage Ψ_c in the rocksize instrument, is to invert the above integral equation [7.2] so as to solve for sieve size distribution $f(D)$ given the measurements $p(L)$, ie to find Φ so that the inversion process in equation [7.3] may be effected if possible. The solving for Φ assumes that the above equation can be applied by arbitrary shaped particles.

$$f(D)=\Phi^{-1}\{p(L)....\} \qquad 7.3$$

Equation [7.1] is a special case of the general *linear-integral* equation (Kanawal, 1971) which is given in equation [7.4] below.

$$h(x)f(x) \quad + \quad g(x) \quad = \quad \int_a^b K(x,y)f(y)\,dy \qquad 7.4$$

Fixing the upper limit and letting $h(x)=0$ in equation [7.4] gives the *Fredholm* integral equation of the first kind is given in equation [7.5].

$$g(x) \quad = \quad \int_a^b K(x,y)f(y)\,dy \qquad 7.5$$

Equation [7.5] is the form for the many inversion problems found in nature, where the measurement is $g(x)$ and $f(y)$ is the unknown function to be estimated, and where x and y are some variables. $K(x,y)$, and similarly the term $p(L\mid D)\frac{\overline{L}}{\overline{L}_D}$ from equation [7.1], are known as the *kernels* of the integral equations [7.5] and [7.1] respectively. Phillips (1962) presents methods for handling non-singular linear integral equations similar to [7.1], and for solving for $f(x)$ which in this research is the size distribution $f(D)$. In his paper he comments at the time that there is very little literature on solving linear integral equations of the first kind such as equation [7.5], and states further that no method has been very successful for systems with *arbitrary kernels* and when the measurement function $g(x)$ is known with only *modest accuracy*. He concludes that the success of solving equation [7.5] and hence [7.1], depends to a large extent on the accuracy of the measurement $g(x)$, and the shape of the kernel $K(x,y)$, assuming that $K(x,y)$ is known in the first place.

In the ideal case of particles of known shape, eg spheres, the kernel can be derived as shown in chapter 3, to give $K(x,y)=\frac{x}{\sqrt{(x^2-y^2)}}$ for *areal* intersections . Inserting this kernel into equation [7.5] results in the *Abel integral equation* of the first kind with fixed limits as given below .

$$g(y) = \frac{y}{\overline{g}}\int_y^{\infty}\frac{f(x)}{\sqrt{(x^2-y^2)}}dx \qquad 7.6$$

where $\overline{g}$ is the average areal measurement given by $\overline{g}=\int_0^{\infty} yg(y)dy$. Jakeman and Anderssen (1975a), (1975b) derive in detail explicit solutions to the Abel equations arising from the intersection of particles with different probes. For the particular case of spherical particles intersected by *areal* probes the solution to equation [7.6] becomes,

$$f(x)=-\frac{2xm}{\pi}\int_x^{\infty}\frac{1}{(y^2-x^2)^{1/2}}\left\{\frac{d}{dy}\left[\frac{g(y)}{y}\right]\right\}dy$$

$$=-\frac{2m}{\pi}\frac{d}{dx}\left\{\int_x^{\infty}\frac{1}{(x^2-y^2)^{1/2}}G(dy)\right\} \qquad 7.7$$

where $G'(y)=g(y)/dy$, also see Cahn and Fullman (1956). For the case of spherical particles intersected by *linear* probes we get the working equation

$$g(x)=\frac{\pi x N_V}{2N_L}\int_{x/2}^{\infty}f(y)dy \qquad 7.8$$

the solution which is

$$f(y)=\frac{-N_L}{\pi N_V}\frac{d}{dx}\left\{\frac{g(2x)}{x}\right\} \qquad 7.9$$

where N_V is number of particles and N_L is number of linear intercepts. Jakeman and Anderssen (1975b), and Anderssen (1976) derive in detail numerical methods to solve for the explicit solutions to the Abel equations, which for areal distributions is given by equation [7.7]. The solution to the working equation [7.8] for the linear-intercept problem on spheres, is given in equation [7.9] and appears simpler. However from the work of Jakeman and Anderssen (1975a) it is observed that as the particle shape deviates from spherical, the formulae for the working equations and their solutions for both areal and linear intercepts become more complex and intractable. In addition deriving the kernels becomes more difficult because the particles' shapes cannot be easily modelled. Thus because of problematic mathematics there is a strong case for using solutions based on spherical particles for estimating the size distribution of irregular shaped particles.

Jakeman and Anderssen (1975b) concluded that their methods for numerically evaluating the size distribution of near spherical particles using the random sphere approximation was highly reliable. However noting that in general

(1) The inversion process to derive size from sectional measurements is fundamentally ambiguous, (Phillips, 1962), (Twomey, 1977),

(2) The chord-length distributions $p(L)$ measured in this research are very noisy, because the image processing methods used to derive the edge patterns and measure $p(L)$ are error prone, chapters 4 and 5.

(3) The analytical solutions derived in the literature for stereological problems are generally based on the intersection of *spherical* or *regularly* shaped particles and not randomly shaped particles, Jakeman and Anderssen (1975b), Weibel (1980).

(4) A large number of observational data readings are required for numerical accuracy which may not be practically realizable, Jakeman and Anderssen (1975b). See figure 6.7.

(5) Solutions were only tested on simulated data, Jakeman and Anderssen (1975b) and that

(6) Jakeman and Anderssen (1975b) suggest that linear probes be avoided,

implies that approximating the derivation of the size distribution of arbitrary shaped particles with these analytical solutions based on spheres is at least questionable if not erroneous. DeHoff and Rhines (1961) came to the same conclusion when commenting on treating elongated or flattened particles as spheres. The errors in using such analytical solutions for this conveyor belt rocksize problem are compounded by the fact that the derivation of the chord-length intercept distributions of the rocks is biased because of the violation of stereological rules (chapters 4 and 5) in the pursuit of a speedy and practical method to measure the size distribution of rocks online.

Inspection of solutions to the inversion process, equations [7.7] and [7.9], show that they all involve some *differentiation* of the input measurement function $g(x)$ followed (with the exception of linear interceptions) by some product integration, Jakeman and Anderssen (1975a). Differentiation of any function which is degraded by experimental error and noise will result in the amplification of the noise components. As has been discussed previously, the chord-length intercept density measurements $p(L)$ on the rockstream Ω are derived in shaky circumstances with many errors being introduced because of the many assumptions and simplifications made in the image processing, therefore differentiation of $p(L)$ generally is not acceptable for numerical processing. This can be seen in figure 7.1(b) which shows the first derivatives g'_k of two *filtered* chord-length distributions where $g_k' = (g_{k-1} - g_{k-1}) / 2.\Delta L$, $g_k = g(k.\Delta L)$ and $\Delta L = 1$, derived from conveyor belt tests. (All the distributions in figure 7.1 are *raw* chord-length distribution measurements which have not yet been converted to a density distribution, see section 7.2.2 equation [7.11].) Figure 7.1(a) shows the result of filtering a raw chord-length distribution measurement obtained from conveyor belt tests. Although not shown, without filtering, the first derivative of the measured chord-length distribution is absolute noise and therefore meaningless. Thus although equation [7.9] implies that $\frac{d}{dL}g(L) \propto f(D)$ these curves of $g'(L)$ are generally noisy and do not exhibit any behaviour from which size information can be gleaned easily. Only the differentiation of a fitted function produces a less noisy result. However discriminating between different fitted chord-length distributions is very ambiguous, because the variations in the data result in too much uncertainty and variation in the characteristic coefficients of the fitted function to be of any use.

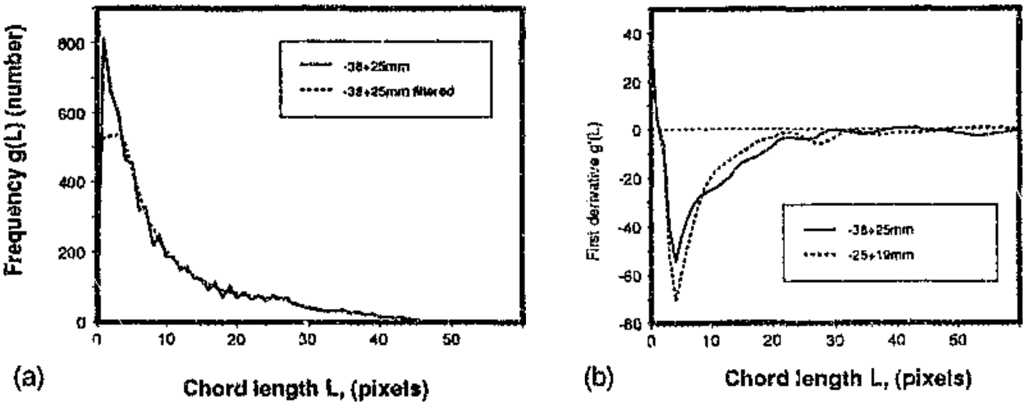

Figure 7.1: (a) Example of a *raw* chord-length distribution $g_k(L_i)$ which has been filtered. Two moving average filters of length 3 and 5 were applied to the distribution sequentially. (b) Result of numerical differentiation of two different filtered distributions.

Attempts to implement, for example, equation 7.9, showed that the above analytical methods are generally unsuited for this application with no guarantee of a working or reliable solution. Therefore for the above reasons, combined with the large programming effort and numerical analysis required, led to the decision to discard the use of analytical solutions methods in favour of alternative methods which are described in the next subsections.

7.2.2 Linear Inversion Methods

With linear inversion methods the basic working equation [7.1] is solved directly with numerical methods instead of deriving explicit analytical solutions which are then evaluated numerically, as discussed in section 7.2.1. The inversion or deconvolution of equation [7.1] could be thought of as simply being

$$f(D) = \Phi^{-1}[p(L)] \qquad 7.10$$

where the chord-length distribution measured $g(L)$ and required size distribution $f(D)$ are *density* distributions where

$$p(L) = \frac{g(L)}{\int_0^{\infty} g(L)dL} \quad \text{and} \quad p(L_k) = \frac{g(L_k)}{\sum_{i=1}^{m} g(L_i)} \qquad 7.11$$

for continuous and discrete distributions respectively. In a real measurement system $p(L)$ and $f(D)$ are sampled signals which are represented by one dimensional vectors in equation [7.12] below.

$$\begin{aligned} \mathrm{p}(L) &= p(L_k) = [L_1, L_2 \ldots L_k \ldots L_m]^T \\ \mathrm{f}(D) &= f(D_l) = [D_1, D_2 \ldots D_l \ldots D_n]^T \end{aligned} \quad \text{where} \quad \begin{aligned} k &= 1..m \\ l &= 1..n \end{aligned} \qquad 7.12$$

The chord-length distributions are measured at ΔL intervals to give m L_k samples, and the size distribution is measured at ΔD intervals to give n D_l intervals. It is assumed in this work that the ΔL_i and ΔD_i intervals are set equal although they need not be so.

If the transformation from size to chord Φ is assumed to be *linear*, then using [7.12] in equation [7.10] gives the relation

$$\mathrm{p}(L) = \mathrm{A}(L,D)\mathrm{f}(D) \qquad 7.13$$

$$\text{where} \quad \begin{bmatrix} \\ \mathbf{L} \\ \\ \end{bmatrix}_{m\times 1} = \begin{bmatrix} & \mathbf{A} & \\ & & \\ & & \end{bmatrix}_{m\times n} \cdot \begin{bmatrix} \mathbf{F} \\ \\ \\ \end{bmatrix}_{n\times 1}$$

and where $\mathrm{A}(L,D)$ is a $m \times n$ transformation (kernel) matrix that relates the chord-lengths measured on rocks to their size distribution. The kernel $\mathrm{A}(L,D)$ can be derived in the following way. Let a *unit* rock-size distribution f_i be defined as a rocksize distribution only having rocks of a single narrow size class $D_i = \Delta D \cdot i$. Let a unique chord-length distribution $\mathrm{p}_i(L_k)$ be measured from each *unit* rock-size *density* distribution f_i. If the total rock size distribution under investigation consists of n size classes, then let n $\mathrm{p}_i(L_k)$ chord length distributions corresponding to the n size classes be measured. These n unique rocksize distributions are given in equation [7.14].

$$\mathbf{f}_1(D_k)=\begin{bmatrix}1\\0\\0\\.\\.\\0\end{bmatrix}\quad \mathbf{f}_2(D_k)=\begin{bmatrix}0\\1\\0\\.\\.\\0\end{bmatrix}\quad \ldots\quad \mathbf{f}_n(D_k)=\begin{bmatrix}0\\0\\0\\.\\.\\1\end{bmatrix}\qquad k=1\ldots n \tag{7.14}$$

which when put together forms a matrix $\mathbf{F}(D)$ given in equation [7.15] below

$$\Rightarrow\qquad \mathbf{F}(D)=\ [\mathbf{f}_1,\mathbf{f}_2,\ldots\mathbf{f}_n]\ =\begin{bmatrix}1 & 0 & 0 & \ldots & 0\\0 & 1 & 0 & \ldots & 0\\0 & 0 & 1 & \ldots & 0\\. & & & & \\. & & & & \\0 & 0 & 0 & \ldots & 1\end{bmatrix}=\ \mathbf{I} \tag{7.15}$$

Each of the n *rocksize* distributions now gives a corresponding and unique *chord-length* distribution with a one to one mapping as given in [7.16].

$$\begin{aligned}f_1 &\rightarrow p_1\\f_2 &\rightarrow p_2\\ &.\\f_n &\rightarrow p_n\end{aligned} \tag{7.16}$$

The unique chord-length distributions measured after conversion to a density distribution with equation [7.11], are given below in equation [7.17],

$$\mathbf{p}_1(L)=\begin{bmatrix}L_{11}\\L_{12}\\L_{13}\\.\\.\\L_{1m}\end{bmatrix}\quad \mathbf{p}_2(L)=\begin{bmatrix}L_{21}\\L_{22}\\L_{23}\\.\\.\\L_{2m}\end{bmatrix}\quad \mathbf{p}_3(L)=\begin{bmatrix}L_{31}\\L_{32}\\L_{33}\\.\\.\\L_{3m}\end{bmatrix}\quad \ldots\quad \mathbf{p}_n(L)=\begin{bmatrix}L_{n1}\\L_{n2}\\L_{n3}\\.\\.\\L_{nm}\end{bmatrix} \tag{7.17}$$

which when combined gives a matrix $\mathbf{P}(L)$ given in equation [7.18].

$$\mathbf{P}(L) \quad = \quad [\mathbf{p}_1, \mathbf{p}_2, \ldots \mathbf{p}_r] \quad = \begin{bmatrix} L_{11} & L_{21} & L_{13} & \ldots & L_{1m} \\ L_{12} & L_{22} & L_{23} & \ldots & L_{2m} \\ L_{13} & L_{23} & L_{33} & \ldots & L_{3m} \\ \cdot & & & & \\ \cdot & & & & \\ L_{n1} & L_{nm} & L_{nm} & \ldots & L_{nm} \end{bmatrix} \qquad 7.18$$

If it is assumed that $m = n$ then we get $\mathbf{P} = \mathbf{AF}$. But because $\mathbf{F}$ is the identity matrix, have $\mathbf{P}$ [illegible] $\Rightarrow \mathbf{A} = \mathbf{P}$. The assumption that $m = n$ can be realized if the chord-length measurement vector is reduced from $m = 200$ [7.1] to $m = n = 5$. The need to compress the measurement from 200 to 5 elements exists because the output measurement was limited to n=5 size classes because of the limited availability of meshes for sieving. In addition the total size range that can reliably be resolved within a image window of 200 by 200 pixels was fixed at approximately 6:1 for the camera setup used in the experiments. This limits the size range of interest to the interval of approximately 10-70 mm.

In this work the chord-length density function $p(L_k)$ is compressed from an array of $k = 200$ elements to $k' = 5$ elements by dividing $p(L_k)$ into five divisions and averaging the elements in each division to give $p(L_{k'})$ ie $p(L_{k'}) = \frac{1}{N_{k'}} \sum_{k=ak'}^{ak'+b} p(L_k)$ where $N_{k'}$ is the number of elements in the k''th division. The choice of boundaries between which the elements of $p(L_k)$ are summed namely, a, $a+b$, are chosen according to a criterion determined in a fairly ad-hoc manner, this being that the size of the divisions increase logarithmically or geometrically in sympathy with the size of the sieve class divisions, see figure 7.2 and table 6.1.

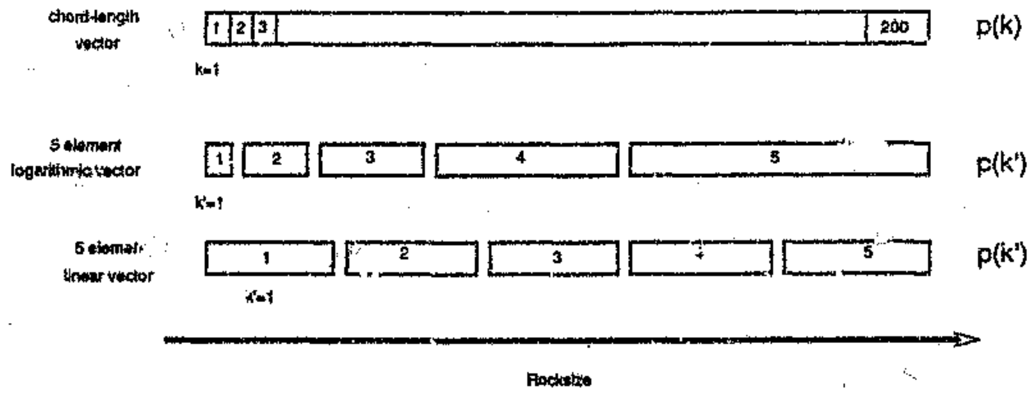

Figure 7.2: Mapping a 200 element linear array $p(L_k)$ to either a 5 element log or linear array $p(L_{k'})$.

[7.1] The image size dealt with is 200 by 200 pixels. Thus the maximum chord-length that can be measured is 200 pixels long.

Assuming that the measurement matrix is reduced so that the kernel is a square matrix, then the solution to the inversion or deconvolution problem now becomes a problem of deriving $\mathbf{A}(L,D)$ using the methods shown in equation [7.14] to [7.18] and then inverting $\mathbf{A}(L,D)$ to give $\mathbf{A}^{-1}$ so that we may solve for the size distribution as given in equation [7.19]

$$\mathbf{f} = \mathbf{A}^{-1}\mathbf{p} \qquad 7.19$$

The problem with solving equation [7.19] is that due to experimental error in the measurements p and the inexact characteristics of the kernel A, equation [7.19] although valid, leads to erroneous and unrealistic estimates of f (Lin et al, 1987). These unsatisfactory results are mainly due to the relative instability of the kernel A which is fairly ill-conditioned although not singular. For example the condition number of a typical kernel matrix derived from conveyor belt tests and shown below [7.20] is $cond(A) = 334$ which indicates that the system is *sensitive* to fluctuations in the measurement vector $p(L_k)$. In addition a few of the eigenvalues [7.21] are complex indicating some oscillatory characteristic to the system. In general the ratio of the largest to smallest eigenvalue for most kernels measured ranged from 30 to $> 10^3$ which also implies some instability with regard to obtaining a solution. The main consequence is that small changes or errors in the measurement can give rise to large and oscillatory changes in the solution which is undesirable.

$$\mathbf{A}_{typical} = \begin{bmatrix} 0.54 & 0.93 & 1.00 & 0.93 & 0.86 \\ 1.00 & 1.00 & 0.98 & 1.00 & 1.00 \\ 0.38 & 0.40 & 0.48 & 0.58 & 0.96 \\ 0.12 & 0.18 & 0.24 & 0.26 & 0.30 \\ 0.03 & 0.03 & 0.01 & 0.02 & 0.01 \end{bmatrix} \qquad 7.20$$

The eigenvalues Λ of the kernel in [7.20] is

$$\Lambda = \begin{bmatrix} + & 2.4376 & & & \\ - & 0.2372 & & & \\ + & 0.0706 & & & \\ + & 0.0095 & + & 0.0520 & i \\ + & 0.0095 & - & 0.0520 & i \end{bmatrix} \qquad 7.21$$

and inverse of $\mathbf{A}_{typical}$ is given below

$$\mathbf{A}^{-1}_{typical} = \begin{bmatrix} -2.526 & 3.151 & -0.874 & 0.049 & -15.345 \\ 4.821 & -3.135 & 3.518 & -15.848 & 56.539 \\ 1.124 & 2.824 & -1.001 & -6.974 & -73.818 \\ -4.612 & -1.088 & -5.267 & 31.737 & 59.087 \\ 1.215 & -0.695 & 3.604 & -9.103 & -7.9404 \end{bmatrix} \qquad 7.22$$

Figure 7.3 shows five output sieve size distributions $f_k(D)$ resulting from inputting five chord-length distributions to a linear inversion system [7.12] using the kernel matrix given above. Note that these five individual chord length distributions were part of the 50 distributions of -50+38mm averaged together to obtain the kernel. The results are useless and have a oscillatory nature. The *sensitivity* of the direct inversion process is shown in figure 7.4 where adding a small perturbation (1% in each class to a perfect chord distribution results in errors in size distribution calculated $f_k(D)$.

A possible cause for the unsatisfactory behaviour of these inversion methods could also be attributed to the method of compression used to reduce the measured chord distribution vector $p(L_k)$. The mapping scheme as shown in figure 7.2 is obviously not the optimum procedure and a more complex mapping of $p(L_k) \rightarrow p(L_{k'})$ may be required.

It is thus suggested that the unsatisfactory behaviour of the inversion processes could be improved by

1. Deriving a better mapping scheme,
2. Increasing the number of sieves n so that more rock size classes are available, and by
3. Using an alternative numerical methods which do not require a size reduction of the chord measurement vector.

An alternative numerical method is to use *least-squared methods* where $(\mathbf{p}\text{-}\mathbf{A}\mathbf{f})^2$ is minimized. The method requires minimizing the squared error objective function (Twomey, 1977)

$$e = \min(\mathbf{p}\text{-}\mathbf{A}\mathbf{f})^T(\mathbf{p}\text{-}\mathbf{A}\mathbf{f}) \qquad 7.23$$

by adjusting some parameters associated with a functional form for f specified a-priori. According to Lin et al (1987) both *direct-inversion* and *least-squared methods* are limited and do not provide a satisfactory means for solving for f . According to Twomey (1977), moving to *least-squared methods* will not have any advantage over direct inversion as far as better stability is concerned. This leaves a third set of methods to be used namely *constrained linear inversion.*

The negative distributions derived in figures 7.3 and 7.4 are meaningless, and demonstrate the limitations of direct linear inversion for estimating sieve size distribution. (Appendix D presents a working example whereby direct linear inversion is used to estimate sieve size estimation from a compressed chord-length distribution.)

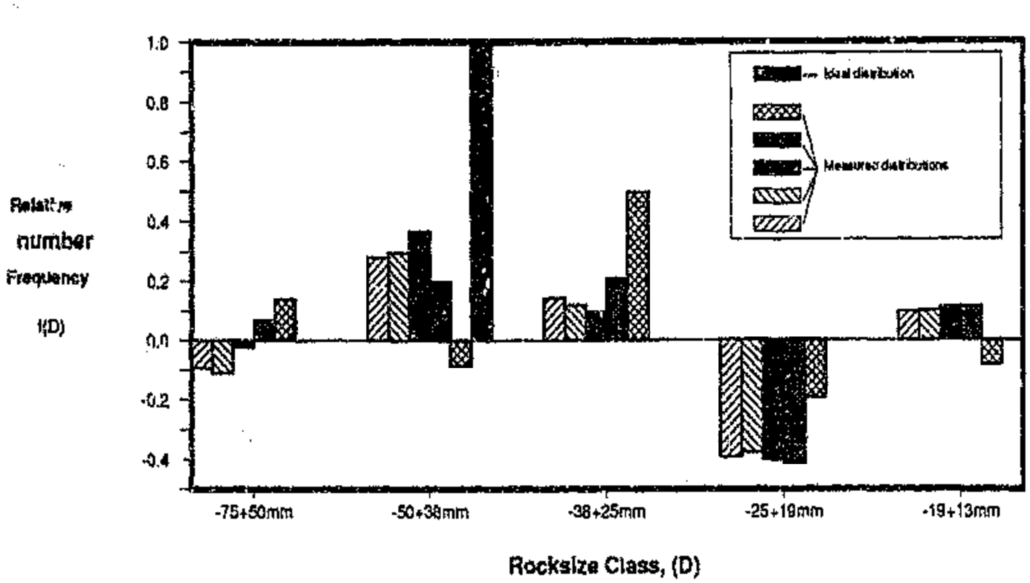

Figure 7.3: Results of using direct linear inversion to solve for the size distribution given a measured chord-length distribution of size -38+25mm. The dark histogram is the ideal response from the inversion process, while the other histograms are the responses of linear inversion to five individual chord-length distributions measured from conveyor-belt scenes.

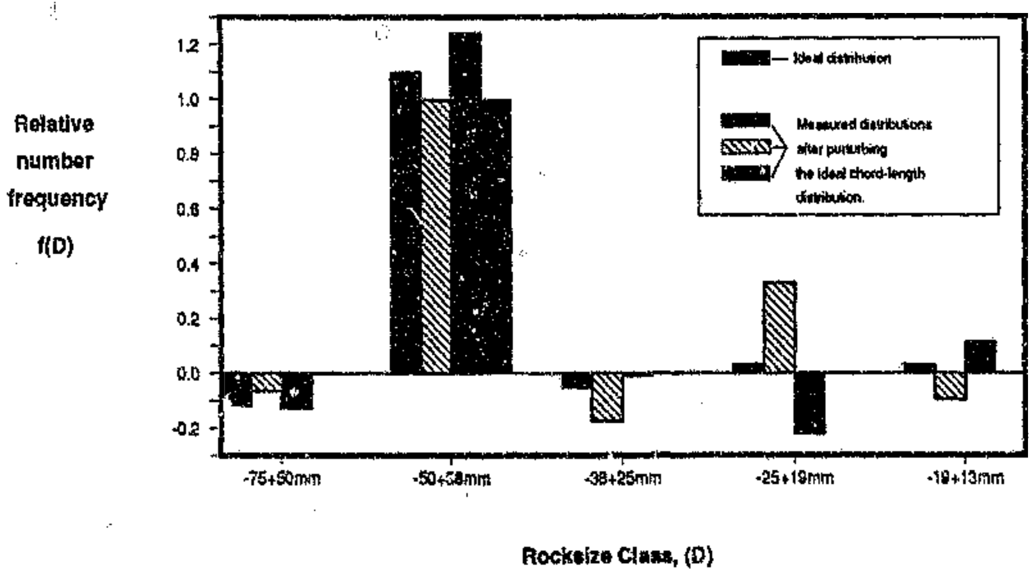

Figure 7.4: Results of adding different combinations of small errors (<1%) or perturbations to *the* chord-length distribution which gives the ideal response, showing the undesirable sensitivity of direct linear inversion methods.

7.2.3 Constrained linear Inversion

Constrained linear inversion is an alternative to the direct inversion techniques discussed in 7.2.2, and is discussed in detail by Twomey (1977) chapter 6.3, and is the method used successfully by Herbst et al (1987) to solve a similar particle-size inversion problem on microscopic particles. In general microscopic particle-sizing problems are different to the conveyor belt particle-sizing problem because *particle identification* in microscopy problems appear to be easier to solve than the rock identification problems from rockstreams. Lin et al (1987), Yu and Gentry (1987), and Kawakami et al (1988) are other researchers who have also investigated constrained linear inversion techniques for estimating particle size distributions.

The *constrained linear inversion* method attempts to minimize the set of possible solutions $f(D)$ to the integral equation [7.1] by imposing additional but arbitrary conditions or criteria on the nature of the solution. It provides a control with which the kernel matrix to be inverted is artificially modified to become less ill-conditioned thus providing for stable inversion. In constrained linear inversion a criterion is imposed that the solution $f(D)$ be as *smooth* as possible. Consequently a *smoothness factor* on the size function $f(D)$. $q(f) \geq 0$ is defined which equals ∞ if the solution $f(D)$ is completely smooth. The smoothness factor $q(f)$ for the size vector $f(D)$ can be evaluated in many ways, for example the sum of the squares of the first differences of $f(D)$ ie $q(f) = \Sigma(f_{i+1} - f_i)^2$ where for clarity $f_i = f(D_i)$.

The smoothness factor $q(f)$ is incorporated into the least squares approximation procedure where the objective is to minimize $| Af - p |^2 + \gamma q(f)$ where γ is a parameter which varies from 0 to ∞ . With γ small we revert back to the least squares method where the solutions tend to be oscillatory. As γ increases the condition of *smoothness* is imposed on f which tends to tune out the oscillations. Increasing γ effectively enlarges the eigenvalues of the matrix modified kernel matrix A to be inverted.

A common measurement of smoothness is the first or second derivative or quadratic of **f** which is given by **Kf** where **K** is defined for the first and second derivative in equation [7.24] respectively.

$$\mathbf{K}_1 = \begin{bmatrix} 0 & 0 & & & & & \\ 1 & -1 & 0 & & & & \\ & 1 & -1 & & & & \\ & & 1 & -1 & & & \\ & & \cdot & & \cdot & & \\ & & & \cdot & & \cdot & \\ & & & & 1 & -1 & 0 \\ & & & & & 1 & -1 \end{bmatrix} \quad \text{or} \quad \mathbf{K}_2 = \begin{bmatrix} 1 & -1 & & & & & \\ -1 & 2 & 1 & & & & \\ & -1 & 2 & 1 & & & \\ & & -1 & 2 & 1 & & \\ & & \cdot & & \cdot & & \\ & & & \cdot & & \cdot & \\ & & & & -1 & 2 & -1 \\ & & & & & -1 & 1 \end{bmatrix} \qquad 7.24$$

The constrained linear inversion problem evolves to minimizing $f^T\mathbf{H}f$ where $\mathbf{H} = \mathbf{K}^T\mathbf{K}$, subject to the constraint that $|\mathbf{Af} - \mathbf{p}| < e^2$ where e is usually the error associated with the error in the measurement $p(L)$ (Twomey, 1977). The *constrained linear inversion* problem is ultimately reduced to estimating $\mathbf{f} = f(D_k)$ with the following equation

$$\mathbf{f}^* = (\mathbf{A}^T\mathbf{A} \quad + \quad \gamma\mathbf{H})^{-1}\mathbf{A}^T\mathbf{p} \qquad 7.25$$

where $\mathbf{f}^*$ is the estimated rock size distribution. The procedure entails iteratively selecting values of γ to minimize the residual $|\mathbf{A}^T\mathbf{f}^* - \mathbf{p}|$ which should be comparable to the overall experimental error in the chord-lengths measured $\mathbf{p}(L)$.

The above strategy was applied to the chord-length distribution data measured on the pilot plant conveyor belt system. The kernel matrix A was derived by measuring chord-length distributions from narrow rock-size distributions and subsequently reduced to a 5×5 kernel array. This kernel was then used in an iterative program which estimated $f(D)$ using [7.25] and by adaptively changing γ to fulfil the requirement with regard to the residual. The results of some tests are shown in figures 7.5 and 7.6 which are mixed as far as accuracy, reliability and stability is concerned. In summary it can be concluded that even constrained linear inversion is not totally suitable for extracting size on-line for process-control purposes.

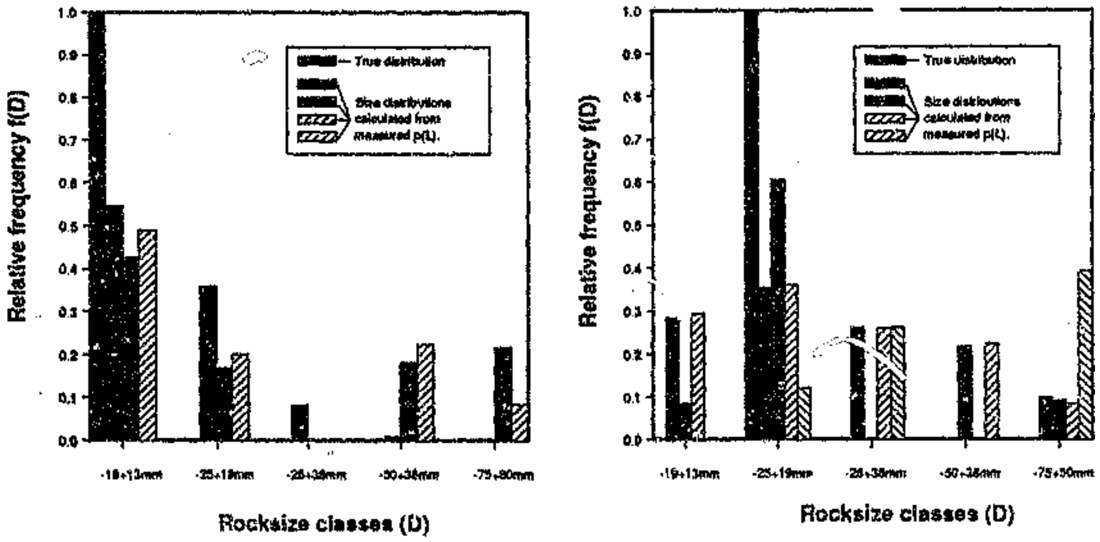

Figure 7.5: Results of using constrained linear inversion. The solid histogram is the ideal distribution. The other histograms are the results of applying measured chord-lengths distributions from rockstreams of size range (a) -19+13mm and (b) -25+19mm.

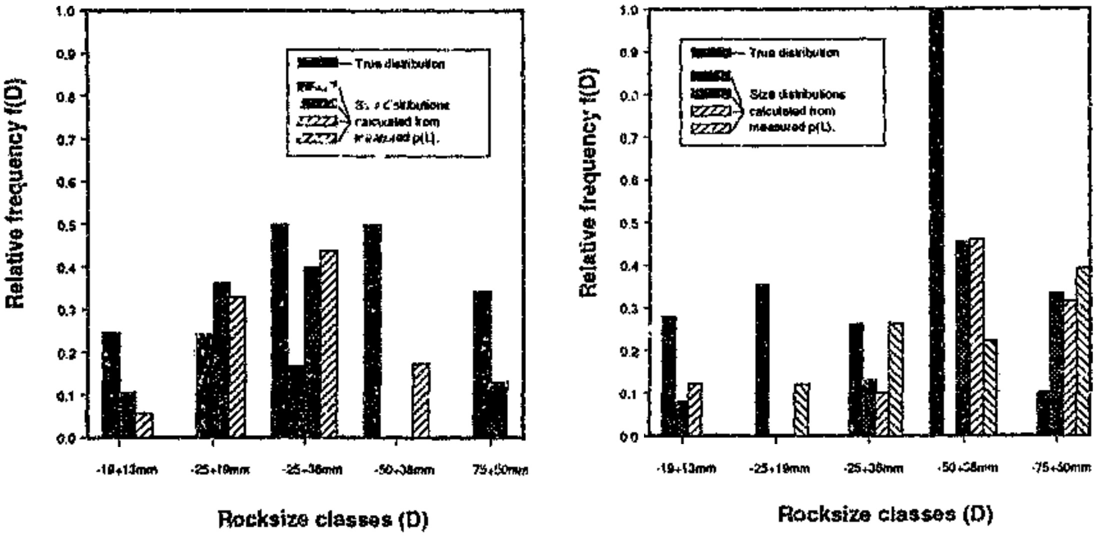

Figure 7.6: Results of using constrained linear inversion. The solid histogram is the ideal distribution. The other histograms are the results of applying measured chord-lengths distributions from rockstreams of size range (a) an equal mixture by mass of -25+38mm and -50+75mm, and (b) only -50+38mm.

7.2.4 King's solution

King (1982) derives an *analytical* solution to the basic working equation [7.1] which does not assume a kernel of a certain shape and which reduces to much simpler form than the solutions given in section 7.2.1 above. In this solution part of the kernel $p(L \mid D)$ which is dependent on rock shape, is assumed to be constant for all D and King states that his method is suited to the rocks found in milling applications. The solution derived by King is given below in equation [7.26]

$$F(M^{1/\alpha}) = \frac{P_v(M)}{\mu_v} - \frac{M^{v+1}}{\beta\mu_v} p(M) - C(M,\beta) \qquad 7.26$$

where $p(M)$ is the density function of the measured data, which for this application is the chord length density $p(L)$ distribution which is derived from the measurement $g(L)$ as shown in equation [7.11]. β is a parameter used to aid in the solution of [7.26] and $C(M,\beta)$ is a correction term defined in equation [7.29]. $P_v(M)$ and μ_v are defined in equations [7.27] and [7.28] respectively. The full derivation is given in King (1982).

$$P_\nu(M) = \int_0^M (M')^\nu p(M')dM' \qquad 7.27$$

$$\mu_\nu = \int_0^\infty M^\nu p(M)dM \qquad 7.28$$

$$C(M,\beta) = \int_{M^{1/\alpha}}^\infty \left\{P_\nu P(M \mid D) - \frac{M^{\nu+1}}{\beta} p(M \mid D)\right\} \frac{f(D)}{M_D^\nu} dD \qquad 7.29$$

King (1982) comments that the correction term $C(M,\beta)$ [7.29] is inconveniently dependent on the unknown size distribution $f(D)$, as well as the kernel $p(M \mid D)$ which is dependent on the shape of the rocks. Thus this solution [7.26], is not totally solved because the solution is not independent of $f(D)$. Nevertheless the solution given in equation [7.26] is very useful because it can be evaluated quite easily from the measurements $p(M)$ with the exception of $C(M,\beta)$.

When simple particles such as spheres are considered the solution [7.26] reduces to equation [7.30] because $C(M,\beta) = 0$. For linear intercepts $\alpha = 1$, and $\nu = i/j = 1$ because $i = 1$ for an IUR line probe and the dimension of the measured variable M is $j = 1$ which gives equation [7.31]. The solution given in equation [7.31] for spheres is also derived earlier by King (1978) to vindicate the original equation derived by Cahn and Fullman (1956) which was challenged by Sahu (1976).

$$F(M) = \frac{P_1(M)}{\mu_1} - \frac{M^2}{3\mu_1} p(M) \qquad 7.30$$

$$\Rightarrow \quad F(D) = \frac{P_1(L)}{\mu_1} - \frac{L^2}{3\mu_1} p(L) \qquad 7.31$$

In this research the correction term $C(L,\beta)$ was assumed to be zero, thus the solution given in [7.31] is used with the chord-length distribution data measured to derive the sieve size distribution $f(D)$.

Practical problems in evaluating $p(L \mid D)$ as well as the numerical problems and uncertainty associated with evaluating $C(L,\beta)$ led to the decision to let $C(M,\beta) = 0$. $C(L,\beta)$ depends on $p(L \mid D)$ which is dependant on the shape of the rocks as well as the actual size distribution $f(D)$ to be determined. Although methods are available to predict $f(D)$ and to solve for $C(M,\beta)$ (King, 1982), further motivation for letting $C(M,\beta) = 0$ is given below.

$p(L \mid D)$ cannot be reliably determined from conveyor belt images because firstly, the shape of the rocks vary with time changing the functional form of $p(L \mid D)$, and secondly the edge patterns from which the chords are measured are not representative of the true rock geometry and size because of inaccurate segmentation (chapters 4 and 5), which accentuates the errors in the measurement $g(L)$.

The problems given above for evaluating $p(L \mid D)$ from *dynamic* images lead to the argument that *static* data of separated rocks in a monolayer should rather be used. However the images of the rockstream captured from the conveyor belt are unique and distinctive from the static images of separated rock piles, which implies that the kernel $p(L \mid D)$ should be derived from conveyor belt images and not static images. Furthermore inspection of the kernels derived from static and dynamic images show that they are sufficiently different from each other in functional form to result in senseless estimations of $f(D)$ if $p(L \mid D)$ derived from static images is used with chord-length measurement from the conveyor belt.

The derivation of $p(M \mid D)$ for dynamic and static images requires manual sieving and its associated problems. In particular not enough chord samples can be gathered from static images because of the manual labour and time required, which results in the measurements of $p(M \mid D)$ being too noisy for unambiguous modelling. In addition $p(M \mid D)$ measured with either static or dynamic images is *not* measured with a strictly true IUR linear probe providing additional sources or bias to the measurement, which perhaps invalidates the whole foundation upon which equation [7.26] is based. Equation [7.31] is certainly invalid because the rock shapes are not spherical.

Figure 7.7 shows the chord-length distributions before the application of King's method. Figure 7.8 shows the results of applying King's solution [7.31] a modified form of [7.26] which are still surprisingly meaningful despite the fact that $C(M,\beta)$ is assumed to be zero, and the solution used [7.31] is based on spheres. The application of King's method exhibits undesirable oscillations at the lower size range, which casts suspicion on the spike at the shorter chord-lengths of the chord length distributions. The effect of artificially removing the spike is shown in figure 7.9. Note that although King's method produces very useful results, it is still a complex solution requiring iteration because varying β influences the shape and values of the results obtained of which all values should all be positive.

Appendix C gives a sample calculation of calculating $F(D)$ from the measured chord-length distribution $g(L)$ using the simplified version of King's solution.

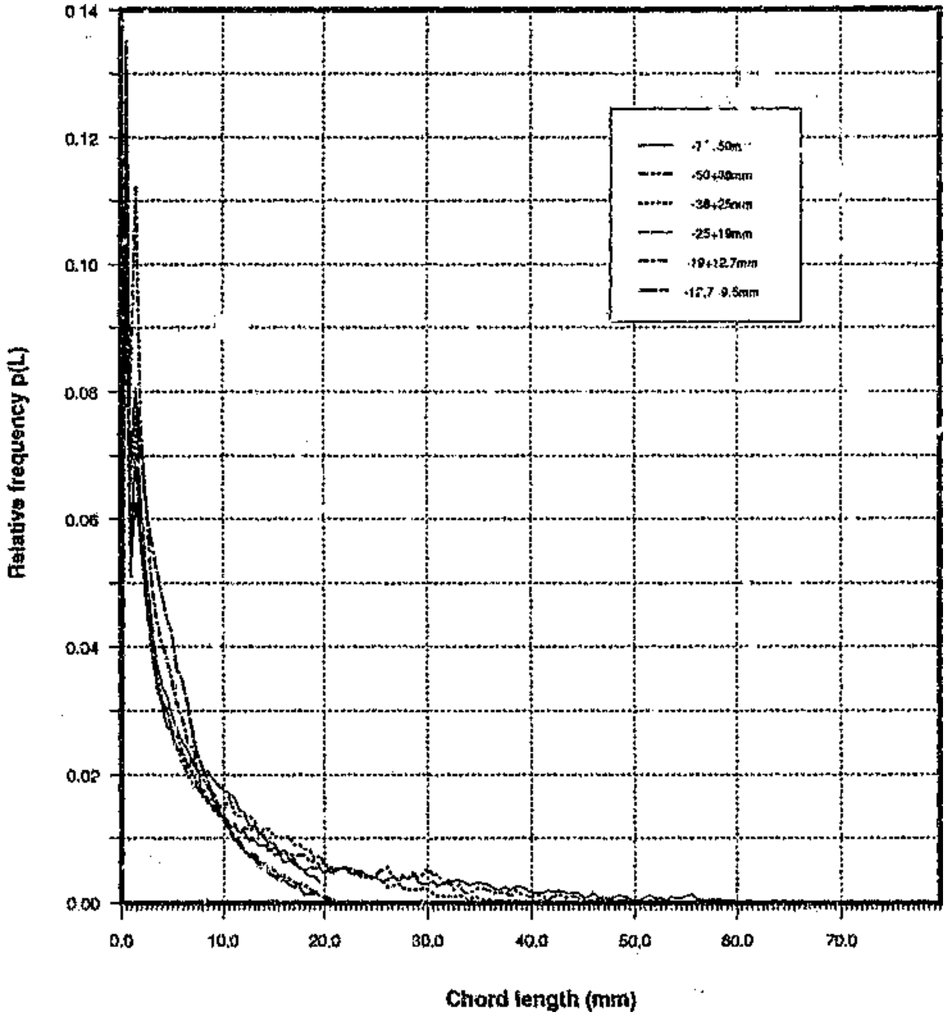

Figure 7.7: Chord-length distributions of rocks $p(L)$ as measured from different sized conveyor-belt rockstreams before the application of King's method.

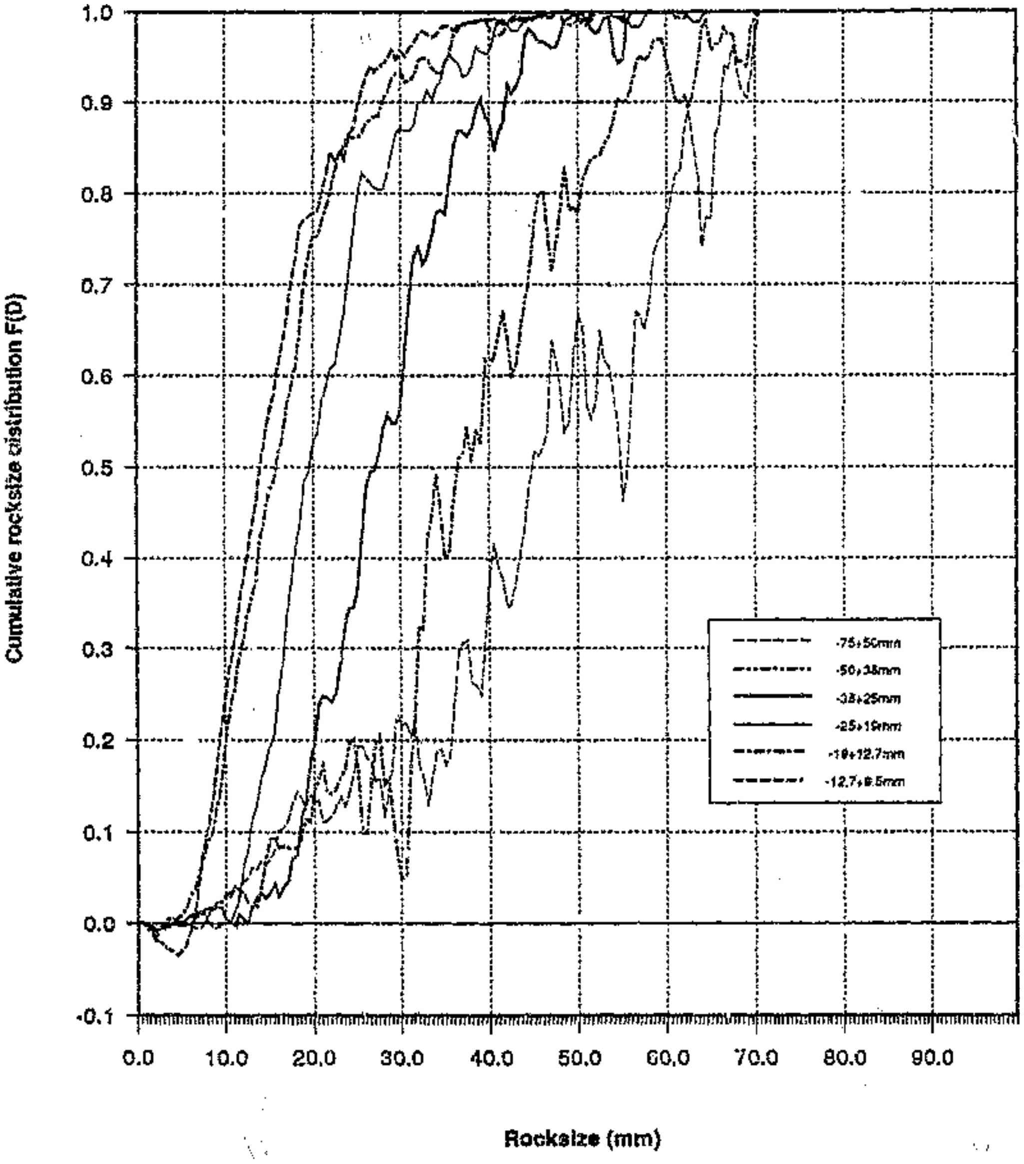

Figure 7.8: Sieve-size distributions as derived by kings formula [7.12]. Note the correction term $C(M,\beta)$ is assumed to be zero, and $\beta = 1.25$ so that most of the solutions are positive, ie $F_i(D) \geq 0$.

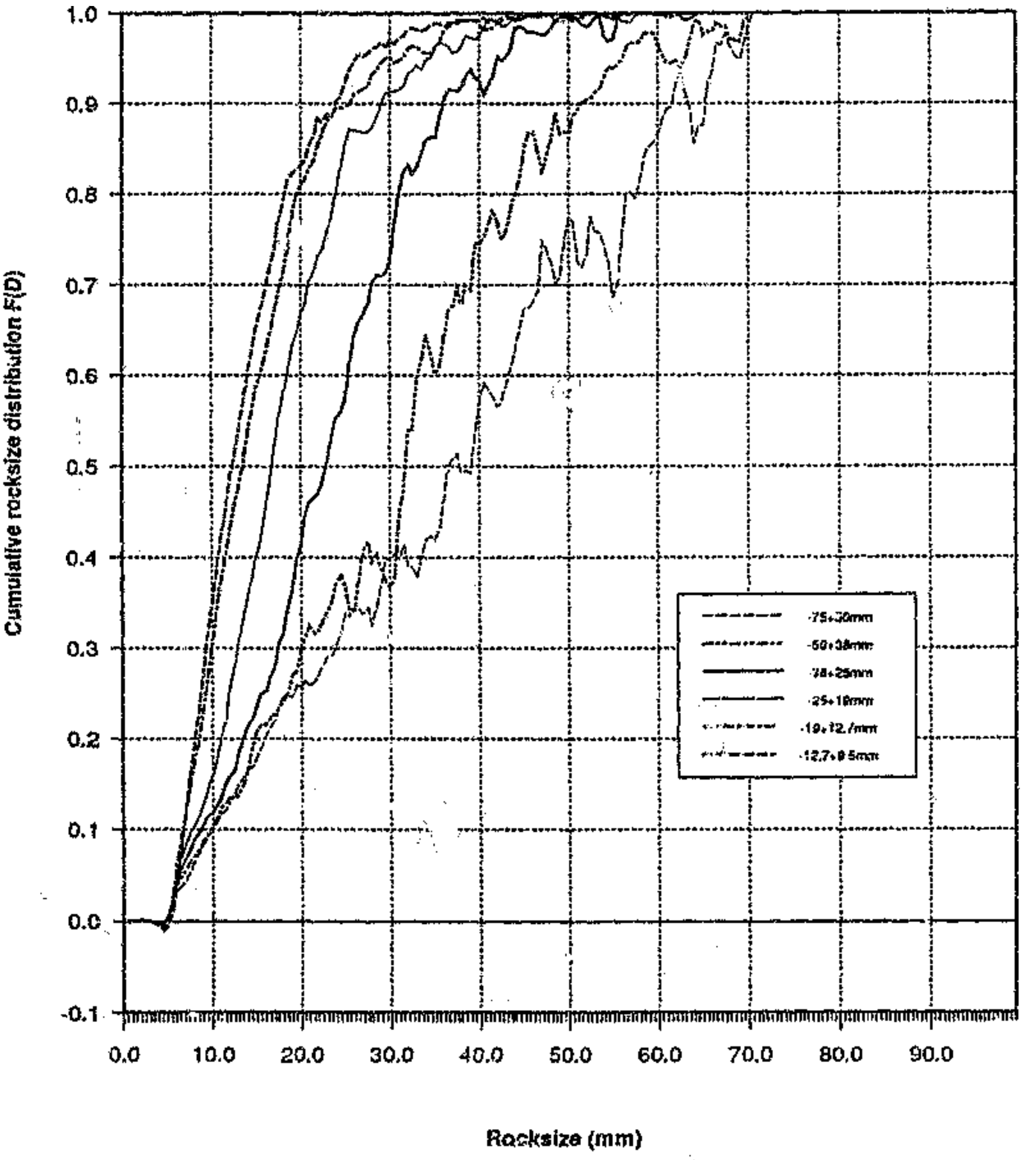

Figure 7.9: The effect on sieve-size distributions as derived by King's formula [7.12] after replacing the spike at the shorter chord-lengths of $p(L)$ with a ramp going from 0.0 to 0.04 for the first 10 values. This effectively removes the spike lying against the vertical axis as shown in figure 7.7. $\beta = 2.40$ and $C(M,\beta) = 0$.

7.3 MOMENT METHODS

Examination of the results of using the techniques derived in subsection 7.2 for deconvolving the basic working equation, shows that there is definitely merit in the use of these techniques. However the large variances in the measurement data together with the fundamental ambiguities and difficulties of the inversion methods and the uncertainties with the calculated size distributions as discussed above has led to the hypothesis that perhaps some other transformation could be used to extract information from the chord-length distributions which

a) does not necessarily relate directly to an equivalent size distribution such as sieve size and which,

b) is simpler to implement, an important consideration as far as real time implementation is concerned

In this chapter a number of new transformations are described which "release" ***meaningful*** size data inherent in the chord-length distribution $p(L)$, without resorting to *forcing* the $p(L)$ to *look* like *sieve* size data. These new transformations were initially developed intuitively after inspection of the results of the inversion methods and an in depth literature survey. Although these transformations have been derived according to a different philosophy to the linear inversion methods discussed above, they nevertheless contain elements remarkably similar to the formulae and relationships developed formally in the literature with regard to size estimation from linear intercepts. In the original philosophy, the objective was to derive *sieve size distribution*. After taking into account the inherent ambiguity of the image processing as well as inversion processes, the new goal is less ambitious and is to derive any size information. In retrospect to this research it is the opinion of the author that the principle of viewing sieve size as the only valid rocksize measurement, is a narrow conceptualization of the whole size problem. However sieve size measurements cannot be written off, because in the absence of alternative methods for evaluating rocksize, it is only sieve size which can be used to verify this new approach.

7.3.1 Cumulative Chord-length Distributions

The approach adopted here starts from a visual comparison of the chord length distributions for different size distributions. Consider the two chord-length distributions shown in figure 7.10. It is observed that these chord-length distributions are noisy and very similar in shape with little to distinguish between them. However the integral of $p(L)$ or the *cumulative* chord-length distribution proves to be a useful transformation which does begin to reveal the differences between these two distributions irrespective of the fact that noise is accumulated with the integration process. These integrals are evaluated according to equations [7.32] and [7.33] for continuous and discrete chord-length distributions respectively.

$$P(L) = \int_0^L p(L')dL' \qquad 7.32$$

$$\Rightarrow \qquad P(L_k) = \sum_{i=0}^{i=k} p(L_i) \qquad k = 0 \ldots n \qquad 7.33$$

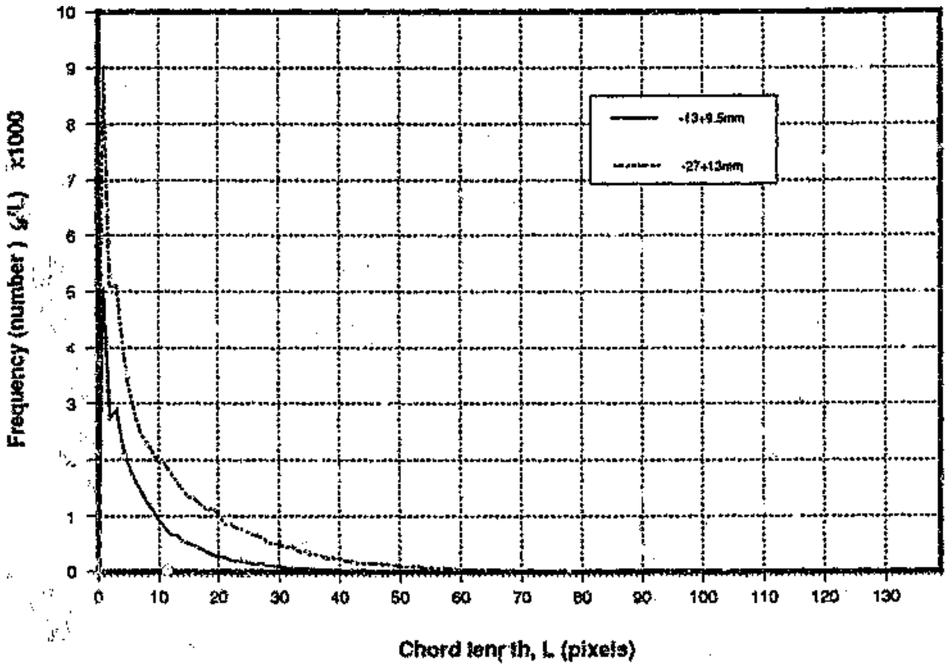

Figure 7.10: Two typical chord-length distributions measurements $g(L)$obtained from conveyor-belt rockstreams. (Adjacent probes used.)

Figure 7.11 below shows the result of this transformation applied to a number of chord-length distributions measured from images of rocks of different size distributions. The integration separates the curves and reflects the relative proportion of larger chords present in the image, which in turn is indicative of the proportion of the larger rocks and their relative differences. Before integration the raw chord-length distributions are transformed to a *density function* $p(L)$ by equation 7.11. The transformation to densities removes the effect of over- or undersampling of chord lengths which is a function of rocksize, so that the only factor that is considered when different distributions are compared, are the ***relative*** number of chord-lengths for each distribution, ie the function shape. This ensures that the undesirable effects of sampling are minimised. The results from this integration are remarkably similar to those determined experimentally by King (1979) on pyrite samples in a different application. This verifies that size distribution knowledge is being extracted by the measurement system despite the problems of moving scenes and occlusion etc.

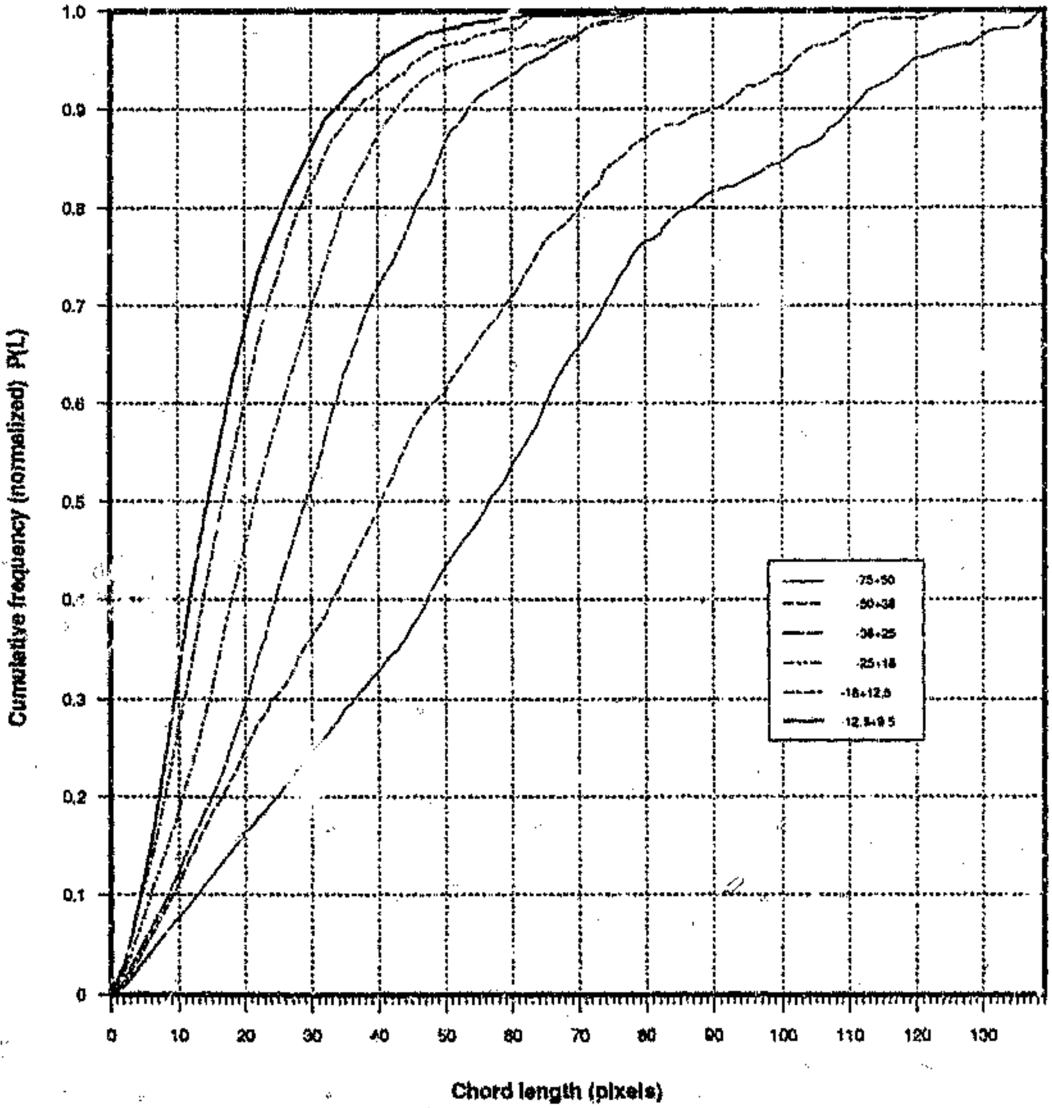

Figure 7.11: Cumulative chord-length distributions $P(L)$ as measured from moving rockstreams.

Figure 7.12 shows cumulative chord-length distributions resulting from static tests conducted on different size distributions of granite obtained with the joining algorithm. The size distribution were synthesized according to the Rosin-Rammler distribution function given in equation [7.33] where n and b are characteristic coefficients and n was varied, Wigeson (1987), Popplewell et al (1988).

$$f(D) = e^{-(bD)^n} \qquad 7.33$$

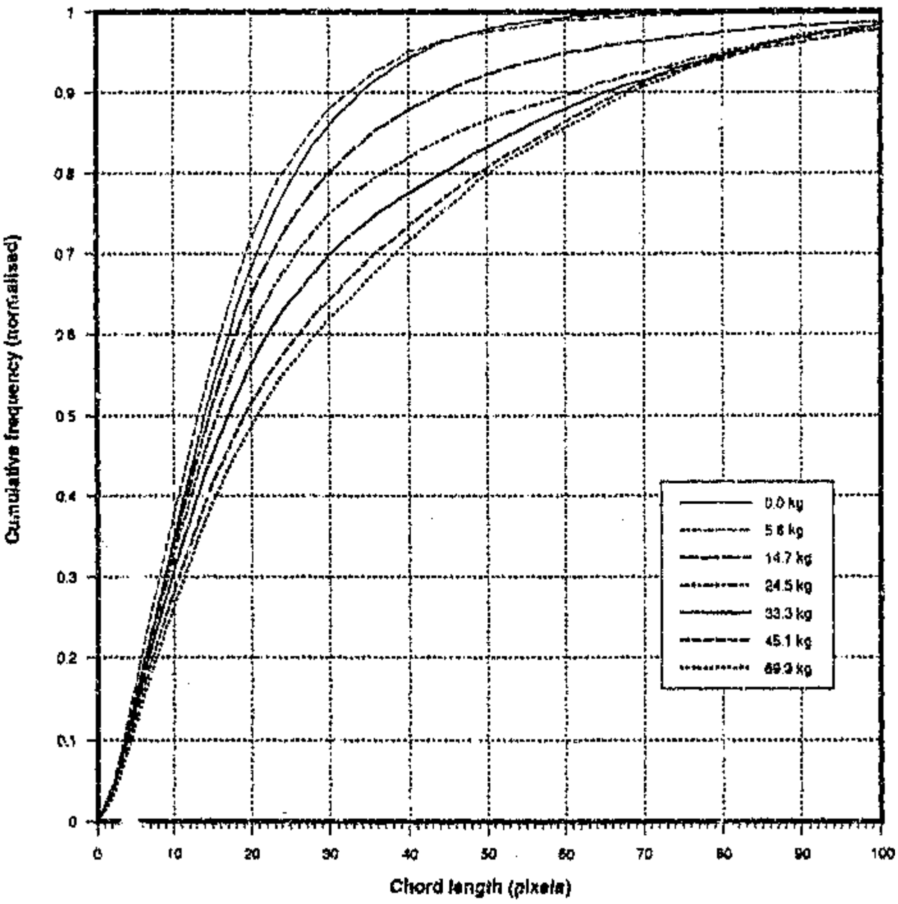

Figure 7.12: Cumulative chord-length distributions $P(L)$ measured from static images of granite rock-scenes with the rock-size distributions synthesized according to the Rosin-Rammler function.

7.3.2 Weighting the Chord-length distributions.

Examination of most of the chord-length density functions $p_i(L_k)$ measured (figures 6.16 and 7.7), show that they have a similar shape: a narrow peak near the origin with the distribution decaying exponentially towards the longer chord-lengths. The shape of the chord-length distribution $p_k(L)$ is a result of the relatively large number of short chord-lengths L_{short} and the small number of long chord-lengths L_{long} measured.

Superficially there appears to be very little difference between the various distributions $p_i(L_k)$ calculated from different rocksize distributions $f_i(D_k)$. However chord-length distributions resulting from the larger rocks exhibit tiny undulations in the vicinity of the larger chords L_{long} which at a first could be attributed to noise, experimental and sampling errors. However results obtained from calculating the cumulative distributions in section 7.3.1 above, show that there *are* differences between the various distributions $p_i(L_k)$'s which integration accumulates and reveals by "pushing" the various chord-length distributions $p_i(L_k)$ apart. It was thus postulated that in order to *reveal* the slightest differences between distributions it is necessary to *amplify* these perturbations in $p_i(L_k)$ with some increasing function that compensates for the decaying nature of $p_i(L_k)$. A linear weighting function $a(L)\propto L$ was chosen, which weights the chord-length distribution $p_i(L_k)$ to give $p_i^*(L_k)$ were

$$p_i^*(L_k)=L_k p_i(L_k) \tag{7.35}$$

Examples of these amplified chord-length distributions $p_i^*(L_k)$ may be seen in figures 7.13 where the differences between similar chord-length distributions are revealed more clearly in the tail. The results shown in figure 7.13 justify this weighting procedure and confirm that the *small* perturbations in the *tail* of the chord-length distribution are vital for differentiating between the various $p_i(L_k)$. In contrast, the distribution function in the vicinity of the shorter chords L_{short} does not appear to contain much information or features for indicating differences between the proportion of smaller rocks in different distributions. A disadvantage to this magnification is that the amplified distributions $p_i^*(L_k)$ are far more noisy. When edge patterns of large rocks are sampled, *small* numbers of *long* chord-lengths L_{long} are measured. This small finite sampling results in a number of chord class bins being empty or near empty bins being adjacent to relatively full bins, which with the linear weighting operation results in unnatural discontinuities in $p_i^*(L_k)$. These discontinuities distort the size differences perceived by the viewer when comparing different chord-length distributions. This problem again emphasizes the need for sampling as many rocks per image and images as possible so that many chords are measured to produce a *continuous* distribution. A solution to this sampling problem is the use of *adjacent* probes (1 pixel apart) which samples a rock a number of times roughly in proportion to its size. Adjacent sampling infringes upon the accepted stereological rule of not sampling an object more than once (Weibel, 1980) and biases the distribution by increasing the number of shorter chords.

In the light of the success of the above linear enhancement function in revealing differences between chord-length distributions which relate to sieve size, a more general weighting function $a(L_k)$ is defined

$$a(L_k) = L_k^\alpha \qquad 7.36$$

$$\Rightarrow \qquad p^*_{\alpha,i} = L_k^\alpha \cdot p_i(L_k) \qquad 7.37$$

where α is some factor, $\alpha \geq 0$. Examples of weighted chord-length distributions $p^*_{\alpha,i}(L_k)$ with $\alpha = 1, 2, 3$ for the same size distribution are shown in figure 7.14. What is surprising is that the amplified distributions $p_{\alpha=2,i}$ appear bell shaped or vaguely similar to the normal or log-normal functions which are often assumed for particle size distributions. Figure 7.15 shows weighted distributions $p_{\alpha=2,i}$ for different size distributions $f_i(D)$. It is important to note that each amplified chord-length distribution $p^*_{\alpha,i}(L_k)$ has been normalized before being placed side by side for comparison. This effectively nullifies the effect of sampling as discussed previously.

Figure 7.16 shows further tests carried out on the conveyor belts where the weighting method developed was used to try and determine quantitatively the relative proportion of large rocks to small rocks. In this experiment small rocks in the size range -13.5+9.7mm were initially loaded on the conveyor belt. Thereafter large rocks (-75+50mm) were progressively added (mixed) in batches to the small rocks circulating on the conveyor-belt system and chord-length measurements made on the processed images captured from these mixed rockstreams. The amount of rocks of both sizes were measured quantitatively in terms of their mass.

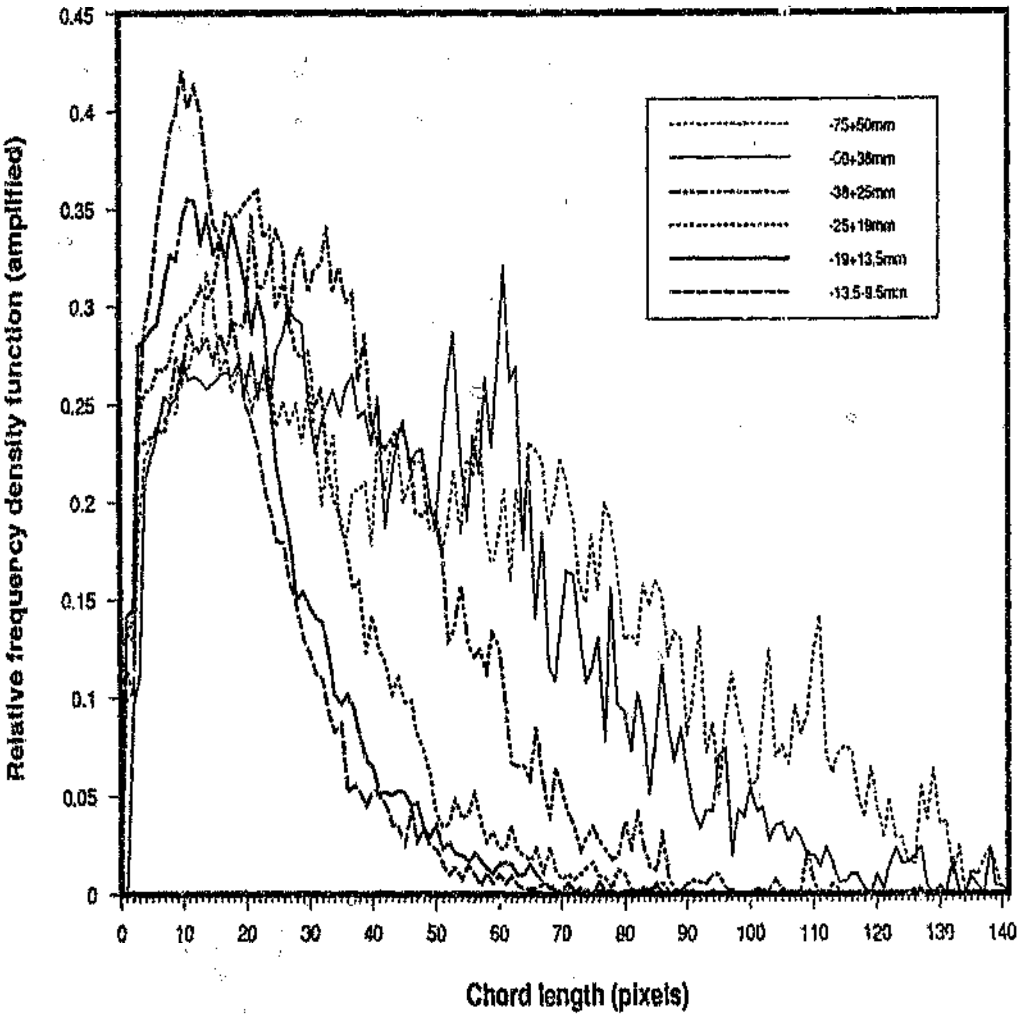

Figure 7.13: Amplified chord-length distributions $p_i^*(L_k)$.

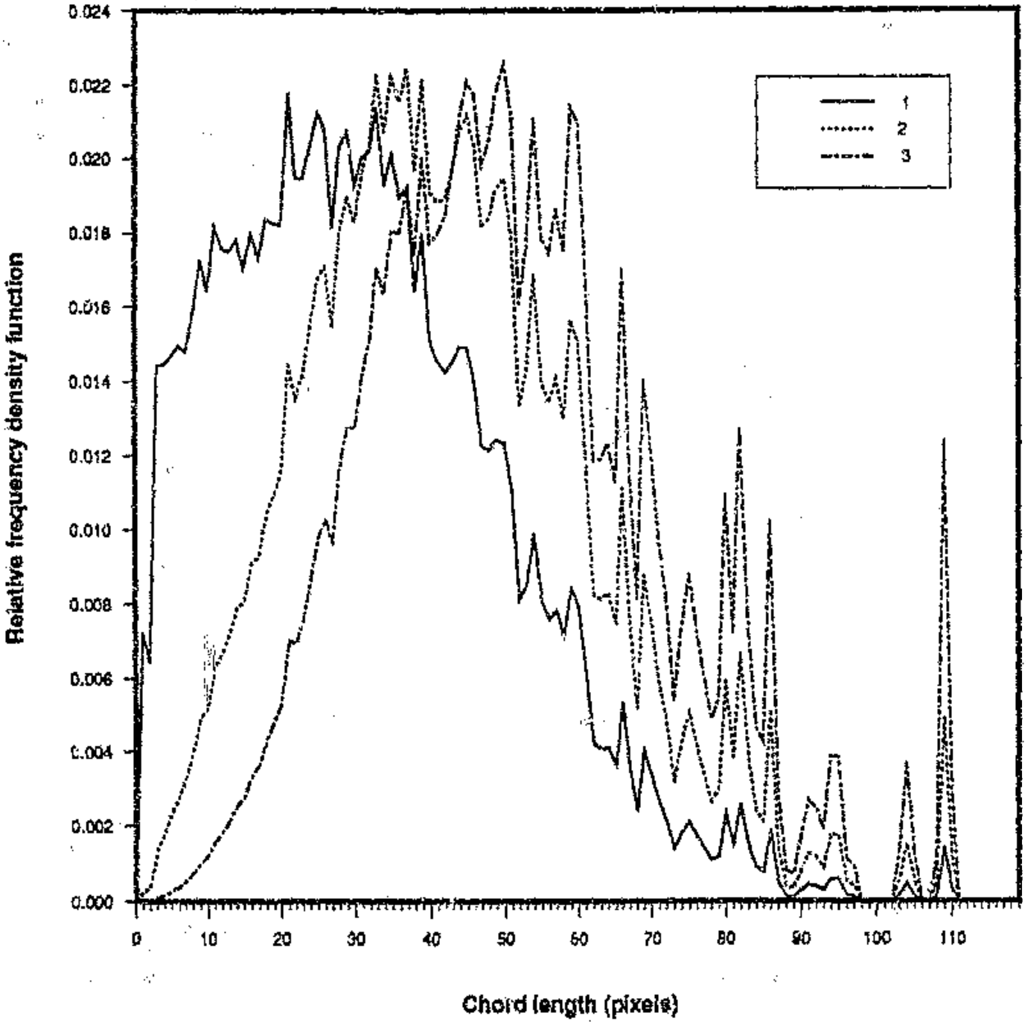

Figure 7.14: Amplified distributions $p_k^*(\alpha, L)$ with $\alpha = 1, 2, 3$ for the same rocksize distribution.

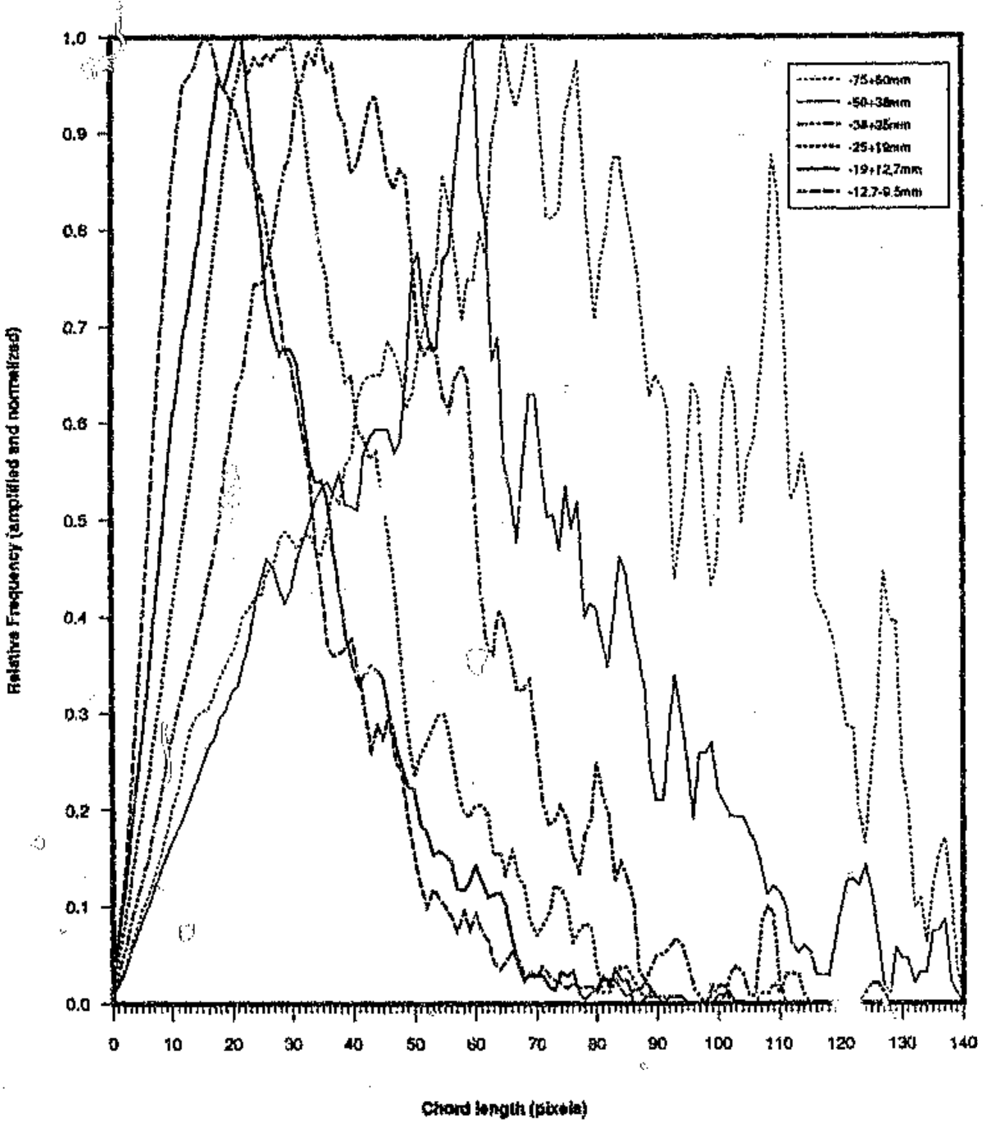

Figure 7.15: Amplified distributions $p^{*}_{\alpha=2,i}(L_k)$ for different rocksize distributions.

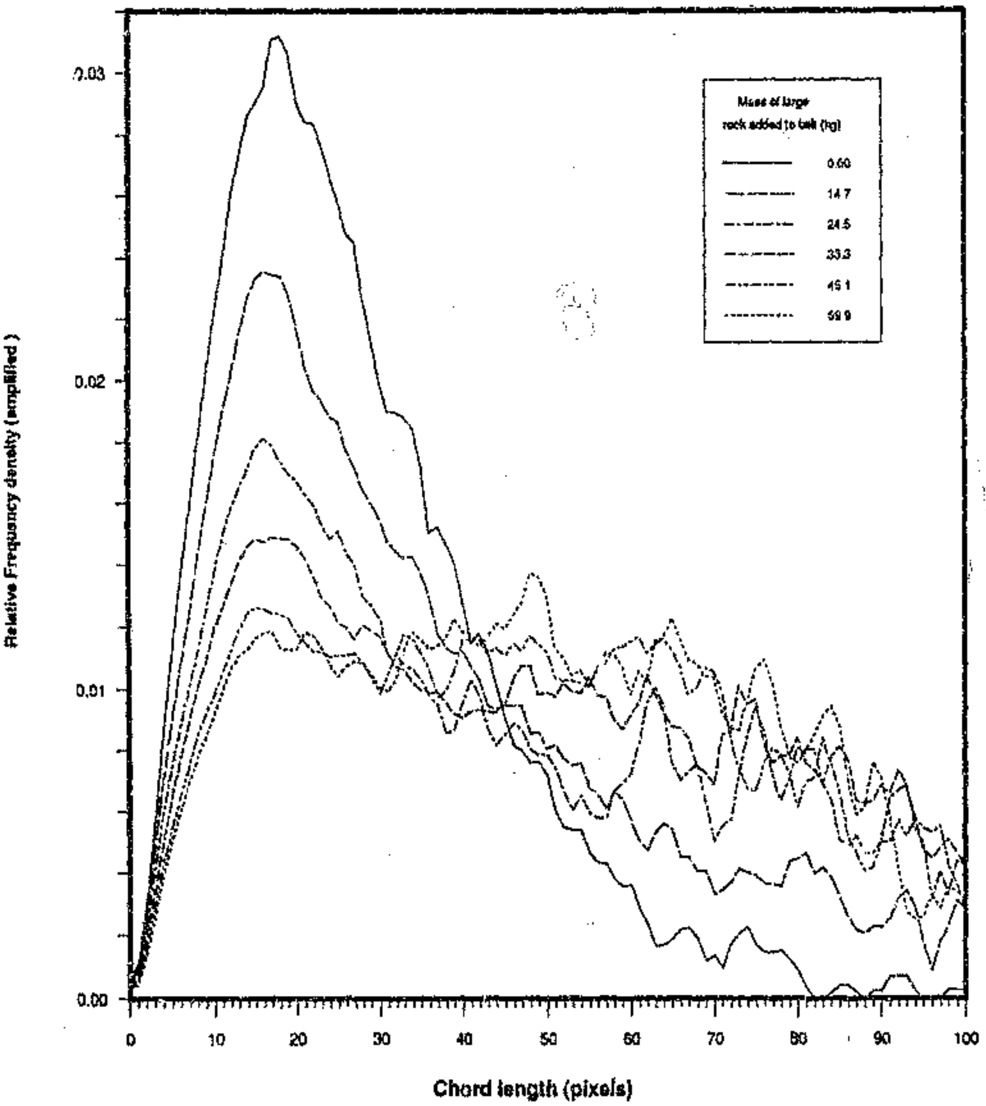

Figure 7.16: Amplified chord-length distributions $p^*_{\alpha=2,i}(L)$ measured from conveyor belt tests with varying quantities of large rock (-75+50mm) being added to the rockstream.

7.3.3 Comparison of King's method with Cumulative and Weighted Methods

Comparison of the ad-hoc approach of *cumulative* and *weighted* transformations with the solution derived by King (1982) equation [7.22] shows some interesting similarities.

Firstly King derives $F(D) \propto P_v(L)$. A similar relationship is derived in this work where $P(L)$ is assumed heuristically to be related to $F(D)$ as developed in subsection 7.3.1. Secondly in section 7.3.2 the weighted distribution $L^2 p(L)$ was found to be remarkably similar to $f(D)$. The second term to King's solution contains $F(D) \propto -L^2 p(L)$.

Although these similarities exist, they are not equivalent and cannot be used as a proof for, and against, the validity of these methods without much further investigation. What can be deduced in retrospect from this comparison is that ***both*** $P(L)$ and $L^2 p(L)$ are ***important components*** to the derivation of size measurements from the chord-length distributions of rockstreams.

7.3.4 Moments of Chord-length Distributions

Both the results of weighting (section 7.3.2) and development of methods to derive $f(D)$ explicitly (section 7.2) indicates that there are fundamental but complex relationships between the rock-size distributions $f(D)$ and the chord-length distributions $p(L)$ as measured from the conveyor belts. The complexity of these relationships together with the general failure of linear methods to solve for $f(D)$ as well as the difficulty in interpreting the results of the cumulative and weighted methods, provides an incentive to develop methods for estimating ***parameters*** relating to the size distribution, rather than the ***full distribution***, which effectively summarizes the data which generally contains too much information anyway. These parameters could for example, be ***average*** rocksize $\overline{D}$ and the ***standard deviation*** $\sigma(D)$ of the distribution. In this sub-section relationships between the ***moments*** of the chord-length distribution $p(L)$ and parameters or moments of the size distributions $f(D)$ are derived, rather than relationships between the full distributions. The n'th moments of the rocksize $f(D)$ and chord-length distribution $g(L)$ are defined respectively to be

$$\mu_D^n = \overline{D^n} = \int_0^\infty D^n f(D)\,dD \qquad 7.38$$

$$\mu_L^n = \overline{L^n} = \int_0^\infty L^n g(L)\,dL \qquad 7.39$$

where $n \in Z$ and μ_D^n and $\overline{D^n}$ are two different notations used in the literature. Conceptually the moments of the chord-length distribution μ_L^n can also be considered to be *summarizing* parameters of the amplified chord-length distribution derived in 7.3.2. At first it appears that in calculating these moments, information is being lost because the estimation of the distribution itself is being abandoned. Generally speaking this is not true, because moments uniquely describe any well behaved distribution, and Hillard (1968) comments that in practice the first few moments of a distribution will suffice in describing it. This is compatible with the statement in chapter 1 that the average and standard deviation of a size distribution are usually sufficient for many applications. In particular the average $\overline{D}$ of $f(D)$ is merely the first moment of μ_D^n , and the standard deviation is the square root of the second moment about the average ie

$$\overline{D} = \mu_D^1 \tag{7.40}$$

$$\sigma(D) = \sqrt{[(\mu_D^2) - (\mu_D^1)^2]} \tag{7.41}$$

Gundersen (1980) states that contrary to expectation, the reduction in information from 3-D structures to 2-D sections brings about only a minor increase in the statistical uncertainty of the central moments of most fundamental structural characteristics of body thus providing another incentive to use these moments. The use of moments is further justified because for mill control purposes, moments or statistical parameters are perhaps more likely to be utilized than the full distributions themselves. The main advantage of moments of $f(D)$ is that they can derived *directly* from the moments of the property measured on sections which in this case are the chord-length distributions. The moment relationships between $f(D)$ and $p(L)$ have been derived and discussed by authors such as Hillard (1968), Barbery (1974) and King (1984). The basic relationships are derived by integrating [7.1] and making use of [7.38] and [2.39] to give

$$\mu_D = k_1 \frac{\mu_L^2}{\mu_L} \tag{7.42}$$

$$\mu_D^2 = k_2 \frac{\mu_L^3}{\mu_L} \tag{7.43}$$

where k_1 and k_2 are factors dependent on the shape of the particles, ie $p(L \mid D)$. For spheres a generic moment relationship is derived (King, 1984) and reproduced in equation [7.44].

$$\mu_D^{n-1} = \frac{n+2}{3} \frac{\mu_L^n}{\mu_L} \tag{7.44}$$

The first three moments μ_L^n of the chord-length distributions were calculated according to equation [7.39] from chord-length distributions taken from different tests carried out on the conveyor belt. The first two moments of the size distributions were then calculated according to 7.42 and 7.43. Unfortunately no useful information could be derived as can be seen in figure 7.17 below. This is possibly a result of using a model derived for spheres in a homogeneous and sparse distribution which should not be used for overlapping piled irregular rocks.

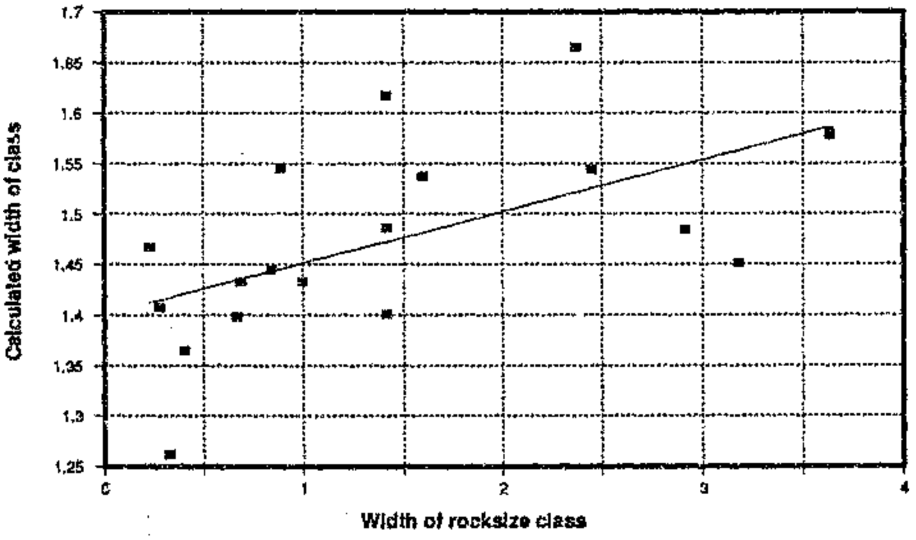

Figure 7.17: Plot of the calculated width of the size distributions $\sigma(D)$ versus the true width of a few size classes according to table 6.1, calculated by the relationship [7.43]. Note that the distributions of each size class was assumed to uniform, and was normalized by the average size of each class.

7.3.5 A New Moment Relationship

Despite the unsatisfactory results with the moments as shown in subsection 7.3.4 above, when the first moment μ_L is plotted against the geometric average rocksize $\overline{D_g}$ a curve of the form shown in figure 7.18 is revealed. This curve shows an almost linear relationship between the average of the first moments of the chord length distribution, and the average (geometrical) sieve size of the rocks being measured. This relationship is surprising because it does not comply with established moment relationships [7.42] and [7.43] above. The average rocksize $\overline{D_g}$ was calculated with equation [7.45].

$$\overline{D_g} = \sqrt{D_{i_{max}} \cdot D_{i_{min}}} \qquad 7.45$$

where $D_{i_{min}}$ and $D_{i_{max}}$ are the minimum and maximum size of rocks for the i'th class, and the rocksize distribution for a given class of rocks between $D_{i_{min}}$ and $D_{i_{max}}$ is assumed to be uniform.

The relationship between μ_L and $\overline{D_g}$ is fairly linear except for the upward trend at the shorter chord-length. This upward trend is attributed to pixel resolution problems where the smaller rocks tend to have the same texture as a larger rock. Further experimentation has shown the (empirical) linear relationship [7.46] for the curve in figure 7.18 where $\mu_L(0)$ and k are constants, to be generally true for averaged chord-length distributions.

$$\overline{D_g} = k\,\mu_L + \mu_L(0) \qquad 7.46$$

Relationship [7.46] cannot be explained in terms of present theory as found in the literature; however it does seem logical that the average chord length measured of all the rocks should be proportional to the average sieve size. This relationship has been found *on average* to be *highly repeatable* for both quartzite and granite rock, as well as the numerous variations of image processing strategies developed in chapters 4 and 5. Based on this experimental evidence, this empirical relationship [7.46] is assumed to be valid.

The *average* first moment for each rock size distribution is calculated by averaging N first moments $\mu_{L_{j,i}}$ measured on N images captured from circulating rockstream Ω_j with size distribution f_j according to equation [7.47].

$$\overline{\mu_{L_j}} = \frac{1}{N}\sum_{i=1}^{N}\mu_{L_{j,i}} \qquad 7.47$$

Figure 7.19(a) shows the result of tests taken over a period of time in order to test repeatability. It can be seen that the measurements of $\mu_{L_{j,i}}$ for each rockstream Ω_j remains fairly constant with a certain amount of variations $\sigma(\mu_{L_{j,i}})$ superimposed. The variations are attributed mainly to surges in the rockstream which reveals parts of the conveyor belt to the camera, and which can be construed as noise. Figure 7.19(b) shows the same data as in figure 7.19(a) except that the data has been smoothed by a 3 element moving window. Figure 7.20 shows how the standard deviation $\sigma(\mu_{L_j})$ of the averaged first moments μ_{L_j} increase with the increase in the average rocksize. This increase in the standard deviation is attributed to the lower number of chords sampled in scenes of larger rocks.

Sample calculations of calcuating weighted chord-length distributions and moments are given in appendix B.

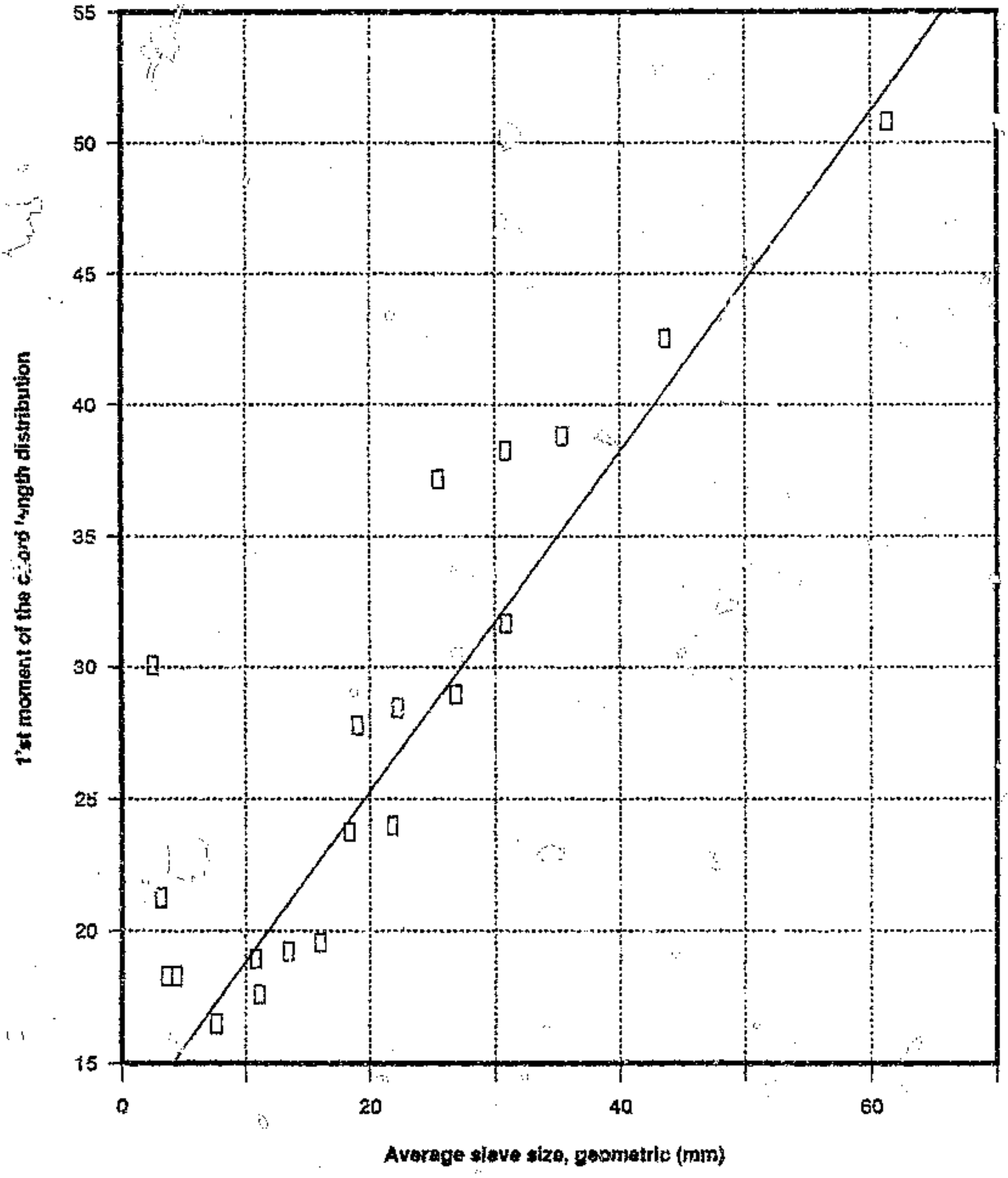

Figure 7.18: The average chord-length μ_{L_j} measured for each rock stream with size distribution $f_j(D)$, versus the geometric average $\overline{D_{sj}}$ of each rockstream.

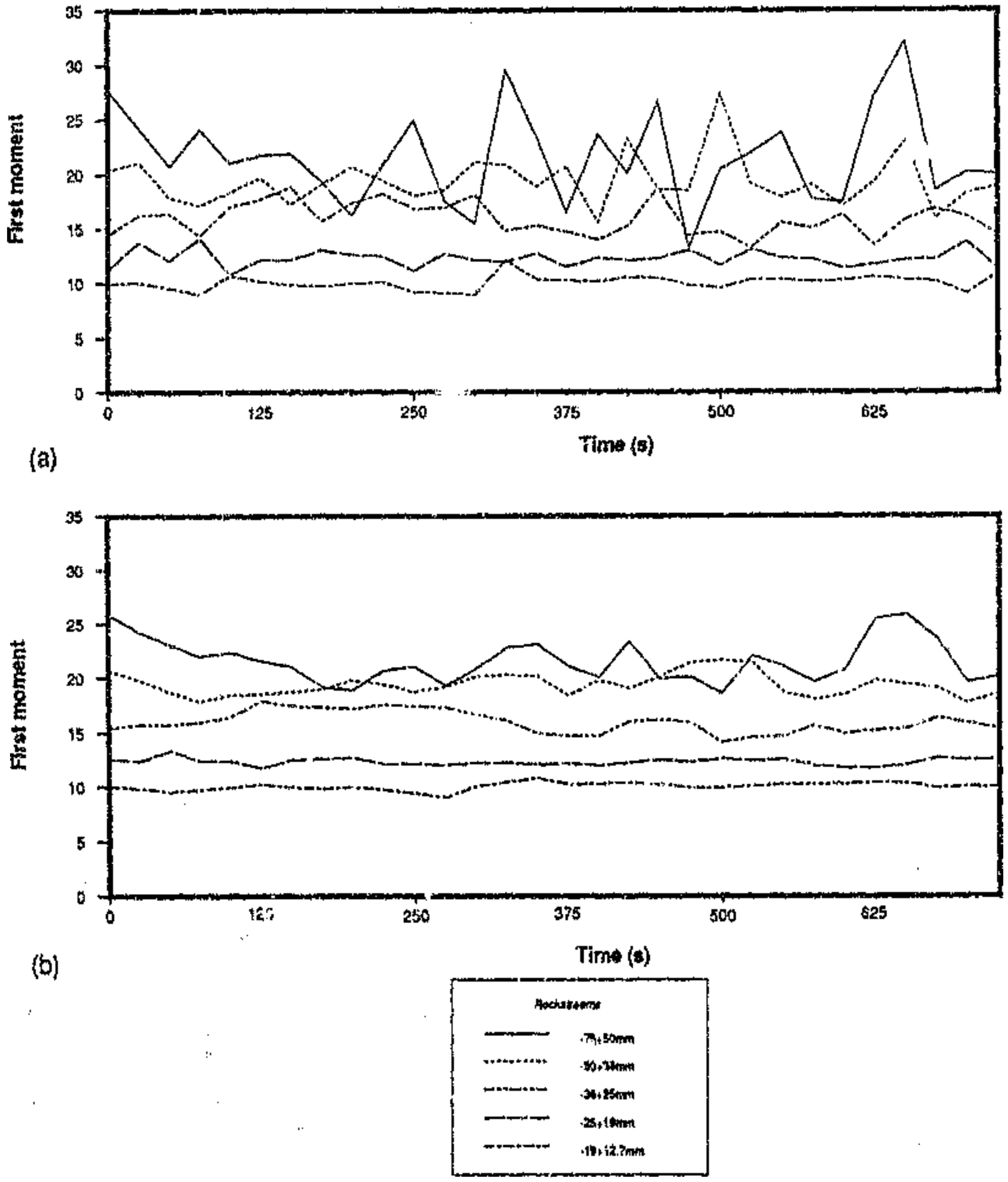

Figure 7.19:

Figure 7.21 shows the average first moments calculated from the mass experiment described in subsection 7.3.2. In this graph the first moment appears to vary almost linearly with the mass of large rock added to the belt.

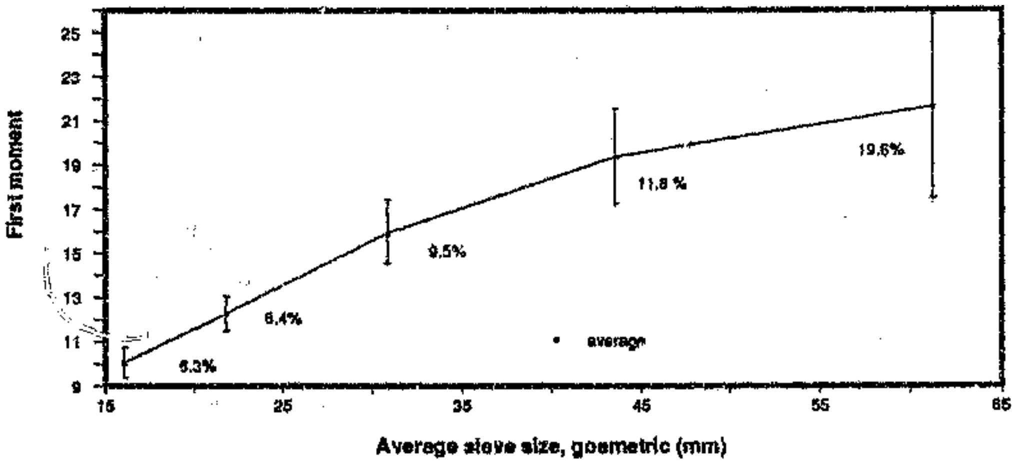

Figure 7.20: Plot of standard deviation $\sigma(\mu_{L_j})$ and average $\overline{\mu^*_{L_j}}$ of the first moments of the chord-length measured for each rock stream Ω_j of different average sieve size $\overline{D}$.

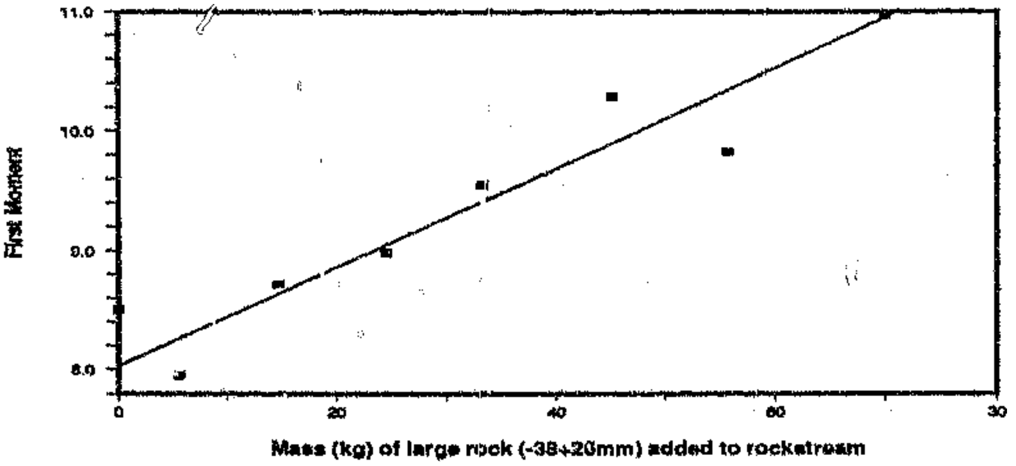

Figure 7.21: Plots of the average first moment of chord-length distribution $\mu_{L_{i,j}}$ measured for each rockstream versus the mass of large rock (-38+25mm) added to the belt already covered with small rocks (-12.7+9.5mm).

7.4 A NEW ROCKSIZE MEASUREMENT PHILOSOPHY

In the sections 7.2 and 7.3 chord-length distributions were transformed to give estimates or parameters of size distributions of the rockstreams Ω . In section 7.2, explicit *analytical* and *linear* methods for solving for $f(D)$ in terms of $p(L)$ were tested and the inversion processes were shown to be difficult to resolve because of the ambiguous nature of the rocksize problem as well as the noisy measurement. For example King's method which is founded on sound stereological principles, generated negative numbers for part of the size distributions, which are physically meaningless[7.2]. In section 7.3 the *cumulative* and *weighted* chord-length distributions or *moment* methods were proposed as alternative measurements. Although these alternative measurements were found to be linked to sieve size, these relationships were not of the form predicted in the literature and which require a different interpretation.

The above work clearly demonstrates the fundamental difficulty of estimating rocksize distribution, to which DeHoff (1982) comments that evidence is accumulating that stereological procedures for estimating certain particle size distributions are statistically unstable. All the results from this research as well as the comments in the literature, provides strong motivation for developing and utilizing alternative methodologies for estimating rocksize distribution. One such methodology is *quantitative serial sectioning* DeHoff (1982), which unfortunately cannot be applied to this rocksize problem for obvious reasons.

In order to "free" the estimation of rocksize from the constraints or limitations that continuously seem to disrupt its determination, a new philosophy for rocksize or size measurement is proposed, which is motivated to a certain extent by the success of the moment methods in section 7.3. This philosophy is based upon the following hypothesis which states that

> "*any measured parameter which varies with any perceived size characteristic of the rockstream Ω can be considered a valid indicator of the size or size distribution of the rocks in Ω*".

This hypothesis is based on two criteria :

1. That the parameter measured *must relate* in a unique and *useful* manner to the size characteristics of the rocks to which the user is referring in his particular application. For example, the first moment of the chord length distribution does relate to average sieve size.

[7.2] These negative values are probably a result of ignoring the correction term or the spike near the origin in the chord length measurement.

2. The parameters measured must satisfy "Matheron's sizing criterion" which consists of three axioms, defined in terms of mathematical morphology in section 7.5.1.

   Matheron's criterion (7.5.1) implies that the extracted parameter does not have to vary *in proportion* to sieve size, but must behave in a certain manner, to which we added the requirements of *repeatability* and *reliability*.

This hypothesis opens the door to other possible size measurement methodologies that could be applied to the measurement of moving rockstreams. For example, the cumulative and normalized chord-length distributions $P(L)$ do vary according to rocksize distribution $f(D)$. However further insight and a empirical approach is required to understand what is changing and what further parameter must be measured from $P(L)$ in order to satisfy the measurement requirement for a particular application. For example, reading off the slope of $P(L)$ at the origin $m_o = \frac{dP(L)}{dL}|_{L=0}$, or the percentage chord lengths at a certain size are some of the possible parameters which may be derived from $P(L)$ to help with mill control. Figure 7.22 shows these possible extracted measurements.

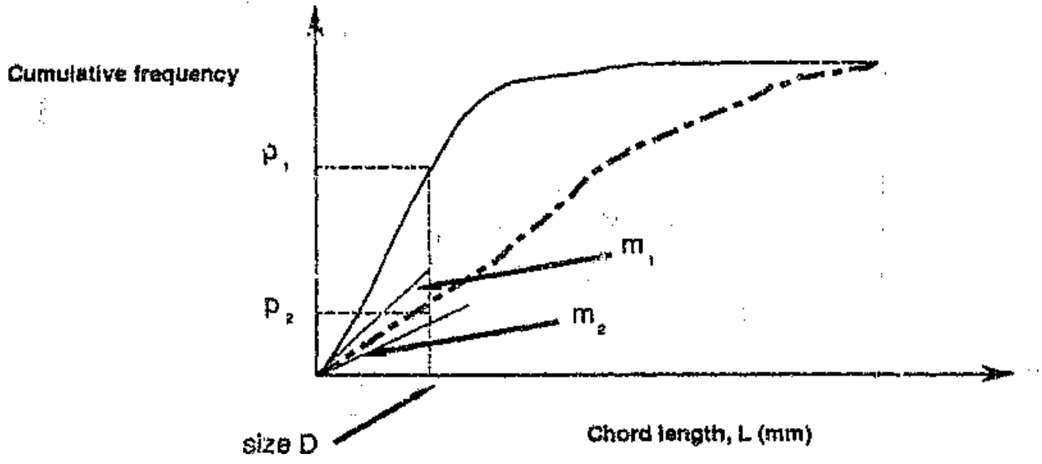

Figure 7.22: Extracting parameters such as slopes at the origin m_1, m_2 or cumulative percentage passing p_1, p_2 from the normalized cumulative frequency distribution of chord-lengths.

This heuristic approach to deriving measurements for a particular application does not require deep philosophizing but rather an experimental attitude. The nature of the raw data from which size parameters are measured must be kept in mind; ie that the data dealt with is simply only the number distribution of chord-lengths measured from "projected" areas of the rocks found on the top of Ω, which is related to rock size in a complex manner. However as will be shown in the next section, the tools of mathematical morphology provide a new methodology whereby new useful sizing transformations are defined which can extract rocksize distribution data that is meaningful and similar, yet at the same time different in concept, to sieve size.

7.5 MORPHOLOGICAL SIZE MEASUREMENTS

In the light of the hypothesis and the experimental and heuristic approach advocated in section 7.4, rocksize measurement techniques can be extended further by considering *morphological transformations* of the rock images, the outcome which is a function of the ***size*** and the ***shape*** of the rocks. If some measurement μ on a morphological transformation Ψ can be effected which varies reliably and sensitively with changing rock size or a required size parameter in accordance to the criteria given above, then we have the basis for some new indicators of rocksize.

The fundamental concepts behind morphological sizing are not new, (Matheron, 1975), (Serra, 1982), (Serra, 1988), (Maragos, 1989b). However the synthesis and application of these transformations to this conveyor-belt rocksize application can be regarded a new development.

The objective of this subsection is to introduce the idea of using mathematical morphology to extract some new parameters related to rock size as a demonstration of the hypothesis given in section 7.4 above. It must also be pointed out that most of these morphological procedures are very computationally intensive and take a long time (30 seconds to 30 minutes for a single image) to run to a 386 PC microcomputer, without any algorithmic optimization and at present are not envisaged as part of the rocksize instrument because of obvious realtime constraints. Obviously specially dedicated or faster hardware as well as optimized software can result in such algorithms being employed in an instrument in the future.

7.5.1 Defining a sizing Criterion

In order to use mathematical morphology for size measurement, an unambiguous criterion for sizing must be defined. This criterion is applicable to any other sizing methodology including the ones developed in section 7.3. Following on Matheron (1975), Serra (1982) states that by definition a sizing criterion in morphology is one which satisfies the *three axioms of Matheron*. In order to explain these three axioms in terms of mathematical morphology we borrow from Serra (1982) where he ascribes the *height of people* as the criterion for size measurement. To classify people according to height means to define a set transformation $\psi_\lambda(X)$ where X is the set of all people, and size is defined by the positive parameter $\lambda \geq 0$. The set transformation could be for example $\psi_{1.4}(X) =$ "the subset of people taller than 1.4m".

The three axioms that the set transformation $\psi_\lambda(X)$ must satisfy are as follows. The transformation must be

I *anti-extensive*

$$\psi_\lambda(X) \subset X \qquad \forall \lambda \geq 0 \tag{7.46}$$

II *increasing*

$$Y \subset X \quad \Rightarrow \quad \psi_\lambda(Y) \subset \psi_\lambda(X) \qquad \forall \lambda \geq 0 \tag{7.47}$$

III The *stronger sieve is the most important*

$$\psi_\lambda[\psi_\zeta(X)] = \psi_\mu[\psi_\lambda(X)] = \psi_{\mathrm{Sup}(\lambda,\zeta)}(X) \qquad \forall \lambda, \zeta \geq 0 \tag{7.48}$$

Axiom I implies, for example, that the set of all people taller than 1.4m is smaller than the general set of people. Axiom II implies that if the set of all males is taken from the main set, than the set of all males taller than 1.4 m is still a subset of the set of all people taller than 1.4m. Axiom III means that if we measure the size of people taller than 1.4m and then from this sub group select people taller than 1.6m, this is the same as selecting people taller than 1.6m which is the stronger sieve or condition. If $\zeta = \lambda$ then $\psi_\lambda[\psi_\zeta] = \psi_\lambda$ which means that the sizing procedure is *idempotent*.

These concepts although simple, are extremely powerful as they define the sizing process in an unambiguous and rigorous manner. Looking back at the sizing methods developed in section 7.2 and 7.3 it can be seen that the transformations developed in those subsections are only true on *average* with respect to the above axioms. The statistical and random nature of the whole measurement problem ensures that an individual measurement could very well violate any one of those axioms. Thus a possible measure of the "goodness" of the sizing transformations developed in this thesis could be how well they conform to the axioms, which is a measure of the confidence in the measurement. The better the size transformations comply with the above axioms implies that less data has to be averaged, which implies better dynamic behaviour and a faster response time of the system.

The full sizing procedure consists of the transformations $\psi_\lambda(X)$ followed by a measurement $\mu = \mu\{\psi_\lambda(X)\}$ where μ is an increasing positive function of λ. In practice μ is the *Lesbesgue* measure or Minkowski measures which are for example area and volume, see Serra (1982) chap. IV D,D1. In the next subsections morphological transformation for sizing rockstreams will be developed which on average conform with the above axioms.

7.5.2 Sizing using Morphological OPENING

Let B be a compact connected subset in the continuous plane $\mathbf{R}^2$ or the discrete (digital) plane $\mathbf{Z}^2$. If we let B by convention have size *one* then the finite set

$$\lambda B = B \oplus B \oplus B \ldots \oplus B \qquad 7.51$$

where $\oplus$ is the dilation operation repeated $\lambda - 1$ times, defines a family of binary patterns generated by the primitive structure B and parametized by the discrete size parameter $\lambda = 0, 1, 2, \ldots$. We now define the multiscale *opening* and *closing* of set X by a family of probes λB by equations [7.52] and [7.53] respectively.

$$X_{\lambda B} = X o \lambda B = (X \ominus \lambda B) \oplus \lambda B \qquad 7.52$$

$$X^{\lambda B} = X \bullet \lambda B = (X \oplus \lambda B) \ominus \lambda B \qquad 7.53$$

Equation [7.52] can be implemented by combining [7.51] into [7.52] to perform the following sequential operations

$$X \ominus \lambda B == \{(X \ominus B) \ominus B \ldots, \ominus B\} \oplus B \ldots \oplus B \qquad 7.54$$

Consider as an example the set of non-overlapping discs X_i where $X = \underset{i}{\cup}\{X_i\}$ as shown in figure 7.23 . These discs range in size from radius $r = 1$ to $r_{max} = 5$ units. The size distribution these circles can be measured by *opening* X with a set of *structuring elements* λB of size λ where λ varies from 1 to some maximum value. The result of an opening with a single structuring element λ will be $X_{(\lambda B)} = X o \lambda B$ where all the circles with radii less than λ will disappear. Thus the set $X_{(\lambda B)}$ is the set of circles with size $> \lambda$ and $X - X_{(\lambda B)}$ is the set of all circles with size $< \lambda$. Performing this operation with $\lambda = 1 \ldots r_{max}$ results in a set of transformed subsets of $S = \{X_B, .. X_{(\lambda-1)B}, X_{\lambda B} X_{(\lambda+1)B} \ldots X_{\lambda_{max} B}\}$ where

$$X_{\lambda B} = \psi_\lambda(X) \qquad \text{and}$$

$$X_{(\lambda+1)B} = \psi_{\lambda+1}(X) = \psi_{\lambda+1}[\psi_\lambda(X)]$$

$$\Rightarrow \qquad X_{(\lambda)B} = \psi_{\lambda-1}[\psi_{\lambda-2} \ldots [\psi_1(X)]] \qquad 7.55$$

and where $X_{1B} \supset X_{2B} \supset X_{3B} \supset \ldots X_{\lambda B} \supset \ldots X_{mB}$.

The generation of this family of sets S corresponds very well to the sieving process, where the shape of the mesh can be conceptually linked to the shape of the probe B . The sieving process separates rocks according to a series of fractions after which the fractions are weighed. In a similar way we require to generate the morphological fractions

$$W_{\lambda} = X_{\lambda B} - X_{(\lambda+1)B} \qquad 7.56$$

for $\lambda = 1 ... r_{max-1}$, and then to make a measurement μ on each set W_{λ} . If the number of entities (connected and closed sets) in each difference set W_{λ} are counted, or their areas calculated, then the size distributions of all the circles may be measured, ie for a single size class f_{λ} we have

$$f_{\lambda} = \mu\{W_{\lambda}\} = Mes[W_{\lambda}] \qquad 7.55$$

where *Mes* is one of the following measurements A, L, N which are the *areas*, *chord lengths* or *number* of elements calculated respectively. Formally the morphological size distribution f_X may be written, Maragos (1989b) as

$$f_X(\lambda, B) = \frac{-d}{d\lambda}\{Mes[X o \lambda B]\} = \frac{-d}{d\lambda}\{Mes[X_{(\lambda B)}]\} \qquad 7.56$$

Figure 7.24 shows the various subsets $S = \{ ... X_{\lambda B} .... \}$ generated from the circles given in figure 7.23, which conceptually looks the same as the sieving operation.

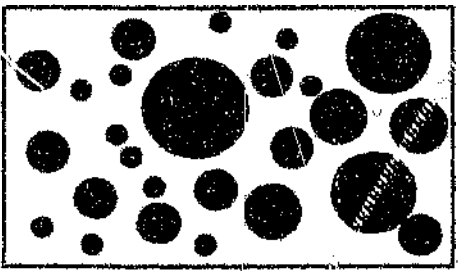

Figure 7.23: Sample set of circles of size $r = 1 .... p ... 5$

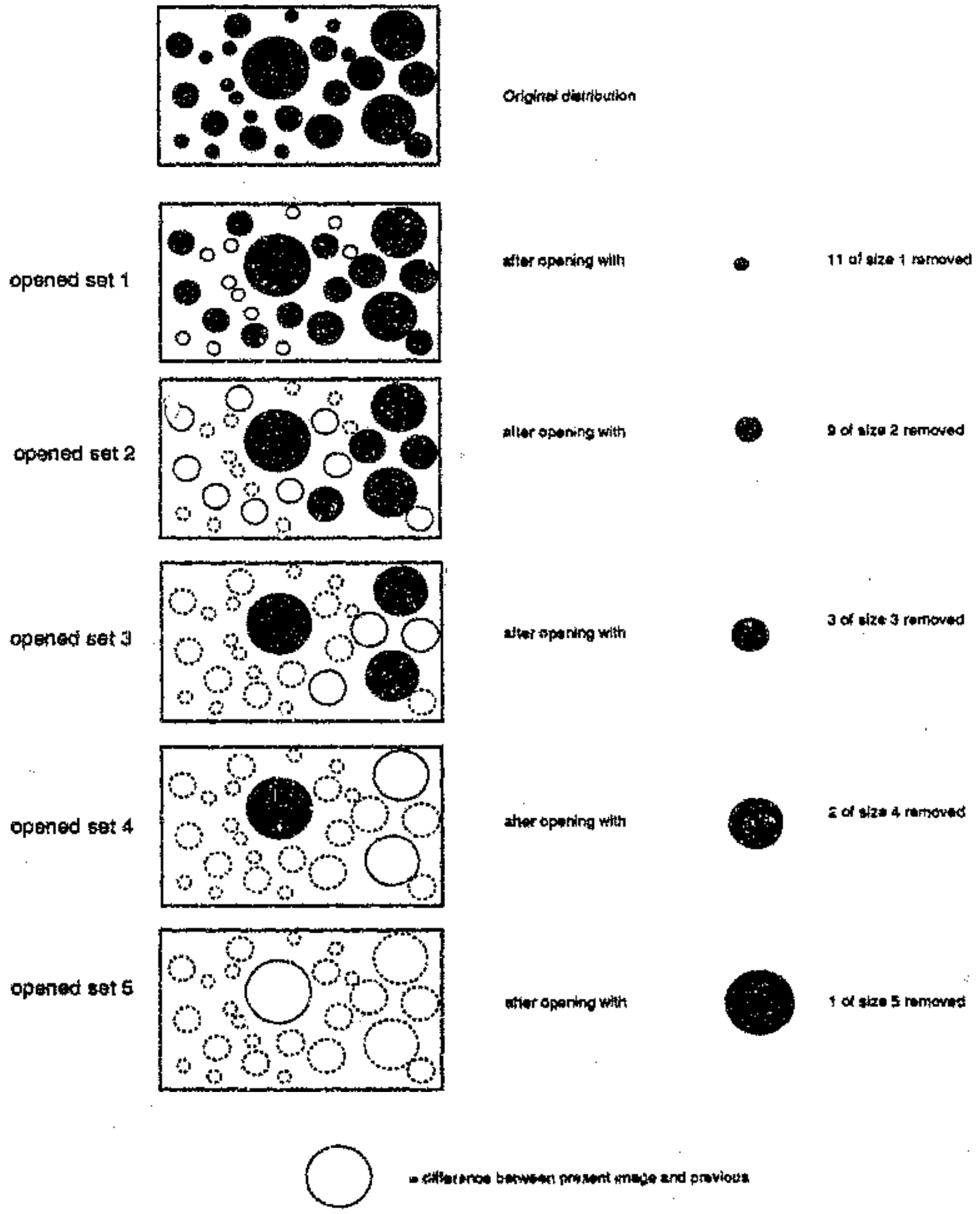

Figure 7.24: Set of circles after successive transformations $\psi_\lambda(X^{\lambda-1})$

This series of opening transformations was applied to a number of rock images captured from the conveyor belt using the algorithm shown in figure 7.25. After extraction of the rock edge patterns successive opening operations were applied to the edge pattern $E^{*}_{\partial x,Y}$ and adjacent chord length measurements made on the images containing the difference sets W_λ. Figure 7.26 shows part of a sequence of opening transforms made on a typical rock image with an elementary ***3X3 cross*** probe. The first moment of the chord length distributions were then calculated for each difference set with a probe of size λ to give a $\mu_L(\lambda)$ and a function $v_{o,\mu}(\lambda)$ which is plotted against λ. Figure 7.27 shows the first moment function $v_{o,\mu_j}(\lambda)$ for different rockstreams Ω_j. Figure 7.28 shows the same data except the first-moment functions have been integrated to give $V_{o,\mu}(\lambda) = \int_0^{\lambda} v_{o,\mu}(\lambda')d\lambda'$ and then normalised to 1.

In an interesting experiment the *differences* of functions v_{diff_j} was calculated and plotted, (figure 7.29), where $v_{diff_j} = v_{o,\mu_j}(\lambda) - v_{o,\mu_{j-1}}(\lambda)$ for sequential size classes of rockstreams. The differences of functions v_{diff_j} for these rockstreams reveal an interesting phenomenon, and this is that along λ axis they correspond spatially to the sieve size distributions when placed alongside one another.

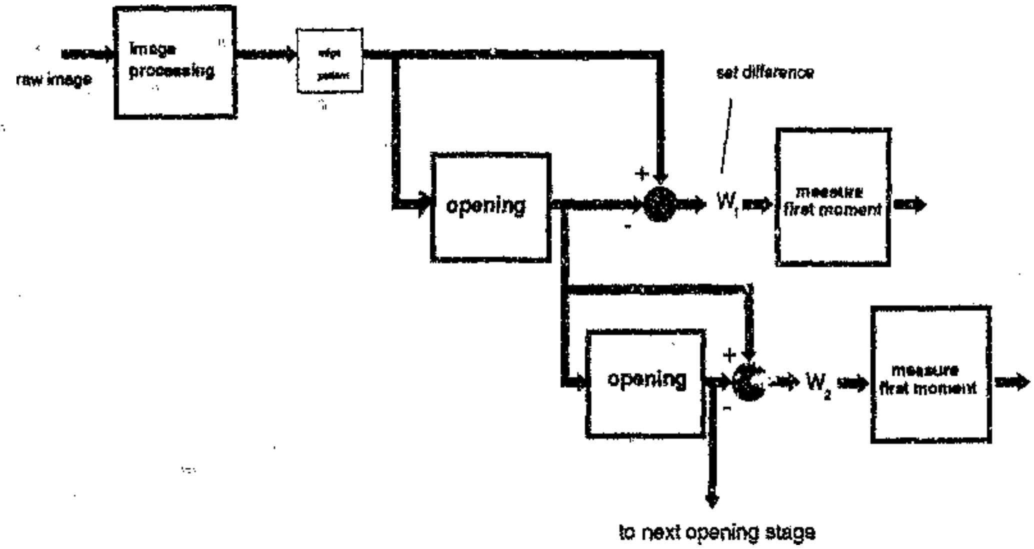

Figure 7.25: Block diagram of the algorithm implemented to calculate the morphological size distribution using the *opening* operation

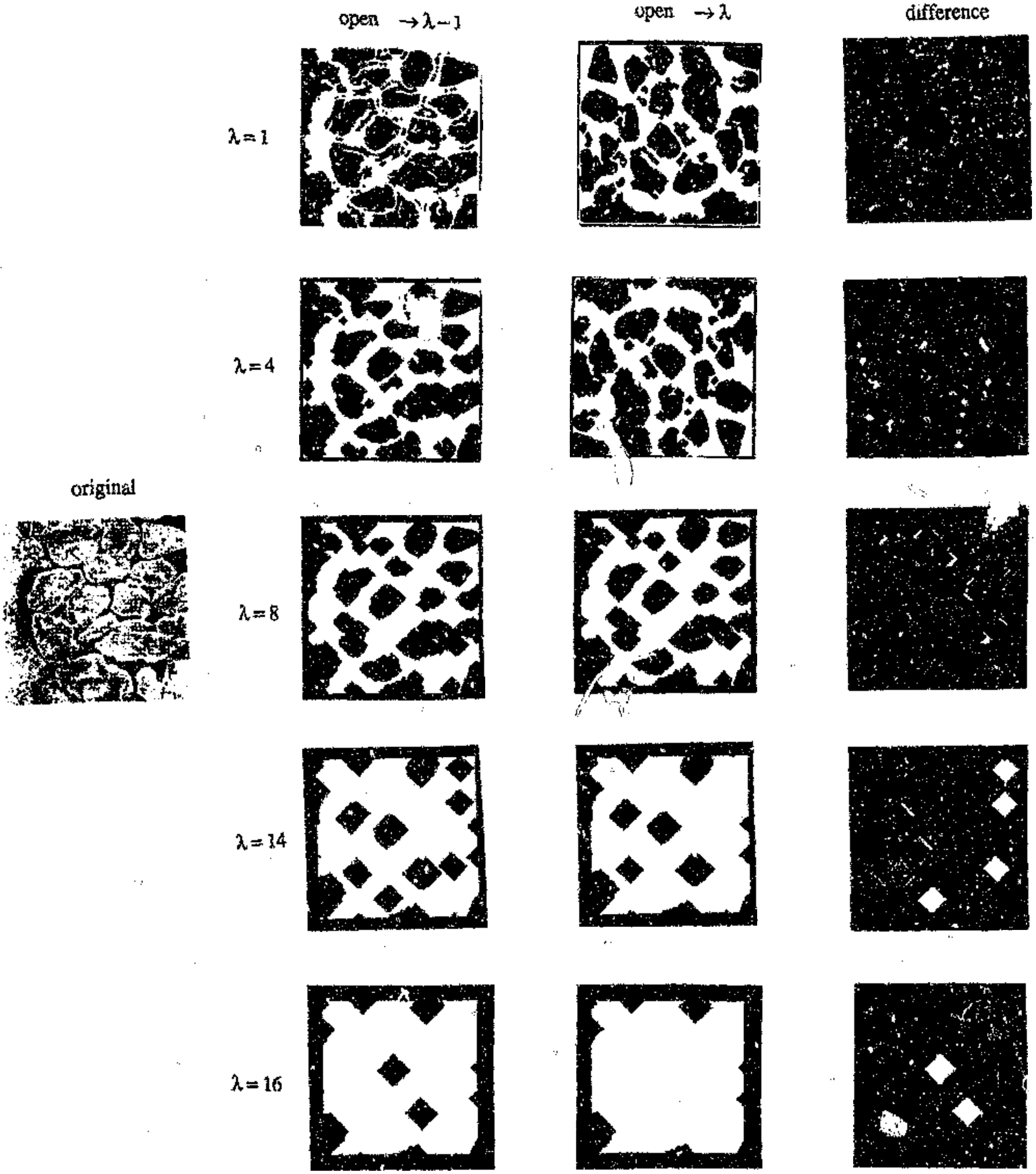

Figure 7.26: Resultant opened-images and difference images W_λ after morphological openings with cross probes λB of varying size.

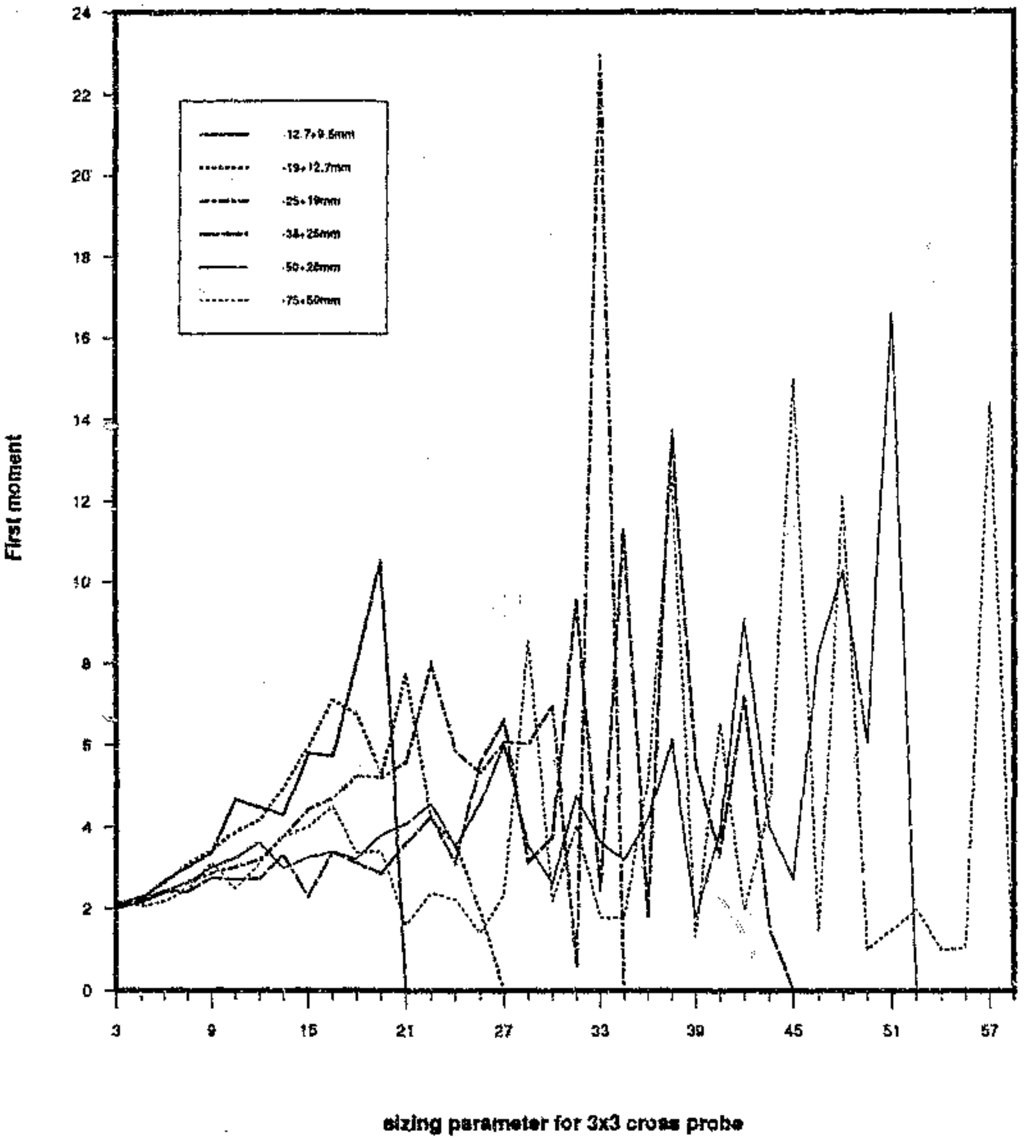

Figure 7.27: The first-moment functions $v_{o,\mu_j}(\lambda)$ measured from the difference sets of successively opened images of different rocksize distributions Ω_j.

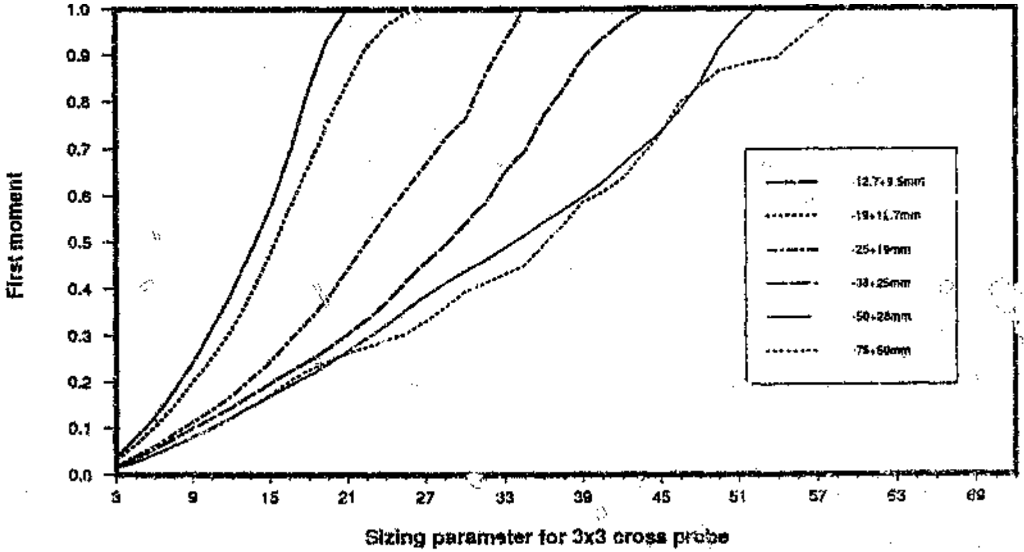

Figure 7.28: The *integrals* or *cumulative* of the first-moment functions $V_{e,\mu_j}(\lambda)$ measured from the difference sets of successively opened images of different rocksize distributions Ω_j, and normalized to 1.

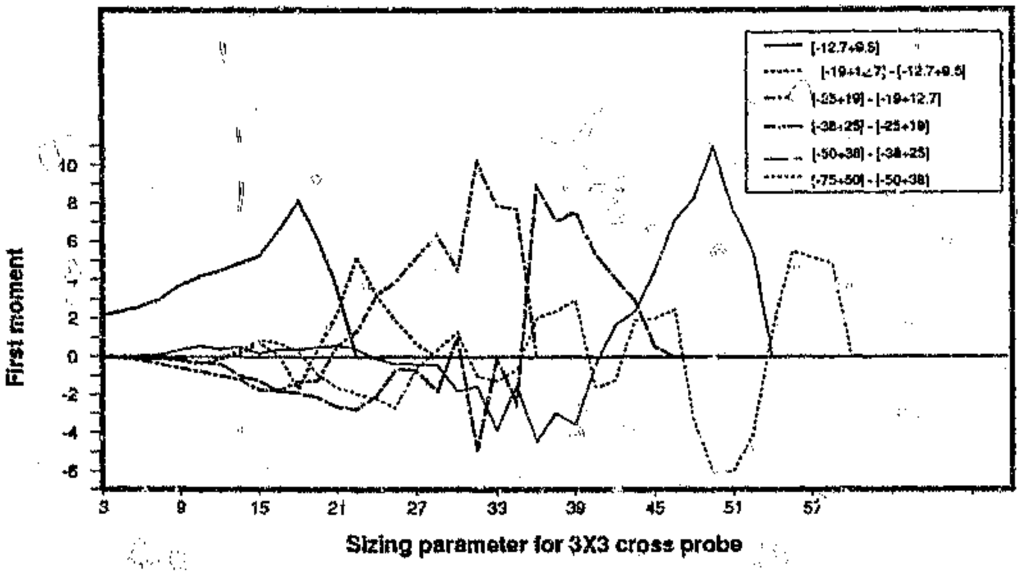

Figure 7.29: *Differences* of the first moment functions of the chord-length distributions $v_{\delta\Omega_j}(\lambda)$ measured from the difference sets of successively opened images of different rocksize distributions Ω_j.

7.5.3 Sizing using Morphological EROSIONS

In the same way that successive openings in subsection 7.5.2 give rise to a series of transformations similar to the sieving process, successive *erosions* also provide the means with which parameters can be generated which are related to size. Note that the concept of erosions does not link as clearly to sieve size as does the opening operation.

A series of test probes λB (3x3 cross), parametized by the size parameter λ is defined, as is used in section 7.5.2 above. However instead performing *opening* on the set of rock "projections" X, the set X is *eroded* to give the set images according to equation [7.57].

$$X_{\Theta,\lambda} = \psi_{\lambda}\{X\} = X \ominus \lambda B \qquad 7.57$$

A measurement μ is then made on $X_{\Theta,\lambda}$ which again could be area, chord length or number. Again with this transformation the measurement μ was chosen to be chord-lengths measured from adjacent probes, to give a first-moment function $v_{\Theta,\lambda}(\lambda)$. Figure 7.30 shows schematically the algorithm used, and figure 7.31 shows the result of successive openings on the projected areas of a typical rock scene. Figure 7.32(a) shows the first moment function $v_{\Theta,\mu}(\lambda)$ plotted against λ and figure 7.32(b) shows the same data except the function have been converted to *density* functions as done in equation [7.11].

What is apparent from figure 7.32(a) and (b) is that the this erosion method does reveal useful size information. Again depending on the application, certain parameters can be derived from these curves which can be used for process control, eg the average slope or x-axis intercept in figure 7.32(b).

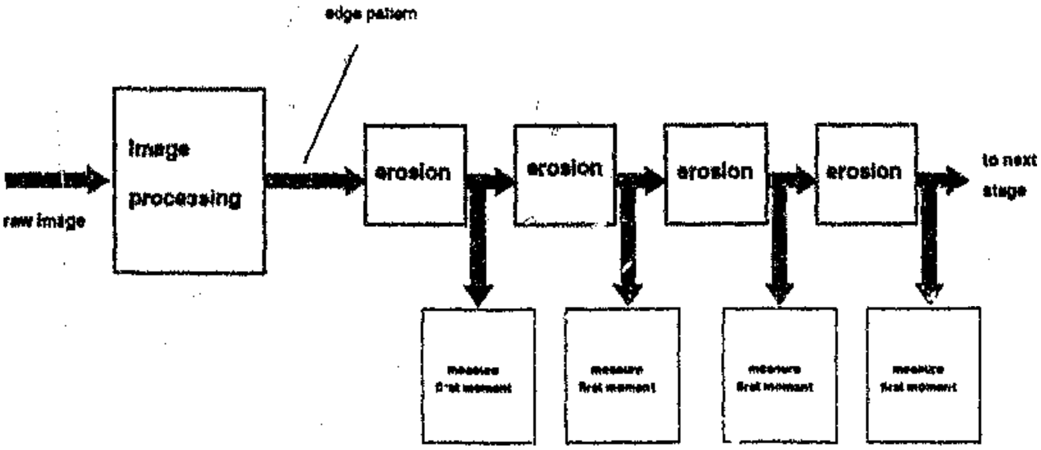

Figure 7.30: Schematic diagram of the algorithm used to obtain the *erosion* size functions.